ATB
Agrartechnik Bornim

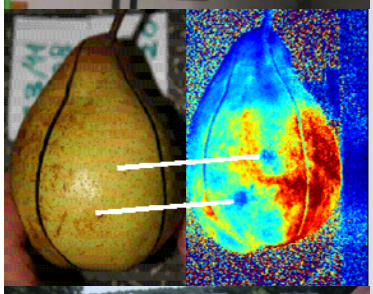

Image Analysis for Agricultural Products and Processes

15. Workshop Computer-Bildanalyse in der Landwirtschaft

27. to 28. Aug. 2009 Potsdam

IVIA

SARDI
SOUTH AUSTRALIAN RESEARCH AND DEVELOPMENT INSTITUTE

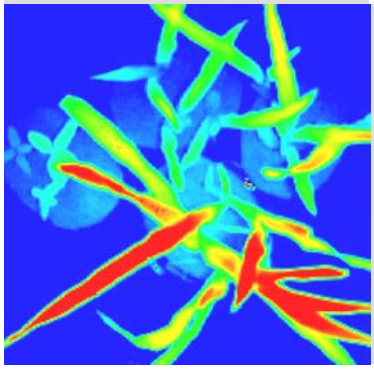

Bornimer Agrartechnische Berichte

Heft 69

Potsdam-Bornim 2009

ATB
Agrartechnik Bornim

Image Analysis for Agricultural Products and Processes

15. Workshop Computer-Bildanalyse in der Landwirtschaft

27. to 28. Aug. 2009
Potsdam

Bornimer Agrartechnische Berichte
Heft 69

Potsdam-Bornim 2009

Published by:

Leibniz-Institut für Agrartechnik Potsdam-Bornim e.V.
Max-Eyth-Allee 100
14469 Potsdam-Bornim
☎ (0331)-5699-0
Fax.: (0331)-5699-849
E-mail: atb@atb-potsdam.de
Internet: http://www.atb-potsdam.de

August 2009

Editor:

Prof. Dr. habil. Manuela Zude

Layout:

Andrea Gabbert

Published by the Leibniz Institute for Agricultural Engineering Potsdam-Bornim e.V. (ATB) with the support of the Federal Ministry of Consumer Protection, Food and Agriculture as well as of the Ministry of Agriculture, Environment Conservation and Regional Policy of the State Brandenburg.

Contents do not necessarily reflect the publisher or editors views in this area.

ISSN 0947-7314

Foreword

A new CIGR working group (Image Analysis for Agricultural Processes and Products) was launched during the last CIGR International Conference in September 2008 in Brazil. The aim of this group is to work together with existing Sections of CIGR to increase the collaboration between institutions, enterprises and individuals in the field of image analysis.

This working group is devoted to encourage research, exchange of information, discussion and any other type of co-operation between industry and academia in the development and testing of software and hardware components and the creation of reference materials related to the use of image analysis methods in agricultural and biosystems engineering.

Thus our objectives are:

* To meet recent demands of process monitoring in agricultural production, during storage and processing of raw materials

* To develop objective, sensitive, and reliable optical tools for receiving analytical data in a non-destructive way.

During 2008, the governing board, constituted by Prof. Manuela Zude (Germany), Prof. Thomas Banhazi (Australia) and myself (Spain) has been working hard to attract interested scientists and enterprises to join this working group. In addition, we heavily promoted our 1st International Workshop on Computer Image Analysis in Agriculture, that is being held in Potsdam.

At present time, our working group has 142 members from 12 countries and 4 continents. Moreover, we have developed a web page (http://www.atb-potsdam.de/CIGR-ImageAnalysis/) and are determined to continue expanding the scope of our working group.
I would like to express my gratitude for the excellent work undertaken by the local organising team of this workshop, led by Prof. Zude. We all know how difficult it is to establish a new Working Group and organising an International Workshop (involving many individuals and Institutions) is not an easy task either. Thanks also to our host, the Leibniz Institute for Agricultural Engineering Potsdam-Bornim, and to all our sponsors (CIGR, EurAgEng, ASABE, IVIA and SARDI). We simply could not organise this meeting without their continuous support.

All the preliminary effort has been made, so now it is time for you to make this meeting fruitful. Enjoy the company of other international experts, share your knowledge, start new co-operative projects and update your current understanding of the Image Analysis field. However, in the process please do not forget to enjoy Potsdam and this wonderful

country of Germany. In summary, I wish you (on behalf of the Working Group and the Workshop organising committee) a very productive and enjoyable time during our 1st International Workshop on Image Analysis!

Professor Enrique Molto

IVIA, AgroIngenieria, Cra. Moncada-Naquera Km 5, 46113, Moncada, Spain

Corresponding author: molto_enr@gva.es

IMG – Program

Aug. 27th to 28th, 2009
Potsdam, Germany

	Thursday, August 27
Thursday 12:00 – 14:00	Registration

	Thursday, August 27
14:00 – 15:45	
14:00 – 14:30	Welcome and introduction *Enrique Molto*
14:30 – 15:00	Hyperspectral imaging for food quality evaluation *Da-Wen Sun*
15:00 – 15:45	Image based 3D inspection of surfaces and objects *Michael Heizmann*
	Coffee Break
16:30 – 17:50	
Chair: Laszlo Baranyai	
16:30 – 16:50	Computer vision developments for the automatic inspection of fresh and processed fruits *José Blasco, Nuria Aleixos, Sergio Cubero, Florentino Juste, Juan Gómez-Sanchis, Vicente Alegre, Enrique Moltó*
16:50 – 17:10	Analysis of color variations on sunflower crop images, owning to changes in environmental illumination. *Gonzalo Ruiz Ruiz, Luis Manuel Navas, Jaime Gómez Gil*
17:10 – 17:30	ImageInspector: a multipurpose system for agri-food products *Gianfranco Venora, Oscar Grillo, Rossella Saccone, Concetta Ravalli*
17:30 – 17:50	Comparison of different classification algorithms for weed detection from images based on shape parameters *Martin Weis, Till Rumpf, Roland Gerhards, Lutz Plümer*
19:00	**Dinner**

Friday, August 28

Chair: Manuela Zude

09:30 – 09:50 Potential applications of hyperspectral Imaging for quality control in dairy foods
Aoife A. Gowen, J. Burger, D. O'Callaghan, C.P. O'Donnell

09:50 – 10:10 Species discrimination using spectral/spatial descriptive statistics
Scott D. Noble, Ralph B. Brown

10:10 – 10:30 How to achieve gold standards in agricultural applications?
László Baranyai, Andrée Jacobs

Coffee Break

Chair: Michael Heizmann

10:45 – 11:05 Usability study of 3D time-of-flight cameras for automatic plant phenotyping
Ralph Klose, Jaime Penlington, Arno Ruckelshausen

11:05 – 11:25 Calculation of flow vector in plants by non-destructive imaging using neutron radiography
Uzuki Matsushima, Wolfgang Graf, Nikolay Kardjilov, Hiroshi Shono, Werner B. Herppich

11:25 – 11:45 Monitoring optical properties of apple tissue during cool storage
László Baranyai, Christian Regen, Manuela Zude

11:45 – 12:05 Systems for multisensor navigation and 3D-modelling
Anko Börner, Ines Ernst, Denis Grießbach

12:15 - 13:15 *Lunch*

13:30 - 15:00 Poster presentations (5 Minutes each)

Preliminary results on the non-invasive diagnosis of superficial scald in 'Rocha' pear by fluorescence imaging
Ana Margarida Cavaco, D. Antunes, J. Marques da Silva, R. Antunes, R. Guerra

Synchrotron x-ray CT of rose peduncles – evaluation of tissue damage by radiation
Uzuki Matsushima, Wolfgang Graf, Simon Zabler, Ingo Manke, Martin Dawson, Gerard Choinka, Werner B. Herppich

Image processing for the determination of jam browning kinetics
Davide Ricauda Aimonino, Lorenzo Comba, Paolo Gay

Detection of weeds using image processing and clustering
Martin Weis, Roland Gerhards

Correlation between vegetation indices and leaf n content and dry matter production in *Brachiaria decumbens*
Mario Cupertino da Silva Júnior, Francisco de Assis de Carvalho Pinto, Daniel Marçal de Queiroz, Enrique Anastácio Alves, Luis Manuel Navas Gracia, Jaime Gomez Gil

Structure investigation of soil aggregates treated with different organic matter using X-ray micro tomography
Keiko Nakano, Werner B. Herppich, Nikolay Kardjilov, Ingo Manke, Andre Hilger, Martin Dawson, Kinya Masuda, Yoshitaka Hara, Uzuki Matsushima

Determination of bread crumb porosity using statistical analysis of surface pattern
Aniko Lambert-Meretei, György Csima, Medea Nogula-Nagy, László Baranyai, András Fekete

Application of morphometric image analysis system to evaluate the incidence of Fusarium head blight wheat infected kernels
Paolo Menesatti, Francesca Antonucci, Corrado Costa, Alberto Santori, Iliana Nicia-relli, Alessandro Infantino

Characterization of morphological properties of apricot stones by image processing
Joszef Felföldi, F. Firtha, R. Hermán, A. Pedryc

Non agressive orange acid and sugar indexes estimation system
Tomas J. Arnau, José M. Sotoca, Filiberto Pla

Hyperspectral reflectance imaging for detecting defects on fruits
Byoung-Kwan Cho, Moon S. Kim, Man-Soo Kim

Methods for head blight recognition: chlorophyll fluorescence and hyperspectral image analysis
Elke Bauriegel, Werner B. Herppich, Antje Giebel, Karl-Heinz Dammer, Horst Beuche, Joachim Intreß, Bernd Rodemann

Optical systems and moduls
Michael Rudolph, Ocean Optics

15:00 – 16:00 Chair: Enrique Molto
Discussion and conclusions
Announcement of next meeting

Hyperspectral imaging technology for food quality and saftey evaluation and inspection

Da-Wen Sun

Food Refrigeration & Computerised Food Technology, University College Dublin, National University of Ireland, Agriculture & Food Science Centre, Belfield, Dublin 4, Ireland.
Corresponding author: dawen.sun@ucd.ie

Over the years, optical sensing technologies have been investigated as potential tools for non-destructive evaluation and inspection for food quality and safety. In particularly, methods based on two mature technologies of imaging and spectroscopy have been widely studied and developed, resulting in many successful applications in the food industry. However further development of these conventional imaging and spectroscopy techniques is limited by their inabilities to obtain sufficient information from individual food items. Therefore by taking the most useful characteristics of these two mature technologies: imaging and spectroscopy, hyperspectral imaging (or imaging spectroscopy) has emerged as a technology with great potential for effective and non-destructive quality and safety evaluation and inspection in the area of food processing.

A conventional imaging system or more specifically computer vision is a common technique for detecting surface features. The system normally consists of lighting and an area detector, with the light source providing illumination to the sample and the area detector capturing mixed spectral contents from the sample. Spatial information of the sample is obtained in the forms of monochromatic or colour images, therefore conventional imaging system is used for colour, shape, size, surface texture evaluation of food products and for surface defects detection in food inspection, however it cannot identify or detect chemical properties or characteristics from a food product.

On the other hand, conventional spectroscopy system is a technique for evaluating chemical properties or characteristics of food products. Such a system generally includes a light source, a wavelength dispersion device, and a point detector. In this system, light is dispersed into different wavelengths after interaction with the sample in order for the point detector to collect the dispersed light to obtain spectral information from the sample. As the point detector has its size limitation, conventional spectroscopy system cannot cover a large area or a small area with high spatial resolution. Therefore the technique does not provide the spatial information which is regularly required for and is critical in food inspection.

With the integration of the main features of imaging and spectroscopy, hyperspectral imaging can simultaneously acquire both spatial and spectral information that is critical to the detection of food safety and evaluation of food quality attributes. A typical hyperspectral system consists of a light source, a wavelength dispersion device, and an area

detector. The images are acquired over the visible and near-infrared (or infrared) wavelengths to specify the complete wavelength spectrum of a sample at each point in the imaging plane. These images are then combined and form a three dimensional hyperspectral cube, with two dimensions for describing spatial information and the third one for spectral information. In this hypercube, each spectral pixel corresponds to a spectral signature (or spectrum) of the corresponding spatial region, recording the entire measured spectrum of the imaged spatial point. Therefore the measured spectrum indicates the ability of the sample in absorbing or scattering the exciting light, representing the inherent chemical properties of a sample. As a result, the technology provides us with unprecedented detection capabilities, which otherwise cannot be achieved with either imaging or spectroscopy alone. If conventional imaging is to provide the answer to the question of where and conventional spectroscopy is to provide the answer to the question of what, hyperspectral imaging is a technique to provide the answer to the question of where is what.

Hyperspectral imaging techniques have received much attention for food quality and safety evaluation and inspection. Many approaches and applications have shown the usefulness of hyperspectral imaging in the food industry. These applications include meat quality assessment, automated poultry carcass inspection, quality evaluation of fish, bruise detection of apples, quality analysis and grading of citrus fruits, bruise detection of strawberry, visualization of sugar distribution of melons, measuring ripening of tomatoes, defect detection of pickling cucumber, and classification of wheat kernels. Interested readers are advised to refer to the following list of publications for further information.

References

SUN D.-W. (2009): Hyperspectral Imaging for Food Quality Analysis and Control, Academic Press / Elsevier, San Diego, California, USA, 15 Chapters

SUN D.-W. (2008): Infrared Spectroscopy for Food Quality Analysis and Control, Academic Press / Elsevier, San Diego, California, USA, 416 pp., 978-0-12-374136-3

SUN D.-W. (2008): Computer Vision Technology for Food Quality Evaluation, Academic Press / Elsevier, San Diego, California, USA, 583 pp., ISBN 978-0-12-373642-0

Image based 3D inspection of surfaces and objects

Michael Heizmann

Fraunhofer Institute for Information and Data Processing, Fraunhoferstrasse 1, 76131 Karlsruhe, Germany
Corresponding author: michael.heizmann@iitb.fraunhofer.de

Abstract: *The shape constitutes an essential property of surfaces and objects. It can be obtained by a variety of contact-free measurement principles based on optical images. In this contribution, common and modern methods of shape measurement based on optical images, which are suitable for determining the macroscopic shape of surfaces, are presented. The characteristic properties of the measurement principles (e.g. with respect to reflectance characteristics and inspection conditions) are highlighted and compared.*

1 Introduction

Compared to usual techniques of capturing images from a scene[1], 3D inspection requires additional effort with respect to the acquisition devices and/or the acquisition time to obtain shape properties. This additional effort must be justified by the opportunity to obtain supplementary or superior information that cannot be obtained without 3D inspection. In this context, 3D inspection of scenes mainly has three objectives:

- Measurement of the physical dimensions of the scene: in this case, the task is to obtain a measurement of geometric properties of the scene, e.g. lengths, planarity, roughness etc. and a respective confidence.
- Analysis of the surface shape: the task here is to characterize the shape properties of the scene by means of methods from texture analysis (GONZALEZ & WOODS 2007, SCHAEL 2005) and pattern recognition (DUDA *et al.* 2001).
- Detection of defects: within this task, significant deviations of shape properties (e.g. geometric measures or textural properties) from a desired property must be detected.

This contribution focuses on techniques that are able to gather shape information on a scene based on optical images, which means that cameras are used for the data acquisition. The advantage of such techniques is that industrial optics has reached a considerable degree of maturity, making such inspection techniques cost-effective.

[1] A scene in this contribution is defined as the part of the real world imaged by the camera. It usually consists of the object of interest and the irrelevant background.

2 Modeling objects and surfaces

Concerning the representation of a three dimensional object, two different models are common in the measurement community:

- 3D models: such models contain surface points, edges or planes of the object in a fully three dimensional representation. Therefore, they are able to represent all shape properties. Views and intersections can be generated, and the models can be used for all Euclidean moves (rotations, translations) without losing significance. Such models are commonly found in Computer Aided Design (CAD).
- 2.5D models (pseudo 3D, depthmaps): in this case, the information on the third dimension (the height or depth) is indicated as a function of the location, e.g. in the representation $z = f(x,y)$ with the height value z and the location coordinates (x,y). 2.5D models are not able to describe undercuts or tunnels, where more than one height value must be assigned to a location. Such models may be modified by translations without loss of significance, however, rotations are only permitted with vertical axis (x = const., y = const.).

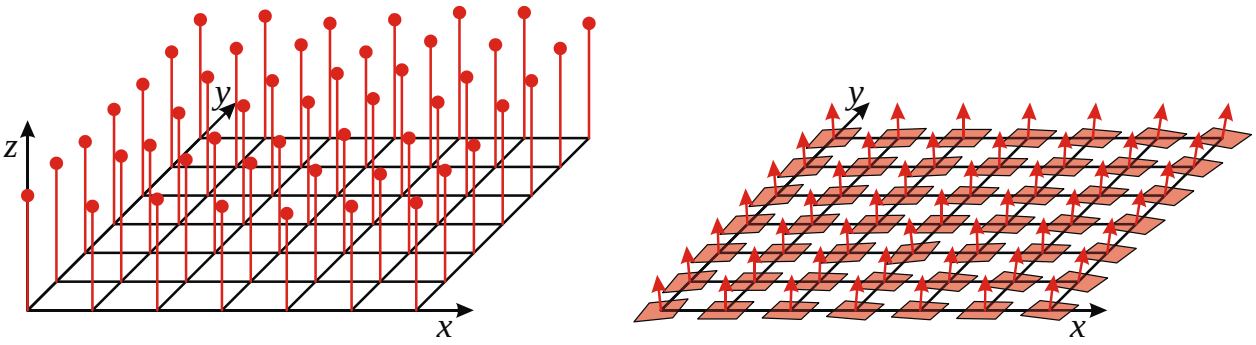

Figure 1: Comparison of two different types of shape information determined by inspection techniques: 2.5D point cloud (left) and local inclination (right)

Techniques for 3D inspection may yield to different types of shape information, see **Figure 1**. First, the information may consist in measured 3D or 2.5D points, which together form point clouds. Second, the measurement may yield the local inclination for each measuring point. Both types of shape information can be combined together with available previous information to form models on the surface to be inspected. These models can be classified with respect to the basic objects used to represent the surface:

- Vertex models: the measured points are the basic objects themselves. Information on edges, planes, or volumes is not available.
- Wireframe models: edges between measured points are the basic objects. Information on planes or volumes is not available. Such models are commonly used to give a quick overview for the display of spatial objects, e.g. for previews in real-time systems.

- Surface models: such models consist of the combination of analytical surfaces (planes, cylinders, spheres etc.) or approximating surfaces (e.g. based on splines). Visible and occluded surfaces can be distinguished; information on the volume is not available.
- Volume models: basic objects are three-dimensional bodies. The models are built by combination of fundamental bodies (e.g. in CAD) or by determination of the closed surface from surface models.

4 A classification of image based 3D inspection methods

Image based inspection methods can be divided into the methods using active and the ones using passive illumination, see **Figure 2**. The characteristic property of the previous ones is the need for an illumination device that has certain specific properties with respect to the illumination field generated by them.

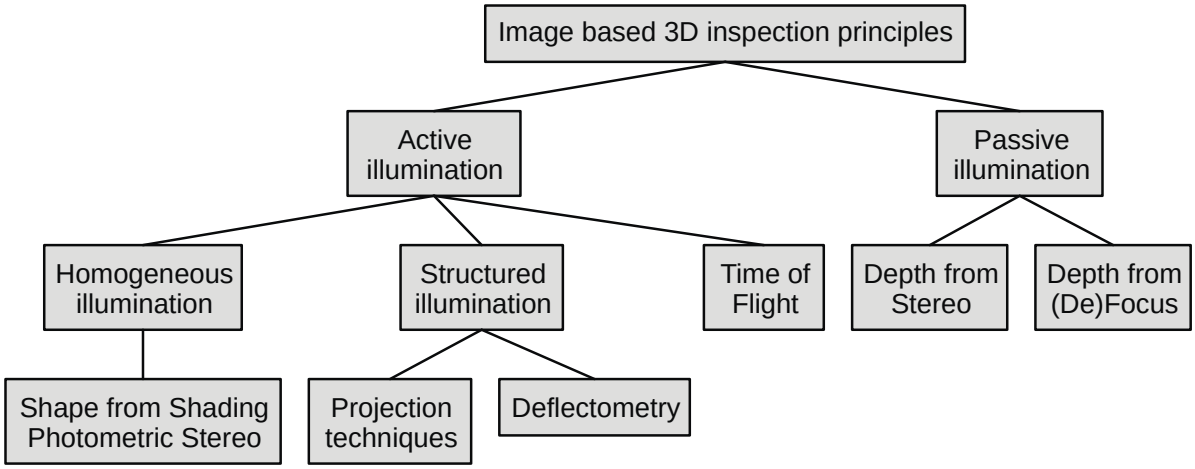

Figure 2: Classification scheme for image based 3D inspection methods

4.1 Active Illumination

The basic principle of active illumination approaches is that the shape of the surface to be inspected acts as a kind of modulation for the predefined illumination field, see **Figure 3**. The modulation result acquired by the camera is then processed in the image evaluation in order to obtain the desired quantitative (e.g. in form of a shape reconstruction or a normal field) or qualitative information (e.g. to detect defects) on the surface.

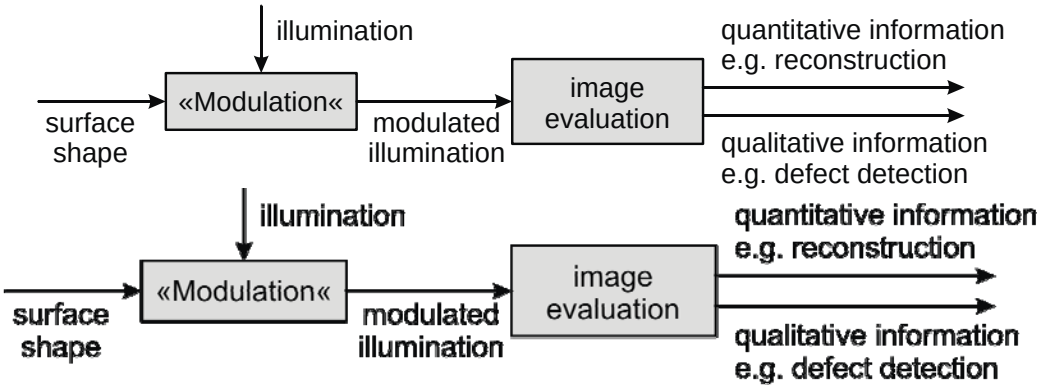

Figure 3: Inspection principle for active illumination approaches

Among the approaches using active illumination, methods of homogeneous illumination (like e.g. photometric stereo), of structured illumination (like e.g. projection methods and deflectometry), and methods based on the measurement of the time of flight can be subdivided.

4.1.1 Homogeneous illumination

Approaches using homogeneous illumination are characterized by a spatially constant illumination field, i.e. the direction, the intensity, and the spectrum of the irradiance is constant within the surface to be inspected. The major approach to use homogeneous illumination for 3D inspection is Shape from Shading (HORN 1989), where the shape information is contained in one or several observations of the surface under different homogeneous lighting directions.

A common realization is established by Photometric Stereo, where at least three illumination directions are used. The lightings can be switched subsequently in order to obtain an image series with varied illumination or applied simultaneously if lightings with distinct spectra are used. Inclined surfaces appear with different radiances that are characteristic for the respective inclination. By means of a suitable modeling of the surface reflectance, the local inclination can be obtained. As an additional outcome, the reflectance of the surface is obtained. The precondition for the applicability of the approach is that the reflectance model must be known a priori, e.g. the Lambertian model in the easiest case. In addition, the surface must not show perfectly specular reflection. Objects with volume scattering, very dark surfaces, strongly instationary reflection properties or steep slopes should be avoided.

Figure 4 shows the example of a packaging foil. Whereas in each image of the illumination series, the shape and the reflectance information are strongly coupled (left image), the photometric evaluation reveals the surface inclination and the reflectance as separated properties of the surface (right images).

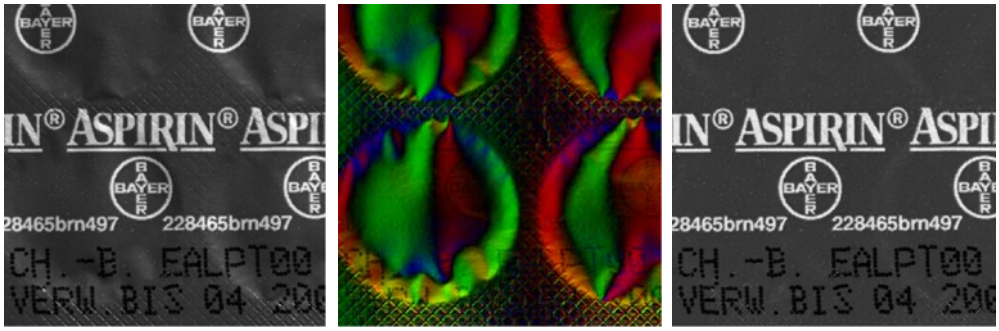

image from the series with directional lighting

surface inclination (color: azimut, intensity: polar angle)

surface reflectance

Figure 4: Photometric inspection of a packaging foil

4.1.2 Structured illumination

In the case of structured illumination, the effects of the interaction between an inhomogeneous lighting pattern and the surface shape are evaluated. An advantage of the principle is its applicability for many surfaces of practical importance, since it is independent to a large extent of the exact optical properties of the surface such as color, reflectance or scattering properties. Depending on the predominant reflectance component (diffuse or specular reflection) projection techniques and deflectometry are preferably applied, see **Figure 5**.

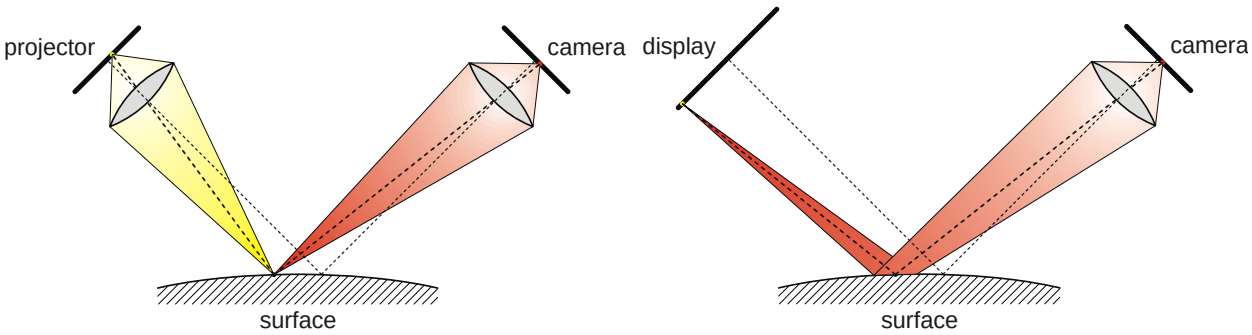

Figure 5: Principle of projection (left) and deflectometry (right)

In projection techniques, a projector (e.g. a laser or a beamer) casts a known sequence of patterns on the surface to be inspected, see **Figure 5** left. The camera receives the mapping of the projected pattern, which is deformed by the surface. The principle is based on the evaluation of the triangles which are established by the projection and the imaging of patterns on the surface. It requires that a part of the incident light is diffusely reflected, whereas the exact reflectance or color is irrelevant. As result, projection techniques provide spatial positions of surface points, which can then be combined to obtain shape information on the surface. Common realizations are laser triangulation, line scanning, and stripe projection.

Figure 6 shows the principle of projection techniques on the example of a line scanning sensor. A line laser projects a line pattern on the surface. A matrix camera is applied as detector. Within one image of the camera, the spatial positions of surface point on a scanning line are acquired. In order to obtain information on an area, the sensor must be moved relative to the surface. That way, shape information is acquired line by line.

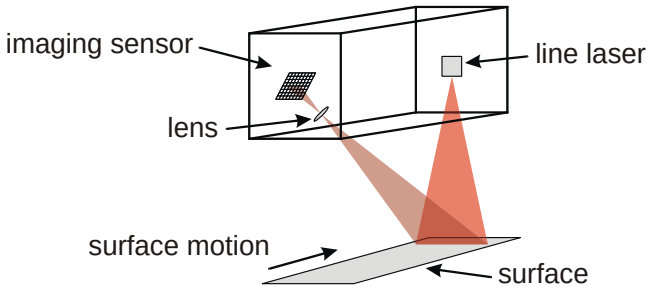

Figure 6: Inspection principle of a line scanning sensor

The principle of deflectometry can be compared to the way a human observer inspects specular surfaces: instead of looking on the surface itself, he observes the reflection of a structured environment in the surface (BALZER 2008, KAMMEL 2005, PETZ 2006), see **Figure 5** right. If the surface is not ideally even, the reflection of the environment is deformed. Thus, the surface becomes part of the imaging system. By evaluating the deformation, the human observer as well as a deflectometric inspection system obtains information on the shape of the surface in form of the local inclination.

The major precondition of the applicability of deflectometry is a significant specular reflection on the surface. If the surface shows mainly diffuse reflection (e.g. matte or rough surfaces), a transition from visual light to larger wavelengths (e.g. near infrared) can be helpful, since the portion of specular surface reflection increases with the wavelength. Moreover, objects with multiple reflections (e.g. glass plates or glass mirrors) cannot be inspected.

In contrast to projection techniques, deflectometry is sensitive to variations of the local inclination, see **Figure 7**. When the local inclination is varied, the camera observes another point on the display in a deflectometric setup (right), whereas for projection techniques, a change in the local inclination causes no direct measurement effect (left).

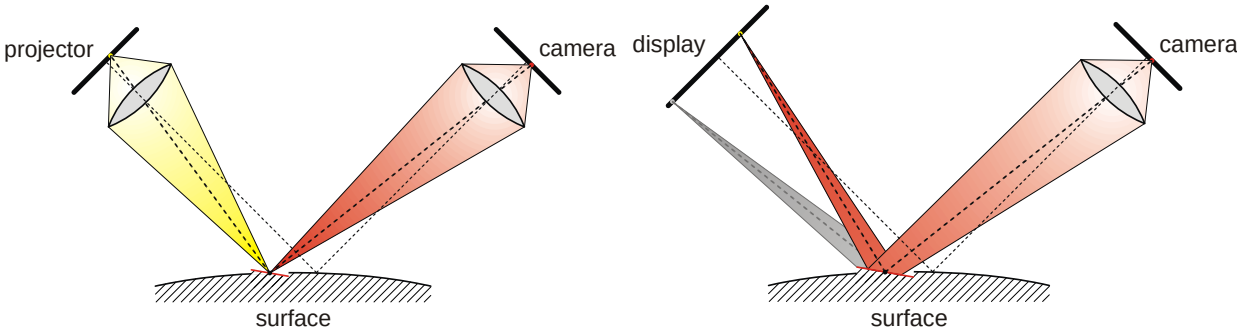

Figure 7: Measurement sensitivity of projection (left) and deflectometry (right)

4.1.3 Time-of-flight imaging

The basic principle of Time-of-Flight imaging is to determine the time that light needs to travel from a light source to the surface and back to a camera and to calculate the distance by means of the speed of light (ZHANG 2003). There are two major realizations of the principle, see Fig. 8. Within the pulse detection principle, the delay of a single reflected light pulse is detected. For the phase detection principle, the intensity of the emitted light is harmonically modulated. In the detector, the phase change of the reflected beam resulting from the distance travelled is registered, which is preferably done by means of Photonic Mixer Devices (PMD), a special sort of CMOS sensors.

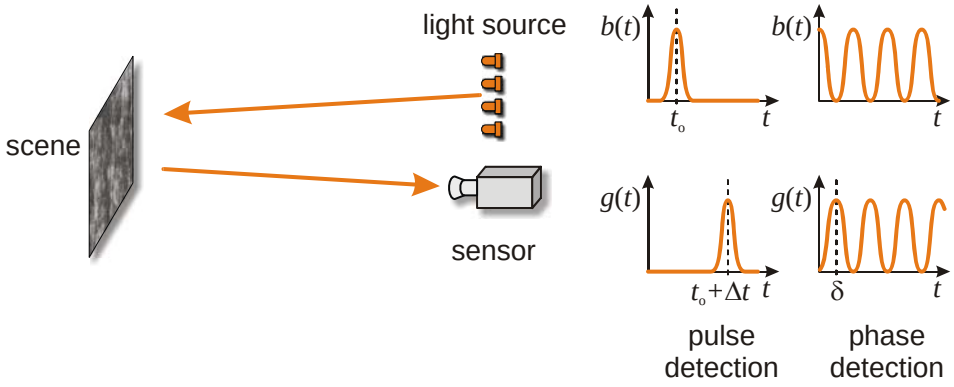

Figure 8: Measurement principles of Time-of-Flight imaging

Like projection techniques, Time-of-Flight imaging requires that a part of the light is diffusely reflected, whereas the exact reflectance is irrelevant. This measuring principle provides spatial positions of surface points. Although measuring time instead of a geometric quantity is a promising principle, it is not yet commonly used in automated inspection, which is mainly due to heavy measuring noise in the data, which up to now avoids reliable results.

4.2 Passive illumination

Inspection principles using passive illumination only need enough light such that the camera can obtain an image. The exact property of the illumination field is not crucial. Stereo methods, which evaluate the perspective deformation of a spatial scene, and depth from (de)focus, which both use the restricted depth of field of a lens system, belong to this class.

4.2.1 Stereo imaging

The measuring principle underlying Stereo imaging is the evaluation of triangles that are present when a scene point is observed from at least two different camera positions (HARTLEY & ZISSERMAN 2008), see **Figure 9**. The different camera positions cause that the scene point is mapped onto points at different positions in the images, depending on its distance to the cameras. For a given image point in one camera, the position of the corresponding image point in the second camera varies on the epipolar line depending on the distance of the scene (blue lines in **Figure 9**). The main task in Stereo imaging is therefore to determine correct correspondences in the images on the epipolar lines. The principle requires that the scene to be observed contains distinct scene points, that the scene has a comparable appearance from all camera positions and that a large part of the light is diffusely reflected. A drawback of the principle is that its sensitivity decreases with the distance. As results, spatial positions of surface points are determined.

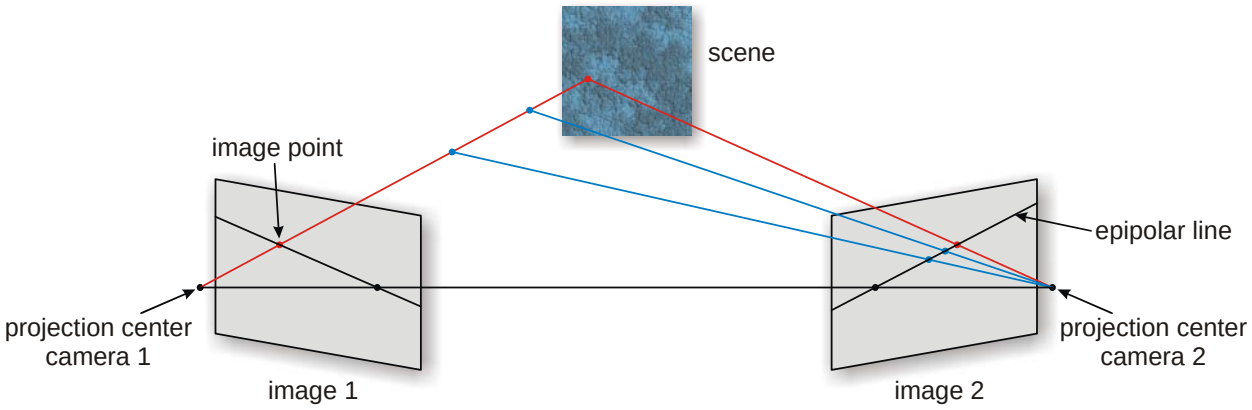

Figure 9: Measurement principle of Stereo Imaging

4.2.2 Depth from (de)focus

The principles Depth from Focus and Depth from Defocus base on the restricted depth of field of a focusing camera lens. Whereas Depth from Defocus models the blurring of the lens and determines the object distance based on this model (e.g. by using the width of blurred edges), Depth from Focus evaluates an image series that is taken while the focusing (e.g. by varying the image distance) or the object distance is changed.

Each scene location is then imaged in focus only once in the series. In order to determine the correct distance to a scene point, the parameter setting that leads to the sharp imaging of the scene point has to be identified, e.g. based on local contrast measures.

Figure 10 shows the principle of Depth from Focus by means of a firing pin print (HEIZMANN 2008): from an image series with varied object distance (left), the image with the optimal local contrast is determined and written into a map with its image number, which can be interpreted–with a proper scaling and smoothing–as depth map (middle). An additional outcome is a synthetic image with enhanced depth of field, which can be obtained by combining the focused image regions of the image series (right).

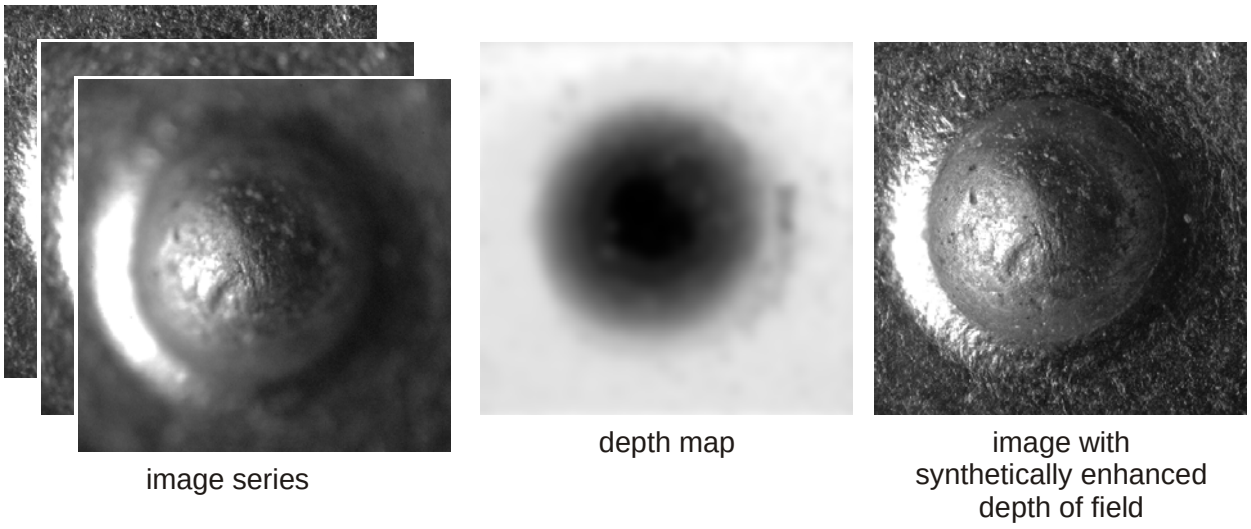

Figure 10: Depth estimation by means of Depth from Focus

5 Conclusions

To determine shape properties of surfaces and objects, numerous image based measuring principles are available. They can be distinguished on basis of the determinable surface property (point position or local inclination), the requirements for the surface properties, the environmental conditions, the sensitivity and resolution, and the time needed for the acquisition. By means of sophisticated methods from image acquisition and signal processing, powerful inspections systems are achievable, which are able to reliably represent the macroscopic properties of surface shape.

References

BALZER J. (2008): Regularisierung des Deflektometrieproblems – Grundlagen und Anwendung. Universitätsverlag, Karlsruhe (in German)

DUDA R.O., HART P.E., STORK D.G. (2001): Pattern classification. Wiley, New York, 2nd ed.

HARTLEY R., ZISSERMAN A. (2003): Multiple View Geometry in Computer Vision. Cambridge Univ. Press, Cambridge, 2nd ed., 5th print.

HEIZMANN M. (2008): Aspects of Image Fusion for Automated Visual Inspection. Pattern Recognition and Image Analysis, 18 (2), pp. 222-230

HORN B.K.P. (1989): (ed.): Shape from shading. MIT Press, Cambridge, Mass.

GONZALEZ R.C., WOODS R.E. (2007): Digital Image Processing. Pearson Prentice Hall, Upper Saddle River, 3rd ed.

KAMMEL S. (2005): Deflektometrische Untersuchung spiegelnd reflektierender Freiformflächen. Universitätsverlag Karlsruhe (in German)

PETZ M. (2006): Rasterreflexions-Photogrammetrie. Shaker Verlag, Aachen (in German)

SCHAEL M. (2005): Methoden zur Konstruktion invarianter Merkmale für die Texturanalyse. Universitätsverlag Freiburg (in German)

ZHANG Z. (2003): Untersuchung und Charakterisierung von PMD (Photomischdetektor)- Strukturen und ihren Grundschaltungen. Universität Siegen (in German)

Computer vision developments for the automatic inspection of fresh and processed fruits

José Blasco[1], Nuria Aleixos[2], Sergio Cubero[1], Florentino Juste[1], Juan Gómez-Sanchis[3], Vicente Alegre[1], Enrique Moltó[1]

[1] Centro de Agroingeniería. Instituto Valenciano de Investigaciones Agrarias (IVIA). Ctra. Moncada-Náquera km 5, 46113 Moncada (Valencia), Spain.
[2] Instituto en Bioingeniería y Tecnología Orientada al Ser Humano (Universidad Politécnica de Valencia). Camino de Vera s/n, 46022 Valencia, Spain
[3] Electronic Engineering Department, Universidad de Valencia. Dr. Moliner 50, 46100 Burjassot (Valencia), Spain
Corresponding author: blasco_josiva@gva.es

Abstract: *The quality of a fresh or processed fruit or vegetable is defined by a series of characteristics which make it more or less attractive to the consumer, such as ripeness, size, weight, shape, colour, presence of blemishes and diseases, presence or absence of fruit stems, seeds, etc. In summary, these characteristics may cover all of the factors that exert an influence on the product's appearance, on its nutritional and organoleptic qualities or on its suitability for preservation. Most of these factors have traditionally been assessed by visual inspection performed by trained operators. However, the application of machine vision in agriculture has increased considerably in recent years since it provides substantial information about the nature and attributes of the produces, reduces costs, guarantees the maintenance of quality standards and provides useful information in real time. Moreover, machine vision opens the possibility of exploring agricultural products in invisible regions of the electromagnetic spectrum, as in the ultraviolet or infrared regions.*

Instituto Valenciano de Investigaciones Agrarias (IVIA) has developed during the past 15 years computer vision systems for the automatic, on-line inspection of fresh and processed fruits and vegetables. This paper shows the most important outcomes in this matter achieved by the department called Centro de Agroingeniería. One of such systems is a machine for the automatic inspection of pomegranate arils for fresh consumption. This machine individualizes, inspects, classifies and separates the arils in four categories, removing those that do not fulfil the minimal specifications. Multivariate analysis models are used to classify the arils with an average success about 90%.

Another application is a machine to classify mandarin segments for canning. The system distinguishes among sound, broken or double segments, and is able to detect the presence of seeds in the segments. The system analyses the shape of the each individual segment to estimate morphological features that are used to classify it into different commercial categories. The machine classifies correctly more than 75% of the analyzed segments. Both systems are currently patent pending.

In the field of computer vision systems for the inspection of fresh, whole fruit, most research has been focused on citrus fruits. While most commercial systems only detect the blemishes on the skin of fruit, a multispectral system has been developed to identify them. The system is capable of identifying the 11 most common defects of citrus skin using near infrared, colour and ultraviolet. It also uses induced ultraviolet fluorescence. The success rate achieved with such system reached 87% when identifying about 800 defects in five species of oranges and mandarins.

The use of hyperspectral sensors makes it possible to conduct a more sophisticated analysis of the scene by acquiring sets of images corresponding to particular wavelengths. Using this technology, we have conducted different works aimed at detecting damages in citrus fruits, including fungal infestation. The acquired multi-dimensional spectral signature characterising a pixel has been used to analyse scenes and to detect different types of defects such as decay, more easily than using standard colour imaging systems.

1 Introduction

The quality of a particular fresh or processed fruit or vegetable is defined by a series of characteristics which make it more or less attractive to the consumer. Such features include ripeness, size, weight, shape, colour, the presence of blemishes or diseases, the presence or absence of fruit stems, seeds, and so forth. In summary, these characteristics may cover all the factors that exert an influence on the product's appearance, on its nutritional and organoleptic qualities or on its suitability for preservation. Most of these factors have traditionally been assessed by visual inspection performed by trained operators. However, the application of machine vision in agriculture has increased considerably in recent years, since it provides substantial information about the nature and attributes of the produce, reduces costs, guarantees the maintenance of quality standards and provides useful information in real time. Moreover, machine vision opens up the possibility of exploring agricultural products in invisible regions of the electromagnetic spectrum, such as the ultraviolet or infrared regions.

The Instituto Valenciano de Investigaciones Agrarias (IVIA) has been developing computer vision systems for the automatic, on-line inspection of fresh and processed fruits and vegetables for the last 15 years. This paper shows the most important outcomes achieved in this field by the Institute's Agricultural Engineering Centre (Centro de Agroingeniería).

2 Inspection of pomegranate arils

Spain produces about 20 000 tons of pomegranate (*Punica granatum* L.) fruits per year and production is concentrated in the period between October and January. Many studies have demonstrated the enormous nutritional and nutraceutical properties of this fruit. However, it is difficult to peel and to extract the edible parts (arils) and this reduces its acceptance by the consumer in favour of other fruits that are easier to prepare. Marketing of pomegranate arils in a way that makes them easy to eat is a way to promote consumption of the fruit.

During the production of the ready-to-eat arils, fragments of internal membranes or skin and other unwanted material are released during the extraction process. Moreover, some defective arils (broken, abnormally shaped or with different physiological disorders) may appear, together with arils of different colours ranging from white to red. Defective arils may shorten the shelf life of the product, and arils with different colours in the same package may degrade the appearance of the product and hence reduce its price.

The objective of this work was to develop an engineering solution for the automatic sorting of pomegranate arils. This included designing mechanisms for separating and transporting the arils, developing real-time computer vision algorithms for inspecting and classifying the arils, developing algorithms and practical devices for synchronising the inspection unit with the sorting system, building a system for classifying the arils into categories, and developing communication and control procedures to supervise the whole machine (BLASCO *et al.* 2008a and 2009a).

The proposed solution was implemented in the construction of a prototype capable of sorting all the objects that left the extracting machine into a maximum of four categories (**Figure 1**). Computer vision algorithms had to assess the colour of each object individually, and had to be capable of discriminating between arils and undesired material. The control algorithms had to synchronise image acquisition from two different cameras, analyse the images and the displacement of the objects on the conveyor belts, and activate the sorting unit. Real-time image processing was essential in order to achieve the required throughput. Intuitive and fast classification techniques were compared and implemented in the prototype, and the solution that was finally adopted was the one that was easiest to operate by a non-experienced user, without compromising quality standards.

Figure 1: Prototype developed for the sorting of pomegranate arils

The algorithms were developed to work with two RGB (red, green, blue) progressive-scan cameras at the same time, since the acquisition of the images is a very time-consuming process (40 ms per image). The image analysis was designed to process one image obtained with one camera in parallel with the acquisition of another image with the other camera. The result is that the processing of one image and the acquisition of the next overlap in time, thus saving time and optimising the operation.

The acquisition of the images is triggered by pulses received from an optical encoder attached to the shaft of the carrier roller and connected to the serial port of the computer. Cameras are triggered as the belts move forward 350 mm. This design makes the acquisition of the image independent of the speed of the belts, and thus ensures that there are never any overlaps or gaps between consecutive images.

The background is removed by a threshold in the red channel, since the red of the arils contrasts sharply against the blue conveyor belts. Once the background had been removed, each connected region was labelled as a possible object of interest (under normal circumstances, it should be an aril or some other material). In the same operation, the program estimated the size and centroid of each of these objects and the average RGB coordinates of their pixels. Extremely small or large objects were classified as unwanted material.

Finally, the average colour coordinates were used to classify the object into one of four pre-defined categories. The procedure to determine the class is described below. After processing each image, the machine vision computer sent the category and position of the object to a second computer (called the *control computer*), which tracked the object until it was sorted. This communication was implemented via TCP/IP.

2.1 Performance

Pomegranates (*Punica granatum*, cv. Mollar de Elche*)* were used throughout the tests. The colour of their arils ranged from white-pink to red-brown. During normal use of this kind of sorting machines in industry, changes caused by the evolution of the colour of the arils throughout the season require frequent retraining of the machine vision system. But these machines are usually handled by workers without any knowledge of computer vision or experience in statistics and they need a fast way to adapt the inspection software to the evolution of the colour of the product. Colour thresholds are intuitive and easy to implement by means of virtual switches in the graphical user interface. A threshold on the ratio between average red and green (R/G) colours of each object was one of the methods chosen for implementation in the prototype and its performance in classifying the arils was compared with a standard linear discriminant analysis (LDA).

Sets of objects for training and validation were built from samples obtained from the extracting machine. Depending on the colour, these objects were sorted into five categories by experienced workers: white aril, pink aril, red aril, brown (decaying) aril and unwanted material. This last category contained mainly the internal membranes, which were mostly white and bigger than the arils. The training set was made up of 100 arils from each colour category and 50 membranes (a total of 550 objects). The validation set consisted of independent samples of 400 arils from each category and 100 membranes (1700 objects). Images of all these objects were acquired using the prototype. The two classification methods were assessed by implementing all the classification functions in the image analysis software and automatically classifying all the objects in the validation set accordingly. These results were then compared with the classification carried out by human experts, in order to build the confusion matrix for each method.

The development and successful commissioning of the automatic inspection machine constituted an important engineering achievement in itself. The classification results were similar for each of the two methods used, the R/G ratio and LDA. **Table 1** shows the confusion matrix for the validation set using the R/G ratio. Raw material was the class in which the best correct classification was obtained (98%). The most sensitive classes from the commercial point of view were red and brown arils, where successful classification reached a rate of 90%.

Table 1: Confusion matrix of the classification performed at the beginning of the season using thresholds on the R/G ratio

Actual \ Classified	White	Pink	Red	Brown	Raw mat.
White aril	92.0%	4.0%	0.0%	2.7%	1.3%
Pink aril	1.5%	91.4%	1.5%	5.6%	0.0%
Red aril	0.0%	2.3%	89.2%	8.5%	0.0%
Brown aril	0.8%	4.7%	5.5%	89.0%	0.0%
Raw mat.	1.7%	0.0%	0.0%	0.0%	98.3%

3 Inspection of satsuma segments

In the industry of mandarin segments, when the fruits come onto the production line they are peeled, the segments are then separated, peeled, inspected and canned. Most the operations are performed automatically, the inspection of the quality being the only part of the process that has not already been automated. Operators carry out visual inspections for broken segments or those that contain seeds as they go past on a conveyor belt. When a defective segment is detected, it is removed from the conveyor belt manually. Problems related to subjectivity, fatigue or the disparity of criteria among operators as to how to decide which are broken and which are not lower the quality of the inspection and, consequently, the final product.

This second study was aimed at sorting mandarin segments in a similar way to the method used in the previous machine. Image processing was used for on-line detection of seeds in the segments and for the detection of broken segments, estimating the degree of breaking. These objects were classified in commercial categories. Pieces of skin or double segments (which are those that were not properly split in previous processes) have to be detected and removed (BLASCO *et al.* 2007a and 2009b). **Figure 2** shows segments pertaining to different categories.

Satsuma segments entered the inspection machine from a vibrating plate that spread them across the width of the machine. The high speed of six narrow conveyor belts then facilitated their separation. Since the average weight of the segments was about 5 g, to achieve 1 ton per hour, the machine inspected about 55 segments per second travelling at 1 m/s.

The computer vision system also consisted of two progressive-scan RGB cameras that acquired 0.65 mm/pixel images. Segments were transported on six semi-transparent conveyor belts, which allowed them to be backlit, thus facilitating the detection of seeds and the segmentation of the shape of the segments.

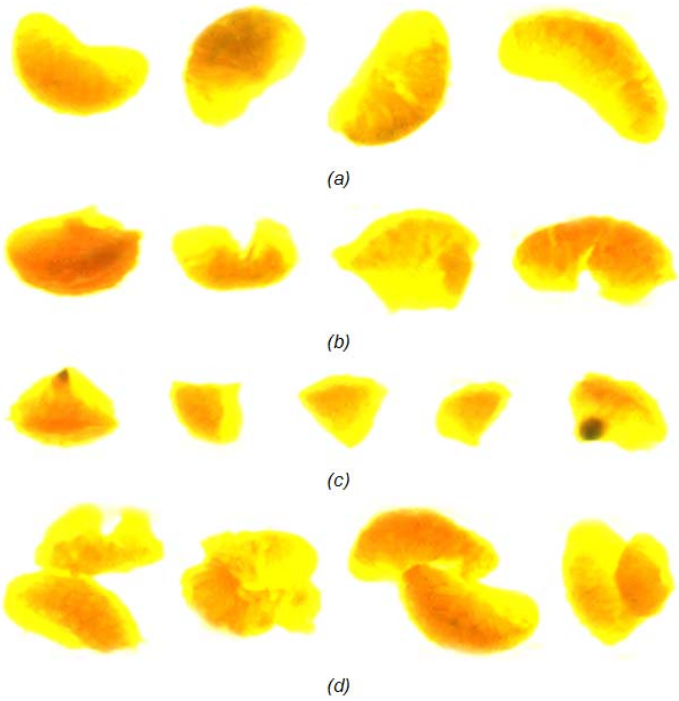

Figure 2: Different classes of segments: a) sound and entire segments, b) broken segments, c) pieces of segments and segments with seeds, d) double segments

When backlit, the objects contrasted sharply with respect to the translucent conveyor belts, thus facilitating the detection and elimination of pieces of raw material and segments with seeds, and also enhancing the silhouette of the objects. The shape of the remaining objects was analysed to estimate morphological features that made it possible to determine whether they were intact segments, broken segments or pieces of them. The sequence of the shape analysis started with the detection of the boundary of the objects. Then, the centroid was calculated as well as the number of pixels in the object. The principal axis of inertia was used to estimate the length and the orientation of the object. Parameters like elongation, roundness, symmetry and compactness were also used to describe the shape of the object. The fast Fourier transform (FFT) of the perimetral signature was also calculated (TAO *et al.* 1995, MIAO *et al.* 2006).

In all, 620 segments (including both good and broken segments) were chosen at random, labelled as good or broken, and then imaged. The morphological parameters described above were calculated for each segment and stored. LDA, with the above-mentioned shape parameters as independent variables and the label as the grouping variable, was used to generate a model to classify *whole* and *broken* segments. The model was then applied to an independent set of 15 000 images of segments in order to assess its performance. These results were compared with the visual classification of the experts.

3.1 Performance

The results of the classification given by the image processing algorithm were compared with the visual inspection of the producer company's experts to obtain success ratios for each category (**Table 2**). The system was capable of detecting 96% of the segments that contained seeds and 96% of pieces of skin that were travelling on the conveyor belt. The rate of success of the algorithms in separating out sound segments was 93%, while the rate of successful detection of broken ones was only 83%, mainly due to the fact that most breakages in many segments correspond to small fragments at one end, and these are difficult for the current system to detect. The average rate of success in the detection of double segments reaches 82%. Specific algorithms have to be developed to detect these small breakages. The average processing time of the images was 48 ms.

Table 2: Confusion matrix of the classification obtained by the automatic system

Classified / Actual	Complete	Broken	Half segments	Seeds	Skins	Doubles
Complete	93.2%	5.8%	0.3%	0.7%	0.0%	0.0%
Broken	9.9%	83.4%	6.7%	0.0%	0.0%	0.0%
Half segments	1.1%	4.7%	94.2%	0.0%	0.0%	0.0%
Seeds	2.5%	0.9%	0.3%	96.3%	0.0%	0.0%
Skins	1.1%	1.5%	1.2%	0.0%	96.2%	0.0%
Doubles	10.0%	3.3%	0.1%	0.0%	4.2%	82.4%

4 Inspection of fresh citrus

Commercial machine vision systems are commonly capable of detecting blemishes on the surface of fruits. They cannot, however, identify them or distinguish between groups of blemishes or determine their severity, which is valuable information for packing houses.

This work illustrates an approach that uses multispectral imaging for identifying the type of defect once it has been detected and separated from the sound skin of citrus (BLASCO *et al.* 2009c).

Images of the same fruit were acquired using three different systems: visible (VIS) and near infrared (NIR) reflectance, and ultraviolet induced fluorescence (UVFL). Two VIS- and NIR-sensitive cameras were used to acquire all the images. A progressive-scan colour camera was used to acquire fluorescence and visible images, which consisted of three monochromatic images of RGB wavelengths (BLASCO *et al.* 2007b). Basically, the colour image acquisition system consisted of a colour camera, a lighting system com-

posed of fluorescent tubes and polarised filters in order to avoid bright spots in the scene. The acquisition of the NIR images was performed using a Hamamatsu Beam-Finder III C5332-01 camera, sensitive from 400 nm to 1800 nm. The lighting system was made up of incandescent lamps. To prevent interference of visible information, a 700 nm cut-band filter was coupled to the camera lens. The fluorescence images were acquired using the same colour camera that was employed to acquire the colour images. In this case, fruits were illuminated using black light fluorescent tubes that emit radiation with a wavelength between 350 nm and 400 nm, and a peak at 370 nm.

Once the images have been segmented (BLASCO *et al.* 2007c), a collection of regions of interest (supposedly sound peel and defects) were identified. Shape analysis using different techniques was also used.

The probability of a region of interest in the segmented image being identified as a particular defect was estimated using a non-linear Bayesian approach. Colour coordinates and morphological features extracted for each region were used as independent variables. Visible and non-visible information was combined in this algorithm to detect dangerous blemishes that can spread a fungal infestation and thus prevent the fruits from being commercialised.

A total of 2132 oranges and mandarins containing different blemishes were collected at random from a packing line and imaged using the acquisition systems described above, thus giving a total of 10 660 images. Another set consisting of 10 images for each type of defect detected with each spectral system (10 x 5 x 11 = 550 images) was also acquired and used to train the algorithms. The defects found on the fruits were described as those that only affect the appearance of the fruit, such as oleocellosis, chilling injury, sooty mould, phytotoxicity, scales, scarring, thrips, and other defects with greater economic importance, such as anthracnose, stem-end injury, green mould (decay caused by *Penicillium digitatum*) and medfly (*Ceratitis capitata*) (Wiedemann) egg deposition. Their size varies from large defects, such as anthracnose or chilling injury, to small ones like scales or medfly. The colour also differs from one to another and may range from the white of stem-end injury, the silver or grey of thrips, the orange or green of *P. digitatum* or the brown of oleocellosis to the black of anthracnose. **Figure 3** shows images of an advanced decaying fruit acquired with the different vision systems.

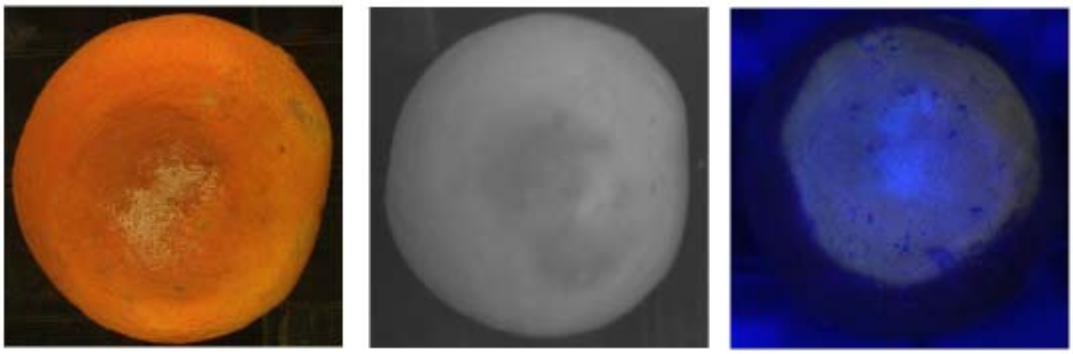

Figure 3: Image of an advanced decay damage acquired using the three acquisition systems. From left to right, visible image, NIR image and UVFL image

Using only colour information, the system can process the images very quickly, since detection can be performed together with the segmentation process. However, there are defects with very similar colours that can be confused. Typical cases are defects caused by scales, which are most commonly confused with thrips (29% of misclassification), or scarring (5% of misclassification). BLASCO *et al.* (2007a) showed that about 65% of defects could be properly identified using colour information alone. Once the morphological parameters described above had been introduced, the correct classification rate reached 82%. By introducing NIR and UVFL images in the analysis, the success rate increased to 86%. However, beyond the numerical results, the greatest increase is achieved in the identification of anthracnose and green mould (95% and 97% respectively), which are dangerous defects that spread these diseases to sound fruits.

A major problem concerning the implementation of this algorithm on line is the large amount of processing time it requires. Although the images should be acquired by different cameras, these tasks can be overlapped in time in such a way that while one image is being acquired, another can be processed. The algorithm that was developed allows this methodology to be used if the order is UVFL, NIR and RGB. But processing all the images is still time-consuming and expensive. NIR and RGB images can be acquired simultaneously, as demonstrated in ALEIXOS *et al.* (2002), by implementing a camera capable of acquiring both images at the same time. In the case of UVFL images, the importance of detecting decay is very high because it can spread to other fruits during their storage or transport.

5 Hyperspectral imaging for detection of fruit decay

Early detection of fungal infections is especially important in packing houses because a very small number of infected fruits can spread the infection to a whole batch, thus causing great economic losses and affecting further operations, such as storage and transport.

The most important post-harvest damage in citrus packing houses is caused by *Penicillium sp* (ECKERT & EAKS 1989). Nowadays, the detection of decaying fruit on citrus packing lines is carried out visually under UVFL illumination, and decaying fruits are removed manually. This procedure, however, may be harmful for operators and operationally inefficient, since the operators must work in shifts of just a few hours. This rate of staff rotation affects the assessment of the quality.

Machine vision systems based only on RGB cameras are unable to detect decaying fruit correctly. The use of hyperspectral sensors makes it possible to acquire a set of images corresponding to particular wavelengths. One of the main problems of these systems is the huge amount of redundant data that is generated and must be removed (CHANG 2003).

In this study, we examined the feasibility of detecting green decay in citrus fruits in the early stages of infection, but avoiding the use of UV illumination. We employed a hyperspectral vision system based on liquid crystal tunable filters (LCTF) similar to the one used by EVANS *et al.* (1998). The system consisted of a monochrome camera (Photometrics CoolSnap ES) with a high level of sensitivity between 320 nm and 1100 nm. It was configured to acquire 551×551 pixel images with a resolution of 3.75 pixels/mm. Two LCTF were used, one sensitive to the visible between 460 nm to 720 nm (Varispec VIS07) and one sensitive to the near-infrared from 730 nm to 1020 nm (Varispec NIR07). Each fruit was illuminated individually by indirect light from halogen lamps inside a hemispherical aluminium diffuser.

The acquisition software was configured to use a different integration time for each particular band that was acquired. Hence, we compensated for the differences in efficiency by calculating a customised integration time for each band (thus, the ones in which the system was less efficient had greater integration times). This compensation was derived from measurements observed from a white reference. For this reason we assumed a flat response over the whole spectral range in all the acquired images. The effect of the reflection of the light over spherical objects was corrected following the work of GÓMEZ-SANCHÍS *et al.* (2008a). We designed a manual fast filter changer that holds and guides the tunable filters, so that images of the same scene could be acquired at visible and near-infrared wavelengths without having to move the camera (GÓMEZ-SANCHÍS *et al.* 2008b). Images were acquired by manually placing the fruit in the inspection chamber and then presenting the damage to the camera. The hyperspectral image was composed of 57 monochrome images of each fruit.

Tests were oriented towards selecting the minimum set of bands that maximise the correct classification of pixels. For this purpose, we studied the evolution of the success rate of classification against the number of bands, once the LDA and CART classifiers had been applied, using the labelled training set and the feature selection methods. The four feature selection methods were: Correlation analysis (CA), Mutual information (MI), Stepwise multivariate regression (SW) and genetic algorithms (GALDA). All four were implemented using Matlab 7.0 (Mathworks, Inc.). All bands present in the labelled train-

ing set were normalised using mean and variance (standardisation) in order to minimise the effect of the scale on data. A labelled training set was used to generate the models. The four selection methods were programmed to iteratively increase the number of selected bands (*k*) from 4 to 57. The bands obtained in each of the iterations were used to classify the pixels using the two above-mentioned classification methods (LDA and CART) and the average classification success rate was calculated for each number of bands.

Mandarins cv. "Clemenules" (*Citrus clementina* Hort. ex Tanaka) were selected because of their economic importance in Spain. Fruits were chosen randomly from the packing line of a trading company. A total of 200 fruits were used: 150 were inoculated with a suspension of *Penicillium digitatum* spores with a concentration of 10^6 spores/ml (PALOU *et al.* 2001); the rest were inoculated with water for control purposes. The fruits were stored for three days in a controlled environment at 25ºC and 99% relative humidity. After this period, all the inoculated fruits presented a circular area of decay with a diameter between 10 mm and 25 mm. The colour of the damage is similar to the colour of the sound skin around it, therefore making it difficult for a human inspector to detect it.

GALDA achieved better success rates for both LDA and CART classification than the other band selection methods. Moreover, when using LDA the maximum success rate reached 92% when using the 57 bands, while in the case of CART this rate rose to 95% using only 20 bands. The bands selected for use with GALDA are (in nm) 460, 480, 520, 560, 590, 600, 620, 630, 680, 730, 740, 760, 800, 820, 870, 880, 950, 960, 980 and 1010. The use of more than these 20 bands did not increase the success rate to any significant degree, the increment being about only 1% after including all 57 bands. **Figure 4** shows the result of the segmentation of a decaying fruit using CART and LDA.

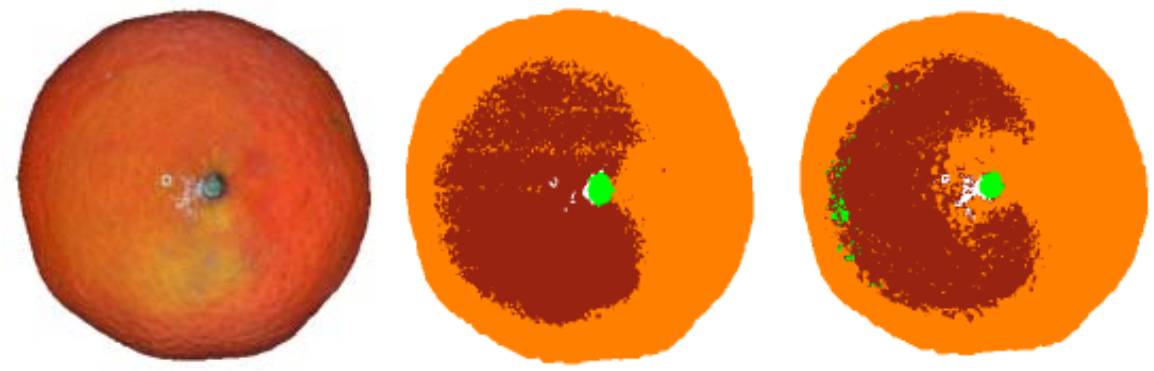

Figure 4: Image of a fruit with decay damage (left). Segmentation using CART (middle). Segmentation using LDA (right)

In general, the best results were obtained with the non-linear classifier (CART), the success rate being above 90% for all classes. **Table 3** shows the confusion matrix obtained with this model. An average success rate of 95.18% (κ=0.9358) was achieved. The

most difficult task in the pixel-classification problem is to discriminate the “sound” class from the “decaying” class, although good results were achieved for all classes.

Table 3: Confusion matrix for the classification of pixels using CART and the 20 bands given by GALDA. (Cohen’s kappa =0.9358, average success=95.18%)

Actual \ Classified	Sound	Decaying	Decaying with spores	Stem
Sound	90.96%	5.56 %	0.31%	1.48%
Decaying	7.58%	93.63%	0.69%	0.88%
Decaying with spores	0.48%	0.54%	98.74%	0.25%
Stem	0.98%	0.27%	0.26%	97.39%

6 Conclusions

Acknowledgments

This work was partially funded by the Spanish Ministry of Science and Technology (MCYT) and European FEDER funds through projects DPI2007-66596-C02-02, DPI-2003-09173-C02-02 and DPI-2007-66596-C02-02, by the Instituto Nacional de Investigación y Tecnología Agraria y Alimentaria (INIA) of Spain through project RTA03-105. and by the Instituto Valenciano de Investigaciones Agrarias (IVIA) through the grant “Identificación en tiempo real de los defectos superficiales de los cítricos mediante el empleo de técnicas de computación paralela y visión artificial”.

References

ALEIXOS N., BLASCO J., NAVARRÓN F., MOLTÓ E. (2002): Multispectral inspection of citrus in real-time using machine vision and digital signal processors. Computers and Electronics in Agriculture 33(2): 121-137

BLASCO J., CUBERO S., ARIAS R., GOMEZ J., JUSTE F., MOLTÓ E. (2007A): Development of a computer vision system for the automatic quality grading of mandarin segments. In: Pattern recognition and image analysis proceedings, Marti J., Benedi J.M. and Serrat J. Eds. Lecture Notes in Computer Science 4478: 460-466

BLASCO J., ALEIXOS N., GÓMEZ J., MOLTÓ E. (2007B): Citrus sorting by identification of the most common defects using multispectral computer vision. Journal of Food Engineering 83(3), 384-393

BLASCO J., ALEIXOS N., MOLTÓ E. (2007C): Computer vision detection of peel defects in citrus by means of a region oriented segmentation algorithm. Journal of Food Engineering 81 (3): 535–543

BLASCO J., CUBERO-GARCÍA S., ALEGRE-SOSA S., GÓMEZ-SANCHÍS J., LÓPEZ-RUBIRA V., MOLTÓ E. (2008): Short communication. Automatic inspection of the pomegranate (*Punica granatum* L.) arils quality by means of computer vision. Spanish Journal of Agricultural Engineering 6 (1): 12-16

BLASCO J., CUBERO S., GÓMEZ-SANCHÍS J., MIRA P., MOLTÓ E. (2009A): Development of a machine for the automatic sorting of pomegranate (Punica granatum) arils based on computer vision. Journal of Food Engineering 90(1): 27-34

BLASCO J., ALEIXOS N., CUBERO S., GÓMEZ-SANCHÍS J., MOLTÓ E. (2009B): Machine vision system for the automatic sorting of satsuma (Citrus unshiu) segments using morphological features. Computers and electronics in agriculture 66 (1): 1-8

BLASCO J., ALEIXOS N., GÓMEZ-SANCHÍS J., MOLTÓ E. (2009C): Recognition and classification of external skin damages in citrus fruits using multispectral data and morphological features. Biosystems Engineering 103(2): 137-145

CHANG C.I. (2003): Hyperspectral Imaging: Techniques for Spectral Detection and Classification. Springer

ECKERT J.W., EAKS I.L. (1989): Postharvest disorders and diseases of citrus. The citrus industry. Vol. 5. Univ. California Press. Berkeley, CA, USA

EVANS M.D., THAI C.N., GRANT J.C. (1998): Development of a spectral imaging system based on a liquid crystal tunable filter. Transactions of the ASAE 41(6): 1845-1852

GÓMEZ-SANCHIS J., MOLTÓ E., CAMPS-VALLS G., GÓMEZ-CHOVA L., ALEIXOS N., BLASCO J. (2008A): Automatic correction of the effects of the light source on spherical objects. An application to the analysis of hyperspectral images of citrus fruits. Journal of Food Engineering 85(2): 191-200

GÓMEZ-SANCHIS J., GÓMEZ-CHOVA L., ALEIXOS N., CAMPS-VALLS G., MONTESINOS-HERRERO C., MOLTÓ E., BLASCO J. (2008B): Hyperspectral system for early detection of rottenness caused by Penicillium digitatum in mandarins. Journal of Food Engineering 89(1): 80-86

MIAO Z.J., GANDELIN M.H., YUAN B.Z. (2001): A new image shape analysis approach and its application to flower shape analysis. Image and vision computing 24(10): 1115-1122

PALOU L., SMILANIK J., USALL J., VIÑAS I. (2001): Control postharvest blue and green molds of oranges by hot water, sodium carbonate, and sodium bicarbonate. Plant Disease (85): 371-376

TAO Y., MORROW C.T., HEINEMANN P.H., SOMMER H.J. (1995): Fourier-based separation technique for shape grading of potatoes using machine vision. Transactions of the ASAE 38(3): 949-957

Analysis of color variations on sunflower crop images, owning to changes in environmental illumination

Gonzalo Ruiz Ruiz[1], Luis Manuel Navas[1], Jaime Gómez Gil[2]

[1] Department of Agricultural and Forest Engineering, University of Valladolid, Palencia, Spain
[2] Department of Communications and Signal Theory and Telematics Engineering, University of Valladolid, Valladolid Spain
Corresponding author: gruiz@iaf.uva.es, lmnavas@iaf.uva.es, jgomez@tel.uva.es

Abstract: *Computer vision can be applied to precision agriculture but the problems caused by open environments must be solved: changes in illumination, uncontrolled conditions, etc. To characterize the influence of illumination, an analysis of color variations was made with sunflower plants. Lots of samples were acquired by a digital color camera along enough hours of the day under direct sunlight. Several parameters were measured from histograms of three color spaces, RGB, rgb and HSI. The analysis showed that H plane (hue) and g plane (normalized green component) are the most immune planes to changes in environmental illumination.*

1 Introduction

Precision agriculture uses several technologies and techniques to achieve objectives such as increasing the performance of crops, reducing environmentally impact and improving working conditions. Computer vision participates in precision agriculture together with others (positioning, sensors). In industrial environments, computer vision is well and successfully implemented, the same way as in laboratories, because of controlled conditions. Quite the opposite, in open farm fields, the variability of environmental conditions makes very difficult to apply computer vision without finding problems. It is necessary to apply more complex techniques to process and analyze digital images. One of the greatest sources of variability is the changes in environment illumination. The illumination goes from direct solar light to diffuse light caused by clouds, from sunrise light to sunset light or from sloping winter sunlight to straight summer sunlight. Sometimes the illumination can be controlled by parasols and artificial lighting under them (ASTRAND & BAERVELDT 2002, AITKENHEAD *et al.* 2003), but it is not always possible in realistic applications of computer vision in crops.

One of the most important aims of the computer vision applied to precision agriculture is to develop algorithms immune to illumination influence or, in any case, to counteract this effect (TIAN & SLAUGHTER 1998, RUIZ-RUIZ *et al.* 2009). To do this, we must know how lighting affects to digital images and specifically in this work it is analyzed the influence

of illumination in color variations in crop images. Once we know the connection between quantity and type of natural illumination and color changes in digital images, we will be able to remove or reduce this influence.

2 Materials and methods

2.1 Sunflower images acquisition

Crop plants used to carry out this study were sunflowers (*Hellianthus Annuus*) in their middle growing stages, with around 8 to 12 leaves (**Figure 1**). They grew from sunflower seeds in a seedbed under controlled conditions to avoid the sort season of sunflower crops in the authors' region (Castilla y Leon, Spain).

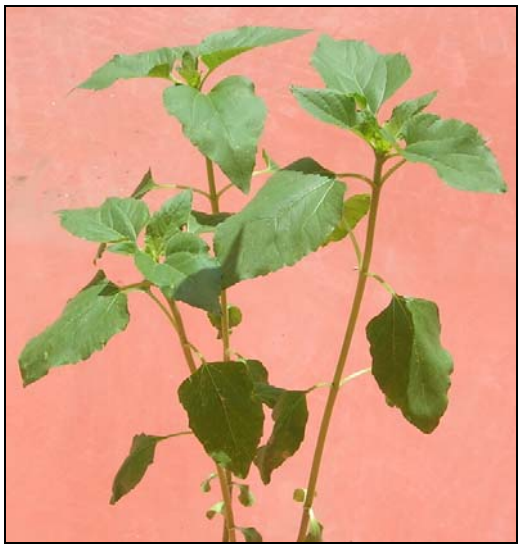

Figure 1: Some sunflower plants used in the study

The camera used to acquire the images was an AVT Marlin F131C, with a 1280×1024 pixels CMOS color sensor. It uses a Bayern pattern to decode color information into YUV color components, which are later transformed into RGB components by the vision software. The camera was mounted in the perpendicular angle to the ground, over the sunflower plants (**Figure 2a**). The acquisition process was automated by using a computer application developed with LabVIEW® 8.6 from National Instruments, the same development system employed for image analysis. The application run in a laptop and the camera was connected to the laptop through an IEEE 1394 (FireWire) controller card and an appropriate FireWire cable.

During each acquisition period, the parameters of the color camera were kept fix and configured as manual parameters to avoid their automatic adaptation. One of the most important parameters to keep fix was the shutter speed or the exposure time. In this

way, the quantity of light that reach to the camera sensor only depends on the natural sunlight in each moment, and not on the exposure time.

(a) **(b)**

Figure 2: Acquisition system: (a) cameras over the plants; (b) light meter and acquisition card

The plants were grouped to obtain a high ratio of image area for the leaves. The background was chosen to simplify the segmentation process; instead of using earth as image background, it was used some uniform ground, red or white. The images were acquired for several hours from the morning to midday or from the afternoon to the evening, always under natural illumination. The time between images was 10 seconds. During the acquisition time the movement of the sun produced changes in the illumination, the same way as the presence of clouds. In some cases images taken under cloudy illumination were removed from the image set to analyze only direct sunlight.

Simultaneously to the image acquisition, the illuminance information was measured by a light meter. It was also connected to the laptop through a data acquisition card, NI-USB 6008, supplied by National Instruments (**Figure 2b**). The magnitude provided by the light meter is lux, that is, lumen by square meter, and its spectral response corresponds to the visible spectrum according with the sensibility of the human eye. This response approximately matches with the sensor response of the color camera. The illuminance information will be useful for trying to establish a relation between it and color information from sunflower plants provided by the camera.

2.2 Segmentation

Thanks to the uniform background of the scene, most of the times a matt white background, the segmentation of sunflower leaves was simple enough. It was used intensity version of the RGB color images, calculated with (1).

$$I = \frac{R + G + B}{3} \tag{1}$$

After that, a clustering process was followed to obtain two groups or classes, sunflower leaves and background. The seeds for clustering initialization were 0 and 255, the limits of intensity value using 8 bits per pixel. The white background caused the corresponding pixels in the CMOS sensor to be saturated; meanwhile pixels representing sunflower leaves had medium intensity values. In this way, clustering segmentation was highly efficient. **Figure 3** shows an example of segmentation.

(a) (b)

Figure 3: Segmentation process: (a) color image; (b) binary segmented image

2.3 Color analysis

After extracting sunflower leaves pixels, several parameters were calculated for the histogram of the planes of three color spaces: RGB (red, green, blue), rgb (normalized RGB) (2) and HSI (hue, saturation, intensity). The 14 parameters are enumerated in **Table 1**.

Table 1: Parameters calculated from the histogram of color planes

Parameter	Description
MIN	Minimum value
MAX	Maximum value
RNG	Range, MAX–MIN
AREA	Ratio of sunflower pixels in the image
MEAN	Mean value
VAR	Variance value
STD	Standard deviation, √VAR
MAD	Mean absolute deviation
MOD	Mode, most frequent value
MED	Median, middle point
P25	Percentile 25, value with 25% of points on its left
P75	Percentile 75, value with 75% of points on its left
IQRNG	Range inter-quartile, P75–P25
MOD-MAX AREA	Ratio of pixels between mode and maximum value in the image

$$r = \frac{R}{R+G+B}; \quad g = \frac{G}{R+G+B}; \quad b = \frac{B}{R+G+B}; \quad r+g+b = 1 \tag{2}$$

The evolution of all the parameters in **Table 1** was visualized and evaluated. To obtain a clear representation of parameters in graphs, the data was filtered using a low-pass filter, specifically a mean filter using the previous six samples and the following six samples of the value to be filtered. With 10 seconds between images, it consisted of averaging images within two minutes. Finally, filtering allowed to identify easier the trend of the parameters. In *Results and discussion* section will be explained which parameters had a significant evolution with time and illumination and the characteristics of that evolution.

3 Results and discussion

From the 14 parameters described above in *Color analysis* subsection, the first four do not have a meaning in color analysis: minimum and maximum values, range and area. For example, area should be constant if sunflower plants had not movement, but in uncontrolled natural conditions some wind can appear. The 10 remaining parameters do have a trend along the time, as seen below for each color space. However one of them, variance, is totally dependent on standard deviation, so it will not be analyzed.

Most of graphs and analysis below correspond to the acquisition of images along the morning, when the illumination increases as the sun raise to the zenith. **Figure 4a** shows the measurement of light meter along a sunny morning without any clouds or mist. The evolution of illuminance is equivalent during the afternoon but it decreases with time. It is shown in **Figure 4b**, where there are some sudden variations owing to the presence of light clouds.

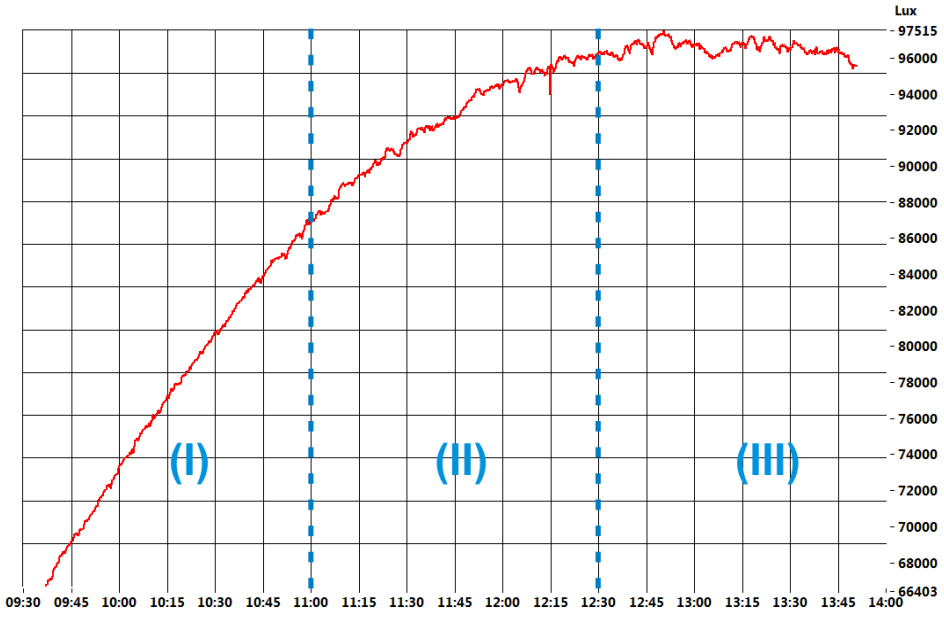

(a)

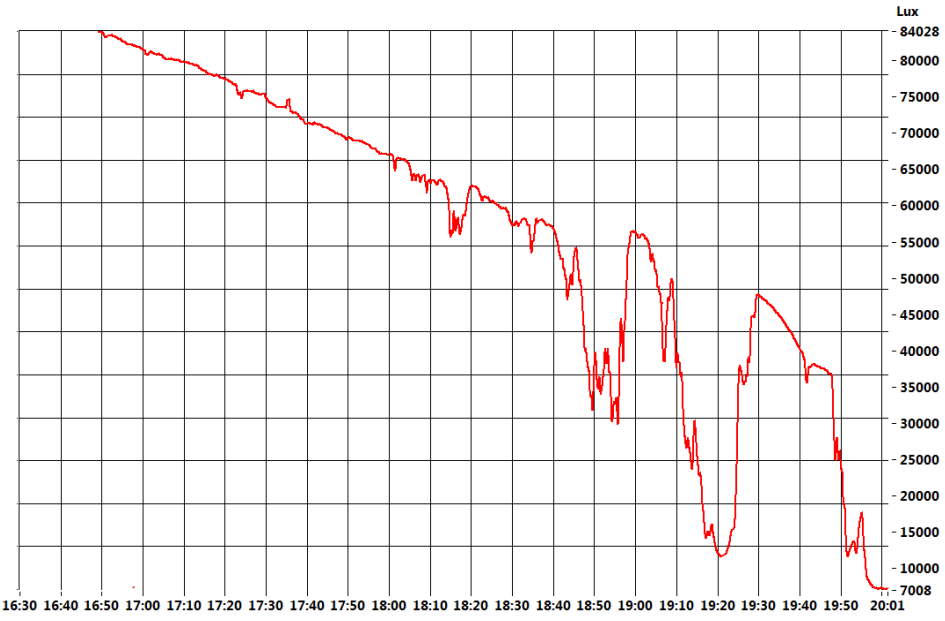

(b)

Figure 4: Illuminance variation during the morning (a), with three regions (I, II, IIII) and the afternoon (b), with the effect of clouds

In **Figure 4a** there is a linear region (I), approximately from the beginning of the acquisition to 11:00. Then, from 11:00 to 12:30 the growth decreases (II) and finally the illuminance is almost flat from 12:30 to 13:45 (III). From this flat period, illuminance starts to

decrease and, finally, reaches a new linear region, at least from 16:50 as shown in **Figure 4b**.

3.1 Mean, median and mode

Mean, median and mode have a similar behavior along the time so in **Figures 5** and **6** are shown the means for the histograms of the three color spaces: RGB, rgb and HSI. In **Figure 5a**, the means for R, G, and B planes have the same trend, each one at one level. In region (I) (linear increase of illuminance) the means grow approximately in a linear way. It is logical since each component in RGB space contain intensity information. In region (II), where the growth rate decrease for illuminance, the same happens for means. Finally in region (III), even though illuminance is almost flat, means for R, G and B decrease.

The evolution of means for the histograms of planes r, g and b is slightly different: the mean of b plane changes in the same way as B plane does; the mean of g plane remain constant along the time; finally, the mean of r plane have the inverse behavior of that one for R plane, it decreases in regions (I) and (II) and increases slightly in region (III). However, the level variations for rgb planes are smaller than variation for RGB.

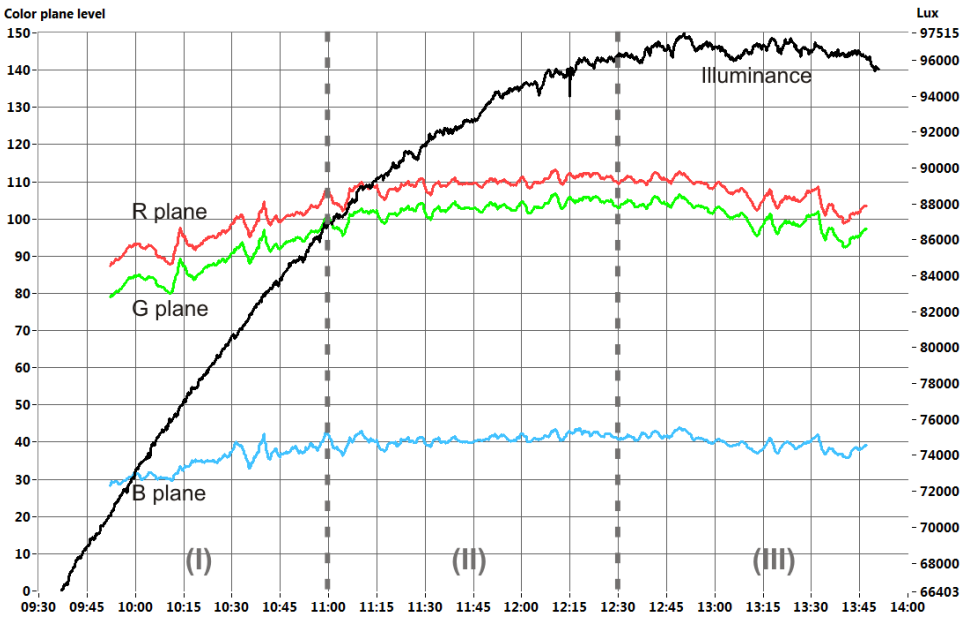

(a)

Figure 5a: Mean variation for the histograms of RGB planes

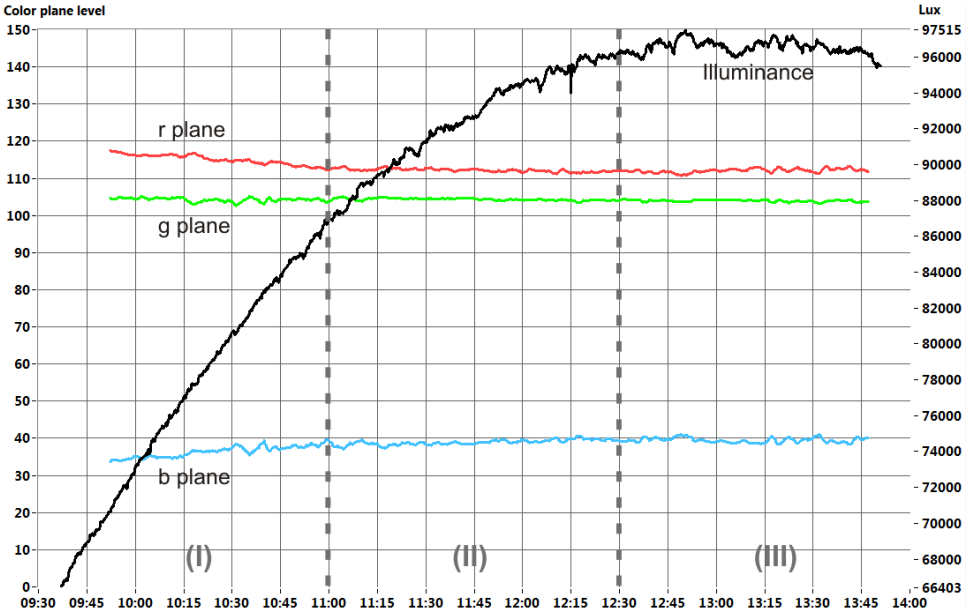

(b)

Figure 5b: Mean variation for the rgb planes

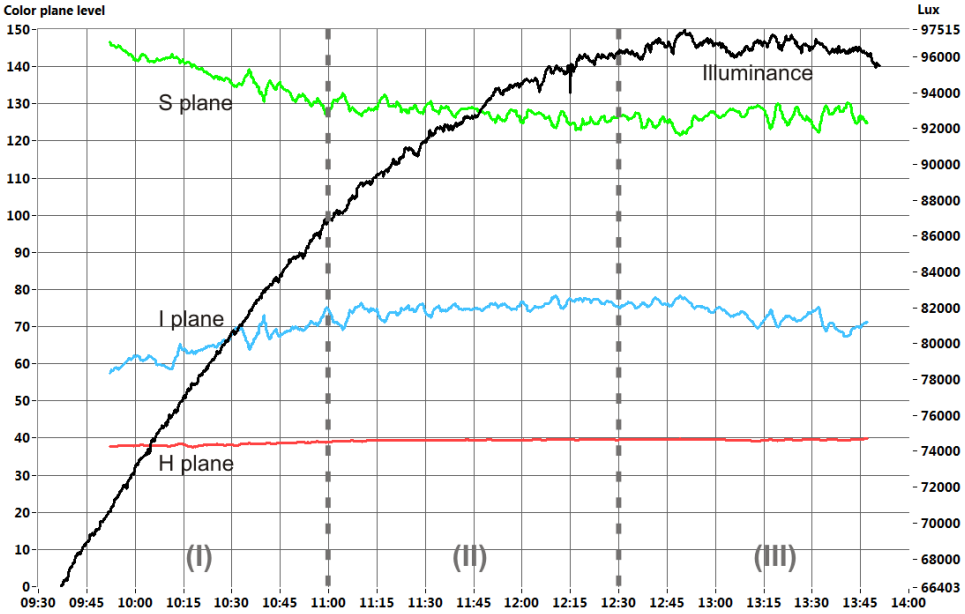

Figure 6: Mean variation for the histograms of HSI planes

Figure 6 shows that the means for S (saturation) and I (intensity) planes have inverse behaviors. Naturally I plane depends completely on changes in illumination. The evolution of mean for S plane says that purity of sunflower leaves color decreases when sun goes to the zenith. Finally, the H plane's mean is almost flat along the time. It increases very slightly in region (I) and is constant in regions (II) and (III).

As a conclusion, only means of g and H planes are immune to changes in natural illumination.

3.2 Standard deviation and mean absolute deviation

Standard deviation and mean absolute deviation are very similar, so only STD is represented in Figure 7. For RGB, rgb (**Figure 7a**) and HSI (**Figure 7b**) the standard deviation has very small variations. It and the mean analysis imply that the histograms move (mean variation) but do not became wider or narrower. Only when the sun is in the zenith the STD increases a little.

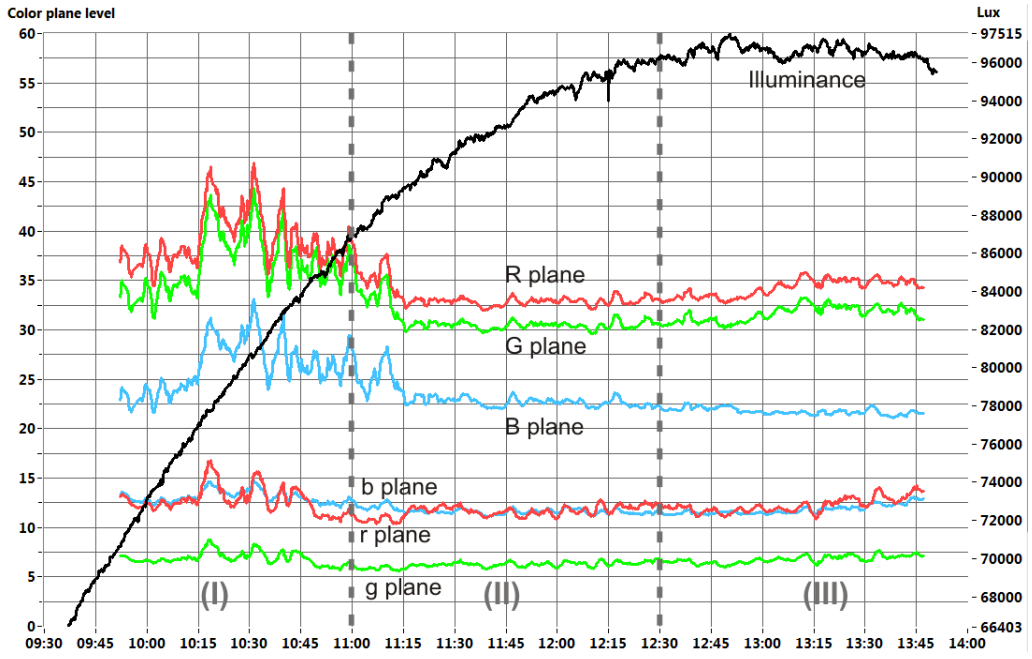

(a)

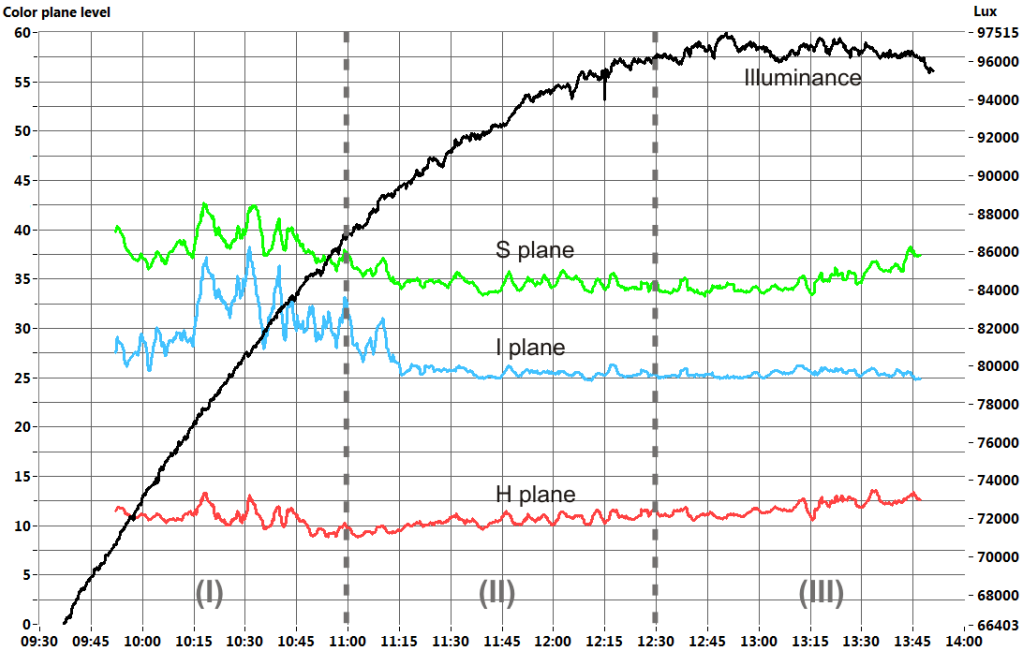

(b)

Figure 7: Standard deviation for the histograms of RGB and rgb planes (a) and HSI planes (b)

The peaks in the STD graphs in **Figure 7** from 10:15 to 10:45 were caused by wind; it moved and turned the leaves causing errors in the measurements. This effect appears again in Figures 8, 9 and 10.

3.3 Percentile 25, percentile 75 and range inter-quartile

The mean of a mono-modal histogram gives its position and the standard deviation gives its width. After analyzing mean and STD in 3.1 and 3.2, we know that changes in environmental illumination affect to histogram position but not to its width.

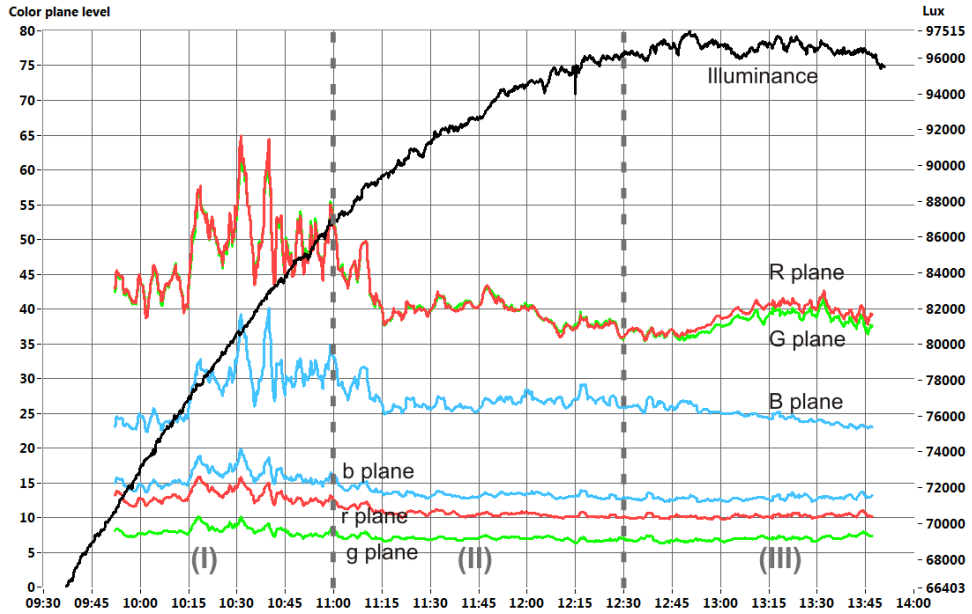

(a)

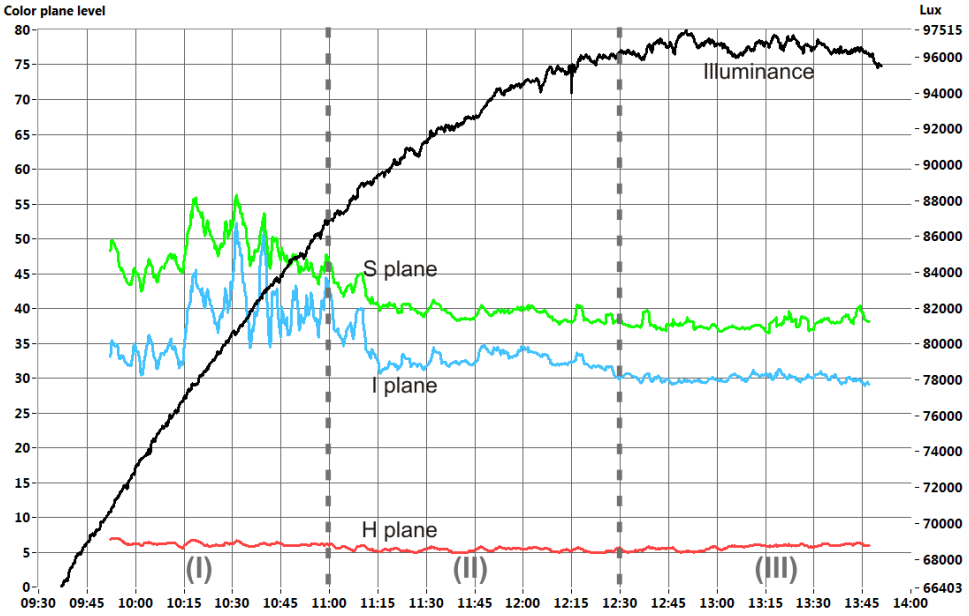

(b)

Figure 8: Inter-quartile range for the histograms of RGB and rgb planes (a) and HSI planes (b)

It implies that quantiles like the percentile 25 and the percentile 75 move when illumination changes but their relative position should be almost constant. It can be checked in **Figure 8**, the inter-quartile range (P75–P25) is almost flat along the time. It only presents the errors caused by wind and the same variations than STD at midday.

Like mean analysis in 3.1, the planes with higher immunity to changes in illumination are g and H.

3.4 Mode-maximum area ratio

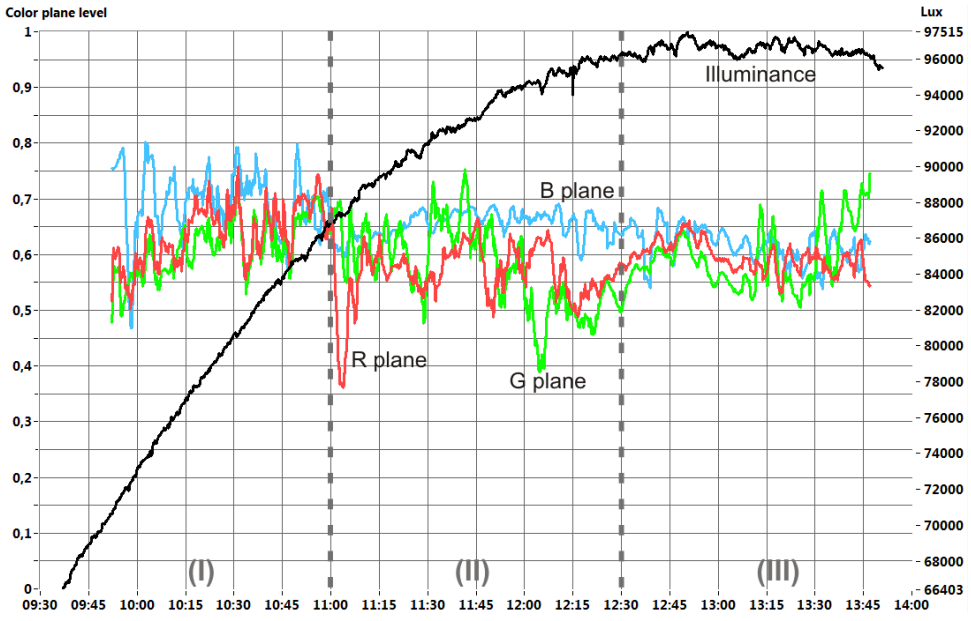

Figure 9: Mode-maximum area ratio for the histograms of RGB plane (a) and rgb planes (b)

This special parameter can be seen as a measurement of the symmetry of the histogram. For a completely symmetrical histogram the mode-maximum area ratio must be 0.5. It means that 50% of pixels are higher than the mode and the other 50% are lower. It also means that the mode is equal to the median.

The histograms of RGB planes are the less symmetrical since the parameter remains always above 0.5. Meanwhile, the histograms of rgb planes are quite symmetrical because of the normalization process. Finally for HSI color space, the histogram of H plane is very symmetrical; the histogram of S is a bit asymmetrical towards low levels and the histogram of I is highly asymmetric toward high levels.

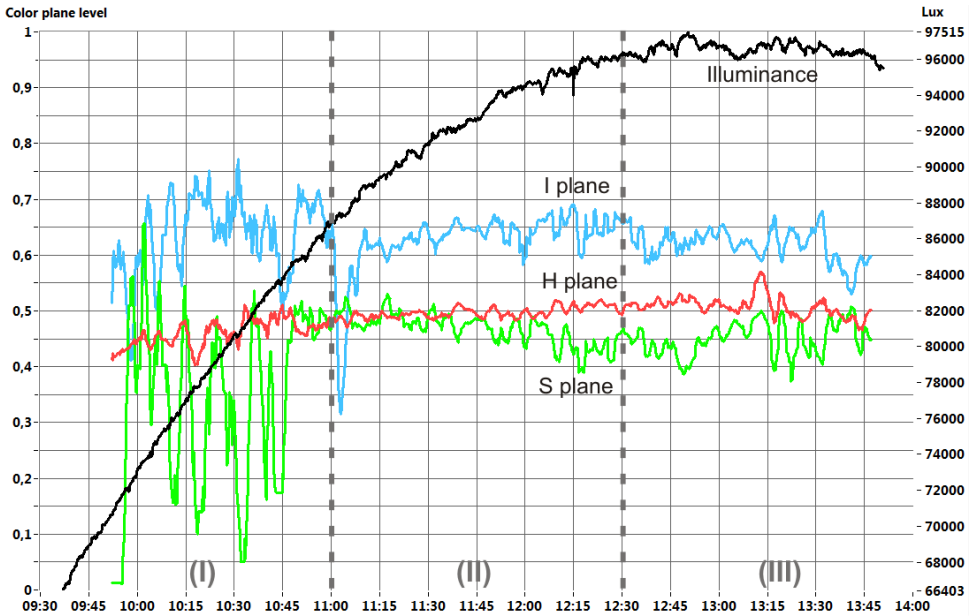

Figure 10: Mode-maximum area ratio for the histograms of HSI planes

4 Conclusion

The analysis of color in sunflower plants images along the day, under sunlight illumination, reveals that some color planes from different color spaces are more immune than others to changes in illumination. Representative parameters of the histograms for RGB, rgb and HSI color spaces were measured: mean, standard deviation, interquartile range and mode-maximum area ratio, etc. The histograms suffer variations with changes in illumination but the g and H planes are quite immune to illumination changes.

Acknowledgements

This work was supported by Grants from the University of Valladolid, financed jointly with Banco Santander Central Hispano, to carry out Doctoral Theses, granted to the author G. Ruiz Ruiz since June 2007. The authors also thank to the Consejería de Edu-

cación of the Junta de Castilla y Leon for the financial support granted through the projects VA064A08 and VA008B08.

References

AITKENHEAD M.J., DALGETTY I.A., MULLINS C.E., MCDONALD A.J.S., STRACHAN N.J.C. (2003): Weed and crop discrimination using image analysis and artificial intelligence methods, Computers and Electronics in Agriculture 39:157-171

ASTRAND B., BAERVELDT A.J. (2002): An Agricultural Mobile Robot with Vision-Based Perception for Mechanical Weed Control, Autonomous Robots 13: 21-35

RUIZ-RUIZ G.. GÓMEZ-GIL J., NAVAS-GRACIA L.M. (2009): Testing different color spaces based on hue for the environmentally adaptive segmentation algorithm (EASA), Computers and Electronics in Agriculture 68: 88-96

TIAN L., SLAUGHTER D. (1998): Environmentally adaptive segmentation algorithm for outdoor image segmentation, Computers and Electronics in Agriculture 21: 153-168

ImageInspector : a multipurpose system for agri-food products

Gianfranco Venora, Oscar Grillo, Rossella Saccone, Concetta Ravalli

Stazione Sperimentale di Granicoltura per la Sicilia, Buganvillea 20, Caltagirone, Italy
Corresponding author: venora@granicoltura.it

Abstract: *Results are presented on the development of a low-cost image analysis system which is helpful in many fields of the agri-food chain.*

Specific image analysis issues were approached and solved by developing specific macros for routine analysis.

Some case studies are reported. Lentil varieties and landraces identification; Italian bean landraces identification and wild species characterization and identification, using image acquired with a flatbed scanner. The obtained data were statistically elaborated to carry out classifiers that used the linear discriminant analysis algorithm for identification purpose.

Basic points of durum wheat chain, such as the grain raw material producing, its milling and semolina yield and processing in bread and pasta, were the subject of qualitative-quantitative evaluation, using the same image analysis technique.

In particular, a robust Bayesian classifier integrated in the durum wheat grain evaluation procedure was carried out, it correctly identifies 99.33% of vitreous kernels, 94.83% of starchy, 96.46% of the piebald and 97.50% of shrunken kernels, moreover it is able to estimate the percentage of semola yield.

The semola quality was evaluated, by means of black and bran points count. The quality of end products such as pasta, was explored for the presence of black points, which according to Italian law, they should not be present. Also bread sliced was evaluated, objectively, by means of image analysis techniques.

These and other applications, that should increase in the future, have stimulated the development of the ImageInspector, a marketable prototype which is at the same time user-friendly, portable and cheap, because the images are acquired with camera or scanner.

1 Introduction

Image analysis is proving to be an objective investigation tool, in particular in the cereal food chain, for the quality characterization and defects detection.

Many small and medium industries in the Agri-food chain, while estimating important the use of systems based on imaging technology, they not found available on the market, systems able to perform those specific quantitative and qualitative analysis at low costs, with no accuracy lost in results.

Even the PGI, PDO European Trademark consortia, could be safeguard their precious products, with this quick, reliable and cheap technology.

For many years in our laboratories we advantage of image analysis technology, to develop applications or *macros* for routine analysis in various fields (GRILLO *et al.* 2007, VENORA *et al.* 2007, BACCHETTA *et al.* 2008, MATTANA *et al.* 2008, VENORA *et al.* 2008, DOUST *et al.* 2009, SYMONS *et al.* 2009, VENORA *et al.* 2009a, VENORA *et al.* 2009b). Some applications, tested in the laboratory have proved very useful and usable at industrial level. For this reason, we were encouraged to develop a system that could accommodate different applications for different uses.

ImageInspector prototype, developed at Stazione Sperimentale di Granicoltura, could be the image analyser for visual assessment, suitable for small laboratories as storage centers, seed industries, mills, pasta factory and bakeries, moreover it could be used in other sectors of the agri-food for raw or processed materials.

2 Materials and methods

ImageInspector consists of hardware components and software for the *macros* management.

A PC or a Notebook with a Microsoft® Windows operative system XP or later. The image acquisition equipment can be a professional flatbed scanner with or without a trans-illuminator cover, or a digital camera integrated in a black-room for excluding environmental light and/or placed on a trans-illuminator table, depending of the user needs. The image acquisition hardware can be exchanged according to the changing preferences or tasks.

All applications of image analysis, the macros that can be used by *ImageInspector,* have been developed using the library of KS400 Image Analysis (Zeiss, Germany), with its proprietary language Klic. The macros can be used as stand alone programs with the software KSrun (Zeiss, Germany), it contains in background the entire library of KS400, but does not allows neither editing not developing of applications or macros.

3 Results

Figure 1 shows a view of *ImageInspector*, in the middle a Notebook with KSrun Software running the macro *Semola. mcr*. In the left the camera mounted on the top of a black-room for excluding environmental light, with a window to place the samples, and a

5.7'' TFT liquid crystal screen monitor for viewing the samples before acquiring, in this case a Petri dish filled with semola for black and bran points count.

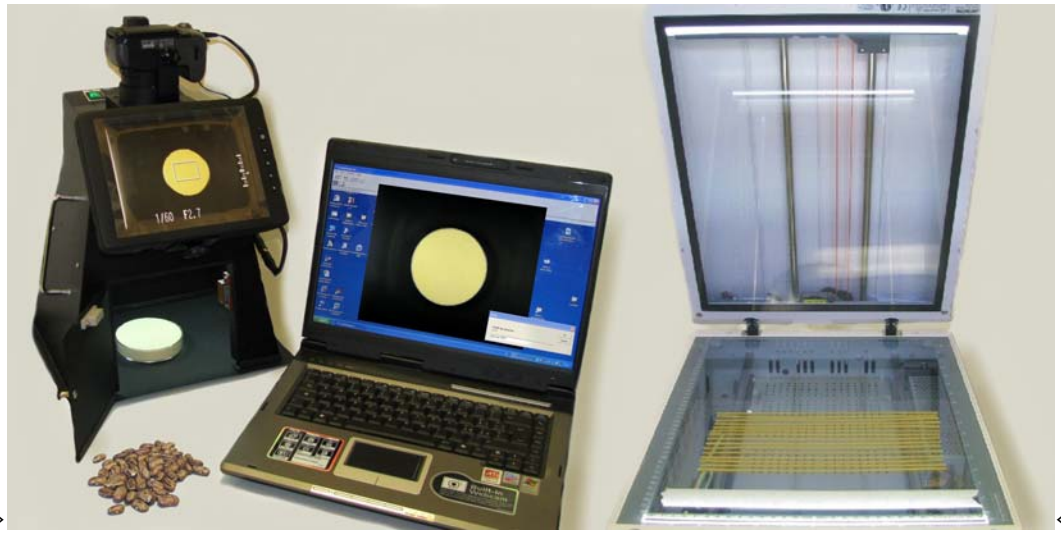

Figure 1: *ImageInspector*

On the right, a professional flatbed scanner with a trans-illuminator cover, ready to run the macro *SpaghettiSpeckCount.mcr.* To see and count the specks on spaghetti strands, it is necessary to acquire transilluminated images.

ImageInspector was already proved to be quick, reliable and consistent in image acquisition and analysis with different macro developed to solve specific problem.

Using the macro *Lens.mcr*, eight lentil varieties and landraces were correctly identified, in the training set (99.80%) and test set (97.10%) respectively (VENORA *et al.* 2007).

Using the macro *Bean.mcr*, fifteen Italian bean landraces were correctly identified in the training set (99.00%) and test set (98.20%) respectively (VENORA *et al.* 2009a).

The macro *Wild.mcr,* was developed to create a database of seeds morfo-colorimetric traits, for the characterization of autochthonous germplasm in entry to the bank and the realization of statistic classifiers for the discrimination of genera and species, within many botanical families. The obtained data, were statistically elaborated to carry out classifiers using, later off-line, the linear discriminant analysis algorithm for identification (SPSS statistic package). Such classifiers showed a performance between 74.3% and 96.4% (BACCHETTA *et al.* 2008). In addition, for the genus *Astragalus*, it was possible to elaborate a classifier able to identify very similar taxa of a species complex, obtaining a performance between 83.7% and 100% (MATTANA *et al.* 2008).

One important problem solved with *ImageInspector* was the Vitreosness amount determination on durum wheat kernels at the storage centers. In particular, a robust Bayesian classifier integrated in the wheat grain evaluation procedure was carried out, it cor-

rectly identifies 99.33% of Vitreous kernels, 94.83% of Starchy, 96.46% of the Piebald and 97.50% of Shrunken kernels, moreover it is able to estimate the percentage of semola yield (VENORA *et al.* 2009b).

The macro *Semola.mcr* allows to evaluate the semola quality by means of black and bran points count, they affects the quality of end products such as pasta (**Figure 1**). The macro *SpaghettiSpeckCount.mcr* is a quick and objective imaging method to count the dark specks in spaghetti strands, acquired using a flatbed scanner with a trans-illuminator cover (**Figure 1**). The method simultaneously measured individual speck size and colour and determined the overall color of the spaghetti product. According to Italian law, any specks should not be present (VENORA *et al.* 2008, SYMONS *et al.* 2009).

Bread, such as pasta, is a very important end product of cereal chain. The macro *Bread.mcr* allow to acquire and measure bread slices, giving an objective evaluation of texture, and its relationship with bread constituents, for example flour type (wheat varieties), ingredients kind and amount, such as leaven or sourdough (GRILLO *et al.* 2007, DOUST *et al.* 2009).

4 Conclusions

The applications here reminded, have stimulated the development of the *ImageInspector*, a marketable prototype which is at the same time user-friendly, portable and cheap, because the images are acquired with camera or scanner. Moreover, many new applications or improvement of the already developed ones coming soon.

To facilitate a wide distribution of *ImageInspector*, whose rapid implementation can be achieved only through co-operation between different institutions operating in different fields, the authors are open for and interested in possible collaborations through the sharing of knowledge. Moreover the Stazione Sperimentale di Granicoltura is open to collaborate with factories to merchandise *ImageInspector*.

References

BACCHETTA G., GRILLO O., MATTANA E. VENORA G. (2008): Morpho-colorimetric characterization by image analysis to identify diaspores of wild plant species. Flora 203 (8): 669-682

Carl Zeiss Vision. (1998): KS-400 image analysis library. Version 3.0. Oberkochen, Germany

DOUST M.A., RIZZO B., GRILLO O., PECORINO B. VENORA G. (2009): Sourdough effects on the crumb texture and shelf-life evaluated with dynamometer and Image analysis measurements in the Dittaino Pagnotta P.D.O., a durum wheat bread produced by a Sicilian bakery industry. In Proceedings of the CIGR Section VI International Symposium on Food Processing, Monitoring Technology in Bioprocesses and Food Quality Management. ed. D.W. SUN, Potsdam, Germany 31 August - 02 September 2009

GRILLO O., ORLANDO A., RAIMONDO I., VENORA G. (2007): Fingerprinting del pane: tecniche di analisi d'immagine per la caratterizzazione, tracciabilità e rintracciabilità. Tecnica Molitoria, 58 (9): 1-14

MATTANA E., GRILLO O., VENORA G., BACCHETTA G. (2008): Germplasm image analysis of Astragalus maritimus and A.verrucosus (subgen. *Trimeniaeus*). Anales del Jardìn Botànico de Madrid 65 (1): 149-155

SPSS. (1999): SPSS Application Guide Base10.0. Chicago, Illinois, USA: SPSS Inc

SPSS. (2006): SPSS for Windows. Version 15.0. Chicago, Illinois, USA: SPSS Inc

SYMONS S.J., VENORA G., VAN SCHEPDAEL L., SHAHIN M.A. (2009): Measurement of spaghetti speck count, size and colour using an automated imaging system. Cereal Chemistry 86(2): 164-169

VENORA G., GRILLO O., SACCONE R., RAVALLI C. (2008): - Speck evaluation on commercial spaghetti using an imaging system. in: From Seed to Pasta : The Durum Wheat Chain - International Durum Wheat Symposium. Bologna Italy, June 30 - July 3 Bologna, Edizioni Avenue Media, Milano

VENORA G., GRILLO O., SHAHIN M.A., SYMONS S.J. (2007): Identification of Sicilian landraces and Canadian cultivars of lentil using image analysis system. Food Research International, 40: 161-166.

VENORA G., GRILLO O., RAVALLI C., CREMONINI R. (2009): Identification of Italian landraces of bean (*Phaseolus vulgaris* L.) using an image analysis system. Scientia Horticulturae 121: 410-418

VENORA G., GRILLO O., SACCONE R. (2009B): Quality assessment of durum wheat storage centres in Sicily: Evaluation of Vitreous, Starchy and Shrunken Kernels using an Image Analysis System. Journal Cereal Science 49 (3): 429-440

Comparison of different classification algorithms for weed detection from images based on shape parameters

Martin Weis[1], Till Rumpf[2], Roland Gerhards[1], Lutz Plümer[1]

[1] *Department of Weed Science, University of Hohenheim, Otto-Sander-Straße 5, 70599 Stuttgart, Germany*
[2] *Department of Geoinformation, Institute of Geodesy and Geoinformation, University of Bonn, Germany*
Corresponding author: Martin.Weis@uni-hohenheim.de

Abstract: *Variability of weed infestation needs to be assessed for site-specific weed management. Since manual weed sampling is too time consuming for prctical applications, a system for automatic weed sampling was developed. The system uses bi-spectral images, which are processed to derive shape features of the plants. The shape features are used for the discrimination of weed and crop species by using a classification step.*

In this paper we evaluate different classification algorithms with main focus on k-nearest neighbours, decision tree learning and Support Vector Machine classifiers. Data mining techniques were applied to select an optimal subset of the shape features, which then were used for the classification. Since the classification is a crucial step for the weed detection, three different classification algorithms are tested and their influence on the results is assessed. The plant shape varies between different species and also within one species at different growth stages. The training of the classifiers is run by using prototype information which is selected manually from the images.

Performance measures for classification accuracy are evaluated by using cross validation techniques and by comparing the results with manually assessed weed infestation.

1 Introduction

The automated identification of weed species in the field is close to be realized as an operational product. Information about weed species, weed density, and weed coverage distribution can be used to manage weeds on a sub-field level either by using chemical or mechanical control. Sampling (using a regular or irregular grid) is necessary to manage weeds site-specifically. Manual weed scouting is time consuming and gets expensive with increasing number of sampling points. BROWN & NOBLE (2005) reviewed the approaches for weed identification, SLAUGHTER *et al.* (2008) identified the robust weed detection as a primary obstacle for robotic weed control technology and reviewed the approaches for weed detection as well as actuator technology. Non-imaging photodiode

sensors have been used without and with artificial light sources (SUI *et al.* 2008) to detect plants and assess weed infestations, but these sensors cannot distinguish between plant species.

Image processing methods were successfully used to distinguish different weeds and crops using shape parameters: PÉREZ *et al.* (2000) computed different compactness features and crop row location information to detect broadleaved weeds in cereals. They reached similar classification performances of about 89% (cereals) and 74% (broadleaved weeds) using a *k*NN and Bayes rule classifier.

A system was developed by SÖKEFELD *et al.* (2007) and OEBEL & GERHARDS (2005) to discriminate weeds and crop from bi-spectral images by using shape features. Field tests led to average herbicide savings of 35-70%. This system was reimplemented and refined. The system aims at detecting weeds and distinguishing them from the crop to make decisions about the best management strategy. In order to derive a suitable classification with the shape features three different algorithms were compared. The objective of this study is the selection of a suitable classification algorithm, therefore properties of different algorithms are contrasted and discussed after applying them to a data set.

2 Materials and methods

Images were taken in the field and processed by using image processing techniques to derive shape features for the objects in the image. A process chain for an automatic classification of different weeds based on the shape parameters was defined in the software Rapid Miner (MIERSWA *et al.* 2006). Two models, one with a base division with regard to the species and another with regard to subclasses for the species were learned on the basis of training data for each of the three classifiers, especially focusing on Support Vector Machines (SVMs). After normalisation with mean zero and standard deviation one the inner evaluation of the classifiers´ performances was carried out by cross-validation. Finally, we applied the learned model to unseen data samples and evaluated the prediction performance by using a manual classified set of images.

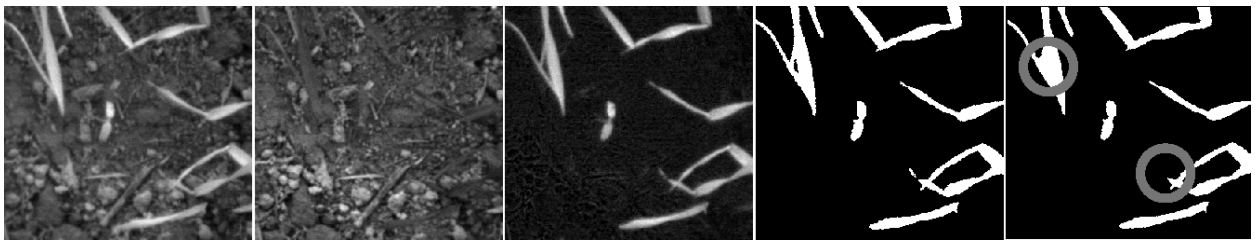

Figure 1: Image processing (from left to right): infrared (IR) image, red (R) image, difference image, thresholded image, morphological operators and size criterion applied. Circles: small region filtered and hole closed.

2.1 Study site

We have used data sets from a field located on the experimental field station of the University of Hohenheim (Ihinger Hof), which is southwest of Stuttgart. The measurements took place in November 2008 in an oil seed rape field (*Brassica napus* L., BRSNN) with some volunteer barley (*Hordeum vulgare* L., HORVS). The latter is the weed species, which can be controlled by a post-emergence herbicide for grass weeds. The crop was in a cotyledon stage and the weed in a one- or two-leaf stage. The images had a ground resolution of 0.25 mm^2 per pixel and the field was sampled along tracks with 3 m distance.

2.2 Image processing

The system uses difference images of the near infrared and red light spectra. The images were taken in the field from a distance of 1 m and were associated with a DGPS (differential GPS) position. Since plants absorb red light (620–680 nm) for their photosynthesis and have a high reflection in the near infrared spectrum (> 720 nm), they appear dark in the red image (R) and bright in the near infrared (IR) as shown in **Figure 1** (the example in **Figure 1** was taken from another series, in which red and infrared images were available, and thus not showing oil seed rape). Other materials (soil, mulch, stones) have a similar reflection in these bands. In the difference of the two images (IR-R) the plants appear bright and the background is dark. This observation principle allows for differentiating between plants and background with a grey level threshold. Some preprocessing steps to reduce noise follow: a size criterion suppresses smaller regions than the cotyledon leaves of oil seed rape (right circle in **Figure 1**) and morphological operations (opening/closing) smooth the contour and connect nearby regions as well as fill small holes (left circle in **Figure 1**).

Shape features are derived for each remaining segment, which are defined as connected components in the binary image. Three types of features are computed: region-based features, that are derived from the pixels of each segment, e.g. size, statistical moments and Hu features (Hu 1962), which are well known for a long time. The second type of features, the contour-based features, is derived from the border pixels of the segments. Fourier descriptors and curvature scale space features fall into this category. The third type of features is derived from the skeleton of the segments, which is the centre line. Combined with a distance transform, which assigns each pixel of the region a value for the distance to the border, statistical measures resemble the thickness of the segments (mean, max, and variance) and are useful to distinguish broad leaves from narrow leaves.

The shapes of different species vary between the different growth stages. Training data for the shape based classification uses classes which describe the species (EPPO-Code), their growth stage (BBCH-Code) and special situations which occur during segmentation (i.e. single leaves L, overlapping O). The following classes were defined for

the subclasses training set: BRSNN10L, BRSNN10N (single leaf and whole plant in cotyledon stage); HORVS10N, HORVS12N, HORVS12O, HORVS12L (N means 'normal' segmentation) and two additional noise classes for elongated and compact noise in the images: NOISE00L, NOISE00X. No other species were found in the images.

All information about the images, positions, classes, the training data and results of the image processing and classification are stored in a relational database. A process chain for an automatic classification in the software Rapid Miner (MIERSWA *et al.* 2006) was defined.

By using a genetic feature selection algorithm the dataset was reduced to the following relevant ten shape features: *areasize, compactness, Drear, Dright, Hu2, Hu3, Ja, Jb, Rmin, skelmax*. These are nine region-based features (J*: inertia of main axes, D*: distances to mainaxes, Hu*: Hu features, Rmin: minimum distance to border) and one skeleton feature (*skelmax*, maximum distance of the skeleton to the border).

2.3 Classification

Classification algorithms aim at finding regularities in patterns of empirical data (training data). If two classes of objects are given the problem is also known as dichotom. Then the classifier is faced with a new object which has to be assigned to one of the two classes. The training data can be formulated as

$$(x_1,y_1),(x_2,y_2),\ldots,(x_n,y_n) \tag{1}$$

where the bold x describes a feature vector of the form $x_1,\ldots,x_m$, and where $y_k = 1$ if x_k belongs to class one and $y_k = -1$ if x_k is in class two. A labelled object y has an assignment to one of the classes and its feature vector x is used for the learning of supervised classifiers. This results in finding a function f which approximates the training data in the best way possible, i.e.

$$y_i = f(x_i) \quad \forall \quad I \in \{1,\ldots,n\}. \tag{2}$$

In this case the classes are different weeds at varying stages of development and the features are shape parameters. However it is not enough to find a function f which fits the training data. Additionally the ability to classify unseen data, which is often called as generalisation ability, is important, too. Finding a function which fits the training data is an 'ill-posed problem' since there is an infinite number of functions having this property. It is a basic assumption of machine learning that the class of functions to be learned has to be restricted. The most simple case is a set of linear functions which have a fixed number of parameters given by the number of features.

Learning a function f starts with a set of labelled training data, which in our case was generated from the segmented images by defining prototypes. Afterwards the learned

function is also evaluated on labelled test data. In the following we introduce the three classification algorithms. First, a short overview on the k-nearest neighbour algorithm and the decision tree learning is given. Afterwards, the support vector machine (SVM) classifier is explained in more detail.

2.3.1 *k*-Nearest neighbour

One example for an instance-based learning algorithm is the k-Nearest Neighbour (kNN) algorithm. It uses the k nearest neighbours to make the decision of class attribution directly from the training instances themselves. Usually, Euclidean distance is used as distance metric. The decision for attaching the sample in question to one of the several classes is based on the majority vote of its k nearest neighbours. An odd number should be chosen for k to allow for a definite majority vote.

2.3.2 Decision tree

Decision tree learning is one of the most widely used and practical methods for inductive inference. There are many algorithms for constructing decision trees. We use the most popular one: i.e. C4.5 (QUINLAN 1993). A decision tree can be seen as a data structure in form of a tree. Every interior node contains a decision criteria depending only on one feature. The features´ relevance for classification is determined by entropy reduction which describes the (im) purity of the samples. For the first split into two parts the feature with the highest relevance is used. After such a decision the next feature is determined, which splits the data optimally into two parts. Since always one feature is considered at a time, a boundary of axis parallel parts is formed. This is recursively repeated on each derived subset. If followed from root to a leaf node the decision tree corresponds to a rule based classifier. An advantage of decision tree classifiers is their simple structure, which allows for interpretation (most important features are near the root node) and visualisation.

2.3.3 Support vector machines

Support Vector Machines (SVM) were invented by VLADIMIR VAPNIK in 1979 (VAPNIK 1982). Basically the SVMs separate two different classes through hyperplanes. If the classes are separable by hyperplanes an optimal function can be determined from the empirical data. The hyperplane is expressed by its normal vector $\boldsymbol{w}$ and a bias b. The class of hyperplanes can be specified in the scalar product space H (feature space) as follows

$$\langle w,x\rangle + b = 0 \quad \text{where} \quad w \in H, b \in R \tag{3}$$

where $\langle w,x\rangle$ means $x_1 \cdot w_1 + \cdots + x_n \cdot w_n$. This yields the corresponding decision function

$$f(x) = \text{sgn}\,(\langle w,x\rangle + b) \tag{4}$$

where the sign function extracts the sign of a real number. It is defined as -1 if $f(x) < 0$ and 1 if $f(x) > 0$ which denotes the two different class labels +1 and -1. Usually there exist many hyperplanes which separate the two classes. The basic idea behind SVMs is that the optimal hyperplane maximises the margin between data sets of opposite classes. In order to construct the optimal hyperplane, the following equation has to be solved.

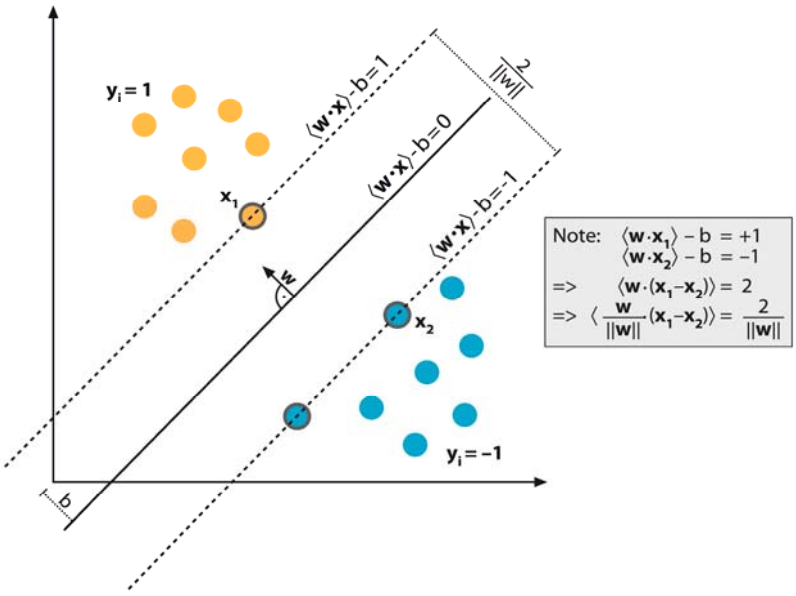

Figure 2: The optimal separating hyperplane is shown as a solid line

$$\frac{min}{w \in H, b \in R} \tau(w) = \frac{1}{2}\|w\|^2 \tag{5}$$

$$\text{subject to} \quad y_i(\langle w,x_i\rangle + b) \geq 1 \quad \forall \quad i \in \{1,\cdots,n\}. \tag{6}$$

The constraint (6) ensures that $f(x_i)$ yield +1 for $y_i = +1$ and -1 for $y_i = -1$, and that the two classes are separated correctly. If $\|w\| = 1$ the left hand side of (6) is the distance of the training sample x_i to the hyperplane. This is the Hessian normal form representation of the hyperplane. The distance of each training sample to the hyperplane can be computed by dividing $y_i(\langle w,x_i\rangle + b)$ by $\|w\|$. The overall margin is maximised if the constraint (6) is satisfied for all $i \in \{1,\cdots,n\}$ with w of minimal length, as given in (5). The distance of the closest point to the hyperplane is $1/\|w\|$. This can be illustrated by considering two training samples, one of each class respectively, and by projecting them onto the hyperplane normal vector $w/\|w\|$ (see Note in **Figure 2**).

The formulas (5) and (6) specify the constrained optimisation problem. It can be transformed to a 'dual' problem, where w and b are eliminated by introducing Lagrange multipliers α_i.

$$\frac{max}{\alpha \in R^n} w(\alpha) = \sum_{i=1}^{n} \alpha_i - \frac{1}{2} \sum_{i,j=1}^{n} \alpha_i \alpha_j y_i y_j \langle x_i, x_j \rangle \tag{7}$$

$$\text{subject to } \alpha_I \geq 0 \quad \forall \quad i \in \{1, \cdots, n\} \quad \text{and} \quad \sum_{i=1}^{n} \alpha_i y_i = 0. \tag{8}$$

This leads to the following decision function

$$f(x) = \text{sgn} \left(\sum_{i=1}^{n} y_i \alpha_i \langle x, x_i \rangle + b \right) \tag{9}$$

where b can be computed by the Lagrange multipliers which do not equal zero. These are called support vectors. All other samples with $\alpha_i=0$ are discarded.

Up to now only linearly separable classes were considered, but SVMs are able to classify samples with a non-linear discriminant. The basic idea of SVMs is to map the data into a new feature space and then solve the constrained optimisation problem. Obviously it seems to be very expensive to compute the mapping into a high-dimensional space. For this reason a kernel function is introduced to make the computation very simple (BOSER 1992). This is referred to as the 'kernel trick', which causes an implicit mapping in the feature space without explicitly knowing the mapping function Φ. Accordingly the scalar product $\langle x,x_i \rangle$ can be substituted by

$$k(x,x_i) := \langle \Phi(x), \Phi(x_i) \rangle = \langle x, x_i \rangle. \tag{10}$$

So far we have made the implicit assumption that the datasets are free of noise and may be classified perfectly. In this case SVMs give 'hard margins'. In practice, this assumption does not hold true in most cases. This problem, however, may be handled by 'soft margins' which allow and penalize classification errors. Accordingly, in 1995 a modification was introduced where slack-variables ξ_i are used to relax the so-called hard-margin constraints (6) (CORTES & VAPNIK 1995), so that some classification errors depending on ξ_i are allowed. The influence of the classification errors are parametrised with the parameter C. A larger C penalizes a wrong classification more strongly.

2.3.4 Multi-class classification

In contrast to decision tree and k-nearest neighbour classifiers, support vector machines handle binary problems. There are several methods to extend them for multi-class classification effectively by combining different binary classifiers. Some methods consider

multiclass problems at the expense of much larger optimisation problems with expensive computation. In the used LIBSVM algorithm (CHANG & LIN 2007) the 'one against one' approach (KNERR *et al.* 1990) is applied in which $k(k\text{-}1)/2$ classifiers are constructed and each one trained with data of two classes. The classification decision is based on a majority vote of the class assignments. If classes have identical votes the one with the smallest index is selected.

3 Results and discussion

Two models, one with three classes according to the species (plus noise) and another with subclasses for the species, were trained for each of the three classifiers based on the training data. The inner evaluation of the classifiers performances was carried out by cross-validation. Finally, we apply the learned model on unseen data samples and evaluated the prediction performance using a manually classified set of images.

The classifiers were initially trained with three classes, one for each species and noise (BRSNN, HORVS and NOISE). A cross-validation was used to assess the performance of each classifier. All three classifiers show a good performance (cross-validation: more than 98% correctly classified objects) to separate the three species from each other.

Table 1: Comparison of the classifiers for the three classes (species) case: the R^2 values for each class are used as performance measure

Classifier\Class	BRSNN	HORVS	NOISE
Decision Tree	0.96	0.97	0.97
SVM	0.95	0.96	0.97
*k*NN	0.97	0.96	0.98

3.1 Comparison to manual classification

A subset of the images (68) was selected and the number of weed and crop plants in each image were manually counted. This is the reference data set, as the number of plants is used to generate a management decision (spray or not). The classification result was assembled for these images to get the number of weed and crop plants per image. These numbers can then be compared to the manually assessed reference data.

The comparison between the classification results and the manually counted planes yields a systematic overestimation of the BRSNN and HORVU classes. This is due to the fact that after the image processing (2.2) the plants are split into parts, especially the oil seed rape plants (BRSNN) were often split into two separate germination leaf

objects. On the other hand, in images with a very high number of oil seed rape the number of plants is underestimated due to overlaps of plants which leads to segments which contain more than one plant in the image processing step. These problems can be taken into account by using a more detailed model for classification by introducing new classes for single leaves and overlaps of plants, as it is done in the following section.

3.2 Classification with subclasses

In order to account for the error of the split objects, training data was created with separated classes (subclasses) for each species. Two growth stages and single leaf classes were added as subclasses.

The classification using the three classifiers led to three confusion matrices, which can be compared in **Table 2**. The submatrices for the species are marked and allow for a comparison of intra- and interclass errors. All three classifiers reach high correct classification rates for the inter-class distinction of the different species (and noise): the submatrices (B*–H*, lower left and upper right) contain a maximum of one wrongly classified object. By weighting the subclasses (0.5 for dictyledonous leaves) there is no overestimation any more, since the automatically number of plants correspond to the manually counted ones.

The introduced subclasses can also be used to show differences between the classifiers. They differ in the classification of intra-species classes (H*–H*, lower right submatrix). The k-NN classifier and decision trees cannot adequately separate the subclasses of HORVS, because the model complexity is not sufficient. The reason why decision tree learning cannot adequate differentiate between the subclasses is caused by regarding only one feature at a time during division into two subsets. Thereby the aforementioned boundary of axis parallel parts is obtained and samples which are not differentiable by this way are not adequately split.

In such cases SVMs have advantages, since they can construct nonlinear separation functions in the feature space. Using a radial basis function kernel to build non-linear class boundaries, a separation of the different subclasses of HORVS is possible. The SVM classifier still provides good classification rates for the difficult-to-separate subclasses, which is an important property and qualifies this algorithm for other datasets containing more weed species.

Table 2: Confusion matrix for three classifiers, the class abbreviations are: BL (BRSNN10L), BN (BRSNN10N), NX (NOISE00X), H_2L (HORVS12L), H_0N (HORVS10N), H_2N (HORVS12N), H_2O (HORVS12O), NL (NOISE00L)

↓ predicted	True class								
SVM	BL	BN	NL	NX	H_2L	H_0N	H_2N	H_2O	precision %
BL	65	0	0	0	0	0	0	0	100
BN	0	46	0	0	0	0	0	0	100
NL	0	0	53	0	0	0	0	0	100
NX	0	0	0	34	0	0	0	0	100
H_2L	0	0	0	0	41	0	0	0	100
H_0N	0	0	0	0	0	14	0	0	100
H_2N	0	0	0	0	0	0	48	0	100
H_2O	0	0	0	0	0	0	0	24	100
recall%	100	100	100	100	100	100	100	100	
k **NN**									
BL	65	0	0	0	0	0	0	0	100
BN	2	44	0	0	0	0	0	0	96
NL	0	0	53	0	0	0	0	0	100
NX	1	0	2	31	0	0	0	0	91
H_2L	0	0	0	0	34	2	5	0	83
H_0N	0	0	0	0	4	10	0	0	71
H_2N	0	0	0	0	13	1	28	6	58
H_2O	0	1	0	0	3	0	0	20	83
recall%	96	98	96	100	63	77	85	77	
Decicion tree									
BL	65	0	0	0	0	0	0	0	100
BN	2	44	0	0	0	0	0	0	96
NL	0	0	52	1	0	0	0	0	98
NX	0	0	1	31	0	2	0	0	91
H_2L	0	1	0	0	31	0	9	0	76
H_0N	0	0	0	0	6	8	0	0	57
H_2N	0	0	0	0	7	0	37	4	77
H_2O	0	0	0	0	0	0	4	20	83
recall%	97	98	98	97	70	80	74	83	

4 Conclusions

Image processing of bi-spectral images was used for the detection of weed and crop densities based on shape features. Three classification algorithms were compared by using manually derived densities for oil seed rape and barley. A simple class scheme, one for each species and noise, can be classified correctly by all compared classifiers (k-nearest neighbours, decision tree learning and support vector machines).

Due to oversegmentation or undersegmentation more classes were intruduced (here: subclasses of the species) to take into account single leaf image segmentation and overlaps of plants. In this case the performance of the three classifiers varies. The model complexity of k-NN and decision tree classifiers is not sufficient to separate the subclasses of HORVS. SVMs comprise a complex function class and construct an adequate model. Thus SVMs can adopt better to the more complex situations with different species, which is of practical relevance for site-specific herbicide variation. In future, this type of classifier will be applied to image series with more different species of weeds and crops.

References

BOSER E.B. (1992): A training algorithm for optimal margin classifiers. In Proceedings of the 5th Annual ACM Workshop on Computational Learning Theory, pp. 144–152. ACM Press

BROWN R., NOBLE S. (2005): Site-specific weed management: sensing requirements – what do we need to see? Weed Science 53(2), 252–258

CHANG C.-C., LIN C.-J. (2007): Libsvm: a library for support vector machines

CORTES C., VAPNIK V. (1995): Support-vector networks. Machine Learning 20(3), 273–297

HU M.K. (1962): Visual pattern recognition by moment invariants. IRE Transactions Information Theory 8(2), 179–187

KNERR S., PERSONNAZ L., DREYFUS G.G. (1990): Single-layer learning revisited: a stepwise procedure for building and training a neural network. In J. FOGELMAN (Ed.), Neurocomputing: Algorithms, Architectures and Applications. Springer-Verlag

MIERSWA I., WURST M., KLINKENBERG R., SCHOLZ M., EULER T. (2006): Yale: Rapid prototyping for complex data mining tasks. In L. UNGAR, M. CRAVEN, D. GUNOPULOS, and T. ELIASSI-RAD (Eds.), KDD '06: Proceedings of the 12th ACM SIGKDD international conference on knowledge discovery and data mining, New York, NY, USA, pp. 935–940. ACM

OEBEL H., GERHARDS R. (2005): Site-specific weed control using digital image analysis and georeferenced application maps – first on-farm experiences. In 5th ECPA, Uppsala, pp. 131–138

PÉREZ A., LÓPEZ F., BENLLOCH J., CHRISTENSEN S. (2000): Colour and shape analysis techniques for weed detection in cereal fields. Computers and Electronics in Agriculture 25, 197–212

QUINLAN R.J. (1993): C4.5: programs for machine learning. San Francisco, CA, USA: Morgan Kaufmann Publishers Inc.

SLAUGHTER D.C., GILES D.K., DOWNEY D. (2008): Autonomous robotic weed control systems: A review. Comput. Electron. Agric. 61(1), 63–78

SUI R., THOMASSON J.A., HANKS J., WOOTEN J. (2008): Ground-based sensing system for weed mapping in cotton. Computers and Electronics in Agriculture 60, 31–38

SÖKEFELD M., GERHARDS R., OEBEL H., THERBURG R.-D. (2007): Image acquisition for weed detection and identification by digital image analysis. In J. STAFFORD (Ed.), Precision agriculture ’07, Volume 6, The Netherlands, pp. 523–529. 6th European Conference on Precision Agriculture (ECPA): Wageningen Academic Publishers

VAPNIK N.V. (1982): Estimation of dependences based on empirical data. New York, NY: Springer

Potential applications of hyperspectral imaging for quality control in dairy foods

Aoife A. Gowen[1], J. Burger[2], D. O'Callaghan[3], C.P. O'Donnell[1]

[1] Biosystems Engineering, School of Agriculture, Food Science and Veterinary Medicine, University College Dublin, Belfield, Dublin 4, Ireland
[2] BurgerMetrics SIA, Jelgava, Latvia
[3] Teagasc, Dairy Products Research Centre, Moorepark, Fermoy, Co. Cork, Republic of Ireland
Corresponding author: aoife.gowen@ucd.ie

Abstract: *Hyperspectral Imaging (HSI), also known also as Chemical or Spectroscopic Imaging, is an emerging technique that integrates conventional imaging and spectroscopy to attain both spatial and spectral information from an object. Technological advances in spectrograph and detector design leading to decreased cost and improved instrumentation have enabled HSI applications to increase in number and widen in scope over the past twenty years. Reported applications of HSI in food science and technology (while not as numerous as those in established HSI disciplines such as remote sensing) are rapidly emerging[1], with the majority of reported research concerning quality control of vegetable, fruit, grain, meat and poultry products[2]. There have been, to date, very few reported applications of HSI to dairy foods; it's use as a research tool in dairy science has not yet been exploited. However, a wide range of quality and safety testing practices in the dairy industry could be complemented and potentially improved with HSI. In this article, potential applications of HSI to quality monitoring of dairy products are presented, specifically in: process monitoring, compositional analysis, prediction of functional properties, authentication and limitations and safety testing. Current limitations of the technology and potential future developments are also explored.*

1 Introduction

The potential of NIR spectroscopy (NIRS) has recently been investigated for solving a number of problems related to dairy food production. Rapid compositional analysis (e.g. moisture, fat, protein content) of dairy products, including cheese, milk and dairy powders, using near infrared spectroscopy (NIRS) has been presented. More complex concepts such as organoleptic and functional properties of dairy products, most notably cheese, have been correlated with NIR spectral characteristics. Classification of cheese according to maturity and sensory characteristics has also been successfully carried out using NIRS. The potential applications of NIRS in monitoring the formation of cheese from milk have been demonstrated, resulting in the development of low-cost sensors for control of coagulation and syneresis. Fluorescence spectroscopy has also been applied

to dairy products; examples include the classification of cheeses according to geographical origin and monitoring oxidation in yoghurts.

Spectrometers integrate spatial information to give an average spectrum for each sample studied; their inability to capture internal component distribution within food products may lead to discrepancies between predicted and measured composition. Furthermore, spectroscopic assessments with relatively small point-source measurements do not contain spatial information, which is important to many food inspection applications. Computer vision systems, which capture spatial information, have been developed for quality control in food processing. Red-green-blue (RGB) colour machine vision systems find widespread use in food quality control for the detection of surface defects and grading operations. Applications of such machine vision systems have been investigated for monitoring quality in dairy foods, for example, in the estimation of functional properties, for characterisation of ingredient distribution and in the prediction of sensory attributes of some yoghurts and cheeses.

However, conventional colour cameras are poor identifiers of surface features sensitive to wavebands other than RGB, such as low but potentially harmful concentrations of contaminants on foods. To overcome this, multispectral imaging systems have been developed to combine images acquired at a number (usually < 10) of narrow wavebands, sensitive to features of interest on the object. Recently, an application of multispectral imaging for dairy products was presented based on a multispectral imaging system based on 8 wavebands in the UV, Vis and NIR wavelength regions for classification of blue cheeses according to their origin.

Hyperspectral imaging can be conceived of as an extension of multispectral imaging; while multi-spectral imagers look at light from up to 10 wavebands, hyperspectral imagers are capable of obtaining spatial information from >100 wavebands; as such, hyperspectral imaging represents a new era in spectroscopy and imaging, combining the potential usefulness of both of these technologies, as further described in the following section.

Hyperspectral imaging (HSI), also known as chemical or spectroscopic imaging, is an emerging technique that integrates conventional imaging and spectroscopy to attain both spatial and spectral information from an object. It was originally developed for remote sensing applications utilizing satellite imaging data of the earth, moon, and planets, but has since found application in such diverse fields as astronomy, agriculture, pharmaceuticals and medical diagnostics.

Hyperspectral images are made up of hundreds of contiguous wavebands for each spatial position of a target studied. Consequently, each pixel in a hyperspectral image contains a spectrum representing the light absorbing and/or scattering properties of the spatial region represented by that pixel (although it should be noted that due to various optical, instrumental and background effects, each pixel spectrum may be influenced by its neighbouring pixels; this becomes a greater problem in high magnification imaging).

The resulting spectrum acts like a fingerprint, which can be used to estimate chemical compositions of that particular pixel. Hyperspectral images, known as *hypercubes*, can be represented as three-dimensional blocks of data, comprising of two spatial and one wavelength dimension, as illustrated in **Figure 1**. The *hypercube* allows for the visualization of biochemical constituents of a sample, separated into particular areas of the image, since regions of a sample with similar spectral properties tend to have similar chemical composition.

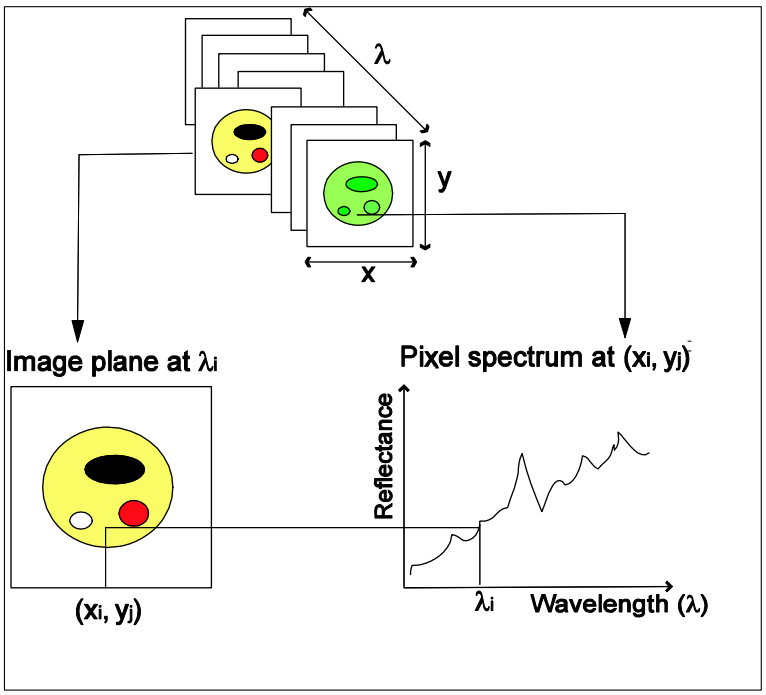

Figure 1: Schematic showing hypercube structure; spatial axes x, y, and wavelength axis (λ)

Some advantages of hyperspectral imaging over conventional NIRS, RGB and multispectral imaging are outlined in **Table 1**. In combining the spectral information provided by spectroscopy and the spatial information provided by imaging, hyperspectral imaging (HSI) offers improved knowledge on the composition and distribution of components in a product. Moreover, HSI is a rapid method (typical scan time < 1 min) compared with traditional quality testing techniques such as HPLC and GC-MS which may take hours including sample preparation steps, and since it is a non-destructive and non-contact technique, samples may be further processed or tested as required without interference with the sample.

The US Food and Drug Administration-led process analytical technology (PAT) initiative aims to understand and control the manufacturing process by monitoring critical performance attributes. The non-destructive, rugged and flexible nature of HSI makes it an attractive PAT tool for identification of critical control parameters that impact on finished product quality. It is anticipated that HSI will be increasingly adopted as a key PAT tool

for the food industry, as has already been the case in manufacturing environments such as the pharmaceutical industry.

Table 1: Comparison of RGB imaging (RGB), Near infra red spectroscopy (NIRS), Multispectral imaging (MSI) and hyperspectral imaging (HSI) techniques for dairy product applications.

Attribute	RGB	NIRS	MSI	HSI
Spatial information	✔		✔	✔
Spectral information		✔	**Limited**	✔
Multiconstituent information	**Limited**	✔	**Limited**	✔
Sensitivity to minor components			**Limited**	✔

1.1 Hyperspectral image acquisition and instrumentation

It is currently unfeasible to obtain information in all three dimensions of a *hypercube* simultaneously; one is limited to obtaining two dimensions at a time, then creating a three dimensional image by stacking the 2 dimensional 'slices' in sequence. There are two conventional ways to construct a *hypercube*. One method, known as the "staring imager" configuration involves keeping the spatial image field of view fixed, while restricting or filtering light throughput, thereby obtaining images one wavelength after another (the use of traditional waveband filters is another option, but becomes difficult when greater than 100 wavebands are required). *Hypercube*s obtained using this configuration thus consist of a three dimensional stack of images (one image for each wavelength examined), which may be stored in what is known as the Band Sequential (BSQ) format. "Staring imager" instruments incorporating tuneable filters have found a number of applications in pharmaceutical quality control, their lack of moving parts representing an advantage in many situations.

Another configuration involves acquisition of two dimensional camera frames representing complete spectral measurements acquired simultaneously from a series of adjacent linearly spaced spatial positions. Acquisition of the full hypercube thus requires relative movement between the object and the detector along the second spatial axis. Such line mapping instruments which record the spectrum of each pixel across a line of a sample simultaneously recorded by an array detector, known as "pushbroom" acquisition results in a *hypercube* stored in the Band Interleaved by Line (BIL) format. This method is particularly well suited to conveyor belt systems, and may therefore be more practicable than the staring imager configuration for some food industry applications.

Some instruments produce hyperspectral images based on a single complete spectrum - point step and acquire mode: complete spectra are obtained at single points on the sample, while the sample is rastered or moved in the X, Y spatial dimensions. *Hypercubes* obtained using this configuration are stored in what is known as the Band Interleaved by Pixel (BIP) format. This is a very time consuming process, but may result in

extremely high resolution spectra with hundreds of wavelength channels. Recent advances in detector technology have reduced the time required to acquire these *hypercubes*.

Typical hyperspectral imaging systems contain the following components: focusing lens, wavelength modulator, detector, illumination and acquisition system as shown in **Figure 2a**. In the case of pushbroom line-scanning HSI systems, a spectrograph is used for wavelength modulation; a line of light reflected from or transmitted through the sample under investigation enters the objective lens and is separated into its component wavelengths by diffraction optics contained in the spectrograph; a two-dimensional image (spatial dimension x wavelength dimension) is then formed on the detector; two-dimensional line images acquired sequentially at adjacent positions from the sample target are stacked to form a three-dimensional *hypercube* which may be processed immediately in real time or stored for further analysis. For such pushbroom systems relative movement between the object and detector is necessary and this may be achieved either by moving the sample (e.g. via use of a translation stage, see **Figure 2b**, or a conveyor belt) and keeping the hyperspectral camera in a fixed position or by moving the camera and keeping the sample fixed.

Wavelength of incoming light in the “staring imager” configuration is typically modulated using a tuneable filter; Acousto-optic Tuneable Filters (AOTFs) and Liquid Crystal Tuneable Filters (LCTFs) are the two most common types employed. AOTFs have been used in the construction of commercially available HSI systems; the main advantages of AOTFs are good transmission efficiency, fast scan times and large spectral range. On the other hand, LCTFs show greater promise for filtering of Raman images. More recently, staring-imager systems have been developed that incorporate a tuneable laser as the light source, thus removing the need for a wavelength modulator. Such systems can produce hyperspectral images in a fraction of the time required by conventional systems based on tuneable wavelength filters, representing a significant advance in the field.

Hyperspectral images can be obtained for reflected, transmitted or emitted light coming from the UV, through the Vis-NIR and up to the short wave infrared (SWIR) regions of the electromagnetic spectrum. The camera, wavelength modulator and illumination conditions determine the wavelength range of the system. Commercially available Vis-NIR HSI systems typically range between 400-1000 nm, and utilize cameras with Charge Coupled Device (CCD) or Complementary Metal Oxide Semiconductor (CMOS) sensors; longer wavelength systems require more expensive IR focal-plane array detectors. The sample/target is usually diffusely illuminated by a tungsten-halogen light source. Data acquisition and storage is a major issue in hyperspectral imaging; a typical image of 320 x 240 pixels in size will contain over 75,000 spectra, each with > 100 spectral data points, resulting in a file containing > 7,500,000 numbers; if each number is stored in floating point double precision (16-bytes), the resultant image will be > 100 MB in size!

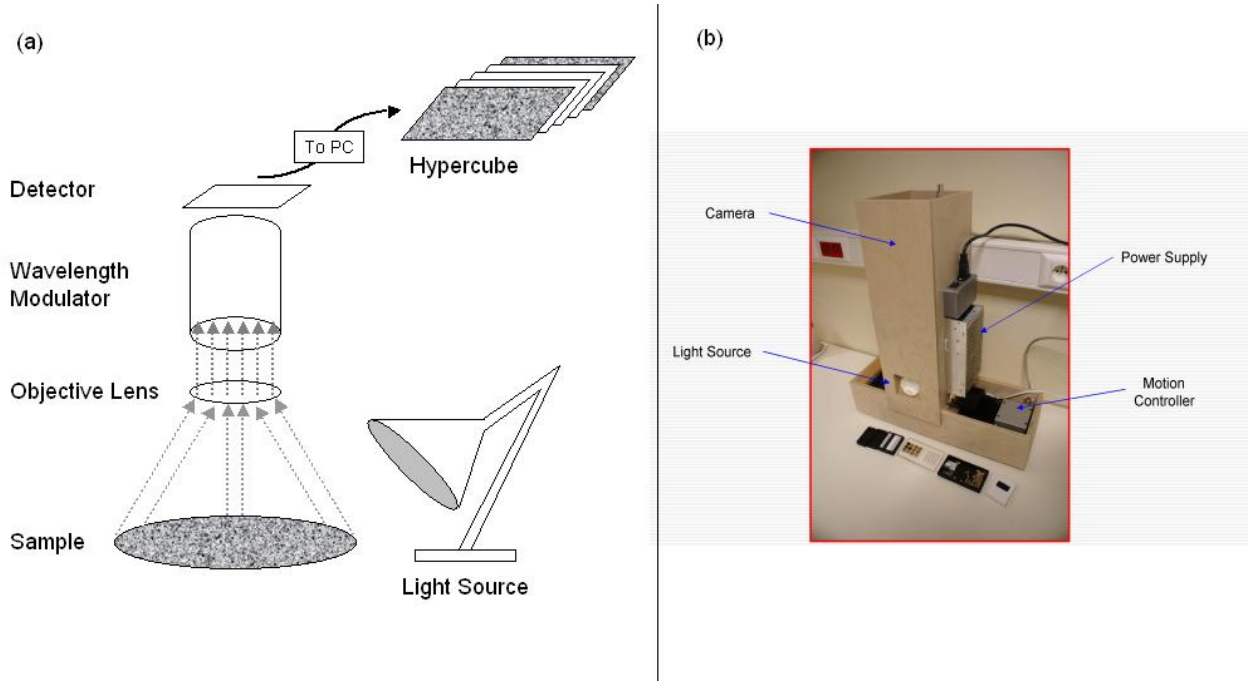

Figure 2a: Schematic showing typical components of a hyperspectral imaging system, (b) example of prototype turnkey pushbroom hyperspectral imaging system.

1.2 Hyperspectral image analysis

Numerous techniques exist to analyse hyperspectral imaging data, all of which aim to optimally reduce the immensity of the data while retaining important spatial and spectral information with the power to classify important chemical or physical areas of a scene. Typical steps followed in analysing hyperspectral images are briefly described below.

Image calibration

Hyperspectral image calibration is required to account for spectral and spatial variations in light source intensity, detector response, and system optics. Calibration of spectral response can be achieved using narrow-band light sources (e.g. laser 'pen lights') or calibrated standard reference materials such as NIST (National Institute of Standards and Technology) glasses, and this calibration should be verified periodically. Spatial calibration over the field of view of the HSI instrument should be carried out using a spatially and spectrally homogeneous sample (e.g. flat ceramic tile). Intensity calibration is required to compensate for changes in the detector response and should be carried out using certified reference standards (e.g. Spectralon grayscale standards). Development of suitable reflectance standards and use of correct calibration transformations remains a challenge in hyperspectral imaging. Spatial and intensity calibration should, at the very minimum, be carried out on a daily basis as small changes in electrical power sources, illumination, detector response and system alignment may result in significant changes in the detected response. Inclusion of *internal reference* standards in each hy-

perspectral image acquired is recommended; this is also a good way to monitor the performance of the system over time.

Spectral and spatial pre-processing

Pre-processing is usually performed to remove non-chemical biases from the spectral and spatial information contained in a hyperspectral image (e.g. scattering effects due to surface inhomogeneities) and to prepare the data for further processing. A number of spectral pre-processing techniques exist, including polynomial baseline correction, Savitzky-Golay derivative conversion, mean centering and unit variance normalisation. Spatial operations usually carried out at the pre-processing stage include (but are by no means limited to): thresholding and masking to remove redundant background information from the *hypercube;* image filtering (e.g. Gaussian filtering) to decrease noise and interpolation (e.g. bilinear interpolation) to decrease image size.

Classification and regression

Classification of hyperspectral images aims to identify regions or objects of similar characteristics using the spectral and spatial information contained in the hypercube. Various unsupervised methods, including Principal Components Analysis (PCA), k-nearest neighbours clustering and hierarchical clustering, can be applied in either the spectral or spatial domains to achieve classification. These methods are particularly useful in the analysis of samples of unknown composition, enabling the identification of spectral and spatial similarities within or between images that can further be used for their characterisation. PCA is commonly used as an exploratory tool in hyperspectral imaging, as it represents a computationally fast method for concentrating the spectral variance contained in the > 100 image planes of a HSI image into a smaller number (usually < 10) of principal component score images. Supervised classification methods, including partial least squares discriminant analysis (PLS-DA), neural networks, linear discriminant analysis and spectral angle mapping require the selection of well-defined and representative calibration and training sets for classification optimisation. One of the major advantages of HSI in this respect is the sheer volume of data available in each hypercube with which to create calibration and training sets.

Hyperspectral image regression enables the prediction of constituent concentration in a sample at the pixel level, thus enabling the spatial distribution or mapping of a particular component in a sample to be visualised. Many different approaches are available for the development of regression models (e.g. partial least squares regression (PLSR), principal components regression (PCR), stepwise linear regression), all of which require representative calibration sets containing spectra with corresponding accurate reference values (e.g. fat content, protein content). This poses a problem in hyperspectral imaging: it is practically impossible to measure the precise concentration of components in a

sample at the pixel scale and therefore impossible to provide reference values for each pixel spectrum. To overcome this, regression models may be built using mean spectra obtained over the same region of sample (or a representative region) on which the reference value was obtained. After model optimisation through training and testing, the regression models developed using the mean spectra can be applied to the pixel spectra of the hypercube, resulting in model predictions at the pixel level. This results in a prediction map in which the spatial distribution of the predicted component(s) is easily interpretable. An example of this approach is presented in the following section.

Image processing

Images from different planes in a hypercube may be combined using algorithms based on straightforward mathematical operators, e.g. addition, subtraction, multiplication and division. Image processing is also carried out to convert the contrast developed by the classification/regression analysis into a picture depicting component distribution. Greyscale or colour mapping with intensity scaling is commonly used to display compositional contrast between pixels in an image. Image fusion or false colour mapping, in which two or more images at different wavebands are represented as red, green, or blue channels and combined to form a new RGB image may be employed to enhance apparent contrast between distinct regions of a sample.

2 Potential applications of hyperspectral imaging in dairy foods

Technological advances in spectrograph and detector design leading to decreased cost and improved instrumentation have enabled hyperspectral imaging (HSI) applications to increase in number and widen in scope over the past twenty years (**Figure 3a**). Reported applications of HSI in food science and technology (while not as numerous as those in established HSI disciplines such as remote sensing) are rapidly emerging (**Figure 3b**), with the majority of reported research concerning quality control of vegetable, fruit, grain, meat and poultry products. There have been, to date, very few reported applications of HSI to dairy foods; its use as a research tool in dairy science has not yet been exploited. However, a wide range of quality and safety testing practices in the dairy industry could be complemented and potentially improved with HSI. Therefore, it is expected that research on its application in dairy science will expand in the future. In the following sections, the few reported applications of HSI to dairy products are discussed, and potential applications are explored.

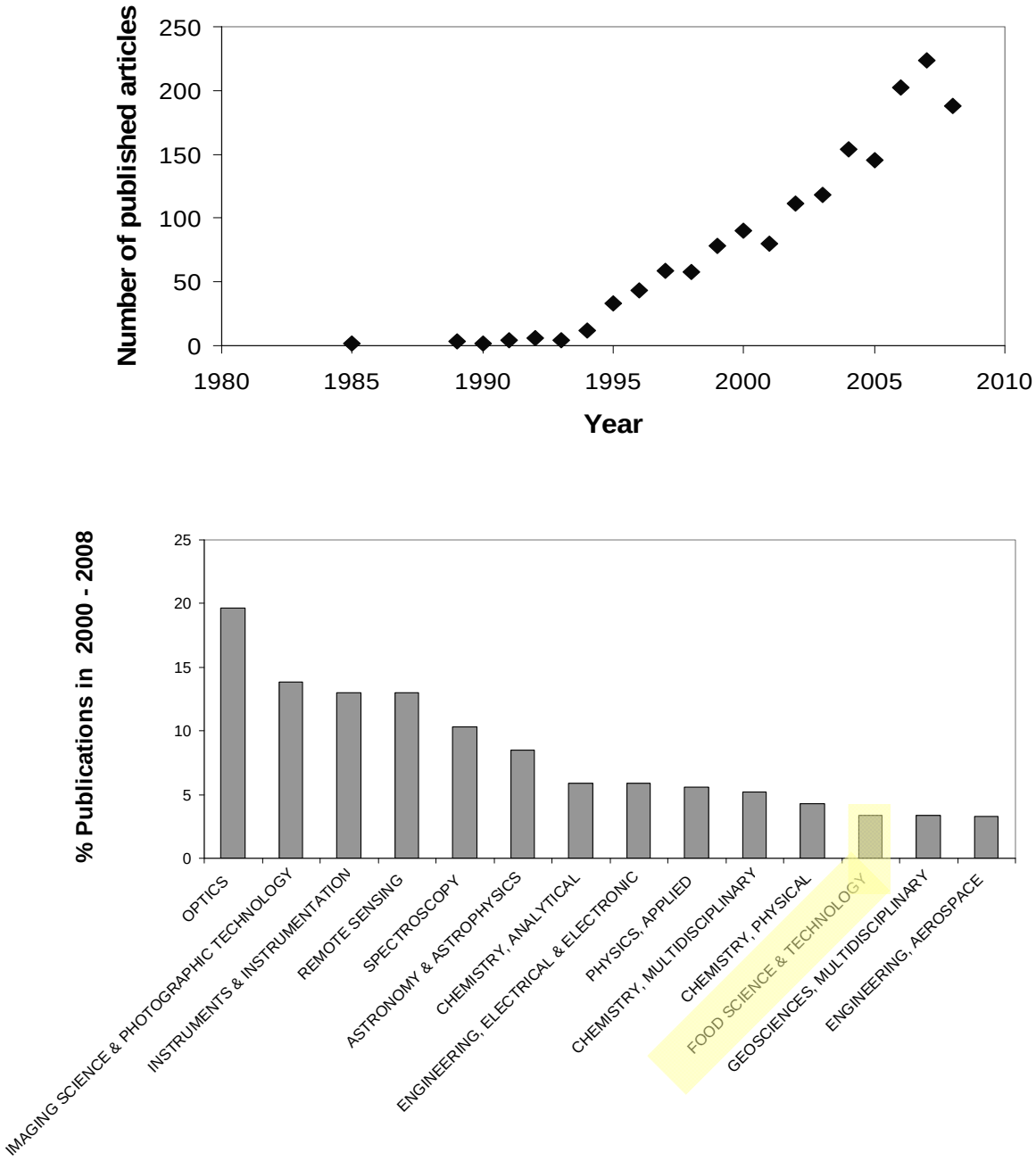

Figure 3a: Number of published scientific articles with “Hyperspectral Imaging” or “Chemical Imaging” or “Imaging Spectroscopy” in the title (Source: Web of Science Citation Reports, January 2009).

2.1 Process monitoring

Dairy products are subjected to numerous heat, pressure, mixing and fermentation stages during processing to produce from milk the wide range of dairy products currently available, such as cream, butter, cheese and yoghurt. Driven by international economic, social and legislative trends, dairy production has increasingly shifted from

small-scale farm production to high volume industrial-scale processing. Advances in computer processing technology have enabled an increased level of integration in the automation and control of dairy processes. Automated dairy processing and manufacturing units are required to consistently meet the stringent safety and quality standards set out by food regulatory agencies. Monitoring these unit process operations and characterizing their influence of final product quality is a major challenge for dairy producers. Potential applications of HSI in the control of some typical dairy processes are described below.

Milk homogenization

The yield and functional properties of subsequent dairy products is influenced by the homogeneity of the milk used in their production. Milk is an emulsion in which globules of fat are dispersed among a matrix of water, sugars and proteins; the fat and aqueous phases of this emulsion do not mix, and large fat globules rise quickly,, causing the formation of a layer of cream on top of the milk. During the homogenization process, high pressure and temperature treatments are applied to reduce the size of fat globules (to approximately 1 - 2μm) in order to produce a stable emulsion. Hyperspectral imaging may be used to measure size distribution of fat globules in milk during the homogenization process, since concentration of fat in milk varies spatially. If HSI could be applied in this context, it could lead to improved characterization of the effects of process parameters (temperature and pressure) on particle size distribution and thus more accurate prediction of the end-point of the homogenization process. However, due to the dynamic spatial nature of liquid samples such as milk, the pushbroom hyperspectral imaging set up would probably not be viable in this particular application. The staring face imager set up may be more appropriate, but the relatively long acquisition times (1-2 min) required for the tunable filter set-up would also pose problems. One compromise to overcome the problems posed in hyperspectral imaging of liquid foods is to scan just one line of a sample; thus obtaining spectra resolved in just one spatial dimension. This would allow for the distribution of different sizes of fat globules to be estimated along one spatial axis, which would be useful in determining the uniformity of homogenization achieved.

Milk coagulation and curd formation

Scattering of light is intrinsically related to the size and distribution of particles in a sample; for example, smaller particles of glass tend to scatter more light and appear whiter in colour than larger ones. Changes in the light-scattering properties of milk due to modifications in the size and distribution of fat globules can be used for automatic non-destructive quality control of the cheese-making process. Monitoring changes in the optical properties of milk arising during coagulation and curd formation using Vis-NIR spectroscopy and RGB imaging is well documented. These light scattering properties

have been successfully exploited in the development of on-line sensors based on Vis-NIR spectroscopy for optimization of the gel cutting step in cheese making. Hyperspectral imaging may offer improved characterization of the coagulation and curd formation processes, through spatial characterization of the spectral response. The time required (typically 1-2 min for current instrumentation) for hyperspectral image acquisition may limit its use, since milk is a spatially dynamic product; hyperspectral line scanning as mentioned in the previous section may also be useful here.

Dehydration

Spray drying is commonly employed for the preservation of dairy products and in the production of milk powders. The resulting chemical, microbial, physical, functional and organoleptic properties of the dairy product are highly dependent on the drying conditions applied. The potential of HSI in monitoring the drying process lies in its ability to provide spatial information on the distribution of water in a sample. Water molecules have known absorbance features in the Near Infrared and absorbance patterns in this wavelength region may also be used to differentiate between free and bound water in a substance. Consequently, HSI may be used to generate moisture distribution profile maps for products during dehydration and to investigate the effects of various drying parameters on final product quality. This would enable estimation of accurate drying end points in dairy powder production and also improve quality assurance of the final product. Moreover, HSI may be used to detect any problems in the drying process, e.g. non-uniform drying due to equipment malfunctions would be detected by non-uniform moisture profiles in a product. Examination of the surface composition of milk powders, which is known to differ from their bulk composition, is another area in which HSI may potentially be applied.

Blending

The HSI technique has an added advantage over traditional bulk quality measurement techniques in its ability to detect problems arising during processing. HSI can be used to spatially map the distribution of components within a food product during manufacturing, allowing direct qualitative comparison with control products. This would be useful in monitoring the process of blending in dairy food production, which is important since the uniformity of blending directly affects the final product quality. For example, regions of ingredient agglomeration in blended dairy products may be identified and related to inadequate blending protocols. The potential application of HSI has already been demonstrated in monitoring of blend homogeneity of powder and tablet forms in pharmaceutical processing . HSI may also be used to estimate particle size distribution during processing, enabling improved monitoring of the blending process, more accurate estimation of blending end points and enhanced insight into the behavior of dairy products during blending.

2.2 Compositional analysis

Dairy products are complex food matrices assemblies of dissolved, suspended and emulsified substances, fat in globulular and continuous forms, proteins, carbohydrates, minerals and vitamins. Traditional wet chemistry methods for compositional analysis of dairy foods are labour intensive, time consuming and require sample destruction. Numerous studies have been reported which demonstrate the effectiveness of Near- and Mid- Infrared spectroscopy for non-destructive prediction of dairy food composition(e.g. for the prediction of fat; protein and lactose). Hyperspectral imaging provides the added potential to simultaneously estimate the spatial distribution of numerous components in a sample while also predicting average compositional information. A number of authors have published work on the application of HSI to estimate the distribution and concentration of active ingredients in pharmaceutical products and its potential for prediction of the location of components such as water, fat and protein in food products has also been demonstrated. Qin and Lu have recently applied hyperspectral diffuse reflectance line scanning for rapid determination of the optical properties of turbid liquids, using the spatially resolved scattering of light in the Vis-NIR region to predict fat content in milk.

In 2006 an application of HSI to cheese products in 2006 in an article on NIR hyperspectral image regression was published. A range of 12 commercial cheese products were tested, specifically selected to span as wide a range as possible in terms of protein, fat and carbohydrate content. The average composition values on the packaging labels were used as standard reference values and a parallel set of reference values for protein and fat content was determined using standard techniques. The challenges of developing accurate calibration models using hyperspectral image data were discussed. One major issue is that reference values were only available for entire bulk samples, not at the individual pixel level! To overcome this limitation, the authors used the mean spectral response from sample images to build calibration models. Partial least squares regression (PLSR) models were developed on mean spectra subjected to various spectral pretreatments, and (considering the prediction error of the regression models) results suggested that applying a 1^{st} derivative Savitsky-Golay smoothing was the most effective spectral pretreatment. Using this approach, a PLSR model with 2 or 4 latent variables could be used to satisfactorily predict fat, protein, and carbohydrate. Typical prediction errors of 1%–2% for protein and fat, and 2%–3% for carbohydrate were obtained, which were greater than the errors in the reference measurements (0.14% protein and 0.41% fat) but similar to results reported for other NIR spectrometers.

The regression models developed on mean spectra and bulk reference values were then applied to pixel spectra for each hyperspectral image studied, to generate prediction maps showing the distribution of each component as estimated by the calibration model. **Figure 4** shows the false colour maps for the 2-latent variable PLSR models for prediction of protein (green), fat (red) and carbohydrate (blue) on the 12 individual cheese samples studied. For comparison purposes, the false colour of the combination of expected values of the three ingredients was depicted in a smaller rectangle below

each prediction image. Colour intensities were scaled such that the ranges of protein, fat and carbohydrate contained in the calibration set were mapped to the full scale values of red, green and blue. The colour matching between expected and predicted values was quite good, indicating the usefulness of HSI in prediction of mean composition. Some inhomogeneous regions are noticeable as changes in colouration of the images, which in some cases do not appear to be uniformly distributed; these may indicate areas of non-uniform fat and protein distribution, which may in turn be related to processing parameters involved in the production of the selected cheeses.

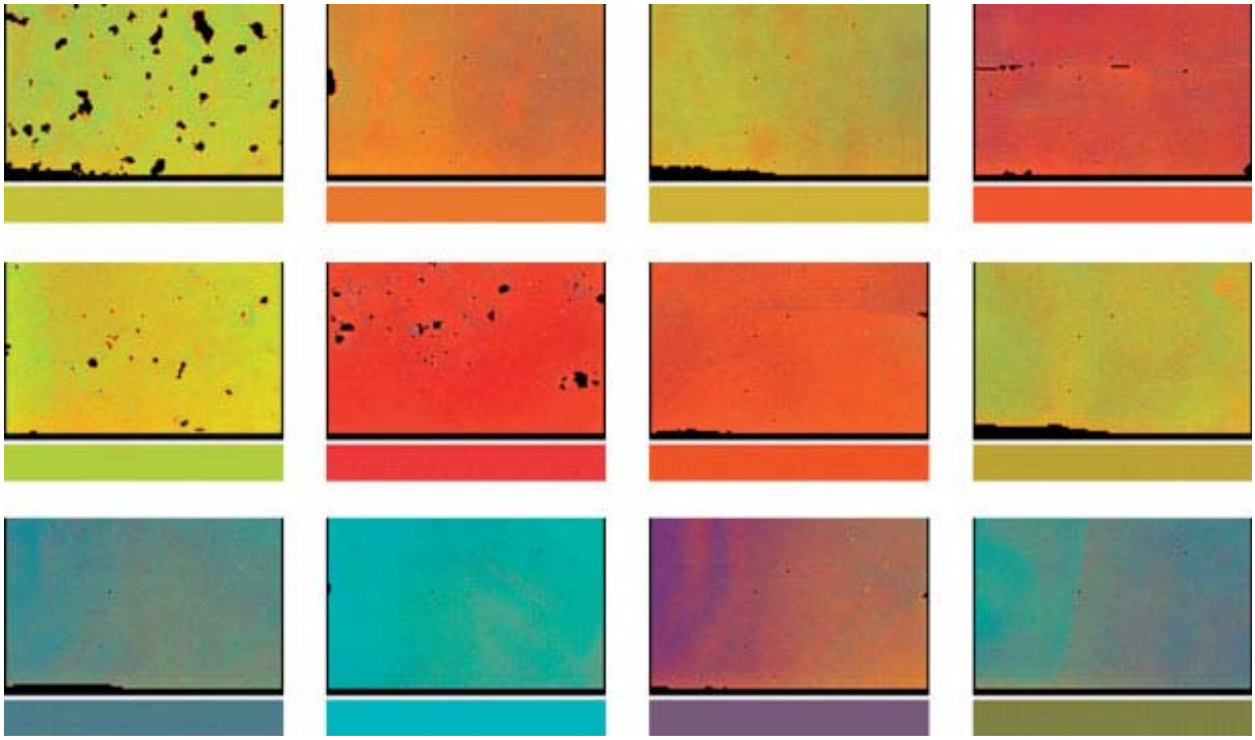

Figure 4: False colour concentration prediction maps for 2 component first derivative spectra models of 12 different cheeses A smaller rectangle below each prediction map indicates the target 'colour' expected. Rectangular cheese regions are 209 x 320 pixels in size corresponding approximately to 50 x 62 mm^2. (BURGER & GELADI 2006).

2.3 Prediction of functional properties

The expression "functional properties" is a broad term in food science, collectively given to factors that describe properties of foods relating to their quality. Functional properties of foods are intrinsically related to their composition and structure; consequently, processing methods that alter dairy product composition and structure directly affect their functional properties. Potential applications of NIR spectroscopy and conventional RGB imaging have been reported for the prediction of functional properties of dairy products; some examples include: turbidity and viscosity of milk; free oil formation and meltability of cheese. Other optical techniques reported for monitoring structural changes related to

functional properties in dairy products include confocal laser scanning microscopy, scanning and transmission electron microscopy and magnetic resonance imaging.

Control of functional properties in dairy products demands an understanding of where the constituent components (e.g. fat, protein) are located in relation to each other, and how they are modified during processing. HSI presents a relatively low cost method for examining the distribution of components within a sample, which may be useful in monitoring the development of functional properties during processing. Hyperspectral imaging would enable improved image contrast not available with RGB imaging, and provide additional insights as to the effect of underlying composition distribution on functional properties. One example where HSI may be particularly useful is in NIR monitoring of free oil production in cheese, as oil is semi-transparent to visible light captured in RGB imaging. Functional properties of milk powders, including flowability and particle size distribution could also potentially be evaluated using hyperspectral imaging, since these properties directly relate to the concentration and size of constituents in the powders expressed as light scattering differences, which may be examined using HSI.

2.4 Classification

Accurate classification is critical for pricing, authentication and categorization of dairy products. Products may be classed based on their geographical origin, composition, functional properties, maturity and on manufacturing methods used in their production; for example, milk and cream products are priced based on their fat content. Therefore, rapid and accurate classification techniques would represent an economic benefit for producers. The multivariate nature of dairy product classification, combined with the knowledge that many dairy food components exhibit characteristic light absorbance and scattering behavior in the NIR make NIR spectroscopy well suited to many classification tasks. Multispectral imaging has been employed in the classification of blue cheeses based on product type and producer using a custom made system capable of recording images at 8-wavebands in the UV-Vis-NIR wavelength regions.

Hyperspectral imaging offers exciting new opportunities in object classification, based on spatial and spectral properties of samples. This method is particularly well suited to the classification of cheese products, where distribution and concentration of ingredients is a key grading parameter. In order to demonstrate the potential of HSI in classification of cheese products, a hyperspectral image of 12 pieces of high fat and low fat cheese slices (purchased from 'Marks and Spencer retail outlet, Dublin), arranged on a piece of black cardboard were obtained using a pushbroom hyperspectral imaging system operating in the wavelength region 400 – 1000 nm. For comparison, an RGB image of the cheese samples studied (obtained using a digital camera) was acquired, shown in **Figure 5a**; all cheese samples appear similar in colour and appearance. However, looking at the mean HSI spectral profiles of each product, it is evident that the full fat product reflects more light in the visible (500 – 950 nm) wavelength range. These spectral fea-

tures may be used to classify each pixel of the hyperspectral image into one of two or more groups. In the present case a spectral angle mapping algorithm, which compared the similarity of the spectrum of each pixel in the hyperspectral image with the mean spectra shown in **Figure 5b**, was applied and each pixel was classified as full fat or half fat depending on it's similarity to each mean spectrum. Although the algorithm correctly classified most pixels, some edge regions in the half fat samples were misclassified, possibly due to lighting in-homogeneities at edge regions.

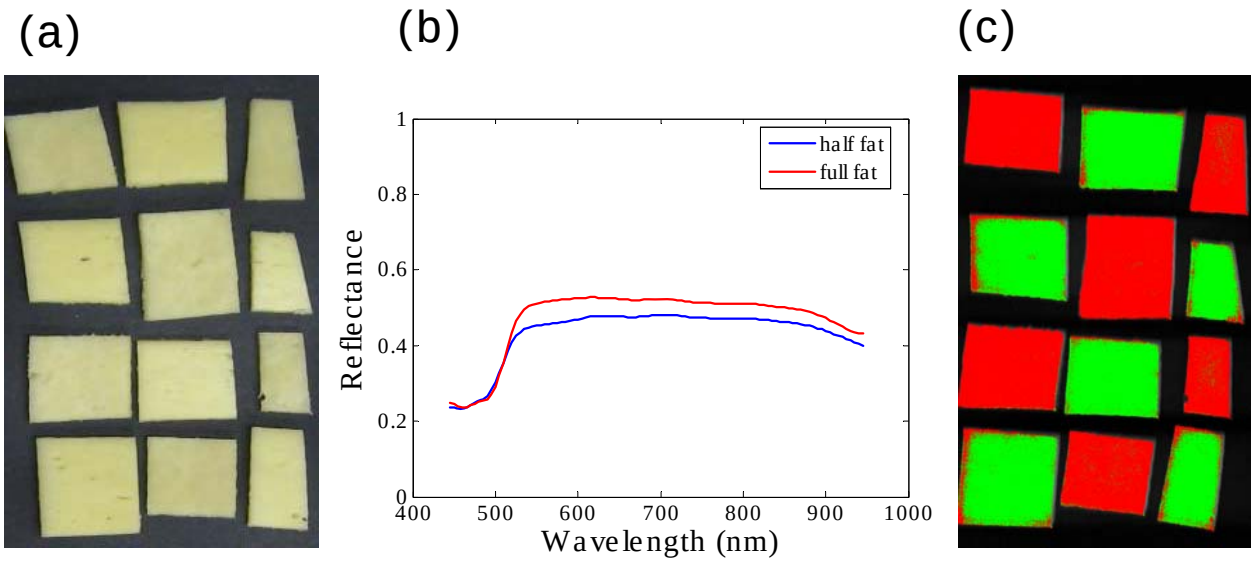

Figure 5a: RGB image of cheese samples studied; (b) Mean spectral of half and full fat cheese samples; (c) cheese classification map (red = half fat, green = full fat) obtained using Spectral Angle Mapper algorithm.

2.5 Safety testing

In order to assure product safety and compliance with food regulatory standards, there is a need for rapid monitoring systems sensitive to low levels of microbial contamination in food production. One of the major successful applications of hyperspectral imaging in food monitoring has been in safety testing of poultry products; an on-line system for detection of fecal and ingesta contamination has been developed. More recently, HSI has been proposed for identification of specific microbial contaminants, suggesting that HSI may be a useful tool for studying the growth of microbial colonies. HSI may prove useful in safety testing of dairy products throughout the various processing stages: from raw milk, to processed milk products, and on to the classification of waste products. The potential of HSI in detection of contamination on dairy foods and identification of pathogenic micro-organisms would be useful at both the laboratory and process monitoring scales. At the lab scale, changes in appearance of dairy products occurring as the product reaches the end of its shelf life, such as the growth of moulds, may potentially be monitored using HSI, leading to the development of early detection systems using HSI. The potential use of HSI in product classification as outlined in the previous section may be useful in authentication of dairy products, ensuring their traceability. The HSI

technique may also be useful for monitoring adulteration in dairy products, offering consumer protection against products containing substituted non-dairy ingredients.

HSI may also find potential application in foreign body detection for the safety assurance of dairy products. As an example, a slice of cheese contaminated with a 3 mm shard of plastic was imaged using a pushbroom NIR hyperspectral imaging system operating in the wavelength range 950 – 1650 nm. A digital RGB image of the cheese is shown (**Figure 6a**), in which the plastic shard, although visible (placed in the upper right hand region of the cheese slice), may be difficult to distinguish from the cheese background. The mean reflectance spectra of the cheese and plastic are also shown (**Figure 6b**), and spectral differences are apparent; the plastic contaminant exhibits a sharp absorption band at around 1170 nm. Principal component analysis was applied to the hyperspectral image, and the resultant second component principal component image is shown (**Figure 6c**). This principal component image, which represents a linear combination of the image at all wavelengths (>100) imaged, shows up the contamination with far greater contrast than the RGB image. This simple example demonstrates the potential of HSI for foreign body contaminant detection in dairy foods.

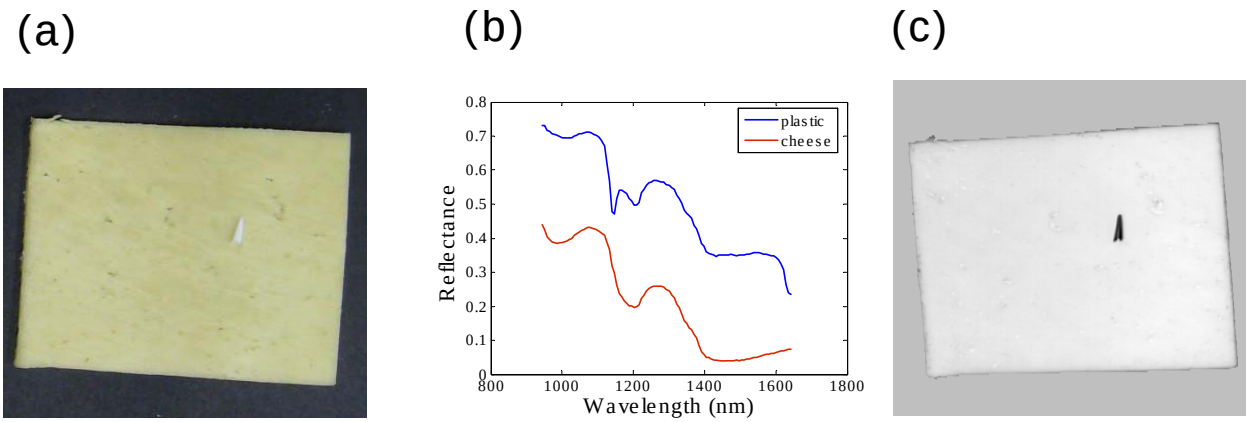

Figure 6a: RGB image of cheese and plastic shard contamination; (b) mean spectra of cheese region and plastic region; (c) image obtained after applying principal component analysis to hyperspectral image of cheese with plastic contamination (plastic contamination appears as dark region on cheese sample).

3 Conclusions

Hyperspectral imaging offers new possibilities to researchers and producers in food science; by combining spectroscopy and imaging, this tool can be used for mapping distribution of constituents over the surface of a sample. This capability may be useful for dairy food analysis at the laboratory research scale and further the development of both laboratory and online monitoring technologies in the dairy industry. Future improvements in precision and speed in hyperspectral imaging are likely to arise with improved lighting systems, higher quality photometric sensors and faster hardware. As hyper-

spectral imaging continues to emerge as a tool for food quality and safety analysis, and with new systems offering much faster image acquisition and processing times than ever before, the potential role for this technology in the monitoring and control of dairy food processes seems very promising. It is anticipated that the number of applications of this technology to problems in the dairy industry will increase rapidly in the coming years.

Plant species discrimination using spectral/spatial descriptive statistics

Scott D. Noble[1], Ralph B. Brown[2]

[1] University of Saskatchewan, Department of Agricultural and Bioresource Engineering, 57 Campus Drive, Saskatoon, SK, Canada. S7N 5A9
[2] University of Guelph, School of Engineering. Guelph, ON, Canada. N1G 2W1
Corresponding author: scott.noble@usask.ca

Abstract: *It has been observed that point-measurement reflectance data collected from plant leaves of the same species and grown side-by-side were not necessarily normally distributed and that the nature of the distribution varied with species and wavelength. The hypothesis tested in this research is that these deviations in the data distributions are species, wavelength, and maturity dependant. Spectral image data (57 wavebands over 400-1000 nm) were collected from 13 species of juvenile crops and weeds at five maturity levels. Distribution normality was tested using the Anderson-Darling statistic. Descriptive statistics (mean, median, standard deviation, skewness, and kurtosis) were calculated at each waveband for random sub-samples of the vegetation pixels for each plant image. The majority of normally-distributed data were found in the visible wavelengths, and were concentrated in a few species. While not strongly separable, the distribution statistic data provided some ability to distinguish between species. It is hypothesized that identification features based on distribution statistics might be more stable over a greater range of environmental conditions as compared to features based more directly on reflectance values.*

1 Introduction

Reflectance spectroscopy techniques for plant identification make use of characteristics of the plant reflectance spectrum, while imaging techniques result in classifiers based on leaf or plant shape. Typically, these approaches are not combined, presumably because the technology for collecting ground-based imaging spectroscopy data has only recently become reasonably available.

The spectral approach is generally criticized as being sensitive to environmental variability, plant maturity, plant stress, illumination, and the simple fact that all green-leaf reflectance spectra are very similar, leaving little to differentiate one species from another (PRICE 1994, ZWIGGELAAR 1998). On the other hand, the attractiveness of spectral data is its relative computational simplicity when compared to shape-based image processing. Image processing approaches are challenged when faced with the relatively

unconstrained and complex natural environments found in practice: occlusion, poor contrast between green leaves, and essentially random plant and leaf orientations.

The development of portable hyperspectral imaging technology permits the use of spectral and spatial techniques for weed/crop identification in a more unified manner. Hyperspectral imaging provides data with the spectral resolution of a spectrometer (<10nm) with the spatial resolution of image data (pixels on the order of millimeters). A number of researchers have been using imaging spectrophotometry equipment (BORREGAARD *et al.* 2000, VRINDTS *et al.* 2002), but have treated the data primarily as spectral without making use of the spatial component. In this work, a simple approach to combining spectral and spatial data using the descriptive statistics of reflectance data over the plant area was explored. This included testing distribution normality with respect to wavelength, species, and maturity. Finally, characters based on the descriptive statistics were selected using stepwise selection, and their ability to distinguish between species tested using linear discriminant analysis.

Data for studies on spectral discrimination of plants have typically been collected using either a spectroradiometer with an acceptance cone that encompasses an entire plant (BROWN *et al.* 1994, SMITH & BLACKSHAW 2003, VRINDTS & DE BAERDEMAEKER 1997, NOBLE 2002) or spectrograph (BORREGAARD *et al.* 2000, VRINDTS *et al.* 2002) system that samples the plant at the spatial scale of leaves or smaller. In these cases the possibility of detecting within-plant spectral differences which may characterize some property of the plant was not considered.

The hypothesis that variability in reflectance values may follow species and wavelength-dependent patterns was suggested by NOBLE (2002), observing that different species appeared to follow different trends in a plot of standard deviation of diffuse reflectance versus wavelength. Following this NOBLE & CROWE (2005) investigated the assumption that the reflectance data were normally distributed, concluding they were not. Further, it was observed that the degree of non-normality was both species and wavelength dependent. The suggestion was made that if multiple reflectance measurements could be taken from many discrete points of a sample, the distributional properties of those measurements may correlate to species. This approach has a precedent in the work of GEBHARDT, & UNKLESBAY (1991) in which descriptive statistics of color channels were included in analysis, and found to be significant.

2 Objectives

The first objective of this study was to test the hypothesis suggested by NOBLE & CROWE (2005) that sets of reflectance measurements taken over the spatial extent of plant leaves (i.e., measurements from hyperspectral imaging) do not have a normal (Gaussian) distribution, and the nature of the distribution varies with species, maturity, and

wavelength. Reflectance distributions and distribution statistics of the red edge location and slope were used as test cases for this hypothesis. A second objective was to test whether or not the distribution statistics could be used to successfully discriminate between plant species.

3 Materials and methods

Data were collected from 13 species of weeds and crops that were grown in trays containing 72 mm square pots. Each tray contained between ten and 18 plants of a single species, and were grown indoors in a growth room. Conditions were a day/night temperature of 25 / 18°C and light supplemented for 16 hours with a mixture of incandescent bulbs and fluorescent tubes providing 330 micromol $m^{-2}sec^{-1}$ PPFD. Hyperspectral image data were collected at several stages in the development of each species, ranging from newly emerged seedlings to barely pre-flowering in some cases. Measurements were taken at five maturity levels. These species are listed in **Table 1**.

Table 1: Plant species in this research, listed by WSSA Bayer code

Weed Species		
Bayer Code	Common Name	Scientific Name
ABUTH	velvetleaf	*Abutilon theophrasti* Medic.
AMARE	redroot pigweed	*Amaranthus retroflexus* L.
CERVU	mouseear chickweed	*Cerastium fontanum* Baumg.
CHEAL	common lambsquarters	*Chenopodium album* L.
CHEGL	oak-leaved goosefoot	*Chenopodium glaucum* L.
CONAR	field bindweed	*Convolvulus arvensis* L.
PLAMA	broad-leaf plantain	*Plantago major* L.
POROL	common purselane	*Portulaca oleracea* L.
TAROF	dandelion	*Taraxacum officinale* Weber
THLAR	stinkweed (field pennycress)	*Thlaspi arvense* L.
Crop Species		
Code	Common Name	Scientific Name
SOYBE	soybean	*Glycine max* Merr.
TOMAT	tomato	*Lycospersicon esculentum* Mill.
WHEAT	wheat	*Triticum aestivum* L.

Sampling

Mosaic images were constructed for each of the 13 species with representatives of all growth stages in a single composite image to better facilitate comparisons across

growth stage within species. The full-tray image at each growth stage was divided into five equal area sections. Each mosaic image contained five sections, one for each of the five growth stages for each species. This also ensured that data were held back for testing purposes. An example of redroot pigweed (AMARE) is shown in **Figure 1**. Standard masks corresponding to maturity and a nominal division by pot were used for all mosaics. The combination of the maturity and pot masks created 15 regions in the mosaic image.

The maturity and pot masks were further combined with the vegetation mask. The vegetation mask was calculated for each mosaic image, segmenting all vegetation pixels from background pixels using reflectance values at 667nm and 760nm in equation 1:

$$vegmask = where\left(\left(\frac{R_{760}}{R_{667}} > 3\right) \wedge \left(R_{760} > 30\%\right)\right) \quad (1)$$

where *vegmask* is the binary mask image, and R_{667} and R_{760} are the reflectance values at bands centered on 667 and 760 nm, respectively. The ratio of reflectance at 760 to 667 nm takes advantage of the reflectance red edge to differentiate vegetation from background. The conditional component requiring reflectance at 760 nm to be greater than 30% (arrived at empirically) rejected false positives caused by moss or algae growth on the surface of the growth medium.

By combining the pot and vegetation masks for a given species, sampling of only vegetation could be done by maturity level, with further division by pot as previously defined, as shown for redroot pigweed (AMARE) in **Figure 1**. This was a pragmatic approach to dividing the images, based on the assumption of having a single plant in each pot of the growth tray. A limitation of this was that a pot could actually represent several small seedlings within the space before thinning, or contain portions of a plant from an adjacent pot that had spread beyond the pot boundaries. Pot misalignment was also an issue for this.

The available vegetation pixels for each pot were then randomly split into five sub samples containing a maximum of 100 pixels each. This resulted in a total of 15 sub samples of vegetation pixels per maturity level for each species, and a total of 75 sub samples per species. Analysis of these sub samples was done at alternate wavebands, with a resulting data interval of approximately 10.4 nm, for a total of 57 wavebands with a full-width-at-half-maximum bandwidth of approximately 5.2 nm.

Figure 1: Left: Sample plant mosaic (*Amaranthus retroflexus* "AMARE"). Right: Resultant division by pot and maturity level. Pots 1-3 are maturity level 1, pots 4-6 are maturity level 2, etc.

Testing reflectance non-normality hypothesis

The normality of reflectance values for each sub sample of plant pixels was checked as a preliminary test of the hypothesis that descriptive statistics of the distribution could be used in identification. If the reflectance distributions were normal, then the skewness and kurtosis data would probably not be useful characters. The normality of each sub sample was tested using the sample-size adjusted Anderson-Darling A^{*2} statistic (STEPHENS 1974, MARSAGLIA & MARSAGLIA 2004). The A^{*2} statistic belongs to the family of empirical distribution function (EDF) goodness of fit statistics, which also includes the Kolmogorov-Smirnov and Cramér-von Mises statistics (SAS Institute Inc., 1999)Population mean and standard deviation were calculated using all vegetation pixels for the particular species and maturity. Test results were examined with respect to wavelength, maturity, and species. The 0.025 significance level was used to ensure that the test was not overly sensitive to sample size.

Extracting descriptive statistic characters

Descriptive statistics (variance, standard deviation, skewness, and kurtosis) were calculated for all 57 wavebands of each sub sample. Skewness provides a measure of the symmetry of the distribution about the mean. Kurtosis indicates the flatness of the distribution, with one extreme being a uniform distribution and the other being an impulse function.

For each maturity level within each species, the normality of each descriptive statistics was tested using the w/s statistic at the 0.05 significance level (KANJI 1999). The w/s statistic is based on the ratio of the sample range to standard deviation, and may be applied to small sample populations, in this case five. This provided a partial test of the similarity of the sub samples within species and maturity, and an indication of whether analysis based on the assumption of normality would be appropriate for the features.

To reduce the number of potential features carried forward, a stepwise discriminant analysis (proc STEPDISC; SAS Institute Inc.,) was conducted. Standard deviation, variance, skewness and kurtosis were included as explanatory variables, with species as

the predicted class variable. The mean and median values were excluded from the reflectance distribution statistics because they do not provide information on the shape of the distribution, only its central location. To minimize the maturity effect, only data for maturity levels 3, 4, and 5 were included. All pot three data were reserved as a test dataset. The top five waveband-statistic combinations selected were carried forward for linear discriminant function analysis and classification (proc DISCRIM; SAS Institute Inc., 1999).

4 Results and discussion

Normality testing

Of the total 55575 sub sample-wavelength combinations, only 6765 (12.2%) of the sub samples were normally distributed at the 0.025 significance level as judged by the size-adjusted Anderson-Darling statistic. The number of normal results varied with species, wavelength, and maturity level. Forty-five percent of the normally distributed sub samples were contributed by only two of 13 species (WHEAT, CERVU), with an additional 42% contributed by POROL, THLAR, and CONAR. These percentages are slightly different than those reported by NOBLE (2006), but in keeping with the overall trends observed.

Almost 70% of normal sub samples were found in the visible wavelengths (400 to 700 nm), across species (**Figure 2**). This pattern of normality versus wavelength is consistent with those presented by NOBLE & CROWE (2005).

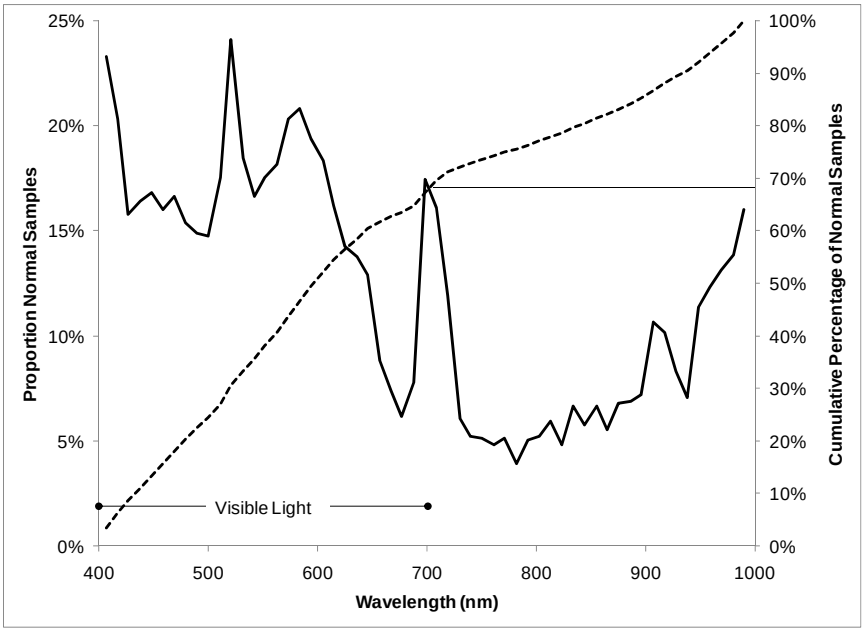

Figure 2: Plot showing the proportion of samples that were normally distributed by wavelength (primary y-axis), and the cumulative proportion of all normally distributed samples by wavelength (secondary y-axis, dashed line)

Table 2: Count of normally distributed sub samples by species and wavelength

Species	Wavelength (nm)						Species Total	Percent Normal
	450	550	650	750	850	950		
ABUTH	11	9	14	0	0	0	34	7.6%
AMARE	22	12	18	1	1	13	67	14.9%
CERVU	20	26	16	9	9	15	95	21.1%
CHEAL	1	16	0	4	3	6	30	6.7%
CHEGL	7	24	0	5	9	8	53	11.8%
CONAR	25	9	12	4	3	7	60	13.3%
PLAMA	20	5	15	0	0	0	40	8.9%
POROL	11	14	15	8	12	15	75	16.7%
SOYBE	14	10	1	1	3	5	34	7.6%
TAROF	33	6	5	2	5	8	59	13.1%
THLAR	11	9	19	1	5	9	54	12.0%
TOMAT	16	8	4	0	0	0	28	6.2%
WHEAT	36	23	7	15	15	25	121	26.9%
Wavelength Sum	227	171	126	50	65	111	750	12.8%
Wavelenth Percentage Normal Samples	23.3%	17.5%	12.9%	5.1%	6.7%	11.4%		

Comparing the relationship between maturity and normality with respect to species (**Table 3**), no clear overall effect of maturity on normality is observed. This is in contrast to the relationships observed with a more sensitive test by NOBLE (2006), where the majority of normally distributed sub-samples (73%) were attributed to the two earliest maturity levels. Examining the trends of individual species reveals a number of apparent trends with maturity (ex. ABUTH normality decreases with wavelength while CONAR appears to increase the count with maturity). It must be noted that due to a number of practical limitations in data collection, maturity levels were primarily indicators of within-species data collection chronology, and that two samples of different species with the same maturity level indicated were not necessarily at the same developmental stage.

Table 3: Count of normally distributed sub samples by species and maturity level

Species	Maturity Level					Species Total	Percentage Normal Samples All Maturities
	1	2	3	4	5		
ABUTH	106	60	34	35	64	299	7.0%
AMARE	32	92	130	48	187	489	11.4%
CERVU	157	89	225	246	229	946	22.1%
CHEAL	31	129	35	28	21	244	5.7%
CHEGL	64	54	105	175	93	491	11.5%
CONAR	41	77	81	164	171	534	12.5%
PLAMA	36	20	77	86	97	316	7.4%
POROL	300	8	157	36	214	715	16.7%
SOYBE	191	17	4	74	45	331	7.7%
TAROF	49	106	73	139	147	514	12.0%
THLAR	121	169	31	140	103	564	13.2%
TOMAT	38	24	98	85	77	322	7.5%
WHEAT	186	142	171	227	274	1000	23.4%
Maturity Sum	1352	987	1221	1483	1722	6765	12.2%
Maturity Percentage Normal Samples	12.2%	8.9%	11.0%	13.3%	15.5%		

Based on the results of normality testing, it is clear that the distributions of reflectance values cannot generally be thought of as being normally distributed. Of note were the relatively few normally distributed sub samples at longer wavelengths (**Table 2** and **Figure 2**). As these wavelengths are more sensitive to cellular structure, this suggests that structure varies independently of pigmentation, and that a degree of non-normal variation in structure is present even at very early stages of growth. The non-Gaussian nature of the distribution does not exclude the possible utility descriptive statistics such as skewness and kurtosis for differentiating between species.

Stepwise discriminant analysis

Partial results of stepwise discriminant analysis for separating between species using reflectance distribution statistics are presented in **Table 4**. The variables most likely to be able to separate between species without accounting for maturity were selected for further character development. The average squared canonical correlation (ASCC) is an indication of separability of the classes, with a value of one indicating complete separability (SAS Institute Inc. 1999). The low value of the ASCC after five variables were en-

tered (0.17) indicates that these features alone would probably not be sufficient to accurately distinguish between species based on a discriminant function classification approach. Becasue the variability introduced by maturity levels was not considered by the STEPDISC procedure, this low estimate of separability was not unexpected. The 13-way classification is also greater than what has been attempted in other studies.

Table 4: First five parameters entered by the STEPDISC procedure for separating species of maturities 3, 4, and 5 only

Rank	Wavelength (nm)	Statistic	Partial R^2	Average Squared Canonical Correlation	Percentage Normal Samples
1	948	Skewness	0.63	0.05	85%
2	594	Skewness	0.51	0.09	85%
3	959	Variance	0.35	0.12	92%
4	719	Std. Dev.	0.43	0.15	74%
5	667	Skewness	0.29	0.17	72%

Prior to further statistical testing, the assumption of normality for the descriptive statistics selected using stepwise selection was tested using the w/s statistic at the 0.05 significance level for each species/maturity combination. The percentage of samples for which normality was not rejected, across species and maturity, for each wavelength and statistic are shown in **Table 4**. Based on these results, the assumption of normality was deemed reasonable for the descriptive statistics selected, and therefore the suitability of tests dependant on the assumption of normality confirmed.

Results of discriminant analysis

The five wavelength/statistic features selected by the STEPDISC were entered into the DISCRIM procedure along with two-thirds of the data for training. **Table 5** shows the classification results using the testing dataset. Random selection would result in a correct classification rate of 7.7%. In all cases, the correct classification rate was better than random. Species with a high correct classification rate did not necessarily have a high rate of false positives (Type II error), indicating that classifier bias was not solely responsible for high correct classifications. No consistent trend between reflectance distribution normality and classification using distribution statistics was observed.

Table 5: Classification results for discriminant function on testing data

		To Species												
		ABUTH	AMARE	CERVU	CHEAL	CHEGL	CONAR	PLAMA	POROL	SOYBE	TAROF	THLAR	TOMAT	WHEAT
From Species	ABUTH	***4***			1			1		1		3	5	
	AMARE	2	***10***					1	1				1	
	CERVU			***11***		1								3
	CHEAL				***9***	2				4				
	CHEGL				4	***9***	2							
	CONAR				2	3	***3***		5	2				
	PLAMA						1	***12***	2					
	POROL		1				2		***10***		1	1		
	SOYBE	2								***3***		1	2	7
	TAROF			5			1		3		***4***			2
	THLAR	1						3	1			***10***		
	TOMAT	3				1		1				1	***9***	
	WHEAT			1			2		4					***8***
Total		**12**	**11**	**17**	**16**	**16**	**11**	**18**	**26**	**10**	**5**	**16**	**17**	**20**
Classification Rate		0.27	0.67	0.73	0.60	0.60	0.20	0.80	0.67	0.20	0.27	0.67	0.60	0.53
Type II Error Rate		0.67	0.09	0.35	0.44	0.44	0.73	0.33	0.62	0.70	0.20	0.38	0.47	0.60

Prior Probability for all classes = 0.0769

5 Summary and conclusions

Normality testing using the Anderson-Darling statistic indicated that the majority of sets of reflectance measurements taken on individual plants were not normally distributed. This finding agreed with those of NOBLE & CROWE (2005) and the hypothesis that reflectance values are generally not normally distributed should be accepted. Of those that were, nearly 70% were found at visible wavelengths. Of normally distributed samples at NIR wavelengths, 87% were from only five of the 13 species investigated, indicating significant species dependency.

The five descriptive statistics with the greatest ability to discriminate between the 13 species as determined by the STEPDISC procedure were skewness at 948, 594, and 667 nm, variance at 959 nm and standard deviation at 719 nm. Correct classifications using these features and linear discriminant analysis were considerably better than random selection, with an overall correct classification rate of 52% in a 13-way classification. While this is not a particularly impressive number, it does indicate that descriptive

statistics may have potential for use in classification, particularly if they prove to have greater environmental stability than using reflectance characteristics alone.

Acknowledgements

Portions of this paper have been adapted from Noble (2006). This work was supported by the Natural Sciences and Engineering Research Council of Canada.

References

BORREGAARD T., NIELSEN H., NØRGAARD L. HAVE H. (2000): Crop-weed discrimination by line imaging spectroscopy. Journal of Agricultural Engineering Research, 75: 389-400

BROWN R.B., STECKLER J.G.A. ANDERSON G.W. (1994): Remote sensing for identification of weeds in no-till corn. Transactions of the ASAE, 37 (1): 297-302

FRANZ E., GEBHARDT M.R. UNKLESBAY K.B. (1991): The use of local spectral properties of leaves as an aid for identifying weed seedlings in digital images. Transactions of the ASABE, 34 (2):682-687

KANJI G.K. (1999): 100 Statistical tests. London: SAGE

MARSAGLIA G., MARSAGLIA J. (2004): Evaluating the Anderson-Darling distribution. Journal of Statistical Software, 9 (2): 1-5

NOBLE S.D. (2002): Crop and weed leaf reflectance and classification. Unpublished M.Sc. Thesis. Saskatoon, Saskatchewan, Canada: University of Saskatchewan, Department of Agricultural and Bioresource Engineering

NOBLE S.D. (2006): Combining spectral and spatial information for automated plant identification. Unpublished Ph.D. Thesis. Guelph, Ontario, Canada: University of Guelph, School of Engineering

NOBLE S.D. CROWE T.G. (2005): Analysis of crop and weed leaf diffuse reflectance spectra. Transactions of the ASAE, 48 (6): 2379-2387

PRICE J.C. (1994): How unique are spectral signatures? Remote Sensing of Environment, 49: 181-186

SAS Institute Inc. (1999): SAS version 8.0 Onlinedoc. Cary, NC: SAS Institute Inc.

STEPHENS M.A. (1974): EDF statistics for goodness of fit and some comparisons. Journal of the American Statistical Association, 69 (347): 730-737

SMITH A.M. BLACKSHAW R.E. (2003): Weed-crop discrimination using remote sensing: A detached leaf experiment. Weed Technology, 17 (4): 811-820

VRINDTS E. DE BAERDEMAEKER J. (1997): "Optical discrimination of crop, weed and soil for online weed detection." First European Conference on Precision Agriculture, Warwick, UK, 537-544

VRINDTS E., DE BAERDEMAEKER J. RAMON H. (2002): Weed detection using canopy reflection. Precision Agriculture, 3 (1): 63-80

ZWIGGELAAR R. (1998): A review of spectral properties of plants and their potential use for crop/weed discrimination in row-crops. Crop Protection, 17 (3): 189-206

Usability study of 3D Time-of-Flight cameras for automatic plant phenotyping

Ralph Klose, Jaime Penlington, Arno Ruckelshausen

University of Applied Sciences Osnabrück/ Faculty of Engineering and Computer Science, Albrechtstr. 30 ; 49076 Osnabrück; Germany
Corresponding author: Ralph.Klose@gmx.de

Abstract: *The implementation of sensors technologies and algorithms for automatic phenotyping are of increasing importance. This paper presents the results of the usability study of state-of-the-art 3D Time-of-Flight cameras for the application of automatic phenotyping under outdoor field conditions. The influences of direct light, speed, humidity and dust on the measurements as well as the charicteristics of the cameras like color dependence, noise level and depth resolution were analyzed regarding application of phenotyping. As a result of this analysis, the usability of the tested ToF cameras will be shown.*

1 Introduction

Phenotyping is the key technology for the evaluation of plants in field trials. The benefit of analyzing the information is the ability to develop strategies for new procedures in order to optimize plant quality or their processing, e.g. during the harvest. Next to spectral information one important part of these phenotyping methods is the exact measurement of the plant's morphological characteristics. For example, typical parameters of interest are the plant profile, leaf sizes, leaf configuration including the angle, plant height or stem thickness. As an instrument for the systematic characterization of the plants in different growth stages, standard measurement scales have been developed, such as the BBCH scale (MEIER & BLEIHOLDER 2007, **Figure 1**).

Until now this analysis is typically executed manually by experts judging the field situation by characterizing random samples taken on the field plot. The result is a statistical overview on the plant's physical characteristics in the field. Since this analysis has to be done manually, it is very time consuming, generates high costs and has a varying reliability. Moreover, the phenotyping is performed by different experts, this may cause additional variations. Taking into account these effects and the fact that the data set represents a statistical overview of the field situation it is often difficult to compare data sets or to develop new strategies for the growth process.

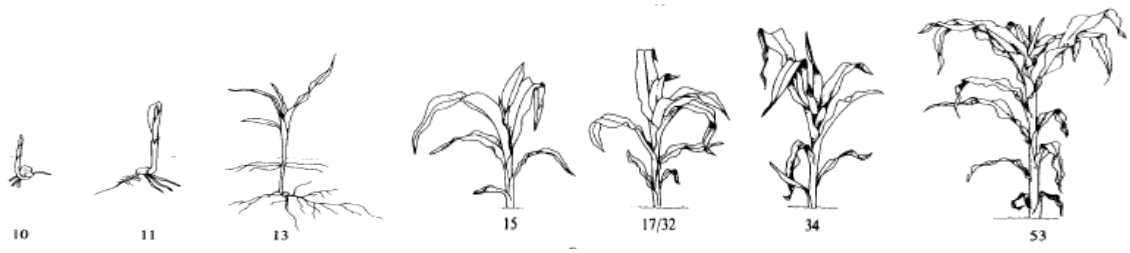

Figure 1: Parts of the BBCH Scale (MEIER & BLEIHOLDER 2007)

As a consequence, the implementation of sensors, system technologies and algorithms for automatic phenotyping are of increasing importance to overcome the disadvantages of the manual methods described above. While static measurements – typically imaging applications – can be performed under well-defined measurement conditions, online applications in the field are still a challenge for corresponding technologies. The benefits of such methods are the comparability of data sets, the objectivity of the data and the measurement in real-time on moving vehicles. The authors have recently shown that a sensor fusion concept together with a high resolution GPS system is even able to analyze (and re-analyze) each single plant (FENDER *et al.* 2006). In combination with an autonomous field robot, it should even be possible to detect all plants in their different growth stages. This work is part of the development of such a field scout, named BoniRob (RUCKELSHAUSEN *et al.* 2009), one application will be the phenotyping of maize plants. To be able to use this new method in combination with an autonomous field robot it is necessary to be able to perform the phenotyping of maize plants while the robot is moving in the field. However, the quality of the phenotyping strongly depends on the quality of the sensor information. For the physical characterization in particular, reliable distance information is the key element. This is especially true for the detection and assignment of overlapping leaves.

2 3D Time-of-Flight

Recently, the first 3D Time-of-flight (ToF) cameras have become available (**Figure 3, Figure 2**, KOLB *et al.* 2008), thereby offering promising options in the field of plant phenotyping (as well as robot navigation and safety). These cameras calculate the distance to objects by measuring the phase shift φ_0 of the reflected light signal to the phase of the light signal of their light source for every pixel of the camera. Therefore the modulator of the light source is directly connected to each pixel. Most of the light sources used by the ToF cameras for illuminating the 3D scenery are built up using LEDs with a modulation of f_{mod} =20 MHz. This frequency results in an unambiguousness measurement range of 7.5 m calculated by the equation below.

$$d = \frac{c \cdot \varphi_0}{4\pi \cdot f_{\text{mod}}}$$

The advantage of Time-of-Flight cameras compared to technologies like stereo imaging, laser-line methods and laser scanners is their ability to generate real-time images of all three dimensions and an additional grey-scale image of the measured reflection without any additional complex calculations.

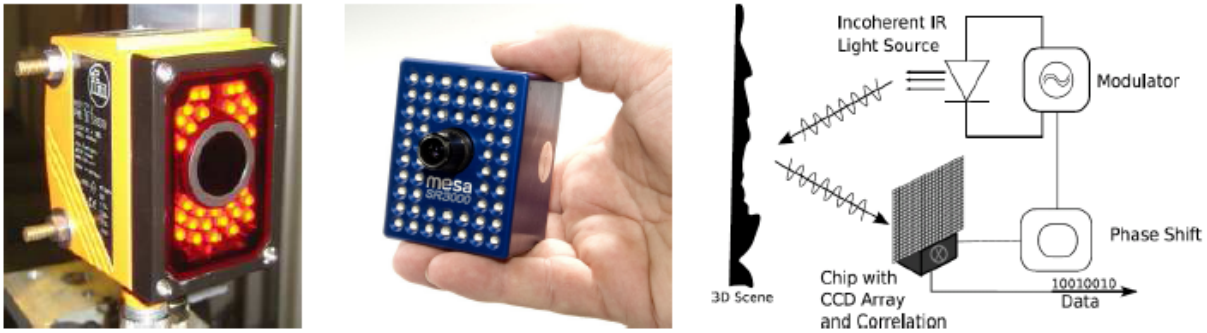

Figure 2: ToF Sensors (KOLB *et al.* 2008)

Figure 3: PMD CamCube

To be able to calculate a complete virtual 3D model of the plant, a multi-view concept (YOUNG *et al*. 2008) with an arrangement of several 3D cameras around the plant will be used (**Figure 4**). With this arrangement it is possible to generate 3D point clouds of the plant from different angles of view. These 3D fragments represented by the point clouds will be used for the calculation of a 3D point cloud and to generate a 3D meshed model of the plant by using methods of three dimensional reconstruction. The resulting three dimensional models of the plants will be a base for the measurement and calculation of the needed plant parameters for the phenotyping of the maize plant according to the parameters of the BBCH-Scale.

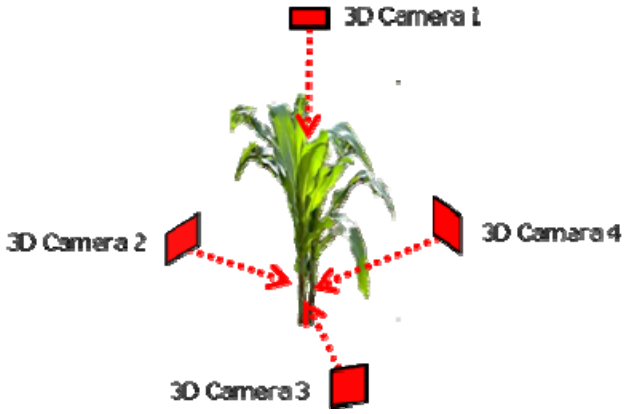

Figure 4: Multi-View arrangement

Table 1: Characteristics

Relevant characteristics of the camera system
Color dependance / sensitivity
Noise
Depth resolution
Long distance / Phase shift

Table 2: Influences

Possible outdoor influences on the camera system
Moving objects, moving system and static objects (Speed)
Direct light
Dust
Drops or water on objects

3 Usability study

Since this method is used in a rough agricultural environment it needs to be robust and has to produce reliable data. Due to the fact that the physical phenotyping data will be based on an analysis of the 3D images taken by the Time-of-Flight cameras, it was necessary to test the functionality of the cameras in agricultural environments. The first step was the evaluation of the general ability of this type of camera to measure the plants physical characteristics. Therefore the camera's resolution, color dependence and noise level as well as the possible occurring phase shift in distances above the specified unambiguousness range of 7.5 m were checked in static measurements (**Table 1**). For these experiments one camera instead of the multi-view arrangement mentioned above was used.

Since the new method for an automatic phenotyping will be used in combination with autonomous field robots (BoniRob project), the next step was the evaluation of the dependence of the image quality to the vehicle speed. In the last step the influence of disturbances (**Table 2**) on the image quality was analyzed. Related to the target application the most important disturbances on the system are direct sunlight, humidity and dust.

For the most of measurements two different ToF Cameras equipped with a PMD chip (KOLB *et al.* 2008) and a modulation frequency of 20 MHz have been available. The first camera used is the IFM Efector 3D with a resolution of 50 x 64 pixel. The second camera is the PMD CamCube with a resolution of 204 x 204 pixels. Both cameras have the ability to transmit the distance and gray scale image. The figures below (**Figure 6, Fig-**

ure 7) show the resulting distance image of the two mentioned cameras taken of plants of different development stages (**Figure 5**).

Figure 5: Plants with different growstages

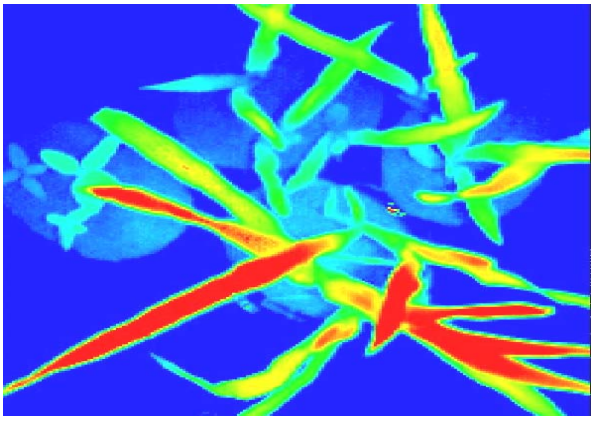

Figure 6: 3D Image of Plants taken with the PMD CamCube

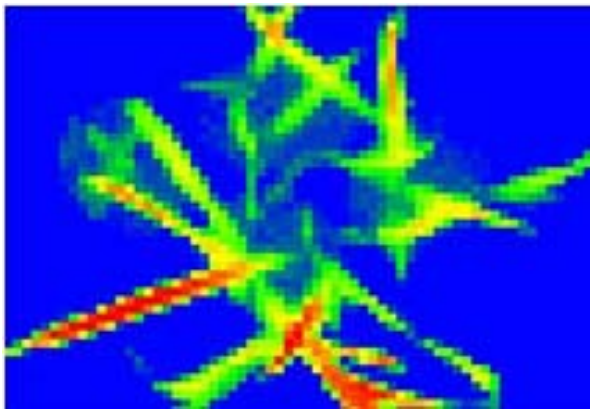

Figure 7: 3D Image of Plants taken with the IFM Efector 3D

The image's colors represent the measured distance to the object, where red is close distance to the camera of 80 cm and blue is representing a distance of 1.10 m. Besides the obvious visible difference in the resolution of the images, it can be seen, that it is possible to detect and to distinguish the leaves of the plants by analyzing their height and geometry, although the depth resolution represented by the different colors is not as high as the resolution of the raw data transmitted by the camera.

For the following measurements of the camera characteristics and the results of influences on the system described above, different experimental rigs (**Figure 8**) were used containing a horizontal rotating table, a conveyor belt and two carriages for indoor and outdoor field measurements with battery power supply. With these rigs it was possible to perform the measurements with adjustable linear and rotational speeds of objects and adjustable height and angle of the cameras under constant repeatable conditions.

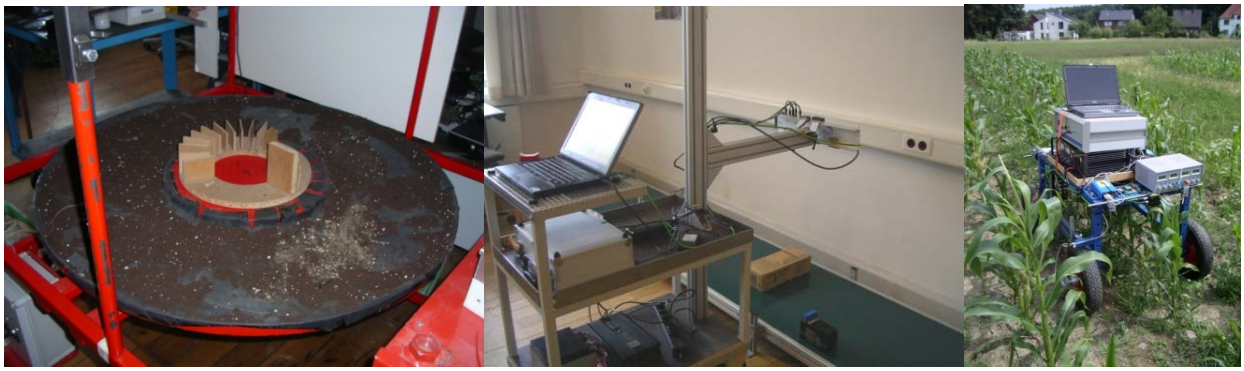

Figure 8: Experimental rigs (Rotating table, conveyor belt and test carriage for outdoor measurements)

The first two measurements are the analysis of the color dependency and noise level of the two cameras. Therefore 3D images of a test pattern, containing ten different color areas of 15 cm x 15 cm size, were taken. The colors to be used were taken from the CIE 1931 color diagram (**Figure 9**) in the RGB color space.

	x	y
Black	0.316	0.295
White	0.301	0.300
Blue	0.205	0.224
Light green	0.334	0.455
Red	0.526	0.297
Yellow	0.479	0.446
Brown	0.415	0.348
Dark green	0.275	0.385
Purple	0.266	0.224
Orange	0.546	0.318

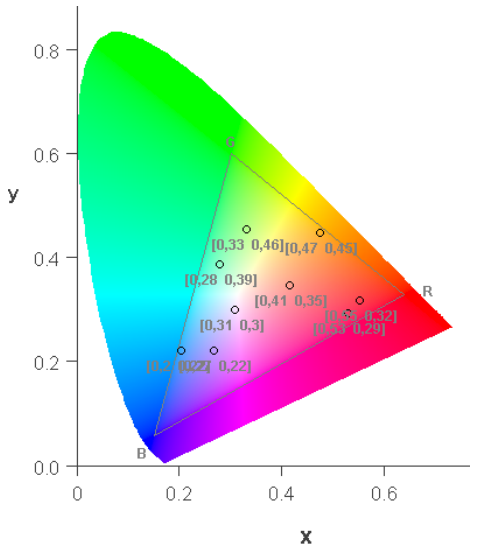

Figure 9: Choosen colors; CIE Color scale (CIE 2009)

The result of the two measurements can be found in **Figure 10** and **Figure 11** (different scales are used!). These two diagrams show the difference mean values of the measured distances in the different color areas compared to the mean distance level measured within the white area. Besides this, the noise level within these areas is represented by the calculated standarddeviation.

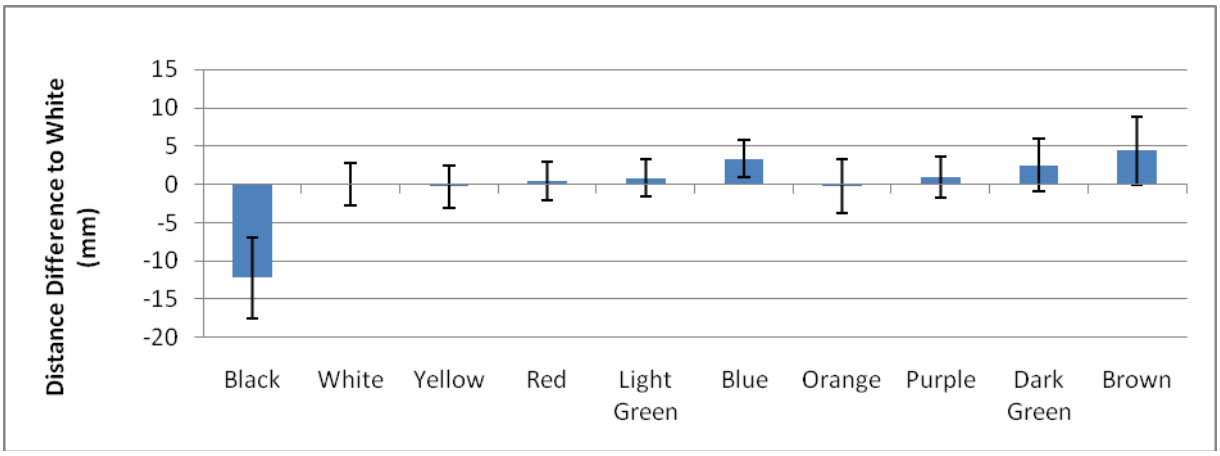

Figure 10: Color dependance IFM

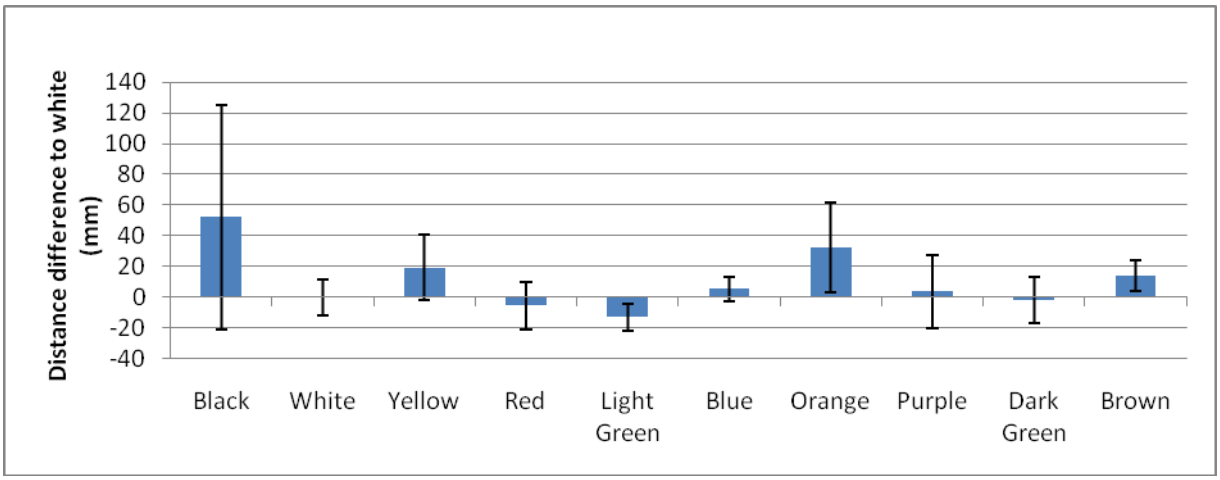

Figure 11: Color dependance PMD

Both diagrams show a difference of the measured distance in the colored area compared to the white area. While the distance differences of the IFM camera, except the one of the black area, are below 5 mm, the distance differences of the PMD camera reach up to 3 cm. In both cases the measured distances of the black area show the highest differences which are a result of the low reflection level of this area compared to the other colors. The noise level of both cameras differ from lower than 5 mm of the IFM camera to a mean value of 1.5 cm and up to 5 cm of the black area of the PMD camera.

The next measurement for the characterization is the estimation of the depth resolution of both cameras. Therefore a test object built up of different step heights was placed in the field of view of the cameras. To reduce the effect of the opening angle and the optics, only two steps at a time are measured. **Figure 12** shows the result of the described measurement.

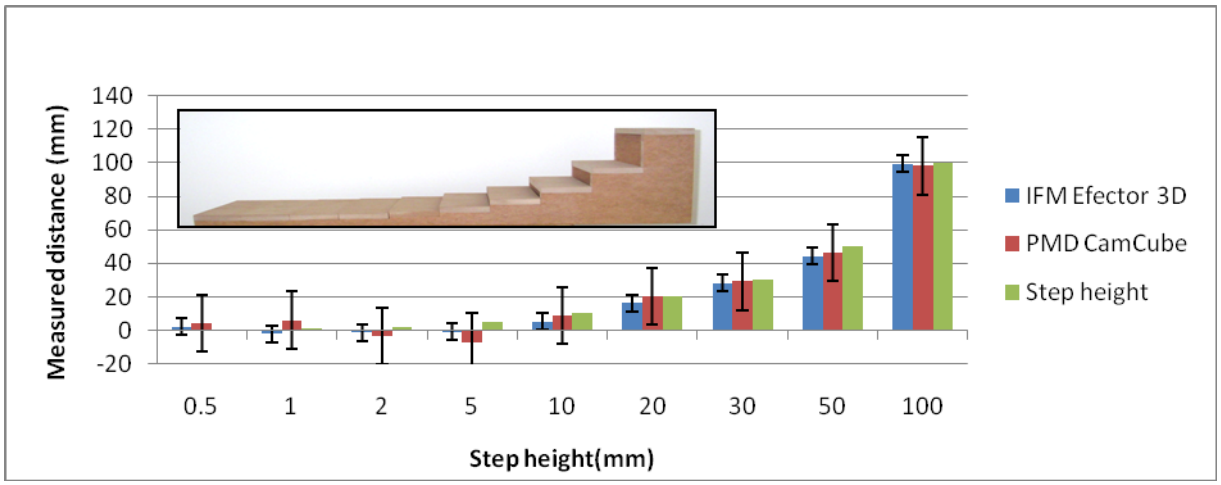

Figure 12: Depth resolution measurement

As a result of this measurement it can be said, that the minimum height difference depends on the mean noise level of the two cameras. Both cameras are able to transmit their data with a resolution of 1 mm, but taking the noise level into account it is not possible to detect height differences of typically less than 1 cm with the IFM camera and 3 cm with the PMD camera.

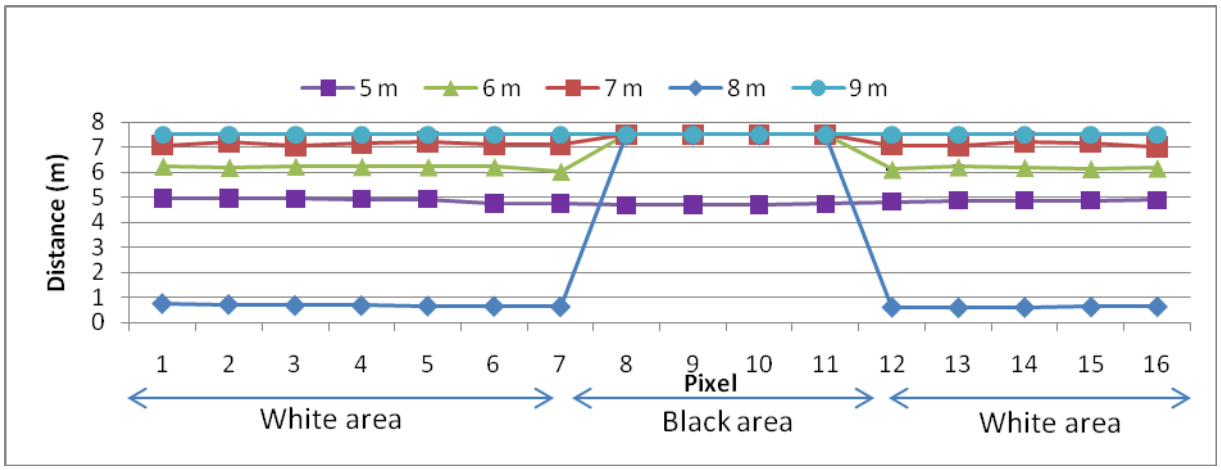

Figure 13: Phase shift measurement

For the next measurement a black paper was placed on a white wall to analyze the effect of the phase shift in long distances of about 7.5 m which equals the unambiguousness measurement range. The image of the camera was adjusted to show one white part of the wall, the black paper and another white part of the wall. The result of the measurement in the diagram (**Figure 13**) above shows, that in a distance of 5 m the camera is still able to measure the distance to the wall in all three areas. As the distance increases 5 m the reflection of the light in the black area of the wall is too low to calculate the distance (this information is indicated in the gray image) so that the dis-

tance is set to the maximum measurement range of 7.5 m. The distances in the white area can still be measured up to the maximum distance of 7.5 m. After this point the phase shift (beginning at 0 m again) is visible for a distance of 8 m which is calculated to be ~50 cm by the camera. This effect continuous until the reflected light intensity is too low for the white area (measurement at 9 m).

The first influence on the camera system to be measured is the speed of objects. Therefore boxes were placed on the conveyor belt and the rotating table in the field of view of the cameras. To be able to analyze the effect of speed on the images, the speed of the objects was changed in three steps up to 3.6 km/h which could also be considered to be a reasonable speed for a field robot.

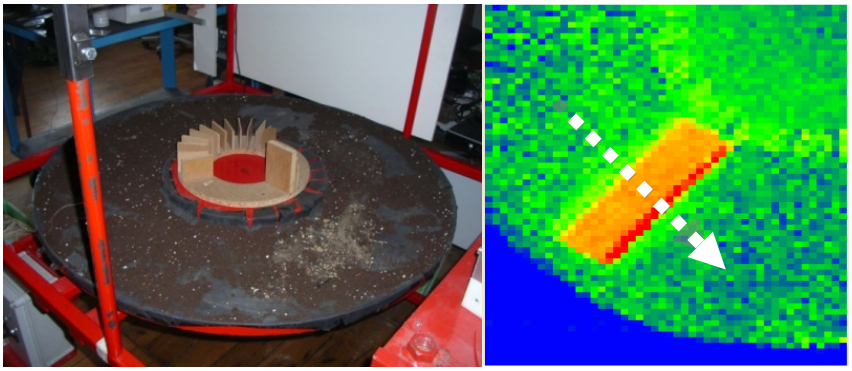

Figure 14: Rotating table and resulting 3D image with indicated measurement line

The measured distances (indicated in figure 14 with a white arrow) are shown in **Figure 15 Figure 16**. The graphs show that the measured distance of the object is constant over the different speeds and over almost the full width of the object except the edge in the shadow of the movement.

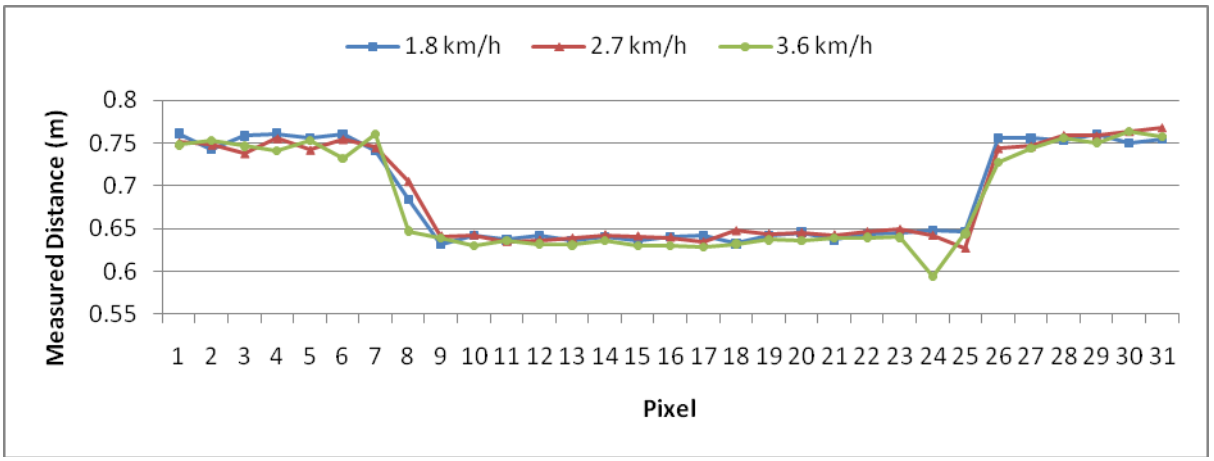

Figure 15: Speed measurement IFM

In this area the increasing speed is resulting in a decreasing measured distance. At the speed of 3.6 km/h the effect has resulted in a height for the IFM camera of about 5 cm and for the PMD camera of about 30 cm. This effect is well known and described in the literature (LOTTNER *et al.* 2007) as “Motion Blur” or “Movement Artefacts” which is caused by the four times the reflected light signal needs to be sampled by the camera chip to be able to calculate the distance. If an object is moving during the four samples a false measurements can occur. Refering to statements of the manufacturers of the PMD chip, the problem of the “Motion Blur” will be gone with the next version of the camera. This new version will be released in July 2009.

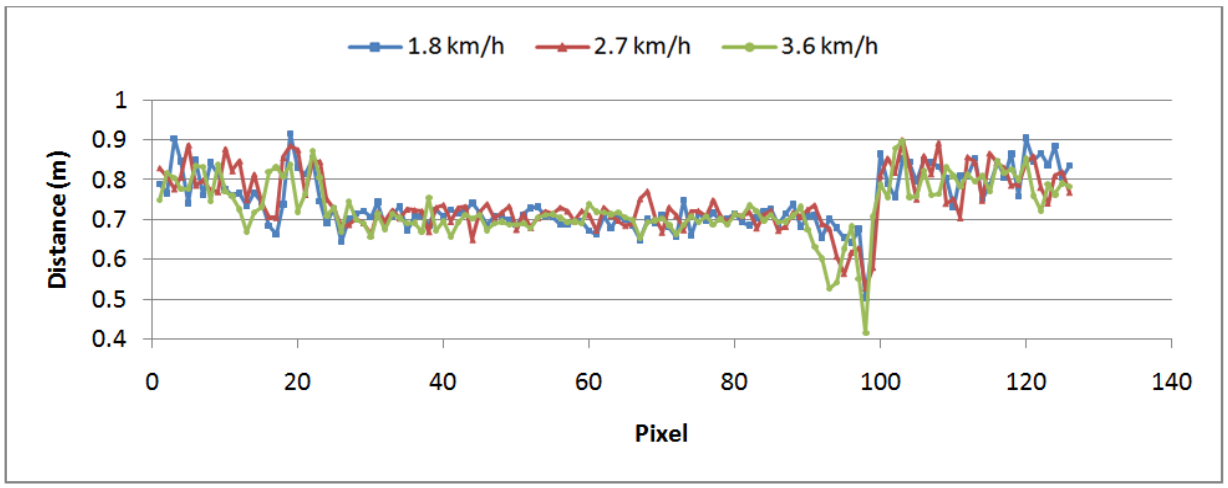

Figure 16: Speed measurement PMD

Another influence analyzed is the effect of direct light on the measured distances of the camera. Therefore, the distance to a white board was measured while a halogen lamp (measurements < 12000 lux) and the sun (measurements > 12000 lux) were in the field of view of the camera. The graphs illustrated in **Figure 17** show the results of this measurement. To be able to compare the results, the distance measured at 3000 lux was used as a reference. It can be seen that the distance error increase with the light intensity. This is a result of the increasing noise level caused by the fact that the pixels are already filled by electrons generated by the sunlight reducing the dynamic range for the modulated light singal. Since the whole image area is affected by the direct light, the increased distance is distributed over the whole image as a homogenous offset.

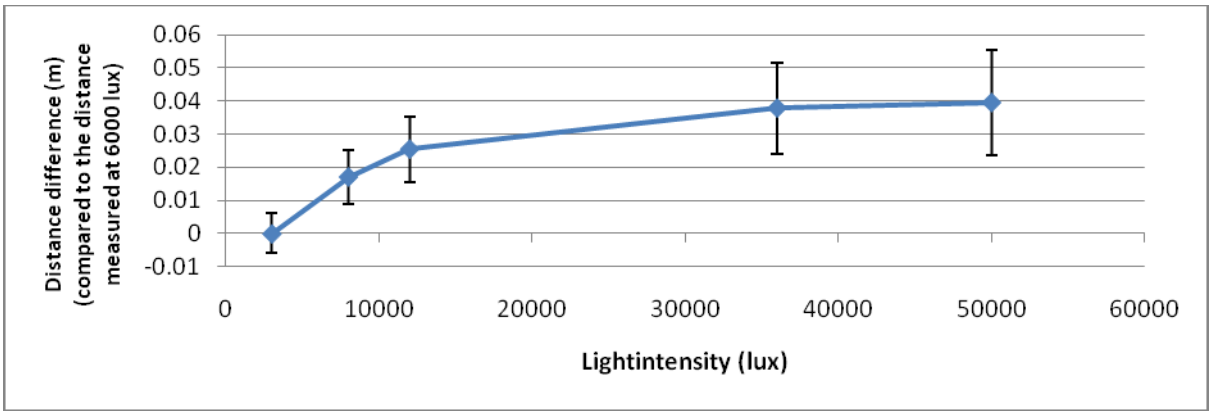

Figure 17: Measurement of direct light

Since the system will be used under outdoor conditions in the field, it is also important to get an idea of what the influence of different types of dust and humidity look like on the resulting camera image. The images in **Figure 18** show the 3D images of the qualitative measurement (color indicates the distance) made while water steam, hair spray, soil and flour were blown into to field of view of the camera. These four different clouds are used as a representation for different densities of dust, since it was not possible to measure the particle size or to guarantee a homogenous distribution of the particles with the given equipment.

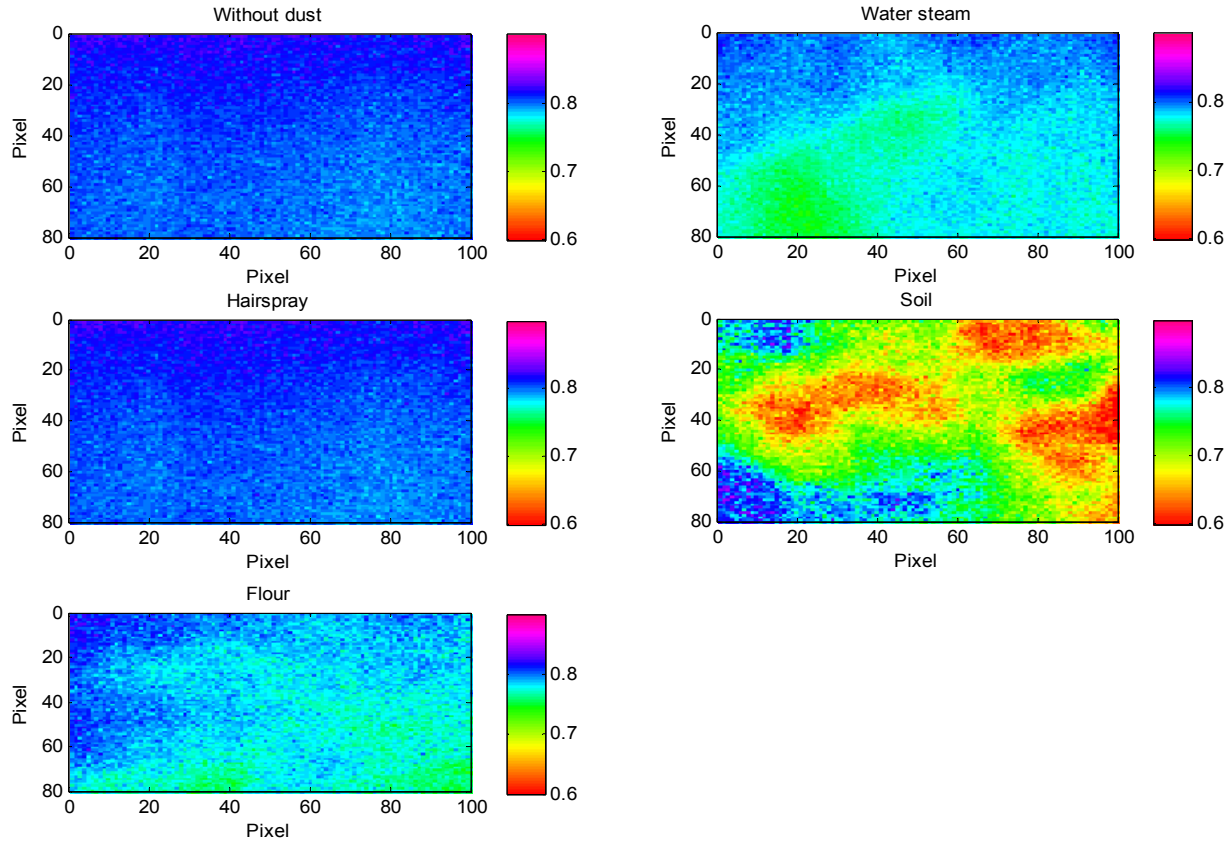

Figure 18: Dust measurement

The image taken of the hair spray shows no difference to the one taken without any kind of dust. The reasons for this are the size of the small fluid size and the density of the cloud compared to the ones of water steam. These water drops are big enough to influence the measured distance of the camera as visible in **Figure 18**. The influence of flour can be compared to the one of water. It results in a change of the distances at the points with the highest density. Since the soil cloud is related to the biggest particle size and density the amount of influenced pixels is the highest.

The last measurement made is the analysis of humidity on an object to the measured distance. Therefore, a white bucket with a plain surface was moistened. The graph of the IFM camera shows an increasing distance difference increasing with the water level. The graph of the PMD cannot be used for this analysis, because the visible distance change is just a result of the higher noise level of the camera.

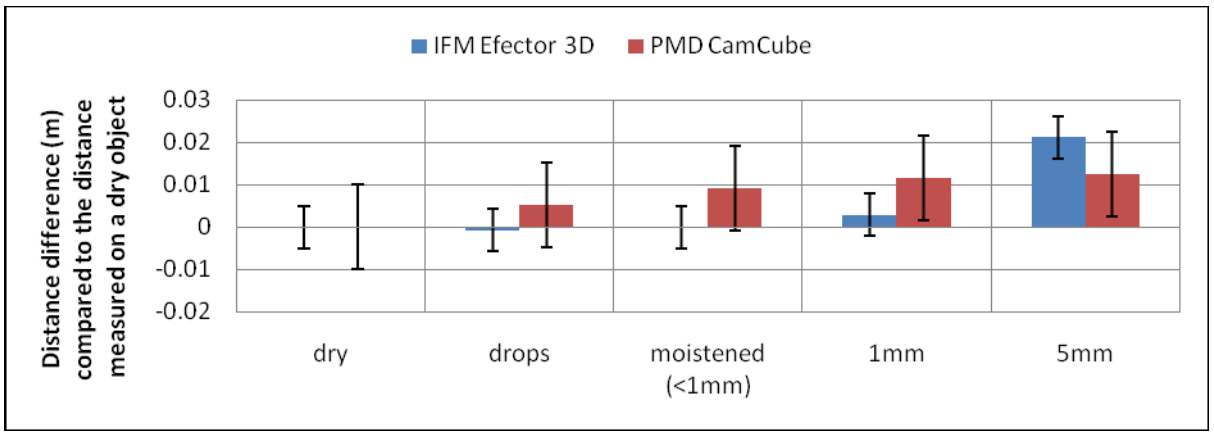

Figure 19: Humidity measurement

4 Conclusions

The analysis has shown that the ToF cameras are usable for the development of a new method for automated phenotyping of maize plants under outdoor conditions. This results of their measured depth resolution of typically up to 1 cm, enabling the user to detect and distinguish different leaves and to measure their size. The two tested ToF cameras have shown a different performance during the measurements. While the main advantage of the PMD CamCube is its high resolution, the IFM Efector 3D has shown a lower noise level which lead to better results for all performed analyzes. With the low color dependance and low noise level of the IFM Efector 3D, this camera type is able to give reliable and repeatable depth information for the geometrical characterization of plants. Since, in an analyzed speed range up to 3.6 km/h, the measured distance of objects will not be influenced by their movement, this system will also be usable in combination with autonomous field robots. The other influences result in homogenous off-

sets over the object, in case of wet objects, or as homogenous offsets in the whole image, in case of direct light. Since these offsets are homogenous they do not affect the calculation of the plants morphological parameters. In contrast to this the occurring of dust with a high density can be a problem for the analysis of the measured distances. However, further investigations are needed to check the ability image processing methods filter the false measurements in case of dust with a low density.

Acknowledgement

This work is supported by the Federal Ministry of Food, Agriculture and Consumer Protection BMELV (Germany).

References

FENDER F., HANNEKEN M., IN DER STROTH S., KIELHORN A., LINZ A., RUCKELSHAUSEN A. (2006): Sensor Fusion Meets GPS: Individual Plant Detection", Proceedings of CIGR EurAgEng/VDI-MEG, 2006

RUCKELSHAUSEN A., BIBER P., DORNA M., ET AL. (2009): "BoniRob – an autonomous field robot platform for individual plant phenotyping" JIAC 2009 Wageningen (to be published)

KOLB A., BARTH E., KOCH R. (2008): "ToF-Sensors: New Dimensions for Realism and Interactivity"; Computer Vision and Pattern Recognition Workshops, 2008. CVPR Workshops 2008. IEEE Computer Society Conference on 23-28 June 2008 Page(s):1 - 5

MEIER U., BLEIHOLDER H. (2007): "The BBCH scale – codification and description of phonological growth stages of plants and their international use in agricultural research"; Proceedings of the International Symposium 08 –10 October 2007 in Stuttgart-Hohenheim, ISBN 978-3-86186-5414, Page(s): 122-125

LOTTNER O., SLUITER A., HARTMANN K., WEIHS W. (2007): "Movement Artefacts in Range Images of Time-of-Flight Cameras"; International Symposium on Signals, Circuits and Systems, 2007. ISSCS 2007. Page(s): 1 - 4

YOUNG MIN K., CHAN D., THEOBALT C., THRUN S. (2008): "Design and calibration of a multi-view TOF sensor fusion system." Computer Vision and Pattern Recognition Workshops, 2008. CVPR Workshops 2008. IEEE Computer Society Conference 2008 Page(s):1 – 7

CIE (2009) – Interactive CIE Software; *www.pfk.ff.vu.lt/**cie**/*

Calculation of flow vector in plants by non-destructive imaging using neutron radiography

Uzuki Matsushima[1], Wolfgang Graf[2,4], Nikolay Kardjilov[3], Hiroshi Shono[1], Werner B. Herppich[2]

[1] *Faculty of Agriculture, Iwate University, Ueda 3-18-8, Morioka, Iwate 020-8550, Japan*
[2] *Dept. Horticultural Engineering, Leibniz-Institut für Agrartechnik Potsdam-Bornim e. V. Max-Eyth-Allee 100, 14469 Potsdam, Germany*
[3] *Institute of Applied Materials , Helmholtz Centre Berlin, Glienicker Str. 100, 14109 Berlin, Germany*
[4] *Humboldt-Universität zu Berlin, Institut of Horticultural Science, Lentzeallee 75, 14195 Berlin, Germany*
Corresponding author:uzuki@iwate-u.ac.jp

Abstract: *Water transport in plants is one of the most important factors for life, because it guaranties plants photosynthesis, the basic process for live on earth. Cold neutron radiography (CNR) with D_2O tracer provides visualization images of water flow in plants non-destructively. In order to calculate flow vector in plants, three optical flow algorithms, Block Matching, Horn-Schunck and Lucas-Kanade, were evaluated. The results showed that Block Matching was the optimum algorithm to calculate plant water flow from D_2O tracers. This algorithm was successfully applied to in situ investigate the flow vectors in the peduncles of three rose cultivars ('Akito', 'Milva' and 'Red Giant', respectively) having high, middle and low bent-neck susceptibility. The highest flow velocities obtained were approx. 45, 80, 19 mm hour^{-1} for 'Akito', 'Milva' and 'Red Giant', respectively. Also, for further grafting studies, calculations of flow vector in tomato seedlings were examined. Even if the seedling stem was thin, the high resolution of the CNR images allowed the exact calculation of flow vectors. Thus, this D_2O tracer vector method could most probably be applied in a great variety of plant water relations studies.*

1 Introduction

Water transport in plants is one of the most important factors for life, because it guaranties plants photosynthesis, the basic process for live on earth. Cold neutron radiography (CNR) with D_2O tracer is a useful method to non-destructively visualize water flow in small plants from root via stem to leaf or flower (NAKANISHI *et al.* 2005, MATSUSHIMA *et al.* 2005, MATSUSHIMA *et al.* 2007). Velocity of water flow can be an indicator of water sink and source strength in plant tissues and/or organs. We developed a method to observe steady water flow by cold neutron radiography using D_2O as a tracer (MATSUSHIMA *et al.* 2007, 2008). Compared to H_2O the mass attenuation coefficient of D_2O is smaller which allows for a better penetration of neutrons. As a result, the flow of D_2O

was clearly observed in small plants such as tomato seedlings and rose peduncles. The second but essential step is to estimate the vectors of water flow in plant samples. The vectors would indicate plant parts that require water. This information would e.g. be useful for proper irrigation of plants under water deficit. This paper describes observations of water flow using CNR technique with D_2O tracer and introduces the applications for agricultural samples.

2 Experiments and calculation approaches

Cold neutron radiography

Neutron radiography visualizes the attenuation of neutrons through a medium. The probability of the neutron's interaction with a nucleus depends on the structure and the stability of the core. Some light elements such as hydrogen and beryllium, boron, lithium, nitrogen, etc. absorb and/or scatter neutrons rather well. On the other hand, neutrons penetrate very heavy elements such as lead, titanium and others rather easily. Elements having adjacent atomic numbers can have a widely differing absorption of neutrons. Hydrogen is one of the elements, which have a large mass attenuation coefficient and, hence, produce clear images. Hydrogen also forms the major constituent of living plants being incorporated in water, sugars, fibers and lipid molecules. By far the most ubiquitous molecule in living plant material is water. Hence, changes in the amount and the distributions of plant water are usually much more pronounced and can occur much faster than changes in other molecules. Experiments were conducted at Position II, CONRAD that is the CNR facility in BER-II, Helmholtz Center Berlin for Materials and Energy (HZB). The neutron flux and *L*/*D* at Position II was 10^7 neutrons/cm^2/s and 250, respectively. TAn advantage of this facility is the low noise in the obtained images. The bended cold neutron guide reduces high energy neutron that creates white spots on neutron images. Kardjilov et al. (2005) and HILGER *et al.* (2006) described CONRAD in more details.

Usage of D_2O tracer and application of algorithms

Steady state water flows or water diffusion can not be detected by radiographic techniques. Therefore, contrast agents, such as Iodine for x-ray radiography are needed to indicate water movement. In our most recent tested approach we use D_2O as a tracer to observe steady water flow. **Figure 1** shows a schematic diagram of the function of D_2O as a tracer in a plant. D_2O, showing much less interactions with cold neutrons than normal water, proved to be a suitable low-contrast tracer. Hence, the combination of CNR with the low-contrast tracer allows the direct visualization of water flow and the calculation of water flow with a high resolution at the tissue level.

To apply D_2O tracer, samples were placed in a crystal glass tube. H_2O and D_2O were alternately injected into the glass tube by a PC-controlled supply system. Due to their different attenuation coefficients for cold neutrons D_2O and H_2O creates positive and negative contrasts. In order to obtain flow vectors of the contrast images, three different optical flow algorithms, Block Matching, Horn-Schunck (HORN & SCHUNCK 1981) and Lucas-Kanade (LUCAS & KANADE 1981) were applied. For the calculations the IntelR Open source Computer Vision library, OpenCV® (opencv.jp; 2009) with C programming language was employed.

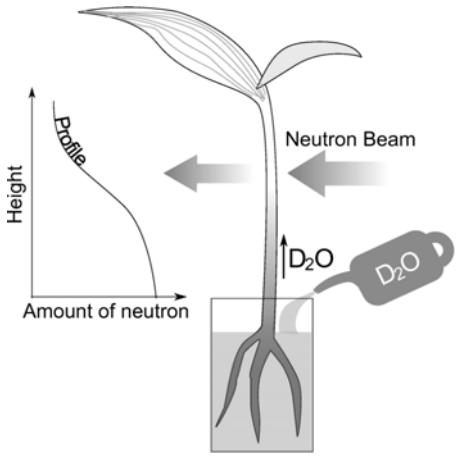

Figure 1: Schematic diagram of the function of D_2O in a plant as a tracer.

3 Water flow vector in plants

Evaluation of three algorithms

First, three optical flow algorithms were evaluated. Roses (*Rosa hybrida* L. 'Milva') were used as plant samples. **Figure 2-A, B** shows D_2O tracer images of adjacent frames. Approximately, tracer flowed vertically, because the sample was nearly uplight. The vertical movement distance ,the double-end arrow, was obtained from the adjacent binarised frames (**Figure 2-E**). **Figure 3-A, B, C** shows calculated vector using the tested algorithms respectively. The mean length of vector obtained using the Block Matching approach was similar to that of the double-end arrow. On the other hand, calculations by Horn-Schunck and Lucas-Kanade resulted in much shorter length of vector. More over, most vectors calculated by Block Matching indicated flow directions that were vertically upwards. However, vectors calculated by Horn-Schunck and Lucas-Kanade randomly indicated flow directions. Therefore Block Matching was the most suitable of the three algorithms tested. Details of this evaluation are given by MATSUSHIMA *et al.* (2009).

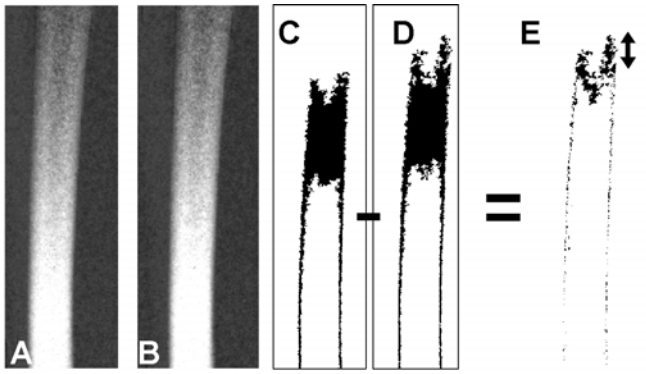

Figure 2: Adjacent frames of images indicating D_2O tracer flow in 5 min (A and B), and those of binarised images (C and D). Difference of C and D is vertical movement distance.

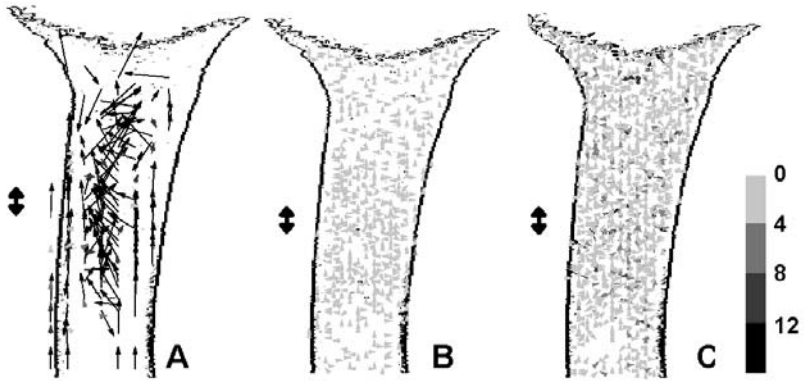

Figure 3: Flow vectors calculated using three different algorithms; Block Matching (C), Lucas-Kanade (D) and Horn-Schunck (E). Aspect ratio of the vector image was changed to show the detail of vector distribution. The unit of grey-scale bar is pixels/frame.

Application for a postharvest study of roses

This method was applied to visualize water flow in rose peduncles in order to compare “Bent-neck” resistance among three rose cultivars. Bent-neck syndrome, an important postharvest problem of cut roses, is probably due to water supply limitations and/or the structural weakness of vascular bundles of the peduncle tissue. The varieties ’Akito’, ’Milva’ and ’Red Giant’, respectively, having low, middle and high bent-neck resistances were employed as samples. Vectors were calculated by Block Matching algorithm. The highest flow velocities of 'Akito', 'Milva' and 'Red Giant' were approximately 45, 80, 19 mm $hour^{-1}$, respectively. The results indicated that water uptake of ‘Milva’ was the fastest. In contrast, roses of 'Red Giant', which generally show the highest resistance against bent-beck among the 3 cultivars obviously exhibited the lowest water uptake rates. Hence, water uptake velocity alone did obviously not reflect bent-neck resistance.

Application for a study of grafting

Grafting is a method to transplant e.g. weakly growing but effectively fruiting shoots (scion) onto strong root stocks. The grafting process is difficult to investigate by yet ex-

isting destructive methods. However, it is very important to better understand the grafting process to be able to rise the success rate. Hence, the final aim of the presented investigation is to evaluate the onset of water transport from root stocks to scions after transplantation. In a first step, it was attempted to obtain water flow vectors in small tomato seedlings (**Figure 3**) of 'Kagemusya' tomatoes. Even in the thin seedlings, D_2O tracer flow vectors were successfully obtained because of the high spatial and temporal resolution of cold neutron radiography images. Thus, this method is applicable to determine quantities of water flow in grafted tomato seedlings.

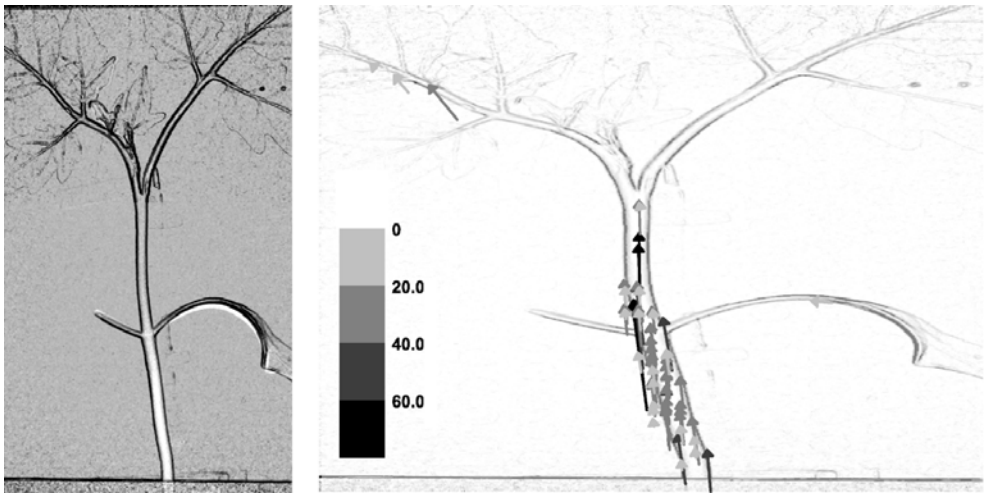

Figure 4: Flow vectors of D_2O tracer in tomato seedlings. Left: Image of D_2O tracer. Right: Calculated vectors using Block Matching. Aspect ratio of the vector image was changed to show the detail of vector distribution. The unit of grey-scale bar is pixels/frame.

4 Conclusions

In case of calculating flow vector of D_2O tracer in plants, Block Matching was the most suitable among three optical flow algorithms. CNR with D_2O tracer and vector calculation by Block Matching were successfully applied to study the bent-neck syndrome of roses and the success of grafting of tomato seedlings. Thus, evaluation of D_2O tracer vectors could most probably be applied in a great variety of plant water relations studies.

References

HILGER A., KARDJILOV N., STROBL M., TREIMER W., BANHART J. (2006): The cold neutron radiography and tomography instrument CONRAD at HMI Berlin. Physica B, 385-386: 1213- 1215

HORN B.K.P. SCHUNCK B.G. (1981): Determining optical flow. Artificial Intelligence 17: 185-203

KARDJILOV N., HILGER A., MANKE I., STROBL M., TREIMER W., BANHART J. (2005): Industrial applications at the cold neutron radiography and tomography facility of the HMI. Nuclear Instruments and Methods in Physics Research A 542: 16-21

LUCAS B., KANADE T. (1981): An iterative image registration technique with an application to stereo vision. In Proceedings of the 7th International Joint Conference on Artificial Intelligence (IJCAI), pp. 674-679. P. J. Hayes, ed. Vancouver, Canada, William Kaufmann

Matsushima, U., Herppich, W., Kardjilov, N., Graf, W., Hilger, A., & Manke, I. 2009. Estimation of water flow velocity in small plants using cold neutron imaging with D_2O tracer. Nuclear Instruments and Methods in Physics Research A **605**: 146-149.

MATSUSHIMA U., KARDJILOV N., HERPPICH W.B., HILGER A. (2007): Development of D_2O tracer method for water flow in plants. In BENSC Experimental Reports 2006, p.138. Berlin, Germany, Hahn-Meidner-Institut

MATSUSHIMA U., KARDJILOV N., HILGER A., GRAF W., HERPPICH W.B. (2008): Application potential of cold neutron radiography in plant science research. Journal of Applied Botany and Food Quality 82: 90-98

MATSUSHIMA U., KAWABATA,Y., HORIE T. (2005): Estimation of the volumetric water content in chrysanthemum tissues. Journal of Radioanalytical and Nuclear Chemistry 264(2): 325-328

MATSUSHIMA U., LEHMANN E.H., VONTOBEL P., FREI G., NICOLAÏ B.M., NISHIZAWA T., KAWAMITSU Y. (2007): Observation of water distribution in cut spray carnation flowers using neutron tomography. In Proceedings of the Asia-Pacific symposium on Quality Management for Agri-Foods in Supply Chains, pp. 119-125. August 7-10, 2006, MCGLASSON, W.B., KANLAYANARAT, S. & ACEDO, A. ed. Bangkok, Thailand, Center of Excellence in Postharvest Technology King Mongku's University of Technology Thonburi

NAKANISHI T.M., OKUNI Y., HAYASHI Y., NISHIYAMA H. (2005): Water gradient profiles at bean plant roots determined by neutron beam analysis. Journal of Radioanalytical and Nuclear Chemistry 264: 313-317

opencv.jp (2009): Intel® Open Source Computer Vision Library. Available at: http://opencv.jp/opencv-1.0.0_org/docs/index.htm Accessed 29 June 2009

Monitoring optical properties of apple tissue during cool storage

Laszlo Baranyai, Christian Regen, Manuela Zude

Leibniz-Institut für Agrartechnik Potsdam-Bornim e.V., Max-Eyth-Allee 100, 14469 Potsdam, Germany
Corresponding author: lbaranyai@atb-potsdam.de

Abstract: *Apples (Malus×domestica) of 'Elstar' and 'Pinova' of three different ripeness stages (unripe, ripe and overripe) were stored in separate chambers with 2°C and controlled atmosphere (2% CO_2, 1.5% O_2) between August 2008 and March 2009. During storage, 30 pieces of each cultivar were randomly selected for one measurement. Monochrome camera (JAI A50IR CCIR, JAI, Denmark) was used to capture images of 720x576 pixel size with 0.1694 mm/pixel resolution. The selected point on the apple surface was illuminated with circular laser beam of 7° incident angle and 785 nm wavelength (LPM785-45C, Newport Corp., USA). The vision system was controlled using LabView 8.6 PDS (National Instruments, USA) software extended with a dynamic library including image processing functions. The observed spatial distribution of intensity was used to estimate optical properties of fruit tissue. Backscattering profiles were computed based on radial averaging relative to the incident point. The logistic shape of the collected profiles was analyzed further to estimate optical properties such as absorption coefficient (μ_a), scattering (μ_s) and anisotropy factor (g). The size of the total backscattering area was also taken into account to describe light penetration and distribution in apple tissue. The method appears reasonable for characterising changes in the optical properties of fruit in postharvest.*

1 Introduction

Investigation of interactions between light and biological materials is of great interest since optical methods provide non-destructive way of quality assessment and monitoring. Mechanical injury of bruising was detected on apples with visible/NIR spectroscopy methods utilizing wavebands around 545 nm and 1200 nm (XING *et al.* 2006). Soluble solids content (SSC) and acidity of 'Fuji' apples were measured using FT-NIR spectrometry in the wavelength range of 812–2357 nm (LIU & YING 2005). Hyperspectral imaging system with artificial neural network was trained and applied successfully to detect chilling injury of Red Delicious apples based on five wavelengths (717, 751, 875, 960 and 980 nm) (ELMASRY *et al.* 2009). This neural network estimated fruit firmness with 9.4 N root mean square error (RMSE) and obtained 98.4% classification accuracy. Decline in firmness of 'Sansa' apple during storage on room temperature (19-23°C) was

monitored with ultrasonic device (KIM *et al.* 2009). QIN & LU (2008) applied hyperspectral technique to analyze how absorption (μ_a) and light scattering (μ_s') are correlated with ripeness of fruits and vegetables. Product specific μ_a and μ_s' spectra were calculated in the wavelength range of 500–1000 nm using the Farrell model. Additionally, based on the obtained optical parameters, the light penetration depth was also estimated for numerous horticultural produces. The internal structures of tissues, such as fibres, were found to affect light distribution and result in distortion of the measured intensity in certain directions (SVIRIDOV *et al.* 2005). Laser beam emitting at 650 nm was used to detect structures in bone and skin according to the distortion in light diffusion (SVIRIDOV *et al.* 2005).

The objective of the presented work was to estimate optical properties of apple tissue during controlled atmosphere cool storage using laser induced backscattering imaging. The selected optical properties include anisotropy factor ($g \in]-1,1[$), which describes the probability of scattering directions.

2 Materials and methods

2.1 Materials

Apple fruits (*Malus×domestica* 'Elstar' and 'Pinova') have been harvested in the orchard near Glindow (Germany). The middle of the field was located at latitude 52N 22' 14.96" and longitude 12E 52' 22.69". The selected area of 25×150 m had North-West to South-East orientation and was split into upper and lower part according to the position of a hill inside. Soil was drier and trees were obviously smaller within the area of the hill. Both upper and lower regions were split into two parts for cultivars 'Elstar' and 'Pinova'. Four rows and 100 trees were used to collect fruits from each quarter of 12.5×75 m. Harvested fruits were classified into the commercial grades of unripe, ripe and overripe by people working on the harvest. Although those people do not make a certified sensory panel, they have several years experience in manual quality assessment. Harvested fruits were transferred into the storage facility immediately. Separate chambers were provided for apples of the same ripeness stage and cultivar. Temperature was adjusted to 2°C. The atmosphere inside chambers consisted of 2% CO_2 and 1.5% O_2. This controlled atmosphere cool storage started in August 2008 and took 157 and 164 days for 'Elstar' and 'Pinova', respectively. The continuous storage was broken for a few minutes in order to perform the measurements in 22 and 24 cases for 'Elstar' and 'Pinova', respectively. For one measurement, 30 pieces of apple were randomly selected. The total amount of 2799 images was investigated during the experiment (**Table 1**).

Table 1: Composition of apple sample (number of images taken)

Ripeness stage	Location within orchard		Total
	Upper	Lower	
Apple of 'Elstar'			
Unripe	232	236	468
Ripe	210	206	416
Overripe	239	240	479
Apple of 'Pinova'			
Unripe	238	234	472
Ripe	240	240	480
Overripe	242	242	484

2.2 Vision system

Digital images of 720×576 pixel size and 0.1694 mm/pixel resolution were acquired. Measurements took place in a darkroom in order to maximize signal to noise ratio. The vision system was consisted of a monochrome camera (JAI A50IR CCIR, JAI, Denmark), zoom lenses (model H6Z810, PENTAX Europe GmbH, Germany), external analog video converter (VRM AVC-1, Stemmer Imaging GmbH, Germany) and a laser module (LPM785-45C, Newport Corp., USA) emitting at 785 nm with 45 mW power. The camera and laser module were aligned in 0/7° geometry. The acquisition process was controlled by LabView 8.6 PDS software (National Instruments, USA) extended with a dynamic library of specific image processing functions.

2.3 Estimation of optical parameters

The incident point was automatically identified as the mass point of the highest intensity area. The intensity values of the illuminated region were collected with radial averaging relative to the incident point. The shapes of these profiles were compared to the results of Monte Carlo simulation in order to estimate anisotropy factor (g) and total interaction coefficient (μ_t, cm^{-1}). Simulations were run with the optical parameters of μ_a=0.63 cm^{-1}, μ_s=30 cm^{-1} and g=0–0.99. The refractive index of n=1.35 was assumed for apple tissue. The profiles were found to rotate as a result of changing anisotropy factor and the decline of measured intensity may be used to estimate the value of this optical property (BARANYAI & ZUDE 2008). Trigonometric function (Eq. 1) was found to describe well (r^2=0.9995, Durbin-Watson D=2.0293) the relationship between slope of the logarithmic profiles and anisotropy factor.

$$y = a + b \cdot \tan\left(x \frac{\pi}{c} \right) \quad (1)$$

The average diameter of the backscattering area at 50% intensity level (FWHM) was computed based on the diffusion theory model and its correlation with optical parame-

ters was investigated (**Table 2**). The best correlation was found with the total interaction coefficient ($\mu_t=\mu_a+\mu_s'$).

Table 2: Correlation between optical parameters and FWHM

Correlation	μ_a	μ_s'	μ_t	μ_{eff}
Pearson (linear)	-0.0475	-0.8645	-0.8653	-0.6828
Spearman (rank)	-0.0393	-0.9990	-0.9996	-0.7354

From practical point of view, the effective attenuation coefficient ($\mu_e=[3\mu_a(\mu_a+\mu_s')]^{1/2}$) is very important since its reciprocal value describes the theoretical penetration depth (QIN & LU 2009). The optical parameters were adjusted in a wide range of μ_a = 0.004–0.63 cm^{-1}, μ_s' = 3.2–35 cm^{-1} in order to find a suitable model. **Figure 1** shows that the total interaction coefficient might be estimated better due to the lower deviations.

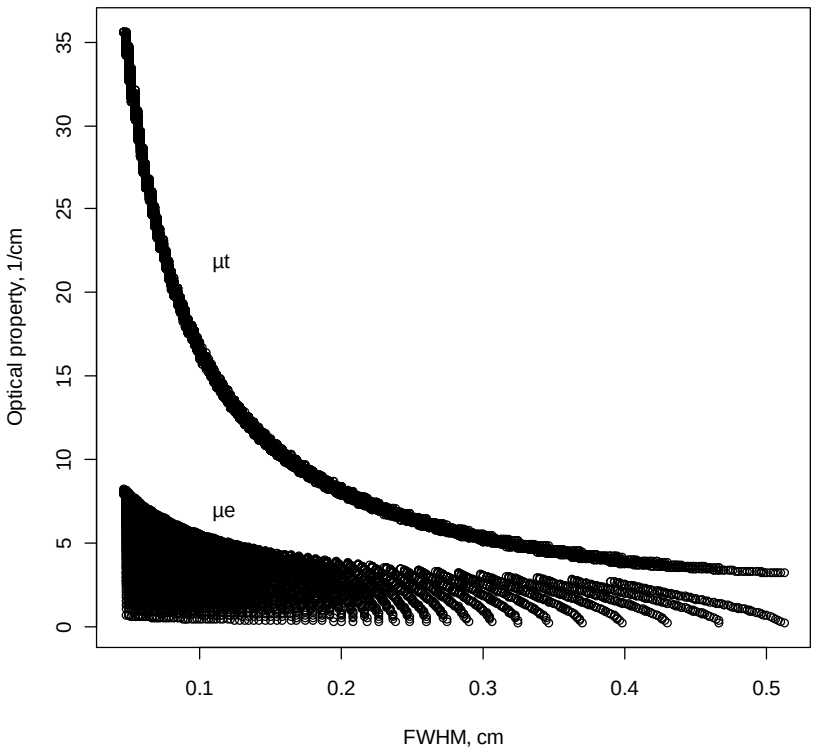

Figure 1: Relationship between backscattering spot size (FWHM), effective attenuation (μ_e) and total interaction (μ_t) coefficients

The reciprocal function fitted well to the 10^4 data points with r^2=0.998. The root mean square error of prediction (RMSEP) was 0.37 cm^{-1} using 10% randomly selected data in 100 repetitions.

The 25% intensity level between minimum and maximum backscattering signal was also calculated. The elliptical distortion of the position of equi-intensity pixels at this level was computed. The ratio of radii measured in perpendicular directions was found to de-

scribe the proportion of reduced scattering coefficients and structural anisotropy (SVIRIDOV *et al.* 2005). The distortion of the circular laser beam is 0.751% on plain surface at 7° incident angle. This offset value was used to correct calculated ratios.

3 Results and discussion

The estimated values for total interaction coefficient (μ_t) are presented in **Figure 2**. The error bars represent the 95% confidence interval of mean values for each day of measurement. The estimated values for unripe, ripe and overripe pieces were more similar for 'Pinova' apples than that of 'Elstar'. Observed values changed up to 15% during storage. The curves for unripe and overripe pieces run parallel until the 81th day of storage, beginning of December 2008, when break occurs in the trend. All groups of apples show this dual behaviour which may indicate that μ_t estimated at 785 nm was also affected by attributes other than firmness. However, similar non-linear relationship was observed between textural acceptability and firmness of apples during storage (KONOPACKA & PLOCHARSKI 2004). The analysis of variances (ANOVA) revealed that estimated values were primarily affected by the storage time, position in the orchard and cultivar, in this order.

The estimated values for anisotropy factor (g) are presented in **Figure 3**. The error bars represent the 95% confidence interval of mean values for each day of measurement. Estimated values change in a narrow band, less, than 2.1%. Each sample group had negative correlation between storage time and anisotropy factor. It means that the effect of general scatterers present in the tissue was slightly decreased. Pieces belonging to the ripe class obtained the lowest correlations for both cultivars. The anisotropy factor, and the gradient of the outline of the backscattering area, changed the most for overripe pieces of 'Elstar' and unripe pieces of 'Pinova'. According to the ANOVA results, estimated values of anisotropy factor were primarily affected by the storage time and ripeness stage, in this order. The analysis of interaction effects confirmed that pieces belonging to different ripeness stages change anisotropy factor with different pace.

The basic statistical parameters of elliptical distortion of the diffusively illuminated area are presented in **Table 3**. The mean value of 1.119 and the distribution of measured data around mean do not show significant distortion. This result indicates that apples did not have significant internal structures. Typical fibrous biological materials, such as human skin or demineralised bone, result in the ratio above 1.5 (SVIRIDOV *et al.* 2005).

Table 3: Statistical parameters of elliptical distortion of illuminated area

Mean	1st quartile	Median	3rd quartile	Std. deviation
1.119	1.083	1.112	1.144	0.049

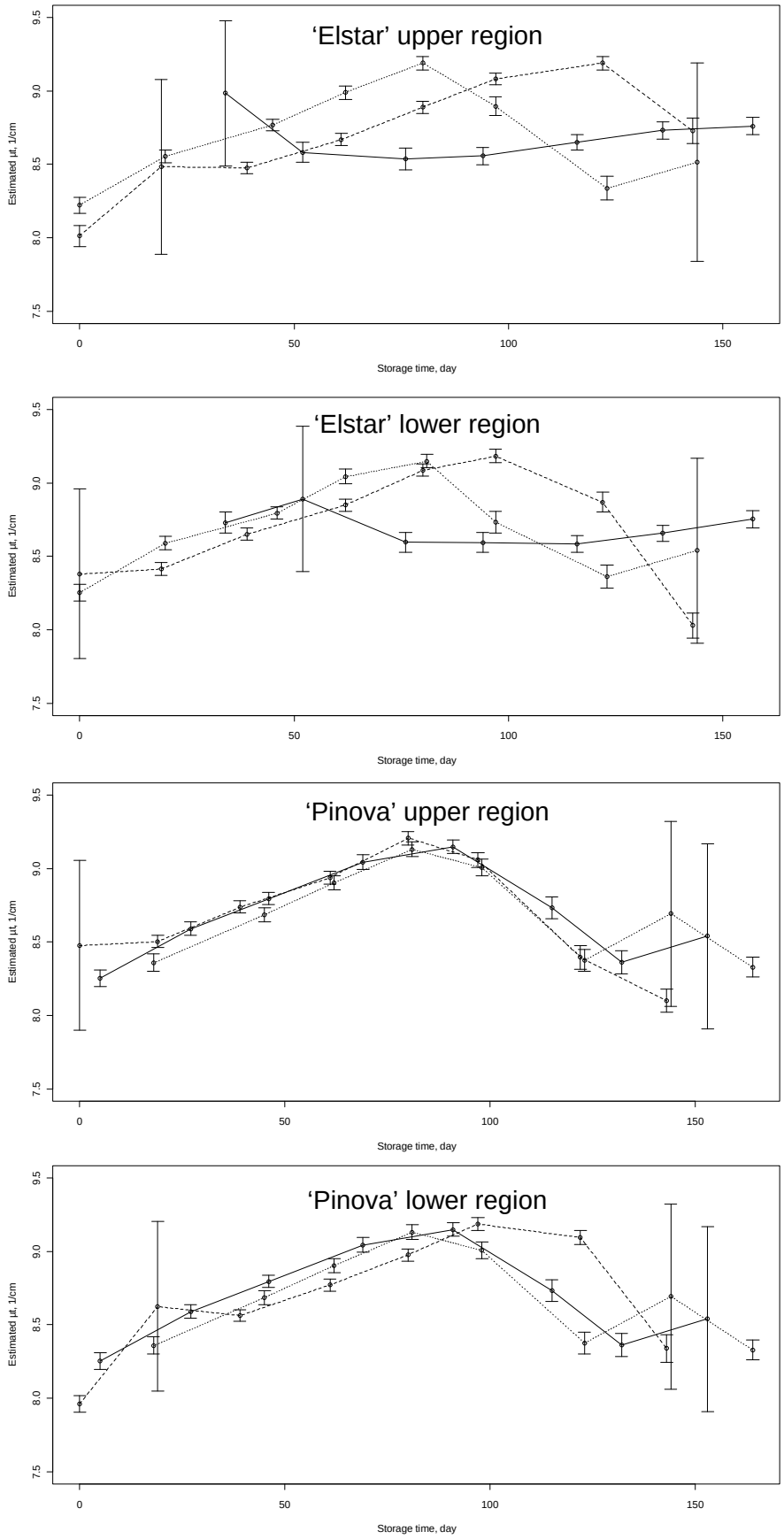

Figure 2: Changes in total interaction coefficient during controlled atmosphere cool storage (···· overripe, — ripe, - - unripe)

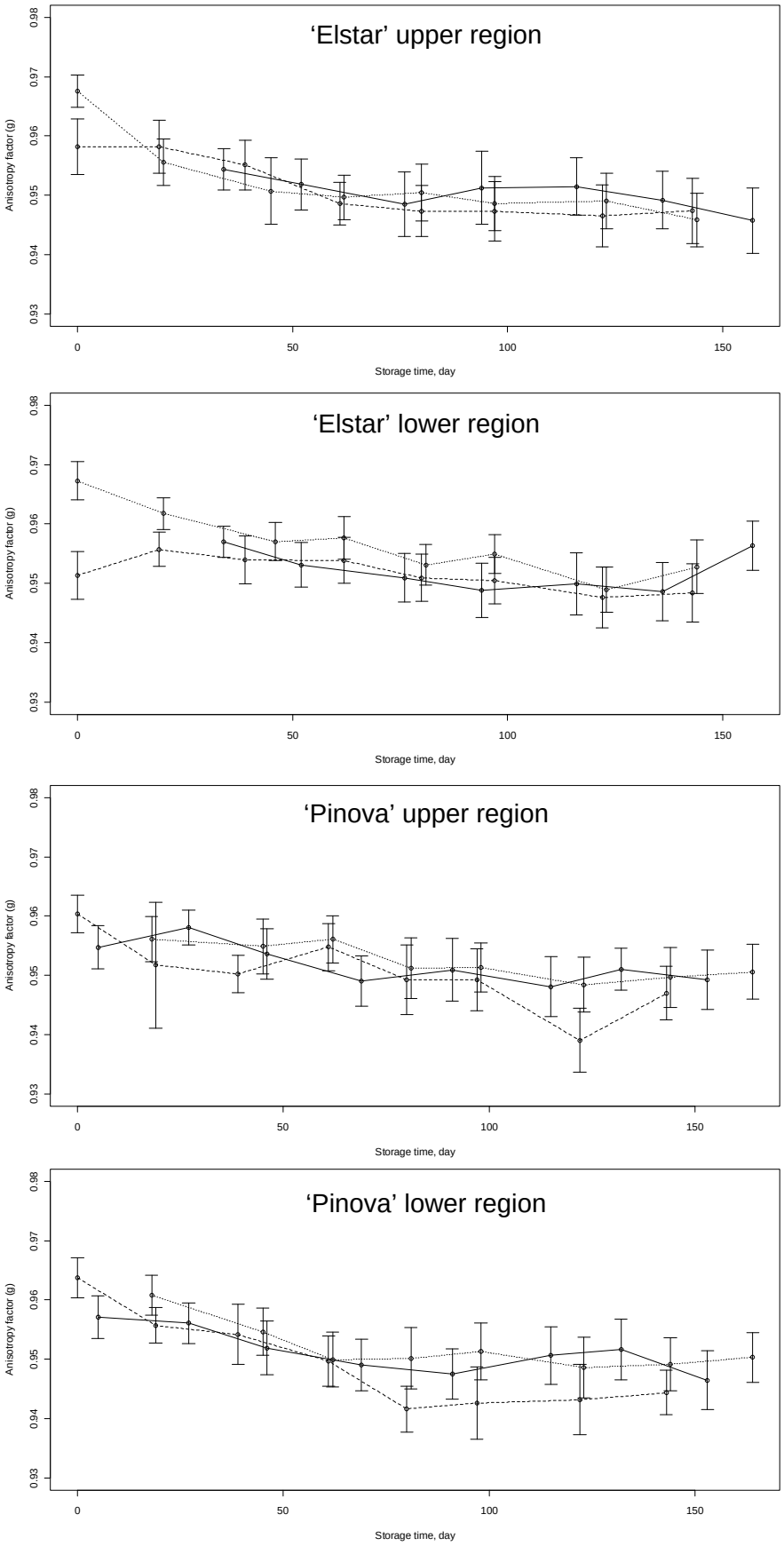

Figure 3: Changes in anisotropy factor during controlled atmosphere cool storage (···· overripe, — ripe, - - unripe)

4 Conclusions

Laser induced diffuse reflectance (backscattering) imaging technique was used to monitor selected optical properties of 'Elstar' and 'Pinova' apples during controlled atmosphere cool storage. The total interaction coefficient (μ_t, cm^{-1}) and anisotropy factor ($g \in]-1,1[$) were estimated on the basis of spatial intensity distribution. The total interaction coefficient was found to increase significantly within the first 81 days and decrease afterwards. The observed break in the trend indicates that μ_t estimated at 785 nm might be affected by more parameters additionally to firmness. Similar behaviour was found in the literature for texture acceptability. The statistical analysis pointed out that observed values were mainly affected by the storage time, position in the orchard and cultivar, in this order. Almost monotonous decrease was observed in case of anisotropy factor. The change in anisotropy factor was less (2.1%) than that of in total interaction coefficient (15%). Analysis of variances revealed that mainly storage time and ripeness stages affected estimated values, in this order. The elliptical distortion of the visible backscattering signal at 25% intensity level was also investigated to determine whether significant internal structures occur or change in the tissue. The comparison of results to literature data did not predict directional structures in apple.

The presented image processing method might be used to describe and monitor optical properties of apples and other fruits during storage and provide additional information for quality assurance rapidly.

References

BARANYAI L., ZUDE M. (2008): Analysis of laser light migration in apple tissue by Monte Carlo simulation. Progress in Agricultural Engineering Sciences, 4: 45-59

ELMASRY G., WANG N., VIGNEAULT C. (2009): Detecting chilling injury in Red Delicious apple using hyperspectral imaging and neural networks. Postharvest Biology and Technology, 52: 1-8

KIM K.-B., LEE S., KIM M.-S., CHO B.-K. (2009): Determination of apple firmness by nondestructive ultrasonic measurement. Postharvest Biology and Technology, 52: 44-48

KONOPACKA D., PLOCHARSKI W.J. (2004): Effect of storage conditions on the relationship between apple firmness and texture acceptability. Postharvest Biology and Technology, 32: 205-211

LIU Y., YING Y. (2005): Use of FT-NIR spectrometry in non-invasive measurements of internal quality of 'Fuji' apples. Postharvest Biology and Technology, 37: 65-71

SVIRIDOV A., CHERNOMORDIK V., HASSAN M., RUSSO A., EIDSATH A., SMITH P., GANDJBAKHCHE A.H. (2005): Intensity profiles of linearly polarized light backscattered from skin and tissue-like phantoms. Journal of Biomedical Optics, 10(1), 014012/1-9

QIN J., LU R. (2008): Measurement of the optical properties of fruits and vegetables using spatially resolved hyperspectral diffuse reflectance imaging technique. Postharvest Biology and Technology, 49: 355-365

QIN J., LU R. (2009): Monte Carlo simulation for quantification of light transport features in apples. Computers and Electronics in Agriculture, 68: 44-51

XING J., BRAVO C., MOSHOU D., RAMON H., DE BAERDEMAEKER J. (2006): Bruise detection on 'Golden Delicious' apples by vis/NIR spectroscopy. Computers and Electronics in Agriculture, 52: 11-20

Systems for multisensor navigation and 3D-modelling

Anko Börner, Ines Ernst, Denis Grießbach

German Aerospace Center (DLR), Institute for Robotics and Mechatronics, Berlin, Germany
Corresponding author: Anko.Boerner@dlr.de

Application of autonomous vehicles mostly relies on pose estimation and 3D environment modelling. In robotics this task is described by the acronym SLAM (Simultaneous localization and mapping). Since these two steps are not mutually dependent on each other and in order to cover a wide range of applications it was decided to separate the research activities.

For navigation a multisensor sensor approach was chosen to assure an accurate and reliable state estimation by Kalman filters. Main sensors are stereo cameras and inertial measurement units, which can be supplemented GPS. In general, data of sensors providing translation or rotation information or their derivates can be involved. Optical navigation approaches are used to detect and track image features and to derive pose information from camera data. Calibration and initialization (determination of offsets, alignments, camera properties) of the multisensor navigation system are essential for high quality solutions.

3D modelling of the environment is executed by applying stereo cameras and calculating depth maps. The high-performance SGM algorithm was implemented in different hardware systems (GPU and FPGA) in order to provide real time capability for medium resolution images. Again, calibration is one of the key requirements for a successful application.

Combination of 3D modelling and multisensor navigation results in improvement of the quality of the retrieved information or even in new products, e.g. 3D models can be georeferenced only, of navigation data are available.

The paper gives an overview about basic technologies and methods on the topics multisensor navigation and 3D modelling and illustrates the capabilities of autonomous vehicles using this knowledge.

Preliminary results on the non-invasive diagnosis of superficial scald in 'Rocha' pear by fluorescence imaging

Ana Margarida Cavaco[1], D. Antunes[2], J. Marques da Silva[3], R. Antunes[4], R. Guerra[1]

[1] CEOT, Universidade do Algarve, Campus de Gambelas, 8005-139 Faro, Portugal
[2] CDCTPV, Universidade do Algarve, Campus de Gambelas, 8000-139 Faro, Portugal
[3] BioFIG, FCUL, Campo Grande, 1740-016 Lisboa, Portugal
[4] Frutoeste - Cooperativa Agrícola Hortofruticultores do Oeste, C.R.L., E.N. 8 Carrascal, AZUEIRA, 2665-009 Lisboa, Portugal
Corresponding author: acavaco@ualg.pt

Abstract: *Superficial scald, a major physiological disorder of pome fruit, is a long-lasting issue waiting for a definitive non-chemical dependent solution. This is our first report on the use of a non-invasive method to detect scald in the valuable Portuguese variety 'Rocha' pear (Pyrus communis* L.*). Mature unripe fruits without any preventive treatment for scald and stored for about 2.5 months under cold normal atmosphere (NA: 0ºC, rH 90–95%) and under cold controlled atmosphere (CA: 0ºC, rH 90–95%, 1.5 kPaO_2 + 0.5 kPa CO_2), were obtained from Frutoeste (Mafra, Portugal). After 6 h at 15ºC, during transportation, and one additional cold-storage week (NA: 1ºC, RH 90–95%) at University of Algarve (Faro, Portugal), fruit was transferred to shelf-life (circa 20^{o}C and 70% RH). Scald Index (SI), severity (SS) and surface scald distribution (SSD) were determined in the beginning of the shelf-life (0 d) and periodically up to the 6th d. These parameters remained constant for each pear along that period: SI was 0-4 in NA and 0-3 in CA pears; SS was 0-3 in NA and 0-1 in CA and SSD was 0-100% in NA and 0-75% of the fruit in CA.*

Fluorescence imaging photos of all fruits were taken periodically with a system made at the physics lab of CEOT, consisting of six commercial blue light LED lamps, two Ar-ion lasers emitting at 475 nm (~1000 µmol $m^{-2}s^{-1}$), lenses for beam expansion, a CCD camera, an optical neutral density filter (ONDF) and an optical band pass filter (OBF) centred at 690 nm. Images were stored and processed by the appropriate software. Two types of images were obtained: blue reflectance images, taken with the ONDF, and fluorescence images, taken with the OBF. Both images suggested a non-uniform field illumination effect. In order to eliminate this effect, images were divided, creating a new image of the ratio Fluorescence/Reflectance, which is expected to be independent on the variations of the illumination field.

All scald typical patches were detected easily by the fluorescence imaging system, as low fluorescence intensity areas, even those very small that were not visible in a normal digital photo. Yet, spots of other origin, such as peel scars were also detected by this system. Additionally, the fluorescence imaging system detected low fluorescence inten-

sity areas, though apparently normal to the naked eye. It is not yet known if these areas would be further expressed as a future scald patch with a longer cold storage.

1 Introduction

Superficial scald is a chilling induced oxidative major disorder of pome fruit, including the Portuguese exclusive and valuable POD 'Rocha' pear (*Pyrus communis* L.). It involves the synthesis of the sesquiterpene (E, E)-α-farnesene and the accumulation of its oxidation primary products, the conjugated trienols (CTols), on the epidermis and hypodermis layers of the fruit, disrupting the cells on the fruit skin (INGLE 2001). Scalded fruits exhibit brown patches on the peel that may cover them totally and attain 6 mm deep. Fruit prices are lowered as soon as the disorder is expressed, and later they won't be sold on the market as fresh commodities anymore. The fruit tendency to develop this disorder relates to nutritional, environmental as well as storage conditions (CHAPON & BONY 1997). Since low temperature is a key and unavoidable factor in 'Rocha' pear storage, superficial scald remains a pressing and economical issue, demanding for strict preventive methods, some of them include critical chemicals for human health, such as diphenylamine (DPA).

Measurements of fluorescence in fruits are omnipresent but, to our knowledge, only (DELL *et al*. 1996) has used fluorescence (Fv parameter) as a predictor of scald in apples, although with limited success. Nevertheless, photosynthetic pigments, particularly, chlorophylls are quite responsive and sensitive under oxidative conditions, their fluorescence signal, changing according to the effect on photosystems and photosynthetic metabolism (SCHREIBER *et al.* 1994). Chlorophyll fluorescence imaging (CFI) gives an image of fluorescence at each point of the fruit or plant tissue, being quite promising as a fast and accurate method to detect stressful conditions for plants (SCHLÜTER *et al*. 2009).

The aim of this study was to test the use of CFI to detect superficial scald in 'Rocha' pear, in order to obtain an early diagnosis of this physiological disorder, and therefore, avoid chemical treatments and economical losses at the initial grading steps after fruit collection.

2 Materials and methods

Fruit and storage conditions

Mature unripe fruits without any preventive treatment for superficial scald and stored for about 2.5 months under cold normal atmosphere (NA: 0ºC, rH 90–95%) and under cold and controlled atmosphere (CA: 1.5 kPa O_2 + 0.5 kPa CO_2, 0ºC, rH 90–95%,), were

obtained from Frutoeste (Mafra, Portugal). After 6 h at 15ºC, during transportation, and one additional cold-storage week (NA: 1ºC, rH 90–95%) at University of Algarve (Faro, Portugal), fruit was transferred to shelf-life (approx. 20°C and 70% RH).

Scald parameters

Scald Index (SI): Sum of all scald patches surface per fruit (0: 0%; 1: >0≤5%; 2: 5-10%; 3: 10-25%; 4: 25-50%; 5: >50%), scald severity (SS) (0: no scald patches; 1: superficial patches; 2: superficial and dry scald patches; 3: deep and dry scald patches) and surface scald distribution (SSD) (% of fruit surface where scald patches appear: 0-100%) were determined in the beginning of shelf-life (0 d) and periodically up to the 6^{th} d. Scald Intensity stands for the % of scalded fruits among the whole fruit set, which in this case was about 300 for both NA and CA. For the following CFI measurements, sub-sets of NA (n = 11) and CA (n = 8) were chosen.

Chlorophyll fluorescence imaging measurements

Chlorophyll fluorescence imaging photos of all fruits were taken periodically along the shelf-life period with a homemade system, consisting of six commercial blue light LED lamps (Phillips, Netherlands; 1W @ 475 nm), two Ar-ion lasers emitting at 50 mW @ 477 nm (total PPFD ~ 1000 $\mu molm^{-2}s^{-1}$, assumed non-saturating), 2 lenses for laser beam expansion, a CCD camera (Ophir BeamStar FX33) with appropriate lenses, an optical neutral density filter (ONDF) and an optical band pass filter (OBF) centred at 690 nm. Images were stored through the camera software and processed in MATLAB® (2008). Several images were averaged in order to eliminate the fluctuation in the intensity of the LEDs due to the mains 50 Hz.

Data analysis

The effects of time and storage conditions on each of the scald parameters were tested by a two-way ANOVA with SigmaStat 2.0 (SPSS Science, USA).

Two types of images were obtained: blue reflectance images (R), taken with the ONDF, and fluorescence images (F), taken with the OBF. Both F and R images suggested a non-uniform field illumination effect. In order to eliminate this effect, images were treated according to the following procedure. Let I (r) be light intensity incident on the fruit surface. Through the imaging lens each point, r, on the fruit surface, is imaged on a

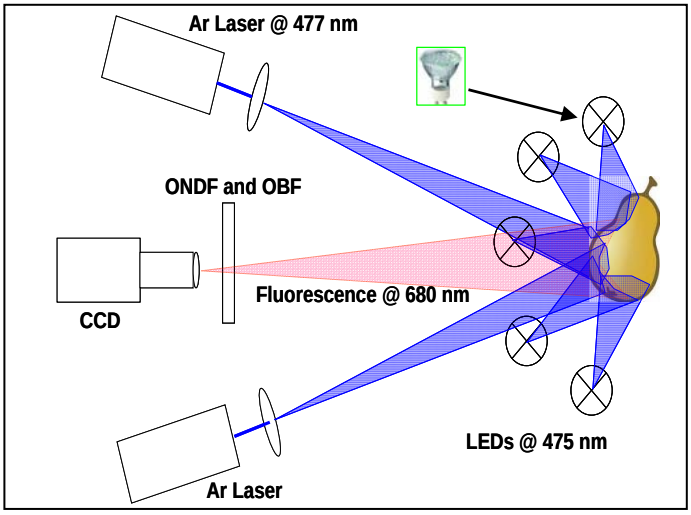

Figure 1: CFI system set up consisting of six commercial blue light LED lamps (1W @ 475 nm), two Ar-ion lasers emitting at 50 mW @ 477 nm, 2 lenses for laser beam expansion, a CCD camera with appropriate lenses, an optical neutral density filter (ONDF) and an optical band pass filter (OBF) centred at 690 nm

pixel p of the CCD sensor and from now on we will identify r by its imaging pixel, p. The counts of each pixel at 477 nm are given by $C_{477}(p)=A_{477}BR_{477}I(p)+N(p)$, where A_{477} is a wavelength dependent factor including the detector quantum efficiency at 477 nm and the filter transmittance, B is an wavelength independent factor including a geometrical factor related with the camera's acceptance angle and the camera gain, R_{477} is the pear reflectance at 477 nm and N(p) is a noise factor, which we have determined by taking a photo with lights off (dark or background photo). By the same token, the counts at 680 nm are given by $C_{680}(p)=A_{680}B\Phi_{680}I(p)+N(p)$, where now Φ_{680} gives the proportionality between fluorescent intensity and incident light intensity (assumed non-saturating). The variable presented in the following pictures is $S(p)=(C_{680}(p)-N(p))/(C_{477}(p)-N(p)) = (A_{680}/A_{477})\Phi_{680}(p)/\Phi_{477}(p))$. This variable is expected to become independent of the illumination profile, as required.

3 Results and discussion

This is the first report on the use of a non-invasive method, namely a CFI system to detect superficial scald in the valuable 'Rocha' pear (*Pyrus communis* L.).

All scald parameters were determined for each fruit in the beginning of shelf-life (0 d) and periodically up to the 6th d and remained constant for each pear along that period (**Table 1**). Scald intensity (%) was higher in the NA 'Rocha' pears group, as previously found (ISIDORO & ALMEIDA 2006) (**Table 1**). Although the limits observed for any of the parameters were different between NA and CA fruits, in what concerns the average values obtained for both groups, they were statistically ($P<0.05$) equivalent.

Table 1: Scald parameters of 'Rocha' pears determined in the beginning of shelf-life (0 d) and periodically up to the 6th d. Results presented are those registered on 6th d for both NA and CA 'Rocha' pears used along this study (NA set: n= 11; CA set: n= 8). Scald Intensity stands for the % of scalded fruits among the whole fruit sets, which in this case were about 300 for NA and CA.

Scald Parameters of pears on the 6th shelf-life day				
Samples	**SI (0-5)**	**Scald Intensity (%)**	**SSD (%)**	**SS (0-3)**
NA	0-4	48	0-100	0-3
CA	0-3	8	0-75	0-1
NA (Mean±SE)	1.64±0.41	-	36.36±9.74	0.86±0.21
CA (Mean±SE)	1.00±0.33	-	34.38±10.49	0.70±0.16

Figures depicted in the following section were chosen among the sub-sets of NA and CA pears used in the study, in order to show the detection potential of this system set up.

All scald typical patches were easily detected by this CFI system, as low fluorescence intensity areas (**Figures 2B.3, C.5** and **3B.5, 6**). Sometimes however, these fluorescence results did not reproduce the apparent homogeneity of the scalded area detected visually, as seen in **Figure 2B** in comparison to **Figure 3C**. The latter might reflect not only the scalded patches, but also the loss of chlorophyll associated to an over-ripening stage for pear 348.

Additionally, the CFI system used was able to distinguish low fluorescence intensity areas on the fruit surface, apparently normal to the naked eye (**Figures 2A.1** and **3B.2, 4**). It is not yet known if these areas would be further expressed as a future scald patch with a longer cold storage.

Yet, spots of other origin, such as peel scars were also easily detected by this system, leading to false positives, if one are only concerned with scalded areas (**Figures 2A.2, C.6** and **3B.3**).

Although in a preliminary stage, the CFI system set up used in this experiment seems quite promising to be further developed as a fast and low cost device to be included as a machine vision system, to be used in on-line grading and sorting, once it shows quite accurately, several kind of surface defects. Additionally, these results also suggest that more studies are needed to explore and hopefully, confirm this method to be used as a simple, friendly-user and non-invasive prediction method to make an early diagnosis of superficial scald of 'Rocha' pear, at the sorting stage and along storage.

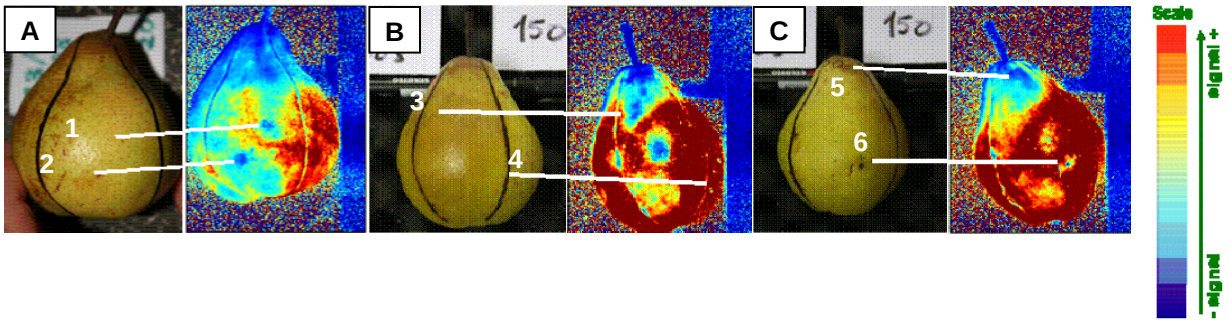

Figure 2: NA 'Rocha' pears 6 d after shifting to shelf-life. A. Non-scalded fruit (1. Starting scald patch not seen by the naked eye?). B. Scalded fruit (3. Scald patch; 4. Non-scalded peel). C. Scalded fruit (5. Scald patch; 6. Peel scar)

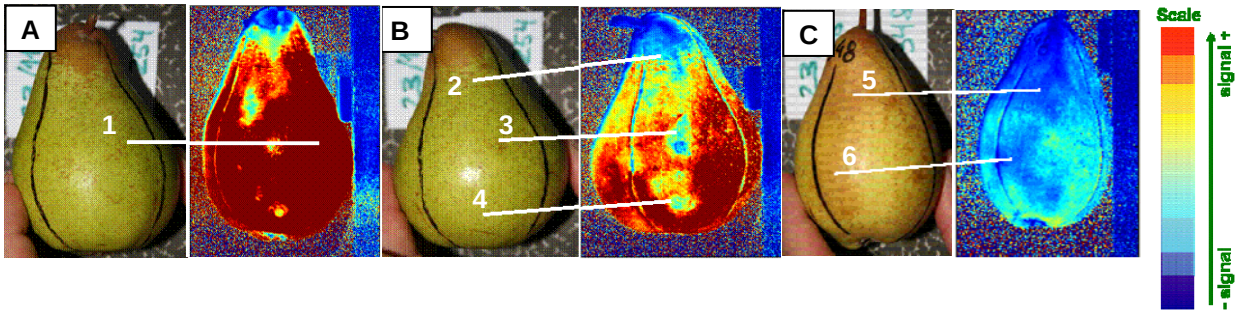

Figure 3: CA 'Rocha' pears 6 d after shifting to shelf-life. A. Non-scalded fruit (1. Normal, uniform peel to the naked eye). B. Non-scalded fruit (2. Starting scald patch not seen by the naked eye? 3. Peel scar; 4. Starting scald patch not seen by the naked eye? C. Scalded surface (5. and 6. Scald patches).

Acknowledgements

Frutoeste (Mafral, Portugal) is acknowledged for providing the pears used in this study. Ana M. Cavaco has a post-doc fellowship (SFRH/BPD/ 11613/2002) of Fundação para a Ciência e a Tecnologia.

References

CHAPON J.F., BONY P. (1997): Apples: scald control and risk prediction. Arboriculture Fruitiére, 44 (506): 37-40. apples and pears. In J. JANICK (Ed.) Horticultural Reviews 27, John Wiley & Sons, Inc., pp. 227-267

DELL J.R., PRANGE R.K., MURR D.P. (1996): Chlorophyll fluorescence of Delicious apples at harvest as a potential predictor of superficial scald development during storage. Postharvest Biol. Technol. 9 (1). 1-6

INGLE M. (2001): Physiology and biochemistry of scald in apples and pears. In J JANICK (Ed.) Horticultural Reviews 27, John Wiley & Sons, Inc., pp. 227-267

ISIDORO N., ALMEIDA D.P.F. (2006): Farnesene, conjugated trienols, and superficial scald in 'Rocha' pear as affected by 1-methylcyclopropene and diphenylamine. Postharvest Biol. Technol. 42, 49–56

MATLAB R2008b®, The MathWorks, Inc., Natick, MA, USA, 2008

SCHLÜTER O., FOERSTER J., GEYER M., KNORR D., HERPPICH W.B. (2009): Characterization of high-hydrostatic-pressure effects on fresh produce using chlorophyll fluorescence image analysis. Food Bioprocess Technol. DOI 10.1007/s11947-008-0143-1 (In Press)

SCHREIBER U., BILGER W., NEUBAUER C. (1994): Chlorophyll Fluorescence as a nonintrusive indicator for rapid assessment of in vivo photosynthesis. *In* SCHULZE, E.D. and CALDWELL, M.M., eds, Ecophysiology of photosynthesis, Springer, Berlin-Heidelberg-New York, pp 49-70

Synchrotron x-ray CT of rose peduncles – evaluation of tissue damage by radiation

Uzuki Matsushima[1], Wolfgang Graf[2,5], Simon Zabler[3], Ingo Manke[4], Martin Dawson[4], Gerard Choinka[4], Werner B. Herppich[2]

[1] *Faculty of Agriculture, Iwate University, Ueda 3-18-8, Morioka, Iwate 020-8550, Japan*
[2] *Dept. Horticultural Engineering, Leibniz-Institut für Agrartechnik Potsdam-Bornim e. V.Max-Eyth-Allee 100, 14469 Potsdam, Germany*
[3] *Department of Materials Engineering, Technical University of Berlin, Straße des 17. Juni 135, D-10623 Berlin, Germany*
[4] *Institute of Applied Materials , Helmholtz Centre Berlin, Glienicker Str. 100, 14109 Berlin, Germany*
[5] *Humboldt-Universität zu Berlin, Institut of Horticultural Science Lentzeallee 75, 14195 Berlin, Germany*
Corresponding author: uzuki@iwate-u.ac.jp

Abstract: *"Bent-neck" syndrome, an important postharvest problem of cut roses, is probably due to water supply limitations and/or the structural weakness of vascular bundles of the peduncle tissue. Synchrotron x-ray CT was used to successfully observe inner structure of the peduncles of 3 rose cultivars, indicating that this technique achieves sufficiently high spatial resolution to investigate complex tissues. However, further investigations with chlorophyll fluorescence analysis and optical microscope imagery reveal heavy damage of the irradiated regions induced by synchrotron x-rays.*

1 Introduction

"Bent neck" is an important postharvest problem for cut roses in which the upper peduncles bend prematurely just below the flower, thus destroying flower quality. This is probably due to water supply limitations and/or the structural weakness of vascular bundles of the peduncle tissue. Previous investigations of water conductivity and water status have revealed that two keys factors of bent-neck symptom are a lack of water conductivity and loss of water from the surface (GRAF *et al.* 2009, MATSUSHIMA *et al.* 2009), and our current aim is to also demonstrate a link to structural strength. Three-dimensional visual analysis would be a useful tool to observe this phenomenon and the high-resolution of the synchrotron x-ray computed tomography (CT) should allow the *in-situ* investigation of the micro-structures of rose peduncles. This method has already been applied to observe plant tissue (LEE & KIM 2008, MENDOZA *et al.* 2007), but is not yet optimized for plant samples. In this investigation, image quality and the influence of the x-ray energy on the degree of tissue damage were studied.

2 Materials and methods

Synchrotron x-ray tomography was conducted at BAM-line, BESSY (Berliner Elektronenspeicherring - Gesellschaft für Synchrotronstrahlung) in Berlin, Germany. Phase-contrast imaging was employed for its capability of measuring plant samples at high energies and with low radiation doses. Even though the density variations of plant samples are small, the shapes of tissues are clearly distinguished by the edge enhancement effect which is de to the partial coherence of the synchrotron x-rays. Roses were irradiated with monochromatic x-ray beams of different energy (30 and 40 keV) to evaluate the image quality and the degree of damage caused to the samples. Three roses (*Rosa hybrida* L.) cultivars of different bent-neck resistance (’Akito’, ’Milva’ and ’Red Giant’) were investigated *in-situ* to examine the cultivar-specific micro-structures and in order to analyze their potential differences in radiation damage susceptibility. During the experiment samples were kept in a water-filled container to prevent water losses from the surfaces of irradiated regions. **Figure 1** shows the experimental set up at BAM-line. The damage was investigated using chlorophyll fluorescence imaging simultaneously to the recording of x-rays, yielding information on the photosynthetic efficiency and integrity of plants. In particular, the factor F_v/F_m is known to be highly indicative of plant stress (HERPPICH 2001). Fresh slices of irradiated samples were subsequently investigated under an optical microscope.

Figure 1: Experimental set up at BAM-Line, BESSY. 1. Sample container filled with water to prevent drying. 2. CCD camera for chlorophyll fluorescence imaging device. 3. CCD camera for x-ray imaging located 1.1 meter downstream of the sample (phase-contrast mode).

3 Results and discussion

Synchrotron tomography clearly visualized the structure of vascular bundle elements and pith parenchyma cells of the rose peduncles (**Figure 2**), indicating that the resolution is high enough to successfully investigate complex plant tissues. Further investigations using this technique should help to clarify whether there are structural differences in vascular bundles that can be related to the occurrence and mechanisms of bent neck syndrome. Concerning image quality, there was no significant difference between x-ray energy of 30 keV and 40 keV with this experimental setup. However, heavy damage of

the irradiated regions was determined by chlorophyll fluorescence analysis and optical microscope images. **Figure 3** shows chlorophyll fluorescence images of each rose cultivar after synchrotron irradiation. The ratio F_v/F_m indicates photosynthetic activity; for the irradiated regions the value fell below 0.3, i.e. photosynthesis was no longer active for this stem part. Irradiated regions could also be easily identified with the naked eye as brown regions where the plant tissue was fragile and broke readily during slicing. **Figure 4** shows an optical microscope image of irradiated region. Color changes of cells from green to brown occurred particularly from the epidermis to the vascular bundles. The white arrow indicates a browning part in the sliced segment. Settings of energy load and duration of synchrotron x-ray irradiation will have to be optimized in further experiments to allow for a less-destructive 3-D analysis of such sensitive living biological material.

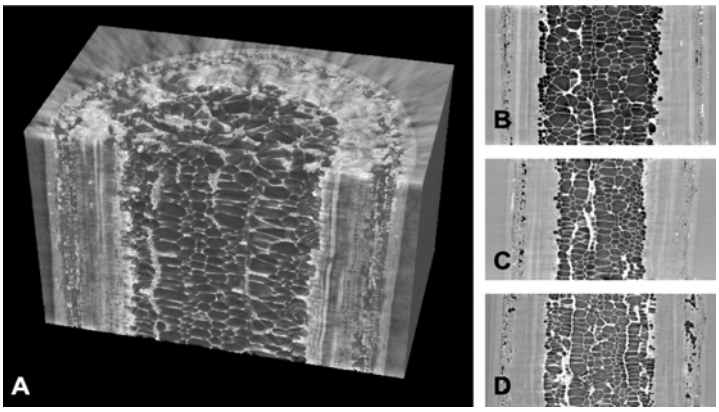

Figure 2: Synchrotron tomography images of rose peduncles. A: 3 dimensional image of 'Akito' peduncle at 40 keV. B, C: Vertical slices of Akito peduncles at 40 keV and 30 keV, respectively D: Vertical slices of 'Red Giant' peduncle at 30 keV.

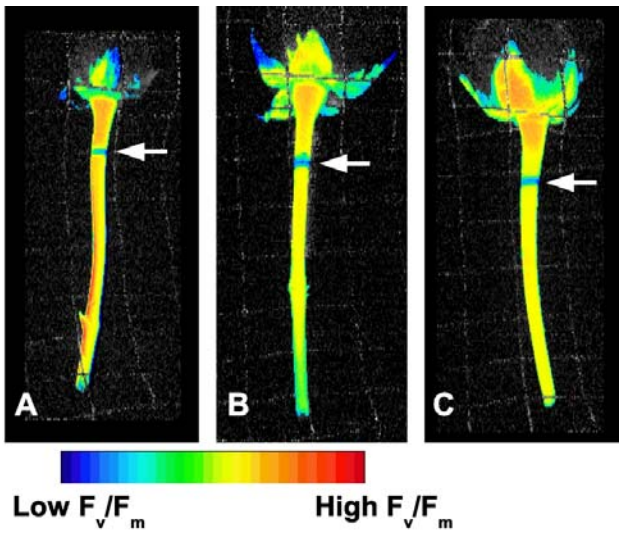

Figure 3: Chlorophyll fluorescence images of each rose cultivar after synchrotron irradiation. White arrows indicate irradiated parts. A: 'Akito', B: 'Milva', C: 'Red Giant'

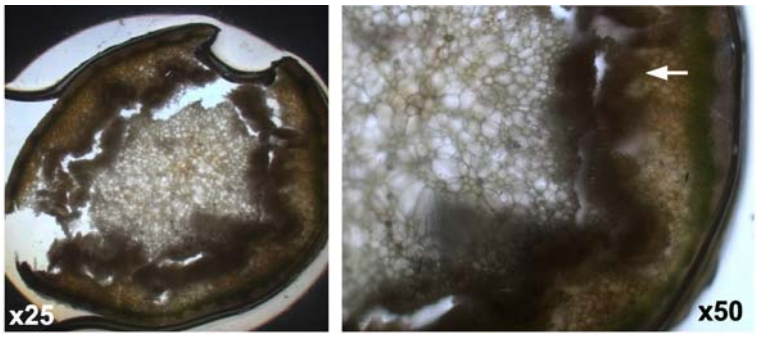

Figure 4: Optical microscope image of irradiated part. ('Red Giant')

4 Conclusions

The inner structure of rose peduncles was successfully observed using synchrotron x-ray imaging. This technique is applicable for the 3-dimensional imaging of plant material, but, when comparing structural changes of plant sample, it is necessary to take into account the effect of any damage caused by irradiation.

References

GRAF W., HERPPICH W. B., HUYSKENS-KEIL S., MATSUSHIMA U., GRÜNEBERG H. (2009): Cell wall chemistry and mechanical strength of cut roses peduncles. The book of abstract, 5th International Symposium Rose Research and Cultivation, May 24-28, 2009, Gifu: 57

MATSUSHIMA U., GRAF W., KARDJILOV N., HILGER A., NISHIZAWA T., GRÜNEBERG H., HERPPICH W.B. (2009): Water flow in cut rose peduncles - destructive and non destructive measurement methods. The book of abstract, 5th International Symposium Rose Research and Cultivation, May 24-28, 2009, Gifu : 30

LEE S.-J., KIM Y. (2008): In vivo visualization of the water-refilling process in xylem vessels using x-ray micro-imaging. Annals of Botany, 101: 595-602

MENDOZA F., PIETER V., MEBATSION H.K., KERCKHOFS G., WEVERS M., NICOLAÏ B. (2007): Three-dimensional pore space quantification of apple tissue using x-ray computed microtomography. Planta, 226: 559-570

HERPPICH W.B. (2001): 6th International Symposium on Fruit, Nut, and Vegetable Production Engineering. Chap. chapter Application, Potential of Chlorophyll Fluorescence Imaging Analysis in Horticultural Research - a mini - review 609 - 614: Institut für Agrituchnik Bornim e.V.

Image processing for the determination of jam browning kinetics

Davide Ricauda Aimonino, Lorenzo Comba, Paolo Gay

D.E.I.A.F.A. – Università degli Studi di Torino, Via Leonardo da Vinci 44, 10095 Grugliasco (TO), Italy
Corresponding author: davide.ricauda@unito.it

Abstract: *The production process of jam involves heat treatments that, in some conditions, can affect the quality of the product. In this paper the colour changes in apple and peach high quality 'Extra Jam' due to heat treatment were investigated using colour image processing techniques. Colour analysis was carried out measuring CIELAB parameters and evaluating the colour difference (ΔE) on the pictures acquired by a professional scanner. These data were compared with the colour coordinates obtained by a colorimeter. Two thermal treatments, 80°C and 90°C, were considered. Colour deterioration was described by a colour difference profile and then modelled by a first order kinetic. Image analysis technique provided more consistent data than colorimeter, resulting a very helpful tool for colour measurement on heterogeneous media as 'Extra Jams'.*

1 Introduction

In 'Extra jam' production processes quality alterations are a noticeable problem because can cause a significant number of rejected lots. During the process, jam undergoes to several thermal treatments that modify its physical and sensorial properties. Prolonging these treatments beyond the optimal levels can compromise the overall quality of the product, making it unpleasant to the consumers even if the bioactive compounds may not have been affected. This condition can be caused by machinery breakdowns, anomalies in the plant or wrong set up of plant parameters. Colour changes are the most evident effect of an excessive heating.

Browning kinetics due to thermal treatments were already studied for the case of the concentration of fruit purees (LOZANO & IBARZ 1997, GARZA *et al.* 1999, IBARZ *et al.* 2000). Unfortunately only few data can be found on the behaviour of jam, when subjected to post-concentration thermal treatments. Concentrated product, in fact, undergoes to heating processes during bottling a final pasteurisation, which can activate further browning mechanisms.

Aim of this preliminary work is to evaluate and identify browning kinetics, due to thermal treatments, in 'Extra jams' by means of colour analysis, comparing image processing

and traditional colorimetric techniques. The knowledge of these kinetics can help manufactures to improve products quality looking for the best trade off between technological requirements (e.g. process times and temperatures profiles, logistics), essential into the production processes, and organoleptic characteristics of final product.

2 Materials and methods

High quality peach and apple 'Extra jams' were brought in the firm (Agrimontana s.p.a.), immediately after the concentration phase during a standard production cycle. Samples, about 10 kg for each kind of jam, were water-cooled and stored at +4°C until they are used for the experimentation.

Thermal treatment of jams was carried out in glass flask (25 mm diameter x 150 mm high), sealed with a tin foil and a rubber band, dipped into two thermostatic baths at the temperature of 80°C and 90°C, with treatment times up to 420 minutes (7 hours). After the target temperature of the jam bulk was achieved, three flasks were extracted from each bath and immediately cooled in a melting ice bath to stop browning reactions. This procedure is repeated every 30 minutes, in the first two hours, and then every hours.

Colour analysis

Colour measurement was carried out with two different techniques: by colour image analysis of the pictures acquired by a professional scanner (Microtek ScanMaker i900) and by colorimeter (Konica Minolta CR-400). The results obtained by the two techniques were compared. In both cases jam samples (not treated sample, 80°C and 90°C) were putted in a white polyethylene (PE) template consisting of a grid of 3x5 holes of 50 mm diameter and 10 mm thick. Images acquisition with scanner was performed arranging the template over a borosilicate glass plate placed on scanner glass. To ensure a homogeneous background, a white PE plate (10 mm thick) was then placed over the template filled with jam samples. Finally, a black box covered the entire system as shown in **Figure 1**. A picture of each template hole containing jam was acquired at 600 dpi resolution.

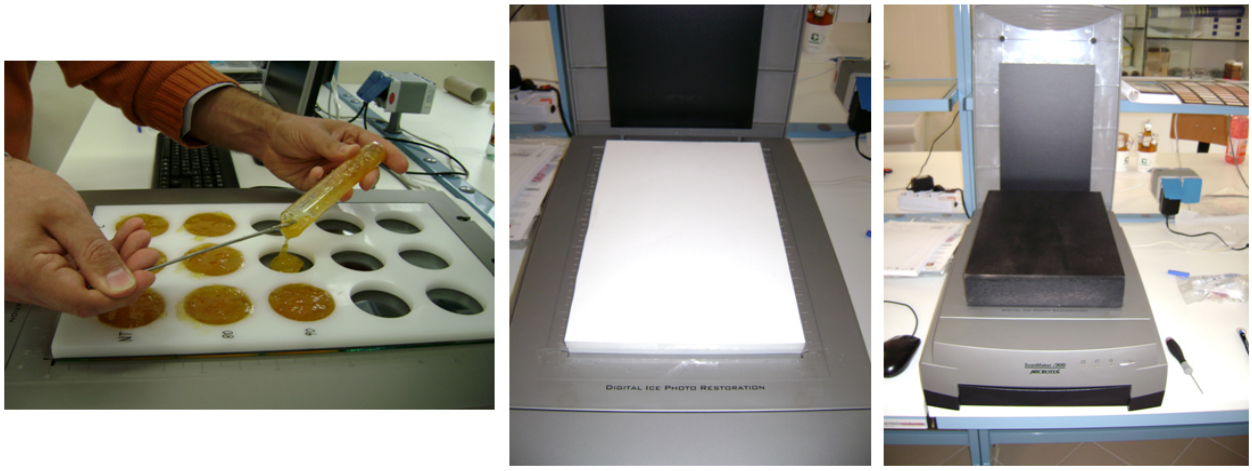

Figure 1: Template filling with jam samples (left), white PE-plate placed over the template (centre) and the black box that covers the system (right)

CIELAB (L*,a*,b*) colour space was considered to evaluate the colour change in jam following the heat treatment. In particular, lightness (L*) and colour difference (ΔE) parameters were used to describe browning kinetics. Colour co-ordinates of each sample were determined by Adobe Photoshop® platform, following a procedure similar to the one described in YAM & PAPADAKIS (2004). Colour parameters were measured inside of an entire hole of the template using a circular mask and the software Histogram Window. Colorimeter (D75 light source and 10°observer) measurements were performed putting the same borosilicate glass plate on the template filled with jam samples. Five measurements for each hole were carried out avoiding the regions with air bubbles.

3 Results

Colour measurement by image processing resulted to be a very fast, functional and reliable technique for jam samples analysis because the whole sample surface is analyzed at the same time. In this case, obtained colour coordinates (L*, a*, b*) are averaged on the set all pixels included within of the circular mask, whereas the sampling area of a colorimeter is in the order of few ten square millimetres. Extra Jam is typically not homogeneous and is characterized by the presence of fruit peaces and gel with different colours. Therefore the measurements with colorimeter leaded to less consistent data.

Colour difference (ΔE) is extensively used to characterize colour changes in foods. For this reason only its behaviour and modelling will be discussed in this work, even if other colour parameters (such as L*, a*, b*, hue and saturation) were be considered during the study.

Colour difference increases with time and treatment temperature as reported in **Figure 2**. Apple jam appears to be more sensitive to heating than peach jam with a grater increase of ΔE during the heating.

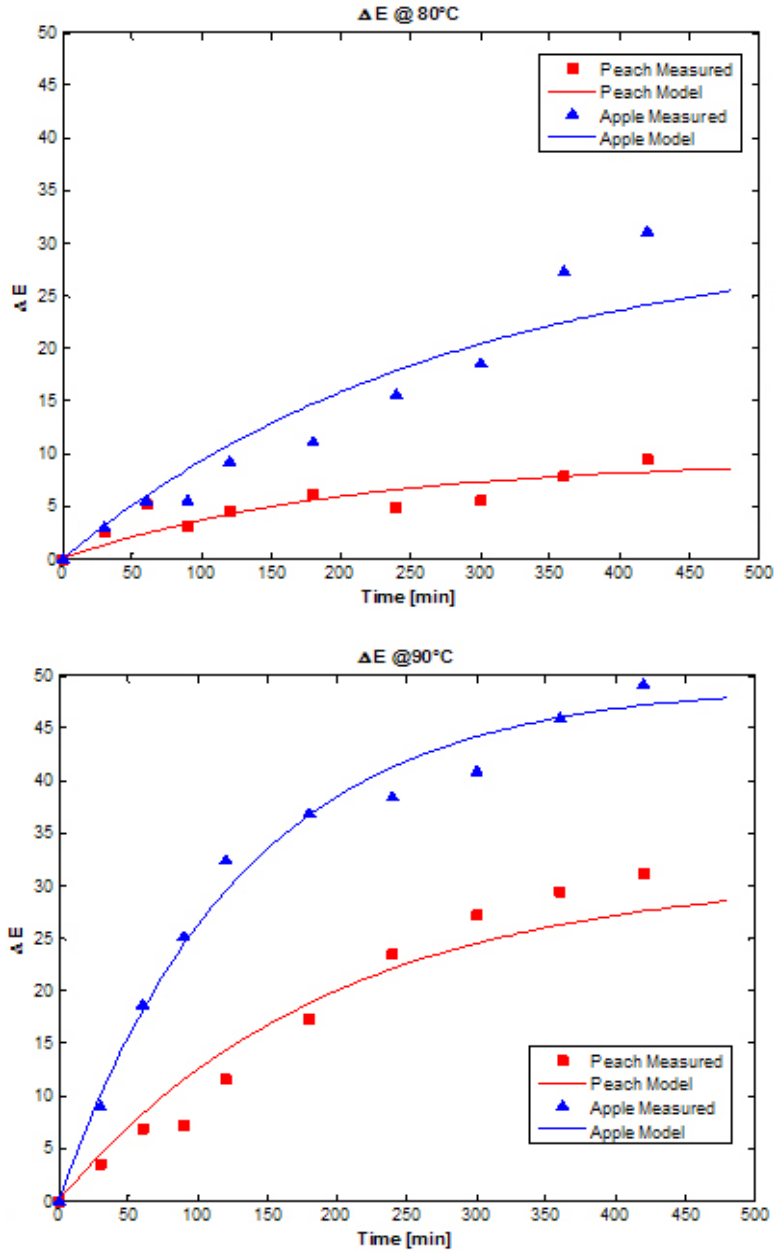

Figure 2: Change in colour difference (ΔE) during heating for peach and apple jams at 80°C (on left) and 90°C (on right)

A first order kinetic model was considered to describe the behaviour of ΔE as function of treatment time. Experimental data were fitted to the following exponential equation

$$\Delta E = \Delta E_{\infty} \left(1 - e^{-k_{\Delta E} \cdot t}\right) \quad (1)$$

where $k_{\Delta E}$ is the time constant (min^{-1}), t is the heating time whereas ΔE_{∞} is the maximum colour difference value reached during the treatment according to LOZANO & IBARZ (1997) and Ibarz (IBARZ *et al.* 2000). Model parameters were determined applying a non-linear regression to equation 1 using SPSS statistical software; the obtained time

constants ($k_{\Delta E}$) and the non-linear regression coefficient are summarised in **Table 1** for each kind of jam and temperature level.

Table 1: Kinetic model parameters and non-linear regression coefficient for ΔE at the different temperatures (80°C and 90°C)

Jam	Temperature [°C]	ΔE∞	$k_{\Delta E}$ [min^{-1}]	R^2
Apple	80	31,05	0,00358	0,891
	90	49,17	0,00764	0,986
Peach	80	9,39	0,00503	0,726
	90	31,18	0,00515	0,946

As can be noted, a first order kinetic model well fit with experimental data obtained during the treatment at 90°C for both jams, whereas the regression coefficient resulted significantly lower in the case of heating at 80°C, in particular for peach jam. The lower consistency of the model for the thermal treatment at 80°C can be explained observing the presence of a latency phase which cannot be described by the adopted model 1.

4 Conclusions

Colour image analysis resulted to be a reliable and suitable technique for measuring colour differences in the case of heterogeneous media such as jam. Furthermore, image processing might be directly employed as on line monitoring technique within jam production processes.

This preliminary work showed that jam browning kinetics can be described by ΔE parameter with first order model. This model resulted to well fit analytical data for the highest temperature values (90°C), whereas others kinetic models have to be considered for 80°C due to the presence of a latency phase in which negligible colour changes occur. Other temperature levels of thermal treatments will have to investigate in order to obtain a complete time-temperature kinetic as well as different models to better describe the behaviour at lowest temperatures.

Acknowledgements

Authors would like to thanks Andrea Perciballi for his work during his graduation thesis; dr. Alessandro Occelli and Agrimontana s.p.a. for the collaboration.

References

GARZA S. IBARZ A., PAGÀN J., GINER J. (1999): Non-enzymatic browning in peach puree during heating, Food Research International, 32 (1): 335-343

IBARZ A., PAGÀN J., GARZA S. (2000): Kinetics models of non-enzymatic browning in apple puree, Journal of the Science of Food and Agriculture, 80 (1): 1162-1168

LOZANO J.E., IBARZ A. (1997): Colour changes in concentrated fruit pulp during heating at high temperatures, Journal of Food Engineering, 31(1): 365-373

YAM K.L., PAPADAKIS, S.E. (2004): A simple digital imaging method for measuring and analyzing color of food surfaces, Journal of Food Engineering, 61(1): 137-142

Detection of weeds using image processing and clustering

Martin Weis, Roland Gerhards

Department of Weed Science, University of Hohenheim, Otto-Sander-Straße 5, 70599 Stuttgart, Germany
Corresponding author: Martin.Weis@uni-hohenheim.de

Abstract: *Knowledge about the distribution of weeds in the field is a prerequisite for site-specific treatment. Optical sensors make it possible to detect varying weed densities and species, which can be mapped using GPS data. The weeds are extracted from images using image processing and described by shape features. A classification based on the features reveals the type and number of weeds per image. For the classification only a maximum of 16 features out of the 81 computed ones are used. Features are used, which enable an optimal distinction of the weed classes. The selection can be done using data mining algorithms, which rate the discriminance of the features of prototypes. If no prototypes are available, clustering algorithms can be used to automatically generate clusters. In a next step weed classes can be assigned to the clusters. Such a procedure aids to select prototypes, which is done manually. Classes can be identified, that are distinct in the feature space or which are overlapping and therefore not well separable. Clustering can be used in some, less complex cases to establish an automatic procedure for the classification. Weed maps are generated using the system. These are compared to the results of a manual weed sampling.*

1 Introduction

The goal of site-specific weed control is the precise application of herbicides in highly infested areas of a field. Since the distribution of weeds is heterogeneous in most cases and stable across years (GERHARDS *et al.* 1997, MORTENSEN *et al.* 1998, GERHARDS & CHRISTENSEN 2003), site-specific weed control can reduce the amount of herbicides used. The spraying has to be controlled by the actual weed infestation. This way the selection and dosage of the herbicides can be optimized for each part of the field. In areas where the weed infestation is below the economic threshold no herbicides are used, in areas with a weed infestation above the threshold different herbicides in be used in varying dosages, adapted to the weed species. The first step therefore is to get information about the distribution of the different species. Manual weed sampling is time- and cost-intensive and therefore cannot be economic in a wider practice. SLAUGHTER *et al.* (2008) give an overview of the techniques for weed detection and find, that the robust weed detection remains the primary obstacle toward commercial develop-

ment and industry acceptance of robotic weed control technology. Therefore a system was developed to measure the weed infestation.

2 Material and methods

To achieve an automatic classification of weeds from images a system was used, which is outlined in **Figure 1**. In the field two images were taken at the same time: one of the red (R), the other of the infrared (IR) spectrum of the light. Additionally the position was determined using an RTK-GPS. Both images are normalized and a difference image computed (IR-R). In this image the plants appear brighter than the background objects like soil, stones, mulch (SÖKEFELD *et al.* 2007). The background objects vanish in the difference image, because have a similar reflection in thr red and infrared spectrum.

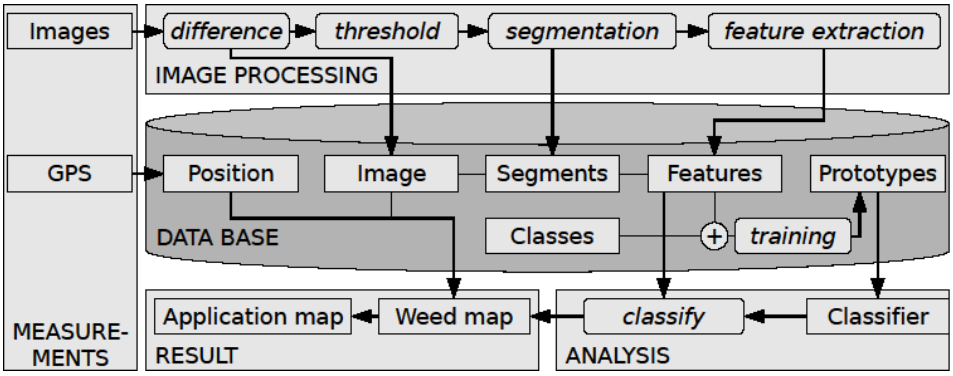

Figure 1: Schematic overview of the image processing

The difference image was analysed using digital image processing and the results are stored in a database (**Figure 1**). The first step is the binarisation with a grey level threshold that segments the foreground objects (white) from the background (black). A segmentation step identifies single foreground objects as objects, which are surrounded by background. Noise can be suppressed in this step, if small regions are filtered out with a size criterion. For the remaining objects features are computed, which characterise the shape of the plants. Geometric features are based on the object pixels, contour features, which are derived from the border pixels (fourier descriptors, curvature), and features based on the skeleton of the regions were computed. Size, compactness and Hu moments (HU 1962) are typical examples for the group of geometric features. The skeletonization was combined with a distance transformation of the regions and lead to a distance vector. Statistical measures from this vector describe then the thickness of the segments. With this step the image processing was complete and the features were used for the following analysis.

In the database all information of the measurement and image processing was stored. The positional information and other metadata (time, camera type, exposure time) are stored together with the file path in the database. During the segmentation step segments were created and their origin (image, image processing parameters), file path and the features were stored in the database. Each segment corresponds to a plant or parts thereof.

The following analysis is based on the values in the database. Prototypes have to be defined for the analysis and a classifier can be trained with this prototype information. Classes were defined within the database, which consist of three parts: the first is the EPPO code (EPPO 2007) denoting the species, the second the BBCH code (HESS *et al.* 1997) denoting the phenological growth stage and the third is an attribute which describes special cases that may occur due to the segmentation, e.g. single leaves or overlapping. In the training step defined classes are related to the segments, these are then prototypes with known class. This step has to be done manually by sighting the segments and assigning a class to selected segments. The training data then resides in the database and forms the training data set together with the features, which is used to train a classifier. The trained classifier then assigns all segments to classes. Together with the positional information the classification result can be assemled to weed distribution maps. The weed distribution maps are used to create application maps, which are used for the site-specific herbicide treatment. Different weed species, which are sensitive to the same herbicides, are grouped for the application map and economic thresholds are used to define the areas which have to be sprayed.

2.1 Feature selection

Not all features have the same relevance for the classification. Each feature adds a dimension to the feature space, which is high dimensional. In our system up to 81 features were computed, which are all numerical. Therefore the prototypes were located in a 81-dimensional feature space and it was necessary to reduce the number of dimensions. A feature selection or feature transformation can be used for this task. Selection algorithms weight features according to their discriminational abilities and select the ones that allow the best discrimination of the classes. The maximum number of features should not exceed 16 and the prototypes were used to select them. Selection algorithms can be grouped into two groups. One group uses the discriminative abilities of each feature or correlations of features to select the best ones. PCA weighting is one example, which uses the coefficients of a principal component analysis to weight the features. The other group of selection algorithms uses classification algorithms. Feature subsets are selected and the performance of a classifier, which uses only these subsets, is used.

Two different algorithms for a weighted selection were used, which are implemented in the data mining program RAPIDMINER (MIERSWA *et al.* 2006). The selection process

consisted of a weighting using PCA weighting and info gain weighting with a following selection, that recursively did a (crossvalidated) nearest neighbor classification. The performance of the classification und therefore the feature subset was rated and feature subsets could be identified, which are optimized for the dicrimination of the classes.

2.2 Clustering

A supervised classifier that uses the training data of the prototypes is used to assign classes to the objects. Unsupervised classification algorithms, also known as clustering, can be used, if no training data exists. These kind of classifiers were used before class information was available and before the manual selection of prototypes has taken place. These algorithms aggregate similar objects to clusters according to the feature information. In this context clustering is interesting in two ways: they can be used to support the training and they show similarities or differences between classes, giving hints on the seperability. Clustering was used here to group plants with similar shapes. In a second step classes can be set for these automatically derived clusters and prototypes can be selected. The advantage of the approach is, that classes with similar features can be identified. The training for classes which are difficult to separate can be optimized this way. If class has a multimodal distribution in the feature space, leading to two or more clusters (see clusters 0, 1 and 2 in **Figure 4**), then an additional classes may be defined. The same applies, if there are still noise objects left: a noise class can be used for them. The resulting prototype definitions are used for the classification.

2.3 Data set

The data for the clustering was derived from images taken in December 2007. The field had a size of 3.5 ha with a winter wheat (*Triticum aestivum* L.) crop. The crop was not emerged at that time and the weeds were grass weeds (mainly *Alopecurus myosuroides* Huds.) and dicotyledon weeds (*Veronica persica* L., *Matricaria chamomilla* L.). The image series contains of 3367 images and their DGPS-coordinates. 160 images were selected from the series, which were near manual sampling points, and used for the training. The number of weeds, separated for each species, were counted manually from the images and compared to the results of the image classification. Additionally a manual field sampling was done using a frame to count the weed densities for each species. The position of the images and manual sampling points are not exactly the same, but differ up to two meters.

A map was created from the results of the supervised and unsupervised classification and the manual sampling. It can be seen that the weed patches can be found with each of the methods (**Figure 2**).

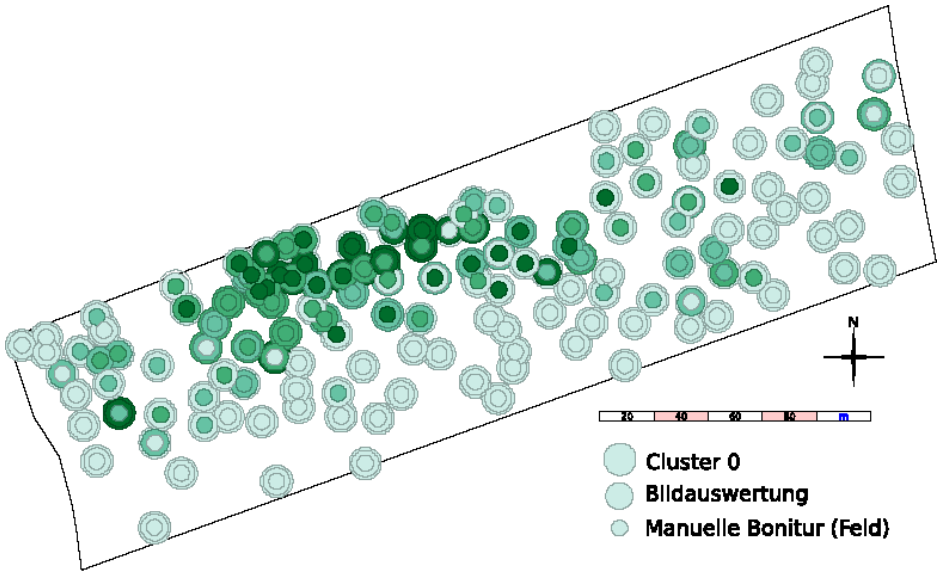

Figure 2: Map of the weed densities using different measurements: outer rings contain results of unsupervised classification (Cluster 0), middle ring shows the supervised classification using prototypes, inner circle manual sampling results

3 Results and discussion

The images were analysed following the schema from **Figure 1**, additionally there was the data of manual measurements from the images. The weeds were counted from the subset of the images, they were also used to select the prototypes. The result of the clustering can be compared to the training data. The clusters and object classes can be visualised in the feature space using three features. **Figure 3** shows the trainingdata of the prototypes on the left and the result of the clustering on the right (clusters numbered from zero to four).

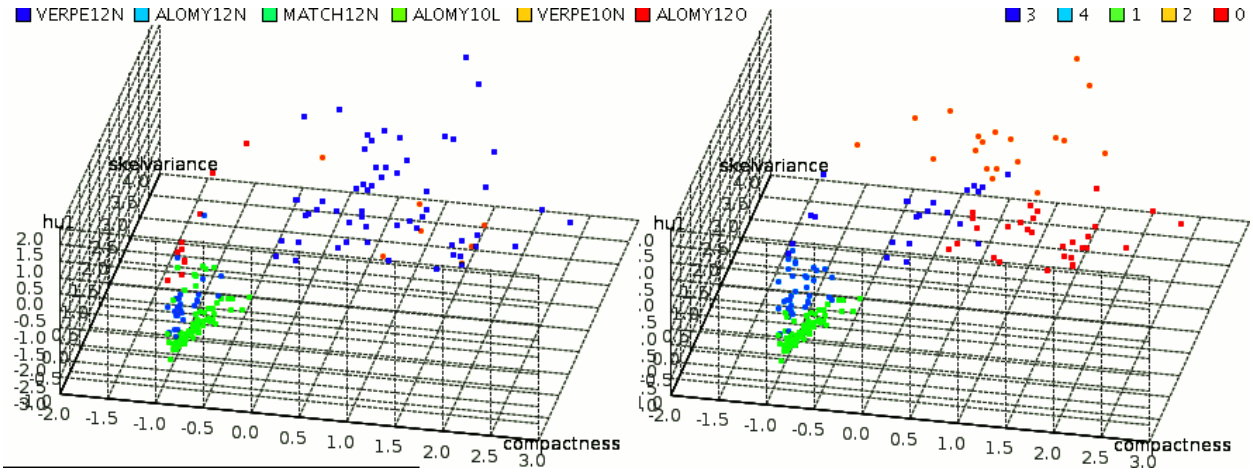

Figure 3: Classes (manually selected prototypes) and clusters (unsupervised classification) in the feature space. The features are compactness, variance of the skeleton distance vector and the first Hu moment

The segments were labeled with colors according to the clusters and combined to label images. The combination of these with the (inverted) difference images is shown in **Figure 4**. Dicotyledon weeds can be found in cluster four, the monocotyledons are in cluster zero to three. The unsupervised classification can distinguish between these important weed classes. By assigning classes to the clusters the training step can be simplified, prototypes can be marked as belonging to that class. This way an efficient training is possible. It can also be seen, that the monocotyledon weeds have a multimodal distribution (single, elongated leaves, overlapped leaves). This can be taken into account in the class definitions for the prototypes, this class can be separated into two subclasses.

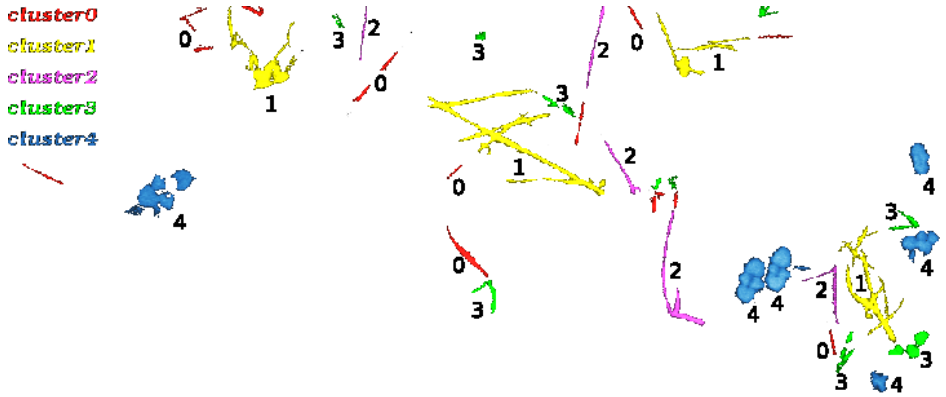

Figure 4: Cluster assignments in an example image, cluster 4 contains dicotyledonous, cluster 0-3 monocotyledonous weeds

Figure 5 relates the manual class assignments for *Alopecurus myosuroides* Huds. to cluster zero. There were some images without objects in the cluster (points on the ordinate), but in most of the images the numbers show the same tendency as the manually determined ones.

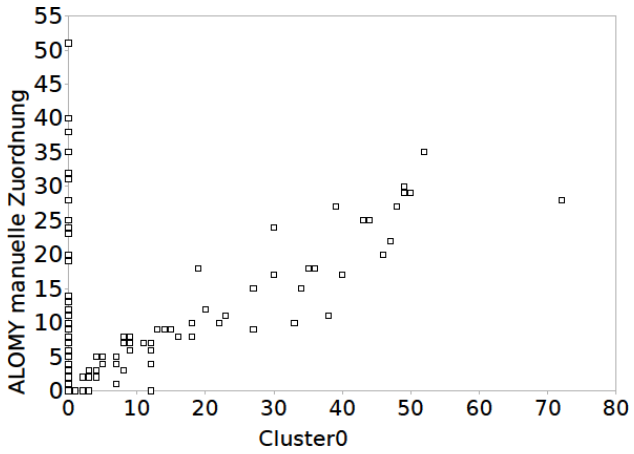

Figure 5: Correlation of the manual class assignments (ALOMY: *Alopecurus myosuroides* Huds.) and cluster zero of the unsupervised classification (clustering)

4 Conclusions

Weed sampling from camera images, as described in this approach, can be used to generate weed maps with high spatial density, which are necessary for a site-specific weed management. The approach uses bi-spectral images, which allow a good separation between plants and background. The analysis is based on the shape of single plants, which are parametrised using shape features. Supervised classifiers need training data, which are selected prototypes of weed and crop plants. The selection of the prototypes can be supported by unsupervised classification (clustering) by assigning classes to automatically derived clusters. This way the separability of the classes according to the shape features can be visually assessed already in the training step and the classes and training data can be adjusted to the situation.

Unsupervised classification could be used to establish a fully automatic approach, if prior information about the weed species are introduced as starting values for the clustering.

References

EPPO (2007): Harmonized classification and coding of the uses of plant protection products. *EPPO Bulletin*, 37(1):25–28, doi: 10.1111/j.1365-2338.2007.01069.x. European and Mediterranean Plant Protection Organization.

GERHARDS R., CHRISTENSEN S. (2003): Real-time weed detection, decision making and patch spraying in maize (zea mays l.), sugarbeet (beta vulgaris l.), winter wheat (triticum aestivum l.) and winter barley (hordeum vulgare l.). *Weed Research*, 43:1–8

GERHARDS R., WYSE-PESTER D.Y., MORTENSEN D.A., JOHNSON G.A. (1997): Characterizing spatial stability of weed populations using interpolated maps. *Weed Science*, 45:108–119

HESS M., BARRALIS G., BLEIHOLDER H., BUHR L., EGGERS TH., HACK H., STAUSS R. (1997): Use of the extended bbch scale - general for the descriptions of the growth stages of mono- and dicotyledonous weed species. *Weed Research*, 37:433–441

HU M.K. (1962): Visual pattern recognition by moment invariants. *IRE Transactions Information Theory*, 8(2):179–187, ISSN 0018-9448. URL http://ieeexplore.ieee.org/xpl/abs_free.jsp%3 FarNumber=1057692

MIERSWA I., WURST M., KLINKENBERG R., SCHOLZ M., EULER T. (2006): Yale: Rapid prototyping for complex data mining tasks. In Lyle Ungar, Mark Craven, Dimitrios Gunopulos, and Tina Eliassi-Rad, editors, *KDD '06: Proceedings of the 12th ACM SIGKDD international conference on Knowledge discovery and data mining*, pages 935–940, New York, NY, USA, ACM. ISBN 1-59593-339-5. doi: http://doi.acm.org/10.1145/1150402.1150531. URL http://rapid-i.com/ component/option,com_docman/task,doc_download/gid,25/Itemid,62/

MORTENSEN D.A., DIELEMAN J.A., JOHNSON G.A. (1998): Weed spatial variation and weed management. In J. L. Hatfield, D. D. Buhler, and B. A. Steward, editors, *Integrated weed and soil management*, pages 293–309, Chelsea, MI, USA, Ann Arbour Press

SLAUGHTER D.C., GILES D.K., DOWNEY D. (2008): Autonomous robotic weed control systems: A review. *Comput. Electron. Agric.*, 61(1):63–78, ISSN 0168-1699. doi: http: //dx.doi.org/10.1016/j.compag.2007.05.008

SÖKEFELD M., GERHARDS R., OEBEL H., THERBURG R.-D. (2007): Image acquisition for weed detection and identification by digital image analysis. In J.V. Stafford, editor, *Precision agriculture '07*, volume 6, pages 523–529, The Netherlands, 6th European Conference on Precision Agriculture (ECPA), Wageningen Academic Publishers. ISBN 978-90-8686-024-1

Correlation between vegetation indices and nitrogen leaf content and dry matter production in *Brachiaria decumbens*

Mario Cupertino da Silva Júnior[1], Francisco de Assis de Carvalho Pinto[2], Daniel Marçal de Queiroz[3], Enrique Anastácio Alves[4], Luis Manuel Navas Gracia[5], Jaime Gomez Gil[6]

[1] Graduate student, Universidade Federal de Viçosa (UFV) / Universidad de Valladolid (UVa), Agriculture Engineering (UFV)/ DTSCI y Telemática (UVa) Valladolid, Spain
[2] Researcher, PhD, Universidade Federal de Viçosa (UFV), Agriculture Engineering Viçosa, Brazil
[3] Researcher, PhD, Universidade Federal de Viçosa (UFV), Agriculture Engineering Viçosa, Brazil
[4] Graduate student, Universidade Federal de Viçosa (UFV), Agriculture Engineering Viçosa, Brazil.
[5] Researcher, PhD, Universidad de Valladolid (UVa), Departamento de Ingeniería Agrícola y Forestal,Palencia – Spain
[6] Researcher, PhD, Universidad de Valladolid (UVa), DTSCI y Telemática,Valladolid – Spain
Corresponding author: cupertinojunior@yahoo.com.br

Abstract: *The goal of the present work was to evaluate the correlation between vegetation indices and nitrogen (N) Leaf content values, and also with dry matter production in Brachiaria decumbens forage at different periods after fertilization. The treatments consisted of five nitrogen rates (0, 50, 100, 150 e 200 kg ha^{-1}), with six replications, evaluate in a completely randomized design. A system composed of two digital cameras, cables, framegrabber and microcomputer was used, with a metal framework of three meters above ground for camera positioning. The system acquired images in two spectral bands, simultaneously, in two phases. In the first phase, accomplished during the period of February to March 2006, the images were acquired at 15, 21 and 32 days after fertilization. In the second phase, accomplished during the period March-May 2006, the images were acquired at 28, 36, 45 and 53 days after the reapplication of the same nitrogen rates. From the original images were determined different vegetation indices, which were submitted to correlation analyses. The correlation values between vegetation indices and N leaf content obtained in laboratory ranged from 0.63 to 0.83 in the first studied phase and from 0.64 to 0.75 in the second phase. The correlation values between vegetation indices and values of dry matter production in the first phase ranged from 0.62 to 0.66 and those in the second study phase from 0.72 to 0.75. The correlation values between all vegetation indices and the tested variables tended to decrease with the days after fertilization. The best index was GNDVI.*

1 Introduction

Managing the nitrogen (N) input in pasture fields can outcome higher yields without polluting the groundwater. A reasoning crop nitrogen management also can decrease the fertilization costs. However, for a correct N input decision, one needs its either determination or determination accurately.

Some research studies have proposed ways to identify the nutritional status related with nitrogen in many crops. Most of those researches have been using the crop spectral response as indicator of N status.

Chlorophyll portable meters estimate the chlorophyll level present in the plant, being this value proportional to the nitrogen content. This method demands physical contact with individual leaf, what is time demanding for using in the context of site specific management.

Others promissory methods are the remote sensing techniques that also acquire spectral information of the plant pigments through sensors, but without physical contact with the plants, using the crop reflectance. The crop reflectance can be evaluated by radiometers, orbital, aerial and terrestrial images. It is believed that with the digital cameras popularization the use of these cameras to measure crop reflectance can turn one of the most economic viable methods (SENA JÚNIOR 2005).

Studies of remote sensing applications in agriculture have used vegetation indices to evaluate the crop reflectance. These indices are used to enhance the vegetation features and also decrease soil, atmospheric and angled effects (EPIPHÂNIO *et al.* 1996).

The goal of this present work was evaluate the correlation among vegetation indices and nitrogen leaf content evaluated in laboratory and also with the dry matter yield in different periods after the fertilization in *Brachiaria decumbens* forage.

2 Material and methods

This study was conducted in an established pasture field with *Brachiaria decumbens* of the Animal Science Department of the Federal University of Viçosa, in Viçosa- MG, Brazil. The project was executed in the period of January to May of 2006.

In the beginning of January was realized the delimitation of the study fields and the soil sampling. The pasture was cut to standardize the plants at a height of 10 cm. Then, 30 plots of 3 x 3 meters which received the treatments were established.

The treatments was arranged in a completely randomized design, consisted of five nitrogen rates (0, 50, 100, 150 e 200 kg ha^{-1}), with six replications. The nitrogen was applied in the form of urea. Before the nitrogen application, based on the soil chemical and physical analyses, and as recommended by CANTARUTTI *et al.* (1999), single superphosphate rate of 50 kg ha^{-1} was uniformly applied to all plots.

After the nitrogen fertilization, began the first study phase acquiring the digital images by two cameras, model STH-DCSG-VAR/-C stereo head by Videre Design Company (California, EUA), mounted in a three meters metallic support. One camera was monochrome and was attached with a near infrared (NIR) longpass optical filter of 695 nm to 1050 nm of wavelength and the other camera was a color (RGB) camera.

The lens was a C-mount with a focus distance of 2,8 mm. The images were saved in the BMP format with 480(V) x 640(H) pixels using the software SRI's Small Vision System (SVS) supplied by the camera maker. The sensor of the cameras that formed the images was the CMOS MT9V022 in the 1/3" format. Each image represented an area of 3.18 x 4.87 m with a spatial resolution about 7 mm. pixel^{-1}. Thus, the whole 3 x 3 m plot was placed on each image.

The images were acquired between noon and 2:00 PM in clear sky conditions. Assuming that the illumination was kept constant during the image acquisition, the pixel value was due to only the spectral properties of the target.

An image block of 240 x 240 pixels was used to represent each research plot. Instead of using of the original pixel values, vegetation indexes were used to highlight the information with respect to the nutritional status of the plants and attenuate the influence of the natural illumination variation in the image. It was assumed that the crop reflectance was equal to the average of the image block pixels.

The image processing was accomplished using the software Matlab (The MathWorks, EUA) version 6.5, with the digital image processing toolbox. The studied indexes were NDVI (normalized difference vegetation index), GNDVI (green normalized difference vegetation index) and SAVI (soil adjust vegetation index) according to the equations 1, 2 and 3.

$$NDVI = \frac{IV - Vm}{IV + Vm} \tag{1}$$

$$GNDVI = \frac{IV - Vd}{IV + Vd} \tag{2}$$

$$SAVI = \frac{IV - Vm}{IV + Vm + L}(1 + L) \tag{3}$$

Being that,

Vm - pixel value in the red band;
IV - pixel value in the near infrared band;
Vd - pixel value in the green band;
L - adjust coefficient;
NDVI - normalized difference vegetation index;
GNDVI - green normalized difference vegetation index; and
SAVI - soil adjust vegetation index.

The “L” coefficient value was assumed 0.5, that is the value used for vegetation with intermediate density and, according HUETE (1988), this value minimizes the influence of background soil for a large variation of leaf area indices.

Besides the images, leaves were collected to analyze the N leaf content at 15, 21 and 32 days after the fertilization (DAF). The N leaf content was measure by 30 different leaves collected along of each plot and the chosen leaves were the newest completely expanded. These leaves were packed in paper bags to determinate the N content in the laboratory.

At 32 DAF, 1 m^2 in each plot was cut to 20 cm of height and weighted. A sample of 300 to 500 grams was placed in paper bags, weighted and left in an oven at 65°C for 72 hours for moisture content and dry matter yield determination.

The non harvested area was also cut to 20 cm height and a second experimental phase was initiated on March 28, 2006 when the same nitrogenous treatments were applied with a 60 kg ha^{-1} concentration of potassium chloride.

During the second phase, the digital images and the leaves to analyze the N leaf content were acquired at 28, 36, 45 e 53 DAF. At 53 DAF, the plants were once again cut to measure the dry matter yield, using the same procedure as the first phase.

Irrigation was not necessary during the experimental periods because of adequate rainfall and weed was controlled manually in all sections whenever needed.

The acquired data were submitted to correlation analysis.

3 Results and discussion

The correlation values among vegetation indices (NDVI, GNDVI and SAVI) and N leaf content and the dry matter (DM) are presented in **Tables 1** and **2** for the first and second experimental phases, respectively. All correlation values were significant at 1% of probability by the t-test.

Table 1: Correlation among vegetation indices and N leaf content and dry matter (DM) at 15, 21 and 32 days after fertilization (DAF) on the first experimental phase.

INDICES	15 DAA	21 DAA	32 DAA	
	N leaf content	N leaf content	N leaf content	DM
NDVI	0,74**	0,81**	0,63**	0,62**
GNDVI	0,76**	0,83**	0,66**	0,66**
SAVI	0,74**	0,81**	0,63**	0,62**

** Significant correlation at 1% of probability; NDVI: normalized difference vegetation index; GNDVI: green normalized difference vegetation index; SAVI: soil adjust vegetation index; N Leaf Content: analyze of nitrogen leaf content; DM: dry matter produced in ton ha^{-1}.

Table 2: Correlation among vegetation indices and N leaf content and dry matter (DM) at 28, 36, 45 and 53 days after fertilization (DAF) on the second experimental phase.

INDICES	28 DAA	36 DAA	45 DAA	53 DAA	
	N leaf content	N leaf content	N leaf content	N leaf content	DM
NDVI	0,74**	0,64**	0,64**	0,59**	0,72**
GNDVI	0,75**	0,65**	0,68**	0,62**	0,75**
SAVI	0,74**	0,64**	0,64**	0,59**	0,72**

** Significant correlation at 1% of probability; NDVI: normalized difference vegetation index; GNDVI: green normalized difference vegetation index; SAVI: soil adjust vegetation index; N Leaf Content: analyze of nitrogen leaf content; DM: dry matter produced in ton ha^{-1}.

The correlation among indices, N leaf content and DM tended to decrease with the progress of the days after fertilization. This was due to the increasing in the number of the leaves, yielding into saturation of the indices values. This fact also was observed by MENESES & MADEIRA NETO (2001), in a study of spectral comportment of plants.

Other important fact to observe when comparing **Table 1** to **Table 2** was that the correlation values decreased from phase 1 to 2. This decreasing of the linear relationship between those variables was probable due to the temperature and luminosity reduction observed in the second phase, which propitiated less response of the plants to nitrogen fertilization.

The highest correlation values with leaf N content and DM were obtained with the GNDVI index in all data acquisition periods and both experimental phases. This result was also obtained by GITELSON *et al.* (1996), where the authors verified that GNDVI was more sensible than NDVI to identify different concentration rates of chlorophyll, which is highly correlated at nitrogen, in two species of plants.

The NDVI and SAVI indices presented correlation values similar in all periods and phases studied. These indices have the same spectral band relation; however the SAVI has the L constant multiplied in the equation that, according HUETE (1998) assist to reduce the soil reflectance influence. Since the soil was totally covered by the forage in all plots, the soil influence on the indices values was minimized. This fact could explain the similarity of the correlation of the NDVI and SAVI.

4 Conclusions

All tested vegetation indices presented significant correlations with N leaf content and DM in all studied periods.

The GNDVI presented the best correlation with all analyzed variables in all periods and phases studied, indicating that the use of green spectral band was more efficient than the red spectral band to discriminate nitrogen.

Acknowledgements

This research was sponsored by the Brazilian Agencies CNPq, CAPES and FAPEMIG. All the mentioned supports are gratefully acknowledged.

References

CANTARUTTI R.B., MARTINS C.E., CARVALHO M.M.; FONSECA D.M., ARRUDA M.L., VILELA H., OLIVEIRA F.T.T. (1999): Pastagens. In: RIBEIRO A.C., GUIMARÃES P.T.G., ALVAREZ, V.H. Recomendações para o Uso de Corretivos e Fertilizantes em Minas Gerais - 5ª Aproximação. Viçosa, MG, p. 332-341

EPIPHÂNIO J.C.N., GLERIANI J.M., FORMAGGIO A.R., RUDORFF B.F.T. (1996): Índices de vegetação no sensoriamento remoto da cultura do feijão. Pesquisa Agropecuária Brasileira, 31 (6): 445-454

GITELSON A.A., KAUFMAN Y.J., MERZLYAK M.N. (1996): Use of channel in remote sensing of global vegetation from EOS-MODIS. Remote Sensing Environment, 58 (3): 289-298

HUETE A.R. (1988): A soil ajusted vegetation index (SAVI). Remote Sensing Environment, 25: 295-309

MENESES R., MADEIRA NETO J.S. (2001): Sensoriamento remoto – reflectância dos alvos naturais. Brasília, 262 p

SENA JÚNIOR D.G. (2005): Utilização de técnicas de visão artificial para ajuste da adubação nitrogenada em trigo. Viçosa: UFV, 149 p. Dissertação (Doutorado em Engenharia Agrícola)

Structure investigation of soil aggregates treated with different organic matter using x-ray micro tomography

Keiko Nakano[1], Werner B. Herppich[2], Nikolay Kardjilov[3], Ingo Manke[3], Andre Hilger[3], Martin Dawson[3], Kinya Masuda[1], Yoshitaka Hara[1], Uzuki Matsushima[4]

[1] *National Agricultural Research Center for Kyushu Okinawa Region, 496 Izumi, Chikugo, Fukuoka 833-0041, Japan*
[2] *Dep. Horticultural Engineering, Leibniz Institute for Agricultural Engineering Potsdam-Bornim, Max-Eyth-Allee 100 D-14469 Potsdam, Germany*
[3] *Institute of Applied Materials, Helmholtz Centre Berlin for Materials and Energy, F-11 Glienicker Strasse 100, 14109 Berlin, Germany*
[4] *Faculty of Agriculture, Iwate University, 3-18-8, Ueda, Morioka, Iwate,020-8550 Japan*
Corresponding author: nakak@affrc.go.jp

Abstract: *Soil aggregation, which is favorable for plant growth, can be modified by the presence of organic matter; farmers thus often apply different materials to promote soil aggregation and enhance its stability. However, the relationship between the type of organic matter used and the resulting properties of the aggregate structure is unclear. Using high resolution micro x-ray computed tomography we investigated the internal structures of aggregates from fields to which a variety of organic material had been applied. The sampling sites are five paddy fields with rice-wheat rotations – four treated with different organic matters and one untreated control – in southwest Japan. The organic materials used were rice straw, rice straw manure, wheat straw, and livestock manure. The soils were classified as Endogleyic Hydragric Anthrosol (Clayic). Imaging samples were hand-picked from bulk soil samples collected in October 2008. Tomography experiments were conducted using an x-ray micro-focus instrument at the Helmholtz Centre Berlin for Materials and Energy; the instrument had a spatial resolution of approximately 5 µm. Organic substances, such as manure, root and seed, in the aggregates were observed. By thresholding the gray-scale of the images, it was possible to distinguish between porous and solid phases. These imaging studies indicated that applying manure to soils effectively increased the porosity of their intra-aggregates. Pores reaching from the core of the aggregate to their surfaces were observed in organic-matter-applied fields and sponge-like pores were identified in manure-fed fields. This suggests that differences in the organic- fertilizers used might affect the pore network within intra-aggregates.*

1 Introduction

Soil aggregation is favorable for plant growth as it enhances the aeration, water retention and permeability of the soil. Aggregated soil has a dual-pore system; the first pore

system is present within each aggregate (intra-aggregate), while the second is located between adjacent aggregates (interaggregate). The interaggregate spaces or cavities are wider and thus play an important role in infiltration and aeration, whereas intra-aggregate pores are relatively narrow and aid in soil moisture retention after drainage. In the field, aggregate structures should be stable against wetting-drying, mechanical loads or tillage for long periods of time. The primary constituents of the aggregates are sand or silt-sized quartz particles, clay and organic matter; the organic polymers act as cementing agents. Aggregate properties are modified by the presence of organic matter, and by texture and land use. Farmers, therefore, often apply various kinds of organic matter in order to promote soil aggregation and to enhance its stability. However, the relationship between the application of different organic matters and the resulting aggregate structure is as yet unclear.

The x-ray computed tomography (CT) technique permits the non-destructive investigation and visualization of soil structure. Due to the progress in this technique, investigators have been able to analyze the detailed structure of the intra-aggregates. SLEUTEL *et al.* (2008) have been able to image a pore size of 1.7 - 2.5 µm, and CHUN *et al.* (2008) have analyzed the differences in the organization and distribution of pores within aggregates of different sizes and found that they can be hierarchical. We used x-ray CT to investigate the intra-aggregates from fields treated with a range of organic matters. Agricultural management was similar in all the sampling fields except for the one treated with organic matter.

2 Materials and methods

Materials

The aggregates were obtained from the research fields of the National Agricultural Research Center for Kyushu Okinawa Region, located in southwest Japan. The sampling sites were four rice-wheat rotation paddy fields treated with different organic fertilizers and one control rotation paddy field. The fertilizers used were rice straw (RS: 10 t ha^{-1}, since 1963), rice-straw manure (RM: 20 t ha^{-1}, since 1963), wheat straw (WS: 6 t ha^{-1}, since 1985) and livestock manure (LM: 50-60 t ha^{-1}, since 2006). The control farm field (Cont.) had not been treated with organic matter since 1963. After harvesting, plant residues were removed from the fields. Conventional chemical fertilizers were applied in all the fields, except for LM-applied field. The grain yields of the organic fertilizer applied fields were significantly higher than that of the control field. The soil in these fields was classified as Endogleyic Hydragric Anthrosol (Clayic) according to the World Reference Base for Soil Resource; the texture and clay minerals of the sample farm fields were similar because of they were located adjacent to each other. Bulk soil samples were collected in October 2008 and sieved through 2-mm screens. Aggregates were subsequently hand-picked from the soil that remained on the screen. For imaging, the aggre-

gate samples were divided into 2 groups: D_1 and D_2 with diameter of 2-4 mm and 6-10 mm, respectively.

Methods

The tomography experiments were conducted using an X-ray micro-focus instrument at the Helmholtz Centre Berlin for Materials and Energy which utilizes a micro focus beam tube (Hamamatsu photonics K.K.; Hamamatsu City, Japan). In the cone beam geometry different magnification ratios could be used by change of the distance between the sample and the beam source; the maximal spatial resolution achieved was approximately 5 µm for the D_1 sample. Radiographs were collected at 0.36°-step interval during the 360° sample rotation by using a flat panel detector (Hamamatsu photonics K.K.). The tomographic reconstruction was performed by back-projection algorithm for cone beam geometry using the software package Octopus 8.3 (Ghent University). Images were processed using ImageJ 1.42 (National Institutes of Health).

3 Results and discussion

Fibrous material could be distinguished in some CT cross-sections (**Figure 1a**). These types of substances were frequently observed in samples from manure-fed fields (RM and LM), but rarely in the samples from the control field. Hence, they could be some components of the manure. Some CT cross-sections showed plant residues, which could be identified from their features (**Figure 1b, c**). However, it was not possible to locate the organic matter complexed with minerals, a configuration that could have helped enhancing the long term stability of the aggregates.

After removing noise from the CT cross-section images by using a median filter (radius 2 pixels), the images were segmented between porous and solid-phase soil with a gray-level threshold of 8000, the lower limit of gray-level for visible organic substances. Nine representative cross-sections were selected each for 2 D_1 samples, and the porosity (the ratio of pore phase area to the total area of aggregate) was calculated. Pore segments having less than 20 µm diameter were neglected, since individual pores smaller than this were difficult to discern. The average porosities of Cont., RS, WS, RM, and LM soils were 1.4 ±1.4%, 3.1 ±2.6%, 1.7 ±0.9%, 2.6 ±2.0%, and 3.5 ±1.8%, respectively. This indicates that applying manure probably increases intra-aggregate porosity. The capillary suction of soils with a pore size of 20 µm, calculated from the capillarity formula, is 15 kPa (=pF2.2). Plants can easily take up water from soils if the suction is below pF2.7. Hence, if the pores in the D_1 aggregates were connected to inter-aggregate networks (i.e. if the water supply to them could be maintained), then the water trapped within them could be used to sustain plant growth.

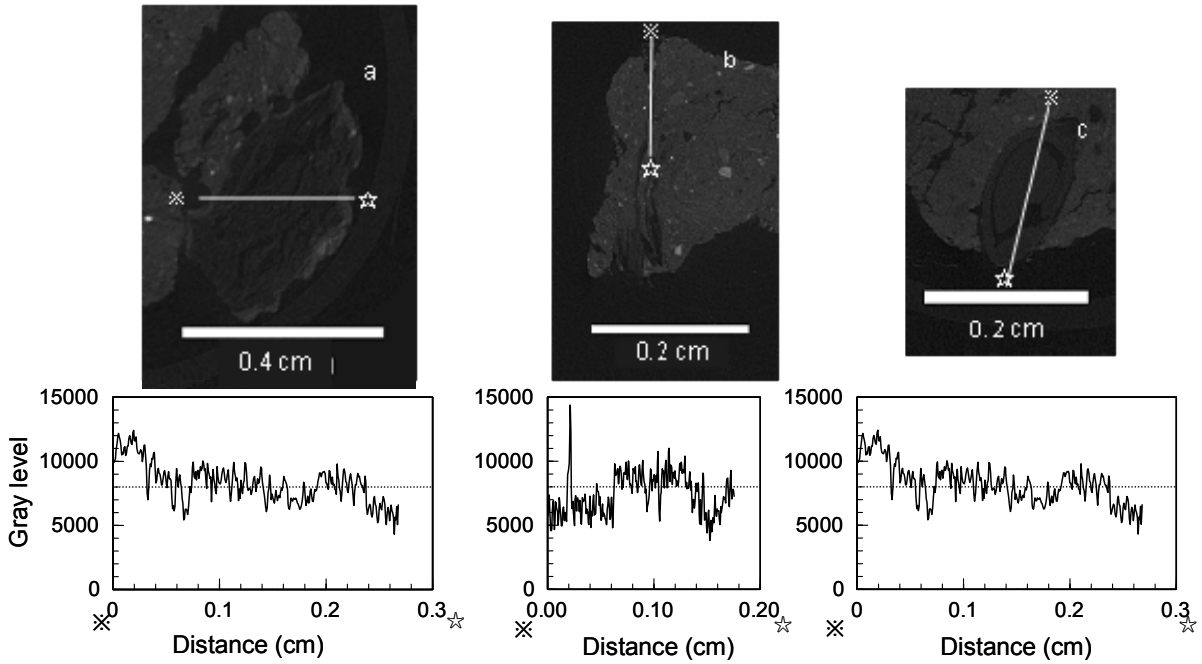

Figure 1: Representative images of organic materials found in the aggregates: (a) livestock manure, (b) root, (c) seed. The plots show the gray level profile along with the white lines.

The D_2 aggregates reflected the difference in sampling fields more clearly in another aspect (**Figure 2**). In soil aggregates from manure-fed fields, especially from the LM field, sponge-like pores could be detected, which generally are more effective in water retention. In organic fertilizer-fed fields, elongated pores that connect the cores of aggregates with the surface were observed. PAPADOPOULOS *et al.* (2009) concluded that such connecting pores help in maintaining the structural stability of the aggregate because they could act as escape routes for entrapped air thus avoiding the slacking of aggregates. In samples from the control field, the elongated and the sponge-like pores were rarely observed. Hence, it can be assumed that the peds from the control field which at best resembled aggregates were only fragments from soil blocks rather than true “aggregates”, although the difference among them could not be judged solely from their surfaces.

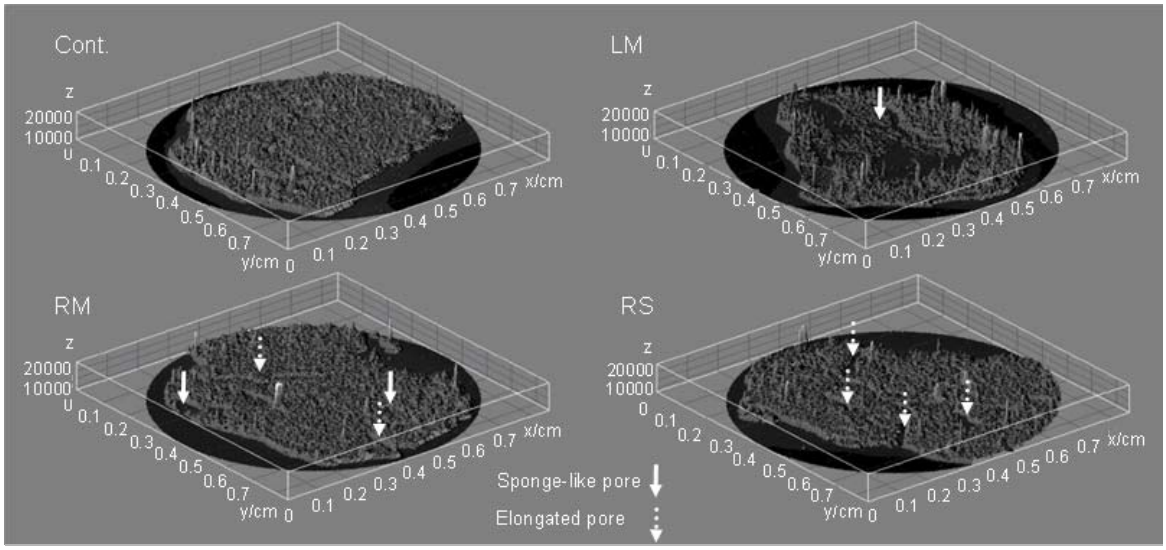

Figure 2: 3D surface-plots of selected porous CT cross-section images of D_2 aggregates constructed with ImageJ (Gridsize:256, Smoothing:0, Lighting:0.25).

4 Conclusions

Using micro x-ray CT tomography, intra-aggregate pore formation in soils from fields fed with different organic fertilizers was compared. Organic matter, especially manure-based matter, increased porosity of the intra-aggregate. Pores that connected the core of the aggregates with the surface were observed in organic matter-applied fields and sponge-like pores were observed in manure-fed fields. Future studies will focus on the shape of these pores, and analyze the effect of each organic fertilizer on the pore network or its structural hierarchy.

References

CHUN H.C., GIMÉNEZ D., YOON S.W. (2008): Morphology, lacunarity and entropy of intra-aggregate pores: Aggregate size and soil management effects. Geoderma, 146: 83-93

SLEUTEL S., CNUDDE V., MASSCHAELE B., VLASSENBROEK J., DIERICK M., VAN HOOREBEKE L., JACOBS P., DE NEVE S. (2008): Comparison of different nano- and micro- focus X-ray computed tomography set-ups for the visualization of the soil microstructure and soil organic matter: Computers & Geoscience, 34: 931-938

PAPADOPOULOS A., BIRD N.R.A., WHITMORE A.P., MOONEY S.J. (2009): Investigating the effects of organic and conventional management on soil aggregate stability using X-ray computed tomography. European Journal of Soil Science, 60: 360-368

Determination of bread crumb porosity using statistical analysis of surface pattern

Aniko Lambert-Meretei, György Csima, Medea Nogula-Nagy, László Baranyai, András Fekete

Corvinus University of Budapest, Physics-Control Department, Budapest, Hungary
Corresponding author: aniko.meretei@uni-corvinus.hu

Porosity is one of the most important parameters of bread crumb. The standard procedure for determination of this property is time consuming and requires special sample preparation. The objective of the presented work was to develop objective and reliable methods suitable for determining characteristics of the bread crumb with respect to the porosity. Pictures of 0.11 mm/pixel resolution were acquired with a Hitachi HV-C20 3CCD camera using both diffusive illumination and light transmission. First order and derivative statistical parameters were compared. Relationship was determined between extracted visual information and porosity. In case of light transmission, slice width strongly influenced the results, therefore correction was necessary. The measured results show that these methods might be suitable for measuring porosity characteristics of bread crumb.

Application of morphometric image analysis system to evaluate the incidence of fusarium head blight wheat infected kernels

Paolo Menesatti[1], Francesca Antonucci[1], Corrado Costa[1], Alberto Santori[2], Iliana Nicia-relli[1], Alessandro Infantino[2]

[1] CRA-ING Agricultural Engineering Research Unit of the Agriculture Research Council, Via della Pascolare, 16, 00016 Monterotondo (Roma) - Italy
[2] CRA-PAV Plant Pathology Research Center, Via G. Bertero, 22, 00156 Rome – Italy
Corresponding author: paolo.menesatti@entecra.it

Abstract: *Fusarium Head Blight (FHB) is a disease of complex aetiology affecting winter cereals worldwide. The disease has a great impact on yield, but mostly on health, due to the ability of several Fusarium species involved in the diseases to produce mycotoxins dangerous to human and cattle. Grading of cereals for industry by means of visual estimation of disease incidence is not always accurate in predicting mycotoxin levels in wheat samples. Rapid and accurate analyses of large wheat samples by means of non-destructive methods are needed. Among several techniques available, image-analyses, taking into account the entire external kernels shapes, have been developed. Preliminary experiments using durum wheat kernels artificially infected with Fusarium graminearum and F. culmorum have been performed in Italy. Samples where acquired with a high resolution scanner. After an automated thresholding procedure performed by an edge detection Sobel filtering, 90 points (x, y) equally angularly spaced (one point every 4°) from the centroid were digitized along the outline. Elliptic Fourier analysis was performed to extract shape data to be analyzed via partial least squares discriminant analysis. Three classes of infection were considered: healthy, shrivelled and chalky. F. culmorum infection is better distinguishable than F. graminearum. Percentages of correct classification resulted to be 68.4% for the F. culmorum infection and 56.9% for the F. graminearum*.

1 Introduction

Fusarium head blight (FHB), also known as scab, is a fungal disease that occurs in several winter cereals worldwide. The disease has a great impact on yield, but mostly on health, due to the ability of several *Fusarium* species involved in the diseases to produce mycotoxins, particularly deoxynivalenol (DON), dangerous to human and cattle. These pathogens cause yield and quality losses due to sterility of the florets and formation of fusarium damaged kernels (FDK) typically shrivelled, light in weight and white or pink in colour (BUSHNELL *et al.* 2003). The relationships between FDK, fungal biomass

and DON content have been extensively studied, but the results are sometimes conflicting (PAUL *et al.* 2005). Most of these methods are destructive, time consuming, expensive and laborious. The proposed Optoelectronic non-contact systems are based on near infrared spectroscopy (Nir) (DOWELL *et al.* 1999). The aim of this work is to suggest a quantitative, non-destructive, cost-effective and rapid image analysis method, based on i) simple low-cost greyscale CMOS video camera for profile acquisition; ii) Elliptic Fourier analysis (EFA) of the kernel outlines; iii) multivariate classification techniques (i.e. PLSDA), to discriminate three different classes of FHB wheat infected kernels in order to correlate estimated and actual FDK.

2 Materials and methods

Data collection

Fusarium infected wheat kernels were obtained by artificially inoculating durum wheat plants, of highly FHB susceptible cultivars Simeto, grown at the CRA-PAV farm (Rome, Italy). At flowering, plants were sprayed with a suspensions of *Fusarium culmorum* (ER-1480) or *F. graminearum* (ER-1481) at the concentration of 1×10^5 conidia ml^{-1} and then covered with plastic sheets for two days after inoculation. At harvest, kernels inoculated were visually grouped in tree classes of FHB infection on the basis of their shape (healthy, shrivelled and chalky kernels covered by white mycelium). A total number of 613 kernels, randomly disposed on the plane of a scanner, were acquired with a high resolution scanner (600 d.p.i. 24 bit color). An automated thresholding procedure was performed by an edge detection Sobel filtering in order to detect the edges. Consequently 90 points (x, y) equally angularly spaced from the centroid (one point every 4°), were automatically digitized along the outlines using the software Matlab (rel. 7.1; PLSToolbox Eigenvector b 4.0) (**Figure 1**).

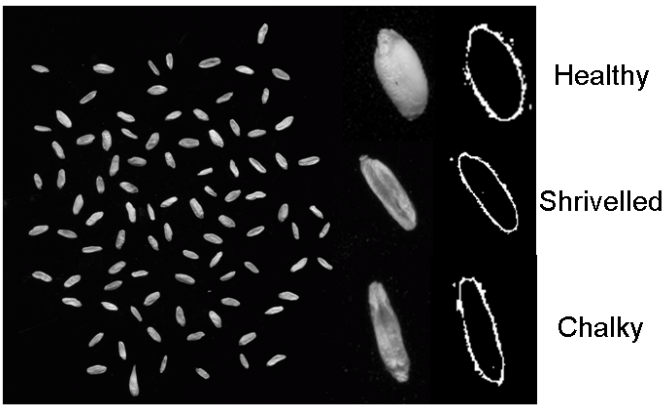

Figure 1: On the left side: samples randomly disposed on the plane of a scanner. On the right side from the top to the bottom: kernels at the three classes of infection (healthy, shrivelled and chalky) before and then the automated outlines acquisition.

Data processing

The overall shape of the artificially infected kernels was studied by EFA on the outline coordinates previously extracted EFA is based on the separate Fourier decompositions of the incremental changes of the *x*- and *y*-coordinates as functions of the cumulative chordal length of an outline polygon. The kernels shape closed contour is expressed in terms of harmonically related trigonometric curves. For each harmonic equation, two Fourier coefficients are computed for both the *x*- and *y*-projections thus, the total number of coefficients is 4*n*, where *n* is the number of harmonics fitted to the outline (CRAMPTON 1995). The total number of harmonics for any outline is equal to half of the total number of outline coordinates (the 'Nyquist frequency'). The Fourier series was truncated at the value of *k* at which the average cumulative power is 99.999% of the average total power (MENESATTI *et al.* 2008). The harmonic coefficients, automatically extracted with Matlab, describe the size, shape and orientation of each harmonic ellipse form the input to multivariate statistics. The classification procedure of the three different classes of infection (healthy, shrivelled and chalky), and affected by the two pathogens, was performed in Matlab on the shape variables (X-block; EFA coefficients) and the shape data were analyzed *via* partial least squares discriminant analysis (PLSDA) (COSTA *et al.* 2009, MENESATTI *et al.* 2008). The X-block values were pre-processed with different Matlab procedures. For the analysis each group was subdivided in: i) 75% of specimens for the class modelling and validation; ii) 25% of specimens for the independent test. PLSDA (SABATIER *et al.* 2003) is a partial least squares analysis (PLS) regression where the response variable is categorical (Y-block; infection status) expressing the class membership of the statistical units.

3 Results and discussion

For the kernels lateral profile the correct number of harmonics (13) was calculated on the whole samplings ('Nyquist frequency' = 45). The PLSDA model performed on EFA coefficients for kernels affected by *Fusarium culmorum* is based on 16 Latent Variables (LV), presents a preprocessing for the *X*-block as absolute value and a Root Mean Square Error of Calibration (RMSEC) of 0.294. The total percentage of correct classification is 68.4%. **Table 1** shows the results relative to the independent test (25%) of the classification procedure performed by PLSDA. In this case the intermediate class (shrivelled) is poorly represented and badly classified (21.1%).

Table 1: Confusion matrix relative to the independent test (25%) of the classification procedure of the three different classes of infection (healthy, shrivelled and chalky) affected by *Fusarium culmorum*. The mean (%) represents the percentage of cases correctly allocated. The percentage of cases correctly allocated derived by relating the number of cases correctly allocated to the class (in bold) to the total number of cases of that class (Total).

Kernels affected by *Fusarium culmorum*					
	Chalky	Shrivelled	Healthy	Total	Mean (%)
Chalky	**21**	0	2	**23**	91.3%
Shrivelled	5	**4**	10	**19**	21.1%
Healthy	2	1	**39**	**42**	92.9%

The PLSDA model performed on EFA coefficients for kernels affected by *F. graminearum* is based on 7 LV, presents a “gls weighting” preprocessing for the *X*-block and a RMSEC of 0.401. The total percentage of correct classification is 56.9%. **Table 2** shows the results relative to the independent test (25%) of the classification procedure performed by PLSDA. The “healthy” class is the best classified (65.6%). The results suggest that *F. culmorum* infection is better distinguishable than *F. graminearum*, probably because this specie is more aggressive than *F. graminearum* and is able to produce stronger damages on kernels.

Table 2: Confusion matrix relative to the independent test (25%) of the classification procedure of the three different classes of infection (healthy, shrivelled and chalky) affected by *Fusarium graminearum*. The mean (%) represents the percentage of cases correctly allocated. The percentage of cases correctly allocated may be derived by relating the number of cases correctly allocated to the class (in bold) to the total number of cases of that class (Total).

Kernels affected by *Fusarium graminearum*					
	Chalky	Shrivelled	Healthy	Total	Mean (%)
Chalky	**6**	3	3	**12**	50%
Shrivelled	6	**11**	3	**20**	55%
Healthy	1	10	**21**	**32**	65.6%

4 Conclusions

This work was developed to verify the technical and methodological feasibility of the proposed method in order to evaluate the infective incidence of FHB. The shape analysis appeared an important technique to discriminate different classes of FHB wheat infected kernels. The results obtained will be validated on a higher numbers of both, artificially and naturally FHB infected wheat seed lots. Image analysis allows a higher speed of analysis, an increase of the evaluated seeds number and the repeatability of the measure and overpassing the subjectivity of the expert view.

Acknowledgements

This work was funded by the project HighVision (DM 19177/7303/08) from the Italian Ministry of Agricultural, Food and Forestry Politics.

References

BUSHNELL W.R., HAZEN B.E. PRITSCH C. (2003): Histology and physiology of Fusarium head blight. In Fusarium head blight of wheat and barley, pp. 44-83, K. J. Leonard & W. R. Bushnell eds. APS Press, St. Paul

COSTA C., MENESATTI P., AGUZZI J., D'ANDREA S., ANTONUCCI F., RIMATORI V., PALLOTTINO F. MATTOCCIA M. (2009): External shape differences between sympatric populations of commercial clams *Tapes decussatus* and *T. philippinarum*. Food and Bioprocess Technol doi: 10.1007/s11947-008-0068-8

CRAMPTON J.S. (1995): Elliptic Fourier shape analysis of fossil bivalves: some practical considerations. Lethaia, 28: 179-186

DOWELL F.E., RAM M.S. SEITZ L.M. (1999): Predicting scab, vomitoxin, and ergosterol in single wheat kernels using near infrared spectroscopy. Cereal Chemistry, 76: 573-576

MENESATTI P., COSTA C., PAGLIA G., PALLOTTINO F., D'ANDREA S., RIMATORI V. AGUZZI J. (2008): Shape-based methodology for multivariate discrimination among Italian hazelnut cultivars. Biosystems Engineering, 101 (4): 417-424

PAUL P.A., LIPP, P.E. MADDEN L.V. (2005): Relationship between visual estimates of Fusarium head blight intensity and deoxynivalenol accumulation in harvested wheat grain: a meta-analysis. Phytophatology, 95 (10): 1225-1236

SABATIER R., VIVEIN M. AMENTA P. (2003): Two Approaches for Discriminant Partial Least Square. In Between Data Science and Applied Data Analysis, SCHADER M., GAUL W., VICHI, M. eds. Berlin, Springer-Verlag

Charecterisation of morphological properties of apricot stones by image processing

Jozsef Felföldi[1], F. Firtha[1], R. Hermán[2], Andrzej Pedryc[2]

[1] Corvinus University of Budapest, Department of Physics and Control, Budapest, Hungary
[2] Corvinus University of Budapest, Department of Genetics and Plant Breeding, Budapest, Hungary
Corresponding author: jozsef.felfoldi@uni-corvinus.hu

Abstract: *The morphological characteristics of the apricot stones of different cultivars show much higher variability, as it is typical in case of other fruit species. The variety of forms is easy to observe sensorially (directly or using a reading-glass), however it's hard to describe exactly, in a quantitative way. The widely accepted international standard is based on comparison with standard cultivars, the results are given in a special point system, developed for this purpose. The information, provided by this evaluation system is not suitable for identification of the cultivars, but it can be used for distinguishing two sample sets. The aim of our research work was to develop quantitative methods for description of the stones. The statistically validated quantitative parameters offer the possibility of applying them as morphological markers for identification of the cultivars or for other genetic analyses without leaning on any standard samples as references. The traditional measurement methods are able to determine only the simplest geometrical parameters of the samples (such as length, width or thickness). However, the special characteristics, connected to the different cultivars, are related to much more complex shape parameters. Computer based machine vision system and image processing was applied for quick, automatic shape feature extraction and determination of new, quantitative shape characteristics.*

1 Introduction

The apricot is considered to be among the most delectable and consumable of all fruits. Fruit are used in fresh and dry form, canned or preserved as jam, marmalade or pulp. Distillates and wines are made from both cultivated and non-domesticated apricot both in Europe and Asia (JOSHI *et al.* 1990, GENOVESE *et al.* 2004).

The early botanical descriptions of the different apricot species were based primarily on leaf shape and pubescence, and these characters were not always consistent between specimens. Bailey's (BAILEY 1916) categorical distinctions of apricot species and botanical varieties used leaf characteristics. Even the taxonomy of apricots by Chinese investigators was also based mainly on leaf characteristics (HOU 1983). The classifica-

tion by Rehder (REHDER 1940) distinguished plums from apricots on the basis of ovary pubescence, being absent or glabrous in the plums and present or pubescent in apricots.

Studying the relevant characteristics of distinct species or pomological/botanical varieties are more and more important for breeding and other particular classification purposes (ASMA & OZTURK 2005, BADENES *et al.* 1998).

The morphological characteristics of the apricot stones of different cultivars show much higher variability, as it is typical in case of other fruit species. The variety of forms is easy to observe sensorially (directly or using a reading-glass), however it's hard to describe exactly, in a quantitative way. The widely accepted international standard (UPOV 2008, IPGRI 1980) is based on comparison with standard cultivars, the results are given in a special point system, developed for this purpose. The information, provided by this evaluation system is not suitable for identification of the cultivars, but it can be used for distinguishing two sample sets.

The aim of our research work was to develop quantitative methods for description of the stones. The statistically validated quantitative parameters offer the possibility of applying them as morphological markers for identification of the cultivars or for other genetic analyses without leaning on any standard samples as references.

The traditional measurement methods are able to determine only the simplest geometrical parameters of the samples (such as length, width or thickness). However, the special characteristics, connected to the different cultivars, are related to much more complex shape parameters. Computer based machine vision system and image processing was applied for quick, automatic shape feature extraction and determination of new, quantitative shape characteristics.

2 Materials and methods

The base of the tests was the collection of the Genetika és Növénynemesítés Tanszék containing the stones of approximately 300 sample sets (all Hungarian cultivars, important foreign cultivars and hybrid families needed for genetic analyses). The sample sets are represented by 14-20 stone samples. For the development of the methods, six hybrid samples of definitely distinct morphological properties were selected (**Figure 1**).

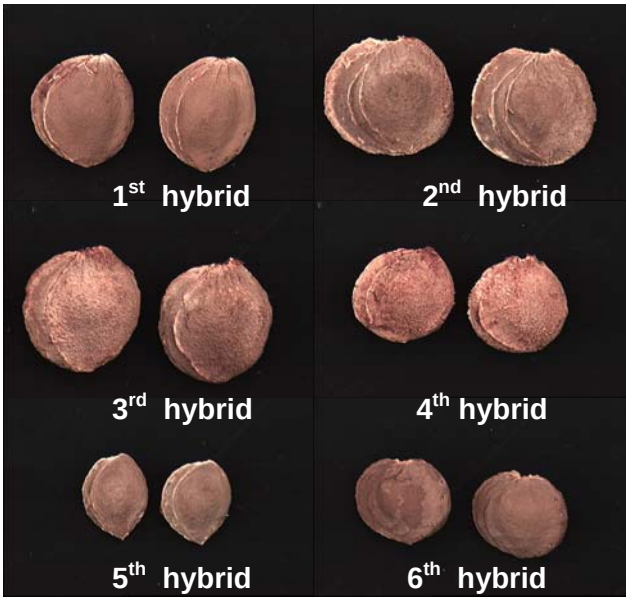

Figure 1: Stone samples of tested hybrid cultivars

The digital images were recorded by a Hitachi HV-C20 professional, 3-chip CCD camera, fitted to a PC via an add-on card for frame grabbing. The recorded images were stored in a 768 x 576 resolution, true-colour bitmap file for the further assessment.

Special diffuse lighting system was applied for taking the photos, were the samples were illuminated only by reflected light. The images were recorded in 4 different setups for all samples (**Figure 2**):

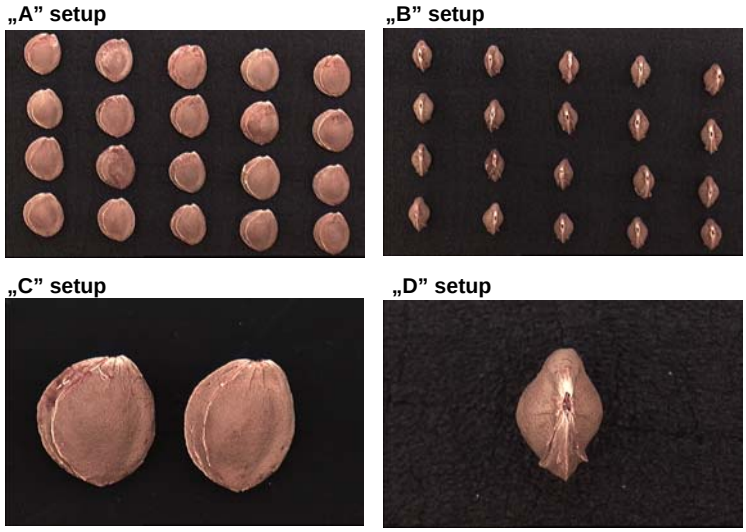

Figure 2: Image recording setup

„A" setup: stones in side view – 14-20 stones of one hybrid on one picture
„B" setup: stones in top view – 14-20 stones of one hybrid on one picture
„C" setup: stones in side view – magnified images of 2-2 stones per hybrid on one picture (for investigation of the surface texture properties)
„D" setup: stone in top view – magnified image of 1-1 stones per hybrid on one picture (for investigation of the crest-like formation on the side part of the stones)

The recorded images were analysed with a special image processing software (FFImgPro), developed at the Department of Physics and Control of CUB). The algorithm is for segmentation of the objects and the background according to the statistical analysis of their colour properties, for determination of the area and average RGB colour parameters of the objects and for saving the data into a file. Also, the co-ordinates of the border-points of the objects are determined, and stored for shape assessment. The quantitative shape was performed by the “Shape” software (FELFOLDI 2000). The algorithm determines the following geometrical parameters:

- length of the stone
- maximum width of the stone
- position of the maximum diameter along the longitudinal axis (0 .. 1)

The geometrical results are given in pixel-number or – after calibration – in mm. The main advantage of the image processing methods is the possibility of determination of new, quantitative and objective shape characteristics by analysis of the shape data. In the research work, presented here the periodicity parameters of the outline functions (related to the main symmetry properties of the stones) were taken into investigation. These parameters can be determined by Fast Fourier Transformation (FFT) of the outlines and the FFT components can be connected to definite symmetries, e.g.:

- FFT2: elliptic shape
- FFT3: triangle-like shape
- FFT4: quadratic shape, …

For statistical analysis of the results Excel, and SPSS for Windows (Ver. 10.0) software were used.

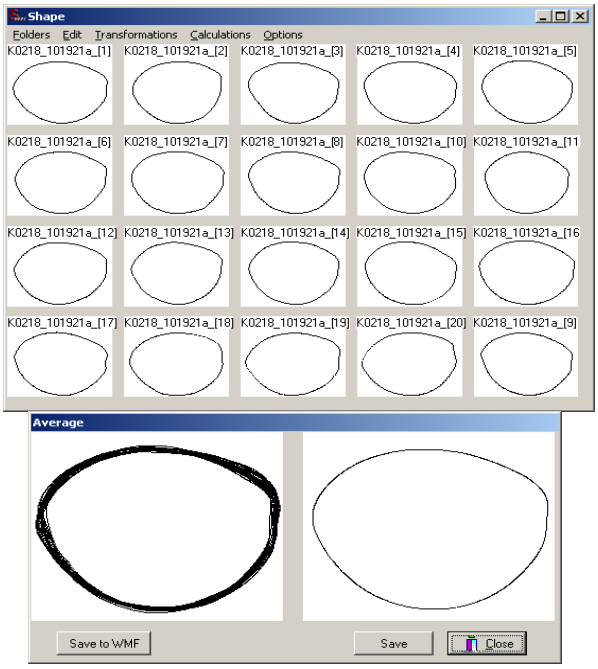

Figure 3: Outlines of the samples of 1st hybrid (20 pieces) and averaged outline, characteristic for the hybrid

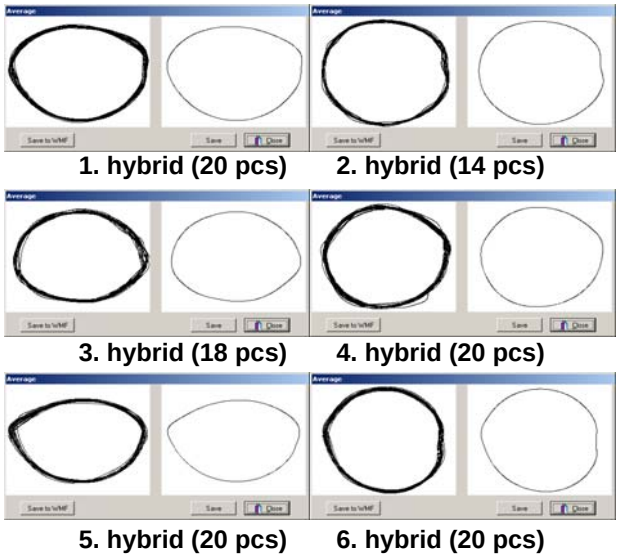

Figure 4: Averaged outlines of the tested hybrids

3 Results

ANOVA

One factor analysis of variance was used for statistical comparison of the main geometrical parameters of the tested stone samples (length and width). These parameters alone were not enough for unambiguous separation of the hybrid sample groups. The results are illustrated on **Figure 5**, showing the average values of the tested parameters with their 95% confidence interval.

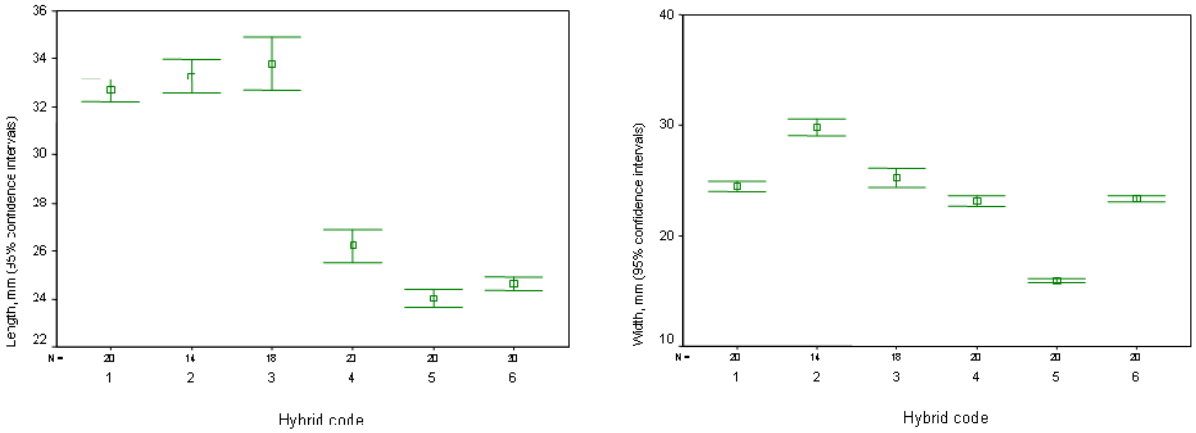

Figure 5: Confidence intervals of length (a) and width (b) parameter of hybrids

Discriminant Analysis (DA) including more quantitative parameters

1. DA of the length and width: only the 2nd and 5th hybrids are separated from each other, the other four hybrids are not distinguishable according to these parameters (**Figure 6**)
2. DA of shape characteristics: besides the geometrical parameters (length and width) the FFT components of the outline function were included as well. In this case, four hybrids (1st, 2nd, 5th and 6th) can be distinguished perfectly, however this information was not effective enough for separation of the further 2 sample sets (**Figure 7**)
3. DA of shape and colour characteristics: the average colour components of the samples were added to the parameters used in previous investigation. This analysis provided with 100% perfect separation of every hybrid included in the test (**Figure 8**).

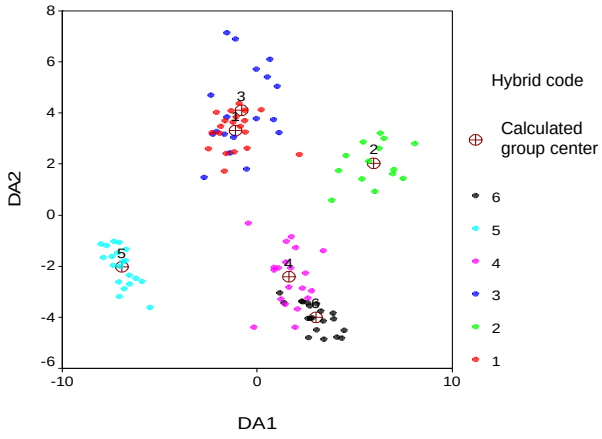

Result of Classification

Hybrid code	Calculated class 1	2	3	4	5	6	Total	
1	14	0	6	0	0	0	20	piece
2	0	14	0	0	0	0	14	
3	8	0	10	0	0	0	18	
4	0	0	0	16	0	4	20	
5	0	0	0	0	20	0	20	
6	0	0	0	2	0	18	20	
1	70	0	30	0	0	0	100	%
2	0	100	0	0	0	0	100	
3	44,4	0,0	55,6	0	0	0	100	
4	0	0	0	80	0	20	100	
5	0	0	0	0	100	0	100	
6	0	0	0	10	0	90	100	

Figure 6: Separation of the tested hybrids according to Discriminant Analysis of their length and width parameters

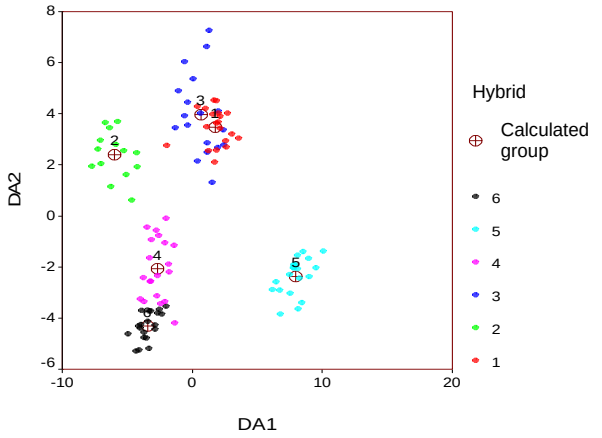

Result of Classification

Hybrid code	Calculated class 1	2	3	4	5	6	Total	
1	20	0	0	0	0	0	20	piece
2	0	14	0	0	0	0	14	
3	1	0	17	0	0	0	18	
4	0	0	0	19	0	1	20	
5	0	0	0	0	20	0	20	
6	0	0	0	0	0	20	20	
1	100	0	0	0	0	0	100	%
2	0	100	0	0	0	0	100	
3	5,6	0	94,4	0	0	0	100	
4	0	0	0	95	0	5	100	
5	0	0	0	0	100	0	100	
6	0	0	0	0	0	100	100	

Figure 7: Separation of the tested hybrids according to Discriminant Analysis of their shape characteristics

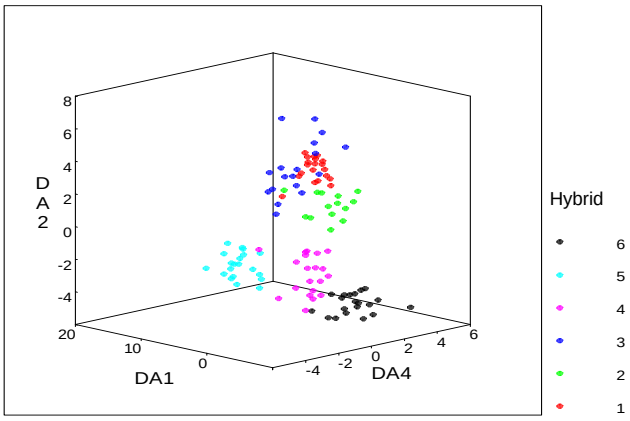

Result of Classification

Hybrid code	Calculated class 1	2	3	4	5	6	Total	
1	20	0	0	0	0	0	20	piece
2	0	14	0	0	0	0	14	
3	0	0	18	0	0	0	18	
4	0	0	0	20	0	0	20	
5	0	0	0	0	20	0	20	
6	0	0	0	0	0	20	20	
1	100	0	0	0	0	0	100	%
2	0	100	0	0	0	0	100	
3	0	0	100	0	0	0	100	
4	0	0	0	100	0	0	100	
5	0	0	0	0	100	0	100	
6	0	0	0	0	0	100	100	

Figure 8: Separation of the tested hybrids according to Discriminant Analysis of their shape and colour characteristics

In further investigations, more samples (hybrids) with less different morphological characteristics will be tested. To increase the efficiencies of the image processing classification method, quantitative description and statistical analysis of new parameters planned to take into account (characterisation of the surface texture, belonging to the given cultivars) and the number, size and position of the crest-like formations on the side part of the stones) (**Figure 9** and **10**).

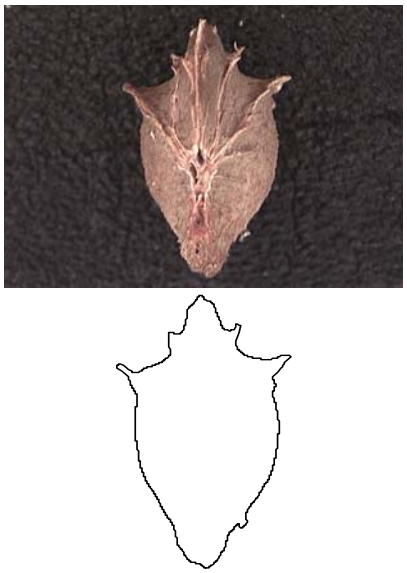

Figure 9: Machine vision representation of the crest-like formation on the side part of the stones

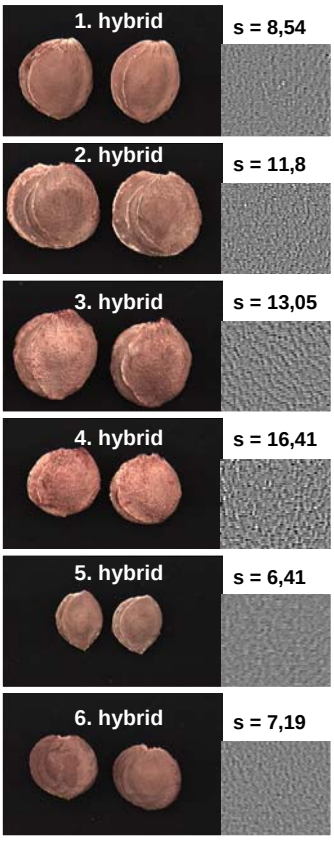

Figure 10: Quantitative description of the surface texture (roughness) of the tested hybrids based on standard deviation of the equalised grayscale surface image

References

ASMA B.M., OZTURK K. (2005): Analysis of morphological, pomological and yield characteristics of some apricot germplasm in Turkey. Genet Resour Crop Evol 52:305–313

BADENES M.L., MARTˊINEZ-CALVO J., LLˊACER G. (1998): Analysis of apricot germplasm from the European ecogeographical group. Euphytica 102:93–99

BAILEY L.H. (1916): Prunus. In: The standard cyclopedia of horticulture, vol. V. P–R.Mount Pleasant Press, J. Horace McFarland Co., Harrisburg, PA, pp 2822–2845

GENOVESE A., UGLIANO M., PESSINA R., GAMBUTI A., PIOMBINO P., MOIO L. (2004): Comparison of the aroma compounds in apricot (Prunus armeniaca L. cv Pellecchiella) and apple (Malus pumila L. cv Annurca) raw distillates. Ital J Food Sci 16:185–196

HOU H.Y. (1983): Vegetation of China with reference to its geographical distribution. Ann Missouri Bot Gard 70:509–548

FELFÖLDI J. (2000): Quantitative shape characterisation of vegetable varieties - Proc. of AgEng'2000 International Conference on Agricultural Engineering, Warwick, Paper No.: 00-AE-007, pp 1-8

IPGRI (1980): International Plant Genetic Resources Institute: List of descriptors for apricot (Prunus armeniaca L.). *EUCARPIA meeting on Tree Fruit Breeding, Angers, France, 3-7 September 1979.*

JOSHI V.K., BHUTANI V.P., SHARMA R.C. (1990): The effect of dilution and addition of nitrogen source on chemical, mineral and sensory qualities of wild apricot wine. American J Enol Vit 41:229–231

REHDER A. (1940): Manual of cultivated trees and shrubs hardy in North America, exclusive of the subtropical and warmer temperate regions, 2nd revised and enlarged edition. Macmillan, New York, NY, USA

UPOV (2008): Protocol for Distinctness, Uniformity and Stability Tests: Apricot. *Community Plant Variety Office. CPVO-TP/070/2 Final*

Non agressive orange acid and sugar indexes estimation system

Tomás J. Arnau, José M. Sotoca, Filiberto Pla

Institute of New Imaging Technologies, Jaume I University, Castellón, Spain
Corresponding author: tarnau@uji.es

Abstract: *This work presents a non aggressive methodology for the measurement of acid and sugar indexes of oranges using spectral information. Our method tries to obtain the value of sugar and acid from a fruit, only analyzing the spectrum of light transmitted through the fruit. We apply support vector machine regression to estimate the parameters that permit us to assess the sugar and acid index content of fruits.*

1 Introduction

Nowadays, the worldwide market makes easier to find what you want and bring it to you. For this reason you need to be competitive to sell your products. In the fruits market you can be more competitive if you know beforehand the acid and sugar content of fruits, because in this case you can be more selective with the destination of the product, for instance, you can use the more sweet oranges to be consumed in the fresh market and the less sweet for orange juice.

It is possible to do a classification of the oranges attending to the level of sugar and/or acid for a quality control system, for example. The conventional analysis that have been used so far to know the acid and sugar indexes of oranges are highly invasive methods. It means that you have to do orange juice and analyze it in a chemistry laboratory (LI *et al.* 1996).

A new non aggressive methodology was developed for the measurement of acid and sugar indexes of the oranges using spectrophotometer (NICOLAÏ *et al.* 2007). This method tries to obtain the value of sugar and acid from an orange, only having the results of the spectrum of light that crosses it. There are some papers on nondestructive measurement fruit and vegetable quality with spectroscopy (STEINMETZ *et al*. 1995, TSUCHIKAWA *et al.* 2004). The aim of the present study is to report the analytical results of our method on validation by transmittance of oranges for the estimated ones.

We have tried to obtain a method with non parametric regression and without a model. Thus we have used the support vector machine (SVM) (HSU *et al.* 2003). This is a useful and popular technique for data classification and regression. A classification task usually involves with training and testing data which consist of some data instances.

The goal of SVM is to produce a model that predicts the target value of data instances in the testing set, which are giving only the attributes. Applying this to our case, we have done measurements of the spectrum of light that crosses the orange. As a validation, we made orange juice in the laboratory with the oranges to obtain the values of the acid and sugar. We have applied the SVM to this relationship database.

2 Materials and methods

Samples

The samples of our system are oranges taken from trees located at the east of Spain, in fact, all of them from an area next to Castellón. Our set of oranges was composed by three hundred oranges harvested in subsets of ten oranges of several varieties picked up weekly during the ripening season.

System

The system is composed by an illuminating box with twelve halogen lights inside, each one with a consumption power of 150 watts; the measure system used is a Hamamatsu MiniSpectrometer TM-VIS/NIR CCD-ASeries with an achromatic collimated lens; the spectral response range of the spectrometer is rated between 320 and 1000 nanometers. The method consists of measuring the light signal that crosses the orange. To do this, we use the device described above trying to obtain only the light that crosses the orange. For this purpose, a torus made of foam was used. Over this torus the orange is put, and the extreme of the sensor is located below the fruit (**Figure 1**).

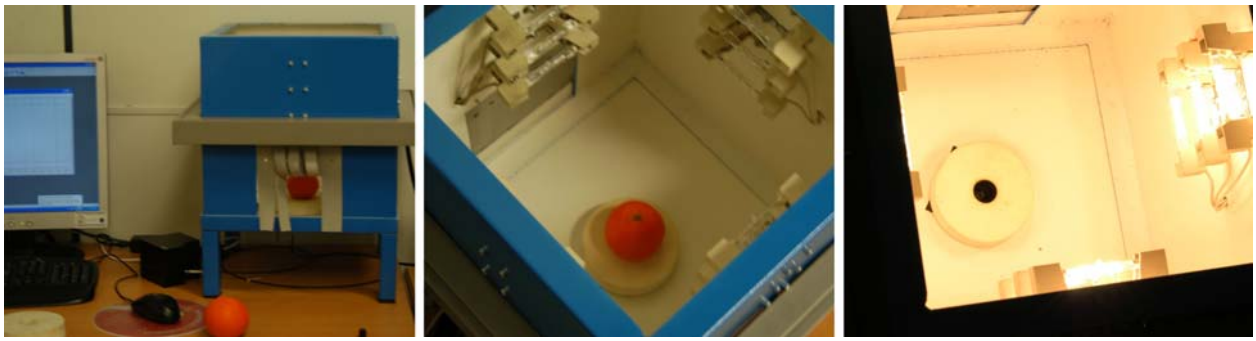

Figure 1: An overview of the system

After the signal was recorded, orange juice of the samples was obtained to measure the acid and sugar empirically. To do that, the standard technique was used to know the acid index of an orange. And, to know the sugar index we have used a refractometer.

Database Analysis

Given the spectrum signal and the corresponding recorded sugar and acid indexes, SVM regression was applied to estimate the parameters. It means that we have two data sets (sugar and acid) with 2048 values of wavelength and the values of sugar and acid indexes relatives to that signal for every orange. With these two databases we have done several tests trying to improve the results: first we have applied SVM to the data with half set of the data for training and the other half for the test. Next, we have done the same using a 10-fold cross validation data system, having 10% of data for training and 90% for test.

3 Results and discussion

To assess the reproducibility of our technique, we have analyzed about 300 oranges in several months, since the beginning of the period of ripeness to the end of it. We have built a database that associates the values of the spectrum and the data obtained in the analysis of the acid and sugar. The estimation of relationship of those values is realized by SVM regression.

To increase the accuracy of the results, we have tried several methods including Hold-Out and 10-Fold Cross Validation obtaining similar results in all cases. The absolute error of our method is 1.24 in a range between 5.61 for the minimum value and 17.14 for the maximum value of the acid; and for the sugar, the absolute error is 0.97 in a range between 11.0 for the minimum and 16.0 for the maximum.

Figure 2 shows the relationship between the obtained signal by the SVM and the original signal (red color). The blue signal is for the training set (fifty per cent of data), and the green one is for the test data.

In **Figure 3** appears the relationship of the observation data versus prediction data after SVM regression was applied. The optimum case would be if all the dots where located in a line that cuts the graph by two empty parts. Therefore, all the predicted data fits with its corresponding observed data.

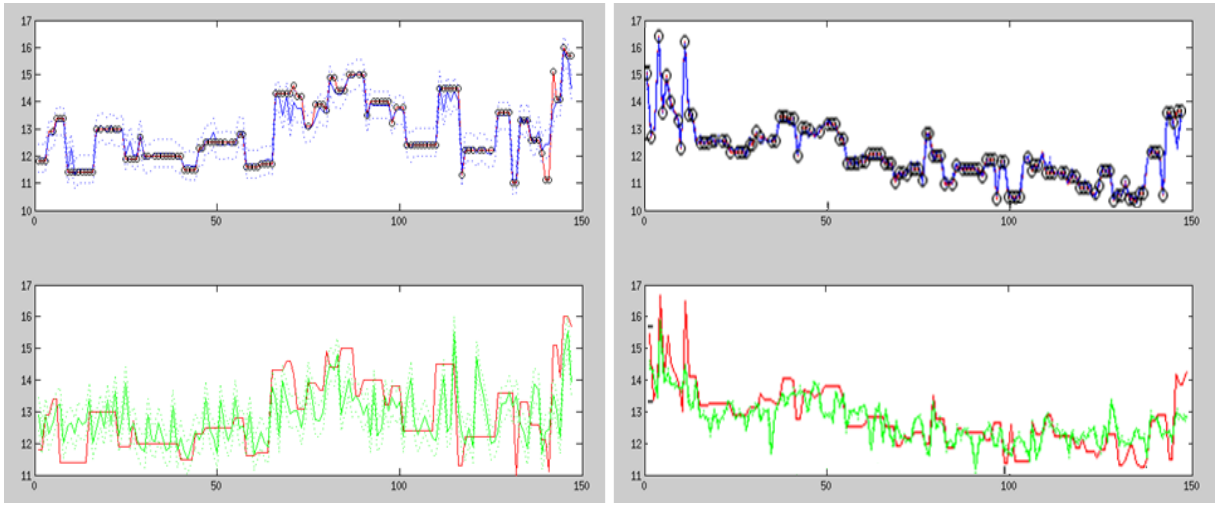

Figure 2: In these pictures the red line represents the original signal. Left graphs represent training (up) and test (down) signals for sugar indexes. Right are for acid.

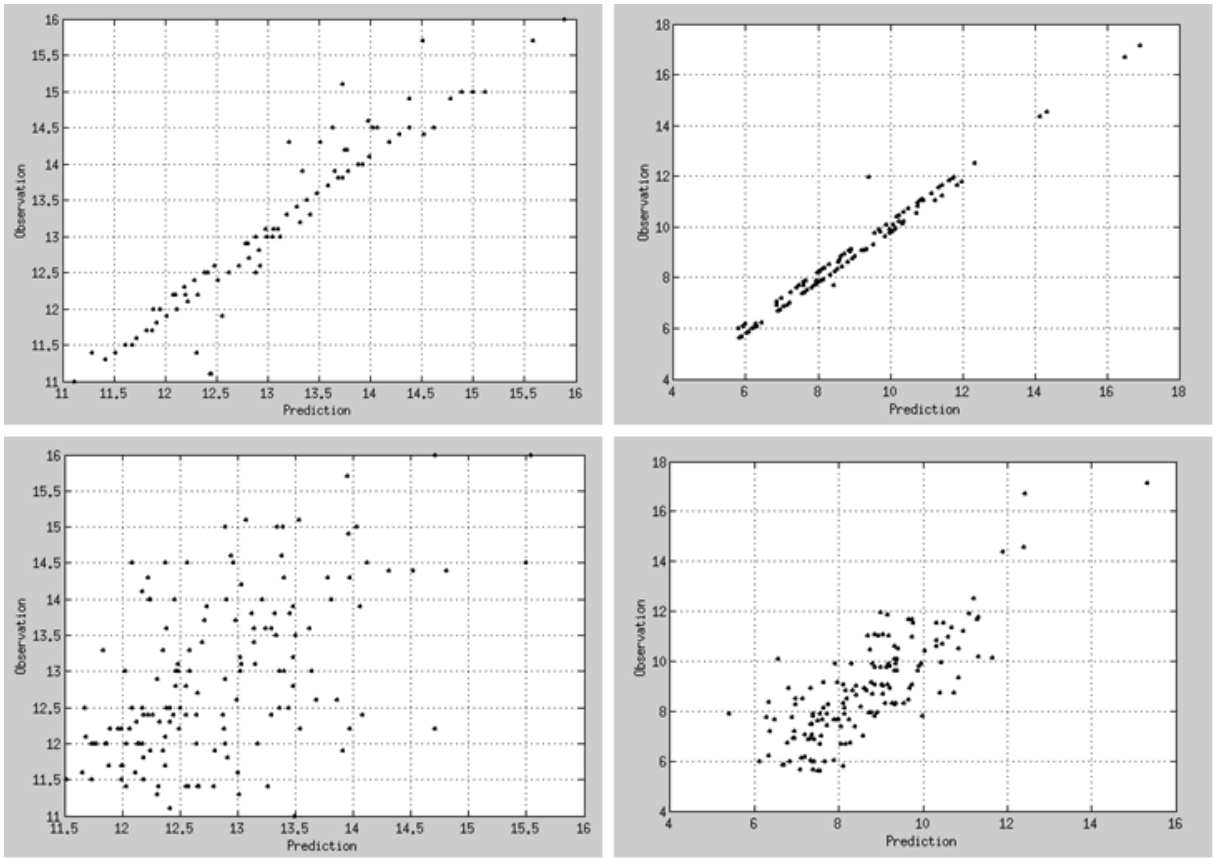

Figure 3: Top graphs represents observation versus prediction for training set. Below of them are located the graphs of the test set. Left are for sugar and right are for acid indexes.

4 Conclusions

The reproducibility and internal correlation of measurements made of our newly developed technique is high for both experiments.

After the experiment was done, an accuracy near to twenty per cent of error in sugar indexes and only ten per cent in acid indexes were obtained. This result implies that this method it is enough worthy to know beforehand the sugar and acid of an orange, and that information can be used by postharvest centers to choose the destination of every orange.

Acknowledgements

This work has been partially supported by projects CSD2007-00018 and PET2005-0643 from the Spanish Ministry of Science and Innovation, and by the project P1 1B2007-48 from Fundació Caixa-Castelló.

References

HSU C.-W., CHANG C.-C., LIN C.-J. (2003): A Practical Guide to Support Vector Classification, Technical Report, Department of Computer Science, National Taiwan University. [Online]. Available: www.csie.ntu.edu.tw/_cjlin/libsvm

LI, W., GOOVAERTS P., MEURENS M.(1996): Quantitative analysis of individual sugars ans acids in orange juices by near-infrared spectroscopy of dry extract, Journal of Agricultural and Food Chemistry, 44: 2252-2259

NICOLAÏ B.M., BEULLENS K., BOBELYN E., PEIRSA., SAEYS W., THERON K.I., LAMMERTYN J. (2007): Nondestructive measurement of fruit and vegetable quality by means of NIR spectroscopy: A review, Postharvest Biology and Technology, 46: 99-118

STEINMETZ V., BIAVATI E., MOLTÓ E., PONS R., FORNES I., (1995): Predicting the maturity of oranges with non destructive sensors, In Acta Hort. 421. Ed.: Th. H. Gieling, B. Bennedsen, W. T. M. van Meurs; 2nd International Symposium on Sensors in Horticulture, 421: 271-278

TSUCHIKAWA S., HAMADA T. (2004): Application of time-of-flight near infrared spectroscopy for detecting sugar and acid contents in apples, Journal of Agricultural and Food Chemistry, 54 (9): 2434-2439

Hyperspectral reflectance imaging for detecting defects on fruits

Byoung-Kwan Cho[1], Moon S. Kim[2], Man-Soo Kim[1]

[1] *Chungnam National University, Dept. of Bioindustrial Machinery Engr, Daejeon, Republic of Korea*
[2] *USDA-ARS, Food Safety Laboratory, Beltsville, MD, USA*
Corresponding author: chobk@cnu.ac.kr

Feasibility of hyperspectral reflectance imaging technique for the detection of defects underneath fruit skin was investigated. Defects exist underneath the fruit skin are not easily discernable by using conventional color imaging technique. Development of sensitive detection methods for the defects is necessary to ensure accurate quality sorting of fruits. Hyperspectral imaging techniques, which combine the features of imaging and spectroscopy to simultaneously acquire spatial and spectral information, have demonstrated good potentials for identifying and detecting spectral and spatial anomalies due to detects and contamination on biological substances. In this study, uses of a high spatial resolution hyperspectral reflectance are presented as tools for selecting multispectral VIS/NIR bands to detect defects on fruits. Several supervised classifiers are explored to select optimal wavebands and threshold values. Results demonstrated good potential of the hyperspectral reflectance imaging for detection of defects underneath the fruit skin.

Methods for head blight recognition: chlorophyll fluorescence and hyperspectral image analysis

Elke Bauriegel[1], Werner B. Herppich[1], Antje Giebel[1], Karl-Heinz Dammer[1], Horst Beuche[1], Joachim Intreß[1], Bernd Rodemann[2]

[1] *Leibniz Institute for Agricultural Engineering Potsdam-Bornim, Max-Eyth-Allee 100, D-14469 Potsdam, Germany*
[2] *Federal Research Centre for Cultivated Plants – Julius Kühn-Institut, Messeweg 11/12, D-38104 Braunschweig, Germany*
Corresponding author: ebauriegel@atb-potsdam.de

Fusarium infections on ears of cereal can cause yield losses. Mycotoxin contaminated products made from cereal grain can cause serious health problems in human and animal.

At present, the mycotoxin content of the grain are determined by time consuming and expensive laboratory methods like Fast-DON-ELISA-tests and HPLC at the harvest time.

The early recognition of head blight infected ears together with GPS could be helpful for a selective separated harvest of mycotoxin loaded crops.

The detection of diseased wheat ears caused by the pathogen *Fusarium culmorum* were tested by means of the two image analysis methods under laboratory conditions.

The chlorophyll fluorescence image analysis describes with the quotient of variable to maximal fluorescence the photosynthesis activity of plants. With cumulative Fv/Fm-value at 0.3 could distinguish the degrees of disease. The disease could already verify up to the 6th day after inoculation at plants with 5% symptoms.

As second method we used a hyperspectral scanner with the wavelength range of 400 nm to 1000 nm. Time series of images of healthy and artificially *Fusarium*-infected ears were recorded. The image analysis software ENVI was applied to define disease specific spectral signatures. Specific object classes were built as basis for classification of diseased and healthy ears. With ‘Spectral Angle Mapper’ as an appropriate method for classification healthy and diseased ear tissue could be clearly distinguished.

At time series analysis could not differ between diseased and healthy ears in the growth stage BBCH 65 (end of blooming) and during the ripeness (BBCH 85). Nevertheless a time frame of about ten days is open for a very good detection with both two methods.

Optical Analysis

for Agricultural Products and Processes

Quality control with NIRQuest

Near infrared spectroscopy is a great measurement method for sugar and moisture analyses. The NIRQuest spectrometer can measure up to 2500 nm and is an excellent sorting tool for quality grading of agricultural products.

PAR measurements with the Jaz light meter

The Jaz lightmeter is the universal tool for monitoring natural and artificial light conditions in greenhouses. The Jaz light meter gives you the full spectral information, but can also report in key parameters like PAR, Lumen, Lux and colour temperature.

Oxygen measurements with NeoFox

NeoFox is a fluorescence-based optical sensor system that can be used to monitor oxygen. NeoFox has fast response times and does not consume oxygen. In agricultural applications, optical oxygen sensors are used for soil oxygenation analysis, water quality analysis and fermentation and climate control.

Crop analysis using transmission and reflection measurements

Measuring the transmission and reflection of petals and leaves can be used for chlorophyll quantification, colour measurements, health and stress indication and environmental studies.

Ocean Optics

Ocean Optics EMEA | Maybachstrasse 11 | 73760 Ostfildern
www.oceanoptics.eu | info@oceanoptics.eu | +49 (0)711-341 696 0

Authors Index

In der Reihe
Bornimer Agrartechnische Berichte

sind bisher erschienen:

Heft 1	Technik und Verfahren der Landschaftspflege	1992
Heft 2	Beiträge zur Lagerung und Verarbeitung pflanzenbaulicher Produkte	1993
Heft 3	Technik und Verfahren in der Tierhaltung	1993
Heft 4	Technik und Verfahren der Landschaftspflege und für die Verwendung der anfallenden Materialien	1994
Heft 5	Verfahrenstechnik der Aufbereitung, Lagerung und Qualitätserhaltung pflanzlicher Produkte	1994
Heft 6	Biokonversion nachwachsender Rohstoffe und Verfahren für Reststoffbehandlung	1994
Heft 7	Preußische Versuchs- und Forschungsanstalt für Landarbeit und Schlepperprüffeld in Bornim 1927 bis 1945	1995
Heft 8	Qualitätssicherung und Direktvermarktung	1996
Heft 9	Konservierende Bodenbearbeitung auf Sandböden	1996
Heft 10	Anwendung wärme- und strömungstechnischer Grundlagen in der Landwirtschaft	1996
Heft 11	Computer-Bildanalyse in der Landwirtschaft Workshop 1996	1996
Heft 12	Aufbereitung und Verwertung organischer Reststoffe im ländlichen Raum	1996
Heft 13	Wege zur Verbesserung der Kartoffelqualität durch Verminderung der mechanischen Beanspruchung	1997
Heft 14	Computer-Bildanalyse in der Landwirtschaft Workshop 1997	1997
Heft 15	Technische und ökonomische Aspekte der Nutztierhaltung in großen Beständen	1997
Heft 16	11. Arbeitswissenschaftliches Seminar	1997
Heft 17	Nachwachsende Rohstoffe im Land Brandenburg Stand Aktivitäten und Perspektiven einer zukunftsfähigen und umweltgerechten Entwicklung	1998
Heft 18	Qualität von Agrarprodukten	1998
Heft 19	Computer-Bildanalyse in der Landwirtschaft Workshop 1998	1998
Heft 20	Beiträge zur teilflächenspezifischen Bewirtschaftung	1998
Heft 21	Landnutzung im Spiegel der Technikbewertung – Methoden Indikatoren, Fallbeispiele	1998

Heft 22	Kriterien der Nachhaltigkeit in der Verfahrensentwicklung für die Nutztierhaltung	1999
Heft 23	Situation und Trends in der Landtechnik / Erneuerbare Energien in der Landwirtschaft	1999
Heft 24	Institut für Landtechnik der Deutschen Akademie der Landwirtschaftswissenschaften zu Berlin 1951 bis 1965	1999
Heft 25	Computer-Bildanalyse in der Landwirtschaft Workshop 1999 / 2000	2000
Heft 26	Computer-Bildanalyse in der Landwirtschaft Workshop 2001	2001
Heft 27	Approaching Agricultural technology and Economic Development of Central and Eastern Europe	2001
Heft 28	6th International Symposium on Fruit, Nut, and Vegetable Production Engineering	2001
Heft 29	Measurement Systems for Animal Data and their Importance for Herd Management on Dairy Cow Farms	2002
Heft 30	Produktion, Verarbeitung und Anwendung von Naturfasern	2002
Heft 31	Computer-Bildanalyse in der Landwirtschaft Workshop 2002	2002
Heft 32	Biogas und Energielandwirtschaft - Potenzial, Nutzung, Grünes Gas^{TM}, Ökologie und Ökonomie	2003
Heft 33	Sozioökonomische Aspekte zu Perspektiven des Offenlandmanagements	2003
Heft 34	Computer-Bildanalyse in der Landwirtschaft Workshop 2003	2003
Heft 35	Energieholzproduktion in der Landwirtschaft Potenzial, Anbau, Technologie, Ökologie und Ökonomie	2004
Heft 36	High-Tech Innovationen für Verfahrensketten der Agrarproduktion. Statusseminar 2003	2004
Heft 37	Computer-Bildanalyse in der Landwirtschaft Workshop 2004	2004
Heft 38	Die Landmaschinenprüfung in der DDR 1951-1991 und ihre Vorgeschichte	2004
Heft 39	Energieverlust und Schimmelpilzentwicklung bei der Lagerung von Feldholz-Hackgut	2005
Heft 40	Computer-Bildanalyse in der Landwirtschaft Workshop 2005	2005
Heft 41	Demonstration der Langzeitwirkung bedarfsorientierter Fungizidbehandlung mit dem CROP-Meter	2005

Heft 42	Biochemicals and Energy from Sustainable Utilization of herbaceous Biomass (BESUB)	2005
Heft 43	Ozontes Waschwasser zur Qualitätssicherung leichtverderblicher Produkte - Entwicklung einer *Fuzzy-Logic*-Steuerung des Waschprozesses	2005
Heft 44	Messsystem zur Bewertung des Unkrautvorkommens	2005
Heft 45	Anwendung der Thermographie zur Optimierung der Belüftungssteuerung bei der Lagerhaltung landwirtschaftlicher Produkte	2005
Heft 46	Membranbioreaktor zur Aufbereitung von Schlachthofabwässern	
	Prozesssteuerung von Biogasanlagen mit Kofermentation	2005
Heft 47	Verschleißeinfluss auf das Förderverhalten von Drehkolbenpumpen	2005
Heft 48	Qualitätserhaltung und Qualitätssicherung von Bioobst und Biogemüse in der Nachernte	2005
Heft 49	Miniaturisiertes Datenerfassungs-System zum Implantieren in Früchte und zur Messung ihrer mechanischen Belastung durch Ernte- und Nachernteverfahren	2005
Heft 50	Prozesskontrolle der Qualität von frischem Obst und Gemüse mit Hilfe eines Multigas-Sensors	2005
Heft 51	Entwicklung eines Echtzeitsensors für die Stärkebestimmung bei Kartoffeln als funktionaler Bestandteil eines optoelektronischen Verleseautomaten	2005
Heft 52	Optimierte Steuerung von Getreide-Schachttrocknern	2005
Heft 53	Möglichkeiten und Grenzen der energetischen Nutzung von Rizinusöl	2005
Heft 54	Non-Destructive Methods for Detecting Health-Promoting Compounds COST Action 924 Working Group Meeting	2005
Heft 55	4^{th} IFAC / CIGR Workshop Control Applications in Post - Harvest and Processing Technology (CAPPT 2006) 26th - 29th March 2006, Potsdam, GERMANY	2006
Heft 56	Computer-Bildanalyse in der Landwirtschaft Workshop 2006	2006
Heft 57	Kontrolle der Frische in der Nacherntekette von Ökogemüse	2006
Heft 58	Entwicklung eines innovativen Dekontaminationsverfahrens als Technologieantwort auf zukünftiges Qualitätsmanagement im Nacherntebereich	2006

Heft 59	Experimental Studies and Mathematical Modelling of Solar Drying System for Production of High Quality Dried Tomato	2007
Heft 60	13. Workshop Computer-Bildanalyse in der Landwirtschaft & 4. Workshop Precision Farming	2007
Heft 61	Energiepflanzen im Aufwind Wissenschaftliche Ergebnisse und praktische Erfahrungen zur Produktion von Biogaspflanzen und Feldholz	2007
Heft 62	14. Workshop Computer-Bildanalyse in der Landwirtschaft	2008
Heft 63	Experten-Workshop Lagerung von Holzhackschnitzeln	2008
Heft 64	Postharvest unlimited 2008	2008
Heft 65	Vom Agrarrohstoff zu neuen Produkten – Verfahrens-technische Forschung im Nacherntebereich	2009
Heft 66	16. Arbeitswissenschaftliches Kolloquium des VDI-MEG Arbeitskreises Arbeitswissenschaften im Landbau	2009
Heft 67	Monitoring der methanbildenden Mikroflora in Praxis-Biogasanlagen im ländlichen Raum: Analyse des Ist-Zustandes und Entwicklung eines quantitativen Nachweissystems	2009
Heft 68	Wieviel Biogas steckt in Pflanzen? Abschluss- Symposium des "Biogas-Crops-Network" (BCN) 7. Mai 2009 Potsdam	2009
Heft 69	Image Analysis for Agricultural Products and Processes 15. Workshop Computer-Bildanalyse in der Landwirtschaft 27 to 28. Aug. 2009 Potsdam	2009

Interessenten wenden sich an:

Leibniz-Institut für Agrartechnik Potsdam-Bornim e.V.
Max-Eyth-Allee 100
14469 Potsdam

Tel.: (0331) 5699-820
Fax.: (0331) 5699-849
E-Mail: atb@atb-potsdam.de

Schutzgebühr: 13,- €